Development of Biomimetic MEMS Microphones Inspired by *Ormia Ochracea* Working in Audio Range

Yansheng Zhang

Department of Electronic and Electrical Engineering

University of Strathclyde

A thesis submitted for the degree of

Doctor of Philosophy

2019

Copyright

Signed: 张婉雯

Date: 28 Oct 2019

Dedicated to My Husband and My Parents

Table of Content

Abstract

The design, fabrication, characterization and analysis of two categories of novel Micro-electro-mechanical-system microphones inspired by the fly *Ormia ochracea*'s ears are presented in this thesis. The first category is the microphone composed of two coaxial single crystal silicon plates rotating along the same beam fixed to a certain thickness substrate that produces four resonance frequencies – two more resonance frequencies than previously published designs, which broadens the working frequency bands that having efficient directional response. Depending on the position of the torsional beam, the first can also be divided into two models: the symmetric dual-plate model and the asymmetric dual-plate model. Both models use the same fabrication process, and the mechanical vibrations of their diaphragms are sensed by deposited piezoelectric material. The symmetric dual-plate model offers sine dependence response at the two rocking modes and cosine dependence response at the bending modes. The asymmetric dual-plate is built to unify the directional response at four resonance frequencies. Its torsional beam is biased from the centre in order to create a mass difference between the diaphragm on the two sides of the torsional beam, which not only results in cosine dependence responses at all four resonance frequencies but also beyond the resonance. The second category is designed particularly for low-frequency hearing aids that enhances the acoustic response at low frequency band below 3 kHz. This microphone has two resonance frequencies of which one is down to 500 Hz, and it is also allocated both capacitive comb-finger sensing and piezoelectric sensing units. It has uniform bi-directional response below the frequency of interest.

Chapter 1 gives the basic knowledge of the acoustic and microphones as well as the literature review of *Omira ochracea* and its previous inspired microphones. Chapter 2 and Chapter 3 relate to the dual-plate multi-band operational microphones, including their modal analysis, finite element simulation and electrical measurement. Chapter 4 presents the MEMS microphone operating at low-frequency range. The noise performance is improved along with the development process. Chapter 5 summaries the features of each categories and lists the future work of the research.

Acknowledgements

Special thanks to Prof. James Windmill of Centre for Ultrasonic Engineering, Department of Electronic and Electrical Engineering, who is also my first supervisor, for all his knowledge, guidance and encouragement throughout the project and the preparation of this thesis. I would not accomplish this much without his support and understanding.

I also wish to thank Prof. Deepak Uttamchandani of the Centre for Microsystems and Photonics, Department of Electronic and Electrical Engineering, who is also my second supervisor, for all his patient mentor and continued inspiration during my research process.

Thanks to Dr. Ralf Bauer of the Centre of Microsystems and Photonics, Department of Electronic and Electrical Engineering for offering many suggestions regarding to design details and improvement of the devices as well as providing great experimental equipment training. Also, thanks to Dr. William Whitmer from MRC institute of Hearing Research (Scottish Section) who has a wealth of knowledge on hearing loss and heading aids for giving very much useful suggestions about designs.

Thanks to Dr. Andrew Reid of the Centre of Ultrasonic Engineering for helping take and providing the close X-ray images of interior of the insect's head. Additional thanks to Walter Galbraith and Thomas McCunnie for providing advice regarding to analogue circuit design and helping to build anechoic box for testing, respectively.

I am also thankful for the understanding, patience, and encouragement from my husband, Dr. Chuangnan Wang.

Finally, great thanks goes to everyone in Centre for Ultrasonic Engineering and Centre for Microsystem and Photonics and for everyone who helped me along the way.

This work has been supported in part by the EPSRC under Grant EP/M026701/1 and in part by the European Research Council through the European Union's Seventh Framework Programme under Grant FP/2007-2013 and ERC under Grant 615030.

List of Figures

List of Tables

List of Symbols

Chapter 2

c	Sound speed
B	Adiabatic bulk modulus of the medium
ρ_0	Density of the medium
V_0	Initial volume of a collection of medium particles
dP	Differential pressure change
dV	Differential volume change
P_o	Initial pressure
C_p	Constant pressure
C_T	Constant temperature
γ	Adiabatic index
n	Number of moles
R	Molar gas constant ≈ 8.315 $J{\cdot}mol^{-1}{\cdot}K^{-1}$
T_0	Absolute initial temperature
T	Environmental temperature in degree Celsius
I	Sound intensity
W	Sound power at the measured surface
R_d	Distance from the sound source to the measured point
p	Sound pressure
SPL	Sound pressure level
p_r	Reference sound pressure
IL	Sound intensity level
I_r	Reference intensity corresponding to the reference pressure
ω	Angular frequency of the plane wave
k	Wave number
p_a	Amplitude of the plane waves
t	Time
v	Particle velocity
Z_s	Acoustic impedance
Z_0	Characteristic impedance
$\boldsymbol{k}$	Vector of the wave number
$\boldsymbol{r}$	Vector displacement in r direction
$S(r)$	Surface area of the wavefront at point r
DI	Directional index
W_{ref}	Sound power picked up from the reference direction
W_{total}	Total integrated sound power from all directions

E_0	Maximum acoustic response in directional polar pattern
θ	Sound incident angle with respect to the axis normal to the active surface of the acoustic device
U	Voltage
Q	Charge
d	Distance between the two paralleled plates of a capacitor
ε	Permittivity constant of the medium between the two plates of capacitor
A	Overlapped area of the two paralleled plates
F_e	Electrostatic force
x_0	Initial distance between two paralleled plates of a capacitor
D_i	Electrical displacement matrix
d_{ij}	Piezoelectric coefficient matrix
T_{ij}	Mechanical stress matrix
ε_{ij}	Electrical permittivity matrix
E_i	External applied electric field matrix
$\boldsymbol{[M]}$	Mass matrix of diaphragms
m	Mass of the diaphragm
$\boldsymbol{[C]}$	Mechanical damping matrix
C	Mechanical damping
$\boldsymbol{[K]}$	Mechanical stiffness matrix
K	Mechanical stiffness
$\boldsymbol{x(t)}$	Mechanical displacement response matrix in time domain
$\boldsymbol{f(t)}$	Applied mechanical force matrix in time domain
$x(\omega)$	Mechanical response in frequency domain
S	Frontal surface area of a diaphragm
ω_r	Eigen-frequency (angular) at rocking mode
ω_t	Eigen-frequency (angular) at translational (bending) mode
P	Sound pressure
τ	Time delay of the sound waves reaching to the two diaphragms
d_D	Distance between the particles of two diaphragms
$\boldsymbol{[X]}$	Modal matrix
$\boldsymbol{[q(t)]}$	Modal participation coefficient matrix in time domain
$\boldsymbol{[X]^T}$	Transposed model matrix

X_r	Modal at rocking mode
X_t	Modal at translational mode
$[\boldsymbol{q}(\boldsymbol{\omega})]$	Modal participation coefficient matrix in frequency domain
A_r	Amplitude of displacement of two diaphragms at rocking mode
A_t	Amplitude of displacement of two diaphragms at translational mode
Γ	Relative contributions of the rocking mode and the banding mode subject to unit modal force
Ω	Normalized excitation frequency
η	Eigen-frequency ratio
mIPD	Mechanical interaural phase difference
DS	Directional sensitivity

Chapter 3

[M]	Mass matrix
[C]	Mechanical Damping matrix
[K]	Mechanical stiffness matrix
[x(t)]	Mechanical displacement in time domain
m_i	Participating mass concentrated on the centroid of each diaphragm
c_i	Damping coefficient around each diaphragm
k_i	Stiffness transferred from the torsional stiffness of the central beam that is distributed on each diaphragm
c_{ij}	Damping coefficient between two adjacent diaphragms
k_{ij}	Stiffness coefficient between two adjacent diaphragms
$\boldsymbol{A}$	A square matrix
λ	Eigen values
$\boldsymbol{I}$	Identity matrix
$\boldsymbol{x}$	Eigenvalue vectors
f_{ni}	Eigen-frequencies
m_O	Participating mass concentrated on the centroid of one outer diaphragm
m_I	Participating mass concentrated on the centroid of one inner diaphragm
k_O	Stiffness transferred from the torsional stiffness of the central beam that is distributed on each outer diaphragm

k_I	Stiffness transferred from the torsional stiffness of the central beam that is distributed on each inner diaphragm
k_{c1}	Coupling stiffness between the inner diaphragms and the outer diaphragms on the same side
k_{c2}	Coupling stiffness between the inner diaphragms and the outer diaphragms on the opposite side
k_{t1}	Coupling stiffness between two outer diaphragms
k_{t2}	Coupling stiffness between two inner diaphragms
$\mathbf{[}S_{stiffness}\mathbf{]}$	Stiffness matrix of the material

Chapter 4

$[d_{ij}]$	Piezoelectric coefficient matrix
Q_p	Equivalent charge source of a piezoelectric sensor
R_p	Equivalent insulation leakage resistor of a piezoelectric sensor
C_p	Equivalent shunt capacitor of a piezoelectric sensor
C_c	Capacitance of interface cable between the microphone and the preamplifier
R_i	Total resistance of the interface cable between the microphone and the preamplifer
R_f	Feedback resistor between the output and the inverting input of the preamplifier
C_f	Feedback capacitor between the output and the inverting input of the preamplifier
V_O	Output voltage of the preamplifier
V_p	Voltage generated by the piezoelectric sensor
f_L	Low cut-off frequency
f_H	High cut-off frequency
R_b	Bias resistor
R_g	Gain resistor of preamplifier
R_1	Feedback resistor in the input buffers of an instrumentation amplifier
mSD_{ij}	Mechanical sensitivity difference
OL	Outer larger Plate
IL	Inner larger Plate

OS	Outer smaller plate
IS	Inner smaller plate

Chapter 5

I	Mass moment of inertia of the entire membrane about the rotational beam
M_1	Participating mass concentrated on one diaphragm
M_2	Participating mass concentrated on another diaphragm
α	Mass ratio of two diaphragms
K_t	Torsional stiffness of the rotation beam
K_b	Total bending stiffness of the bridges
L	Distance between the centroid of each diaphragm and the rotation beam
ω	Driving frequency
$\theta(\omega)$	Angular displacement of the diaphragms about the rotation beam in frequency domain
$X(\omega)$	Mechanical displacement of diaphragms in frequency domain
$F(\omega)$	Effective forces placed on the diaphragms in frequency domain
β	Ratio of distance between the centroid of each diaphragm and the rotation beam
Ω	Normalized driving frequency
ω_r	Eigen-frequency (angular) of the rocking mode
ω_b	Eigen-frequency (angular) of the bending mode
A_r	Mechanical displacement amplitude of diaphragms at the rocking mode
A_b	Mechanical displacement amplitude of diaphragms at the bending mode
d_{bias}	Bias value of the torsional beam relative to the centre of the plate
θ_c	Angular difference between the central lines of moveable and fixed capacitive fingers
D_{disp}	Displacement amplitude measured at the end of the moveable finger relative to the central line

θ_x	Rotation angle of the spring along the x-axis
T_V	Internal virtual torque applied on the spring
T_R	External real torque applied on the spring
M_V	Internal virtual torsion moment applied on the spring
M_R	External real torsion moment applied on the spring
EWD	Work done by the external work
IWD	Work done by the internal stresses
l_{beam}	Length of each spring beam section
M_x	Torsion moment applied on the spring in x-axis
N	Number of groups of folded beams
l_{t1}	Length of the initial beam
l_{t2}	Length of the middle beams
l_{t3}	Length of the final beam
J_{t1}	Torsion constant of the initial beam
J_{t2}	Torsion constant of the middle beams
J_{t3}	Torsion constant of the final beam
I_s	Moment of inertia of the beams along the y axis distributed in the middle
w	Width of spring beams
t	Thickness of spring beams
G	Shear modulus
$V_{op}(\omega)$	Measured output voltage of the piezoelectric sensing in frequency domain
H_{vx}	Transfer functions between the open-circuit voltage at the output stage of the piezoelectric ports corresponding to each diaphragm
$C_{sensor}(\omega)$	Total capacitance of the comb fingers in the frequency domain
V_{bias}	Bias voltage on the charge amplifier

Chapter 1

Introduction

1.1 Introduction and research motivation

The first MEMS (Micro-Electro-Mechanical-Systems) microphone was invented in 1980s. Since then, the development of MEMS microphone has been growing dramatically, which is as a result of continuously developing portable electronic devices, voice controlling systems (e.g. smart home and self-driving cars), and medical applications (e.g. hearing aids), etc. Similar to other MEMS force sensors, MEMS microphone (i.e. MEMS acoustic sensors) can be designed with different sensing technologies including capacitive parallel plates or comb-finger structure, piezoelectric sensing, piezoresistive, optical, etc. Each of these technologies has their pros and cons, and they are chosen depending on requirements (e.g. SNR, directional performance, environmental and cost limitations) of different applications. Also, like conventional microphones, MEMS microphones can be designed to have omnidirectional or directional (e.g. bi-directional, unidirectional, etc) performance. The omnidirectional microphones are widely used in acoustic measurement such as noise recoding as it has flat acoustic response against different sound incident angles. Contrary to the omnidirectional microphone, a directional microphone picks up sound with higher gain in one or two specific sound incident directions. This kind of microphones benefits from noise cancelling and is normally applied in voice recording devices, especially in the environment with complex background noise. Currently, the directional microphones can be achieved by microphone arrays which confirm sound incident angle via time difference of sound arrivals between each array element. Another commonly used design is to build a thin membrane with both sides exposed to the sound propagation medium, which introduces sound pressure gradient that has certain relationship with the sound incident angle to the membrane. In order to get

sufficient detectable sound pressure, this kind of MEMS microphones has carefully designed tubes at both sides of the membrane which generates time delay when sound waves reach to the both sides of the membranes through these tubes. In addition, in terms of the single thin membrane design structure, it usually has lower acoustic response in low frequency range as its small dimension results in a higher resonance frequency above the interested frequency range.

In last decade, scientist found one solution that may breakthrough this size limitation of the directional microphone in the hearing mechanism of one type of parasitoid flies, called *Ormia ochracea*. This tiny creature can localize its host crickets mating calls in an extremely high accuracy due to the mechanical coupling between its two tympana linked via a bridge tissue, although the width of this entire hearing organ is less than 2 mm. Even so, its hearing organ has most sensitivity response at 5 kHz which is far below the maximum audio frequency (i.e. 20 kHz) and the resonance frequency of the directional MEMS microphone just with single thin membrane. Due to its size advantage and simple structure, many researchers have developed *Ormia*-inspired MEMS directional microphones during last couple of years based on different applications, from human speech recognition devices to ultrasonic transducers. Most of designs consist of two membranes or plates representing the two tympana of this insect and a mechanical linking part mimicking the bridge tissue between the tympana. Meanwhile, at two points of the structure are fixed to the substrate so that the entire structure performing like a see-saw where the membranes (or the plates) vibrating out of phase at the 1st resonance frequency while they vibrating in phase at the 2nd resonance frequency. According to the measuring parameter, the *Ormia*-inspired MEMS microphone can be divided into two main categories – the one based on measuring the amplitude of acoustic response and the other one based on the differential phase measurement of acoustic response. The microphones based on the amplitude measurement utilizes the sinusoidal relationship between the displacement amplitude of the membranes and sound incident angles at the 1st resonance frequency while the microphones measuring the differential phase value between the membranes which is theoretically linear to the sound incident angles between $\pm 30°$. However, both types of *Ormia*-inspried MEMS microphones have their own shortcomings. For the differential phase measurement design, the membranes are usually clamped at the

circumference hence they do not provide sufficient movement in the membranes, which needs a precise but costly sensing unit (e.g. optical sensing) that are able to detect time differences between electrical signals. In terms of the amplitude measurement designs, as they only have high frequency responses around one or two resonance frequencies, but low response at the frequencies off the main resonance, the SNR of the devices is high across the frequency of interest which is not ideal for human speech recognition applications.

In this thesis, a dual plate multi-band operational *Ormia*-inspired MEMS microphone model will be introduced, which is an amplitude measurement based design. This type of microphone has four resonance frequencies. The overlap of the working frequency bands around two adjacent resonance frequencies increases the overall acoustic frequency response. In other words, it increases the average SNR of the microphone. Several prototypes designed based on this concept will be presented. In addition, the displacement of most previous MEMS designs measuring amplitude is sensed by capacitive sensing units. The unavoidable charge pump is included in the package of the capacitive sensing unit to supply bias voltage which increases the start-up time of the devices. Also, the capacitive microphones are sensitive to dust or moisture due to the air gap between the capacitor electrodes. In this thesis, an Aluminium Nitride (AlN) piezoelectric sensing unit is introduced into all fabricated prototypes. The piezoelectric material generates charge (or voltage potential) only due to the stress applied and so these do not need any charge pump. As there is no capacitive gap, the piezoelectric system is more robust and can handle adverse working conditions. In addition, a piezoelectric *Ormia*-inspired MEMS microphone specified for low-frequency applications will be introduced. This approach enhances the acoustic sensitivity at frequencies below 3 kHz but is achieved by a simple plate structure and a S-type rotating beam which was used be implemented by complex cross beam support structure in the designs from other research group.

1.2 Structure of the thesis

This thesis has five chapters:

Chapter 1 gives a brief introduction on what the MEMS microphones and *Ormia*-inspired microphones are. It also summarizes the advantages as well as the challenges owned by each type of design models that turns into the motivation of the studies which will be described in this thesis.

Chapter 2 gives a literature review of acoustic foundation, history of MEMS microphone development and principle of *Ormia*-inspired microphone.

Chapter 3 firstly introduces a dual-plate *Ormia*-inspired microphone model that has two coaxial plates and theoretically gives four resonance frequencies to expand the frequency range having directionality. In spite of mechanical connection between two plates, each plate has similar mechanical performance as *Ormia*'s hearing organ but not affects each other. This phenomenon can be concluded that each plate independently provides two resonance frequencies to the entire design and the design has directionality at both corresponding resonances.

Chapter 4 shows the design process and characterization of two piezoelectric microphones designed based on the concept model introduced in Chapter 2. Both two microphones have AlN piezoelectric deposited on cantilevers connecting to the vibrational masses. However, one of devices has symmetric mass distribution and the other has asymmetric distribution. The effects of such mass distribution difference on the acoustic response and directionality are discussed in this chapter.

Chapter 5 introduces the first dual-sensing *Ormia*-inspired MEMS microphone operating at low frequency range. It also further explains the reason causing different acoustic response and directionality of *Ormia*-inspired microphones due to different mass distribution and the backside structure of the microphone. This low-frequency operational microphone integrates both piezoelectric and capacitive sensing units.

Chapter 6 summarizes the features of microphones shown in the last two chapters, including their advantages, shortcomings and possibilities of improvement.

1.3 Related publications

1) Y. Zhang, R. Bauer, J.C. Jackson, W. Whitmer, JFC Windmill, and D. Uttamchandani, "A low frequency dual-band operational microphone mimicking the hearing property of *Ormia ochracea*", *Journal of Microelectromechanical Systems*, vol. 27, no. 4, pp 667-676, 2018
2) Y. Zhang, A. Reid, JFC Windmill, "Insect-inspired acoustic micro-sensor", *Current Opinion in Insect Science*, vol. 30, pp 33-38, 2018
3) R. Bauer, Y. Zhang, J.C. Jackson, W. Whitmer, WO Brimijoin, MA Akeroyd, D. Uttamchandani, and JFC Windmill, "Influence of microphone housing on the directional response of piezoelectric MEMS microphones inspired by *Ormia ochracea*", *IEEE Sensors Journal*, vol. 17, pp. 5529-5536
4) Y. Zhang, R. Bauer, W. Whitmer, J.C. Jackson, JFC Windmill, and D. Uttamchandani, "A MEMS microphone inspired by *Ormia* for spatial sound detection", in *2018 IEEE MEMS*, Belfast, UK
5) Y. Zhang, R. Bauer, J.C. Jackson, W. Whitmer, D. Uttamchandani, JFC Windmill, and JC Jackson,
6) "Development of biologically inspired MEMS microphone", in 2017 *IEEE Sensors*, Glasgow, UK
7) R. Bauer, Y. Zhang, J.C. Jackson, W. Whitmer, WO Brimijoin, MA Akeroyd, D. Uttamchandani, and JFC Windmill, "Housing influence on multi-band directional MEMS microphones inspired by *Ormia ochracea*", in *2016 IEEE Sensor*, Orlando, USA
8) Y. Zhang, R. Bauer, JFC Windmill, and D. Uttamchandani, "Multi-band asymmetric piezoelectric mems microphone inspired by the *Ormia ochracea*", in *2016 IEEE MEMS*, Shanghai, China
9) Y. Zhang, JFC Windmill, and D. Uttamchandani, "Biomimetic MEMS directional microphone structure for multi-band operation", in 2014 IEEE Sensor, Valencia, Spain

Chapter 2

Literature Review

Since the first commercial MEMS microphone – SiSonic was released by Knowles in 2011, MEMS microphones have been widely used in mobile applications such as smartphones, laptops, hearing aids, digital assistants, etc. due to their extremely small footprint, high signal to noise ratio and lower power consumption compared to traditional electret condenser microphones. They have been developed from an individual recording device to an array used in smart speakers. Such increasing high-level integration of applications requires the microphones with smaller dimension but higher sensitive response. Therefore, a part of researchers is turning their interest to the biomimetic field and trying to find the solution by learning superiority of the hearing system of the insects, as well as this thesis.

This chapter firstly introduces the basic acoustic theory. The basic acoustic theories are the foundation of acoustic simulation, which are also the guidelines of developing new microphones. To grasp these basic theories will help to understand the sound field surrounded and the directionality of microphones.

The second section of this chapter enumerates important inventions in the history of microphone development and the explains their working principles. By separating the microphones into different types based on their sensing technologies, this part also recounts the reasons of each types of microphone's invention, their pros and cons, and even the reasons of elimination.

The third section relates to the MEMS directional microphones inspired by fly *Ormia ochracea*'s hearing mechanism, introducing from basic mechanical principles of the *Ormia*'s ears to the previous models and designs. Comparing the distinguishing features of each design is the foremost topic of this section.

Last but not least, the fourth section describes the original intentions of this research, following the shortcomings summarized in the third section.

2.1 Basic acoustic theories

2.1.1 Sound propagation and speed

A wave is a disturbance containing pieces of information transferring from one point to another in a medium, except for electromagnetic waves that do not require a medium. Those waves that require a medium are also called mechanical waves. In terms of wave motion, this can be grouped into two categories: longitudinal waves and transverse waves. In a longitudinal wave the particle displacement is parallel to the direction of propagation; in a transverse wave the particle displacement is perpendicular to the direction of propagation. Sound waves, generated by a vibrating source (i.e. a sound source), are typical mechanical waves that travel through compressible media. They can be longitudinal waves when propagating through gas, liquid and solids or transverse waves in solids (e.g. shear waves).

At first, Newton assumed sound transmission was an isothermal process, however the calculation did not match with the experimental results. When the sound source continues to vibrate the medium, the formed sound waves cause oscillations in pressure, but the oscillations are too fast to allow heat transfer from the compression regions (where the particles are closest together) to rarefaction regions (where the particles are furthest apart) in order to keep the temperature constant. Therefore, sound transmission is an adiabatic process. The speed of sound c is often defined by the adiabatic bulk modulus B of the medium as follows [1]

$$c = \sqrt{\frac{B}{\rho_0}}, \qquad [2.1]$$

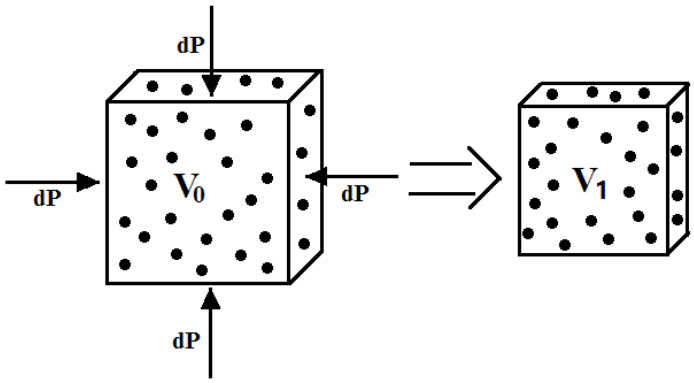

Fig. 2.1 The volume of a collection of particles is changed by differential pressure dP

where ρ_0 is the density of the medium. The adiabatic bulk modulus is a numerical constant that describes the compressibility of the medium. As this research work is related to air coupled microphone designs, in this dissertation there is a focus on the problems of sound transmission in air. Assuming that the volume of a collection of particles changes from V_0 to V_1 due to the change of pressure on the object (see Fig. 2.1), the adiabatic bulk modulus can be expressed as

$$B = -V_0 \frac{dP}{dV}, \qquad [2.2]$$

where dP is the differential pressure change on the particle collection and dV is the differential volume change. For an ideal gas, B is given by

$$B = \gamma P_0, \qquad [2.3]$$

where γ is the adiabatic index which is the ratio of specific heats of a gas at a constant pressure (C_p) to a gas at constant temperature (C_T), and P_0 is the initial pressure. For diatomic gases like O_2 and N_2, $\gamma = 1.4$. For monatomic gases like He, $\gamma = 1.67$. As air is mostly diatomic, the adiabatic index γ is equal to 1.41. At standard room temperature and pressure, the adiabatic bulk modulus B of air is equal to 1.41×10^5Pa and its density is about 1.225 kg·m^{-3}. Therefore, the speed of air is around 340 m·s^{-1}. Additionally, considering the ideal gas law as follows

$$P_0 V_0 = nRT_0, \qquad [2.4]$$

an alternative expression for the sound speed, found by substituting Eq. 2.3 and 2.4 to Eq. 2.1, is

$$c = \sqrt{\frac{n\gamma RT_0}{\rho_0 V_0}}, \quad [2.5]$$

where n is the number of moles, R is the molar gas constant (approximately 8.315 $J \cdot mol^{-1} \cdot K^{-1}$), and T_0 is the absolute initial temperature. Therefore, the sound speed of air depends on the density, which is affected by the environmental humidity and altitude. Also, the sound speed in the air is influenced by the environmental temperature. As most acoustic validation is done indoors, the sound speed of air is given by the following equation:

$$c = 331.4 + 0.607 \times T, \quad [2.6]$$

where *T* is the environmental temperature in degree Celsius.

2.1.2 Acoustical power

A mechanical wave transfers energy in the same direction as wave propagation, and a sound wave is no exception. Usually, the sound energy is indicated by sound intensity and sound pressure. The sound intensity *I* is the rate of sound power flow per unit area ($W \cdot m^{-2}$). The intensity at any distance from the sound source is given by [2]:

$$I = \frac{W}{4\pi R_d^2}, \quad [2.7]$$

where W is the sound power at the measured surface and R_d is the distance from the source. When the distance between the source and the measured point doubles, the intensity decreases to one-fourth of the original. This relationship is also called the *inverse-square law*.

As well as sound intensity, the strength of the sound can also be determined by measuring the sound pressure. The sound pressure *p* is the local pressure deviation between the pressure produced by sound wave and the ambient pressure. The relationship between the sound intensity and sound pressure can be expressed as

$$p = \sqrt{I\rho_0 c}. \quad [2.8]$$

Normally, the sound pressure is indicated by “decibel” instead of Pascal. One of the main reasons for this is for convenience of dealing directly with the enormous range of sound pressure. Another reason is that it can be somewhat better matched with the human sense of hearing. The converted value of sound pressure is also called sound

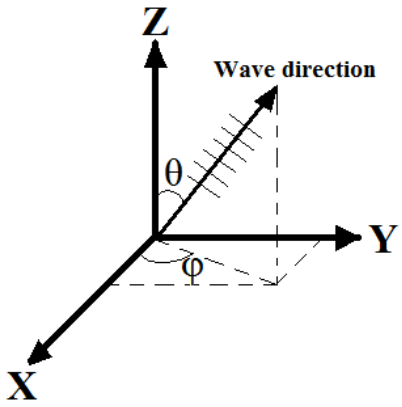

Fig. 2.2 A plane wave travelling in an arbitrary direction

pressure level (SPL), which is defined as the logarithmic measure of sound pressure relative to a reference value as follows

$$\mathrm{SPL} = 20\log_{10}\left(\frac{p}{p_r}\right) \qquad [2.9]$$

where p_r is the reference sound pressure. It is equal to $20\mu\mathrm{Pa}$ in air which is commonly considered as the threshold of human hearing. The upper limit of human hearing is about 10 Pa. In other words, the lower limit of human hearing is 0 dB while the normal maximum sound pressure level for human hearing is over 100 dB. The sound intensity (IL) can also be denoted with a decibel scale, the intensity level:

$$\mathrm{IL} = 10\log_{10}\frac{I}{I_r}, \qquad [2.10]$$

where I_r is the reference intensity corresponding to the reference pressure.

2.1.3 Lumped element model and plane waves

When a sound wave only propagates in one direction, the amplitude and the phase of the instantaneous sound pressure are constants on any plane perpendicular to this direction. In other words, the sound wave is harmonic and homogenous. Such a wave is called a plane wave. Assuming that a plane wave propagates in some arbitrary direction as shown in Fig. 2.2, the complex exponential form of sound pressure at a given point can be written as a time function in the Cartesian coordinate system as follows

$$p(x,y,z,t) = p_a e^{j(\omega t - k_x x - k_y y - k_z z)},$$

$$k_x = k\sin\theta\cos\varphi\,, k_y = k\sin\theta\sin\varphi\,, k_x = k\cos\theta, \qquad [2.11]$$

where ω is the angular frequency of the plane wave, k is the wave number equal to ω/c and p_a is the amplitude of the plane waves.

As a macroscopic phenomenon, the sound wave should satisfy three fundamental physical constraints: *Newton's Second Law*, *Conservation of Mass* and the *Equation of State*. In order to simplify a numerical analysis, a list of assumptions is made as follows

1) The medium is an ideal fluid (including idea gas), in other words, the forces related to the viscosity of the air are negligible.
2) When there is no sound disturbance, the initial velocity of the particles of the medium is zero. Meanwhile, the medium is homogenous, hence the static pressure and density are constants.
3) The rapid sound pressure variations do not allow heat transfer within the medium or to the surroundings (i.e. the adiabatic condition).
4) All the sound induced variations $p(x,y,z,t)$, $\rho(x,y,z,t)$ and $\mathrm{T}(x,y,z,t)$ are much smaller than their static value. The particle velocity $v(x,y,z,t)$ is small compared to the propagation velocity c.

These assumptions are used for all analytical models and simulations presented in this thesis.

Considering a plane wave only flows through a volume element in the z direction as shown in Fig. 2.3, the complex exponential form of sound pressure can be written as follows [3]

$$p(z,t) = p_a e^{j(\omega t - k_z z)}. \qquad [2.12]$$

First of all, the equation deviated from Newton's Second Law can be expressed as follows

$$\frac{\partial p(z,t)}{\partial z} = -\rho_0 \frac{\partial v(z,t)}{\partial t}. \qquad [2.13]$$

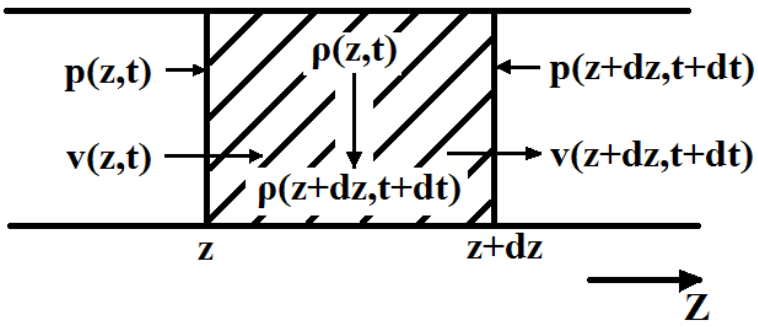

Fig. 2.3 A volume element in a one-dimensional fluid medium

Therefore, substituting Eq.2.12 to Eq. 2.13, the related particle velocity is derived as

$$v(z,t) = \frac{p_a}{\rho_0 c} e^{j(\omega t - k_z z)}. \qquad [2.14]$$

As the plane waves are homogenous (i.e. both instantaneous sound pressure and particle velocity vary linear throughout the medium), it can also be simplified using a lumped element model. Like other lumped element models, such as a frictionless mechanical model that only has a particle imposed by a force *f(t)* then moving in a velocity $v_m(t)$ or an electrical model where a voltage difference *e(t)* across a resistor R_e produces a current *i(t)*, the lumped acoustic model also has an 'across' variable and a 'throughout' variable as shown in Fig. 2.4. Table 2.1 summarizes the 'across' variables and corresponding 'through' variables in all these three typical lumped element models. As a lumped element model, it not only has 'across' variables and 'through' variables,

	'Across' variable	'Through' variable
Mechanical	Force *f(t)*	Velocity $v_m(t)$
Electrical	Voltage *e(t)*	Current *i(t)*
Acoustical	Sound pressure *p(t)*	Particle velocity *v(t)*

Table 2.1 The 'across' variables and 'through' variables of each lumped element model

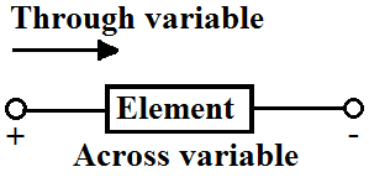

Fig. 2.4 The structure of a basic lumped element model

but also requires 'impedance' to describe the relationship between these two main variables. In terms of the lumped acoustic model, the acoustic impedance Z_s plays an important role to define the relationship between the instantaneous sound pressure and instantaneous particle velocity. For a one-dimensional plane wave travelling in the z direction, the equation of acoustic impedance is given by [1]

$$Z_s = \frac{p(z,t)}{v(z,t)} = \rho_0 c. \qquad [2.15]$$

The $\rho_0 c$ is also called the characteristic impedance Z_0, which is a parameter only depending on the property of the medium.

Returning to the wave equations, the equation of Conservation of Mass is given by

$$\rho_0 \frac{\partial v(z,t)}{\partial z} = -\frac{\partial \rho(z,t)}{\partial t}. \qquad [2.16]$$

It can be interpreted such that the change in the density as a function of time is proportional to the net velocity entering and leaving the volume element. Finally, the equation of state is

$$\rho(z,t) = \frac{1}{c^2} p(z,t). \qquad [2.17]$$

Taking the partial of both sides of Eq. 2.13 with respect to *z* and the partial of both sides of Eq. 2.16 with respect to *t*, then substituting them into Eq. 2.17 the results yields the one-dimensional wave equation referring to sound pressure in z direction and time *t*,

$$\frac{\partial^2 p(z,t)}{\partial z^2} = \frac{1}{c^2} \frac{\partial^2 p(z,t)}{\partial t^2}. \qquad [2.18]$$

By eliminating $p(z,t)$ and $\rho(z,t)$ or $p(z,t)$ and $v(z,t)$, it is also easily to obtain the wave equation associated with particle velocity variation $v(z,t)$ or density variation $\rho(z,t)$.

2.1.4 Spherical waves and far field

In practice, plane waves are hard to find since the amplitude of sound pressure changes with the distance to the source as described in section 2.2.2. Sound waves whose amplitude is inversely proportional to the distance from the origin are described

as spherical waves. Considering a spherical wave that travels in the vector $\boldsymbol{r}$ direction, the instantaneous sound pressure of such a spherical sound wave is given by [4]

$$\mathrm{p}(r,t) = \frac{p_a}{r} e^{j(\omega t - \boldsymbol{k}\cdot\boldsymbol{r})} \qquad [2.19]$$

where $\boldsymbol{k}$ is the vector of the wave number. Again, the three physical constraints in section 2.2.3 are applied to explore such sound waves. The equation of Newton's Second law can be expressed as [4]

$$\frac{\partial p(r,t)}{\partial r} = -\rho_0 \frac{\partial v(r,t)}{\partial t}. \qquad [2.20]$$

As the state equation is not relative to the volume element, it is similar to Eq. 2.18 but replacing *z* with *r* as

$$\rho(r,t) = \frac{1}{c^2} p(r,t). \qquad [2.21]$$

Moreover, basing on the Conservation of Mass, the net mass entering the volume element equals the increased mass in the element varying with time. Assuming that the surface area of the wavefront at point *r* is *S(r)*, the equation of Conservation of Mass can be written as follow [4]

$$\rho_0 \frac{\partial (v(z,t)S(r))}{\partial r} = -S(r) \frac{\partial \rho(r,t)}{\partial t}. \qquad [2.22]$$

Multiplying c^2/S on both sides of Eq. 2.22, then taking the partial of both side of 2.21 with respect to *t* and substituting $S(r) = 4\pi r^2$, the wave equation of a spherical wave is derived as

$$\frac{\partial^2 p(r,t)}{\partial r^2} + \frac{2}{r}\frac{\partial p}{\partial r} = \frac{1}{c^2}\frac{\partial^2 p(z,t)}{\partial t^2}. \qquad [2.23]$$

According to Eq. 2.20, the instantaneous particle velocity is

$$v(r,t) = \frac{p_a}{r\rho_0 c}\left(1 + \frac{1}{j\boldsymbol{k}\cdot\boldsymbol{r}}\right) e^{j(\omega t - \boldsymbol{k}\cdot\boldsymbol{r})}. \qquad [2.24]$$

Therefore, the acoustic impedance $Z_s(r)$ of a spherical wave is

$$Z_s(r) = \frac{p(r,t)}{v(r,t)} = \frac{\rho_0 c}{1+\frac{1}{j\boldsymbol{k}\cdot\boldsymbol{r}}} = \frac{Z_0}{1+\frac{1}{j\boldsymbol{k}\cdot\boldsymbol{r}}}. \qquad [2.25]$$

When $\boldsymbol{k}\cdot\boldsymbol{r} \gg 1$, the point r is defined as being placed in the far-field. In this case, the acoustic impedance is

$$Z_s(r) \approx \rho_0 c, \qquad [2.26]$$

which is the same as the acoustic impedance of the plane wave. Hence, when the test point is in the far-field, spherical waves can be regarded as plane waves.

2.1.5 Directionality

No matter whether considering an acoustic actuator (e.g. a speaker) or an acoustic sensor (e.g. a microphone), more sound energy may be transferred from one direction than another. This property is called directionality. To clearly illustrate the directionality of a variety of acoustic transducers, the directivity index (*DI*) is introduced, and is one of the most critical parameters when testing and choosing these devices. It is the ratio of on-axis pickup energy relative to the total pickup integrated over all directions. To write it in a mathematically way, the expression of the directional index is [2]

$$DI = 10 \log_{10} \frac{W_{ref}}{W_{total}}, \qquad [2.27]$$

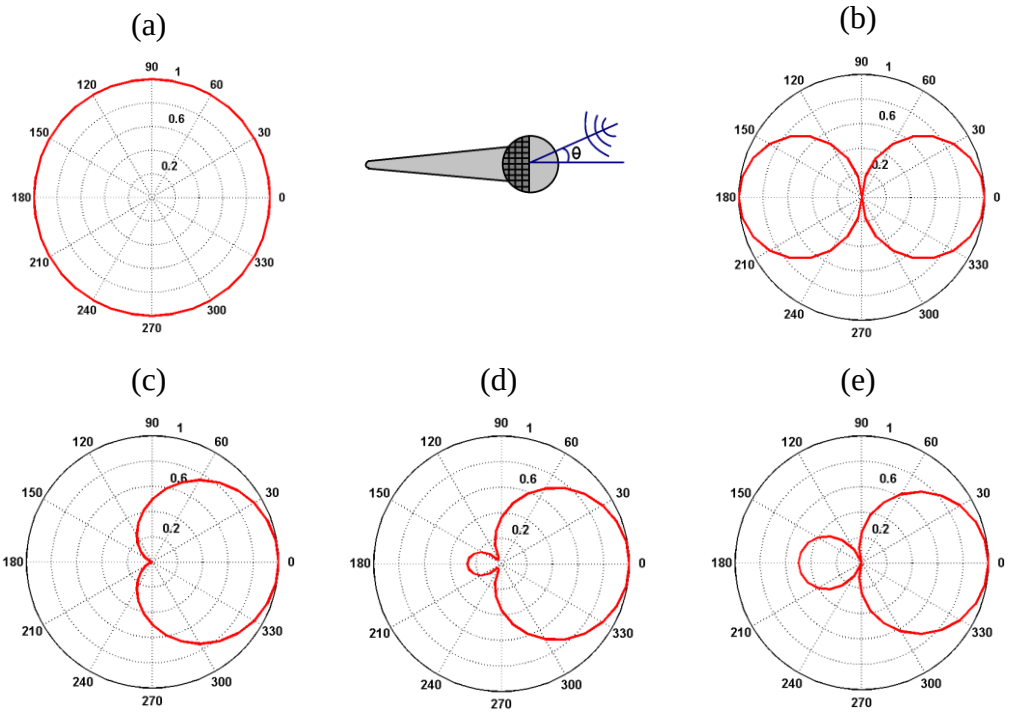

Fig. 2.5 Different types of directional polar patterns: (a) Omnidirectional (b) Bidirectional (c) Cardioid (d) Super-cardioid (e) Hyper-cardioid

where W_{ref} is the sound power picked up from the reference direction and W_{total} is the total integrated sound power from all directions. Another important configuration for specifying the directionality of acoustic devices is the directional polar pattern. Generally, there are three types of directional polar patterns: omnidirectional, bidirectional, and unidirectional.

An omnidirectional polar pattern covers all directions and generates or receives all sound in a 360-degree radius (see Fig. 2.5 (a)). It gives a *DI* of 0 dB. For microphones, the omnidirectional capability increases when the dimension of the moving diaphragm is smaller than the wavelength. Normally, the diameter of the diaphragm is approximately one-tenth of the wavelength. The smaller the size, the better the omnidirectional response at high frequencies. However, it decreases signal-to-ratio (SNR) and sensitivity.

A bidirectional polar pattern shows that the device picks up or generates identical sound power from the front and rear but rejects it from the sides (see Fig. 2.5(b)). The *DI* of such directional behaviour is 4.8. The microphone with such a directional pattern produces a better directional capability than the omnidirectional one.

A unidirectional polar pattern indicates that the acoustic device picks up or transfers more sound energy from or to the front than the back. A unidirectional microphone rejects more background noise than a bidirectional microphone. Therefore, it is used to distinguish sound waves from unwanted noise and applied most commonly in real life applications. According to the value of ratio of the pickup or generated energy from the front to the back, the unidirectional polar patterns can also be discriminated into other patterns, such as the cardioid, the super-cardioid and the hyper-cardioid (see Figure 2.5 (c) to (e)).

Table 2.2 provides the equation of response of each directional pattern and their values of directivity index, where E_0 is the maximum response and θ is the sound incident angle with respect to the axis normal to the active surface of the acoustic device.

Directional polar patterns	Omni-directional	Bi-directional	Cardioid	Super-cardioid	Hyper-cardioid
Response	E_0	$E_0 \cos\theta$	$\frac{E_0}{2}(1+\cos\theta)$	$\frac{E_0}{2}[(\sqrt{3}-1)+(3-\sqrt{3})\cos\theta]$	$\frac{E_0}{4}(1+3\cos\theta)$
DI (dB)	0	4.8	4.8	5.7	6

Table 2.2 Response equations and DI of various directional polar patterns

2.2 Microphone technology

Since 1876 when Alexander Graham Bell received the patent of the first telephone constructed with a moving armature transmitter and associated receiver, microphone technology has developed for 140 years [2]. From a half meter overall size to several micrometres in dimension, microphones have become much smaller and lower in cost. However, on the other hand, with the development of preamplifiers and power supplies, their quality has had a dramatic and stunning increase compared to the first telephone. According to the different operating principles and manufacturing process, existing microphones can be categorized as loose carbon granules microphones, condenser microphones, electrodynamic microphones, piezoelectric microphones, optical microphones, Micro-Electro-Mechanical-Systems microphones, to name some.

2.2.1 Conventional microphones

From the very beginning, the transmitter and the receiver were connected by a wire conducting electrical current. The signals were transmitted only a short distance until the first carbon telephone transmitter was invented by David Edward Hughes in 1878 [5]. Hughes's telephone transmitter that could pick up sound waves from around 460m consists of a thin wood plate diaphragm, a carbon rod and two carbon blocks. The sound waves cause large fluctuations in contact resistance between the rod and blocks mounted on the wood diaphragm, which is the prototype of the loose contact carbon microphone (see Fig. 2.6) that uses carbon granules to replace the carbon rod. Also, Hughes was the first person to use the word 'microphone' to describe his work as it could sense extremely low-level sound waves.

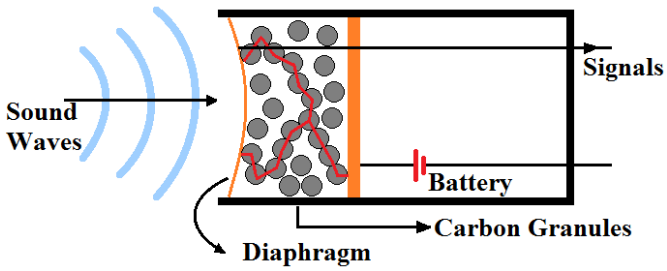

Fig. 2.6 Structure of typical loose carbon granules microphone

In the 1920s commercial broadcasting began. The bandwidth limitation of the carbon microphone increased the demands for higher quality microphones, which led to the inventions of condenser microphones and electrodynamic microphones. The condenser microphone, also called an electrostatic or capacitor microphone, has two conductive plates just like a capacitor. One plate is on the perforated backplate while the other is attached on a diaphragm. The air captured in the holes provides damping at resonance of the diaphragm. A schematic diagram of condenser microphones is shown as Fig. 2.7. When the sound waves impinge on the diaphragm, the vibration of the diaphragm causes the variation of the capacitance between these two plates. Thus, the variation of voltage *U* is inversely proportional to the changes of capacitance *C*, but proportional to the changes of distance d between the two plates as given in the equation,

$$\Delta U = \frac{Q}{\Delta C} = \frac{Q}{\varepsilon A}\Delta d, \qquad [2.28]$$

where A is the surface area of the plates and ε is the permittivity constant of the medium between the two plates. As the condenser microphone is polarized by a dc

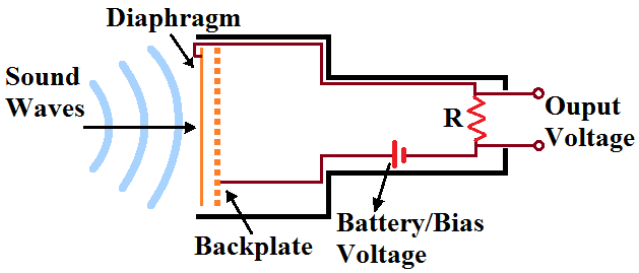

Fig. 2.7 The schematic diagram of condenser microphone

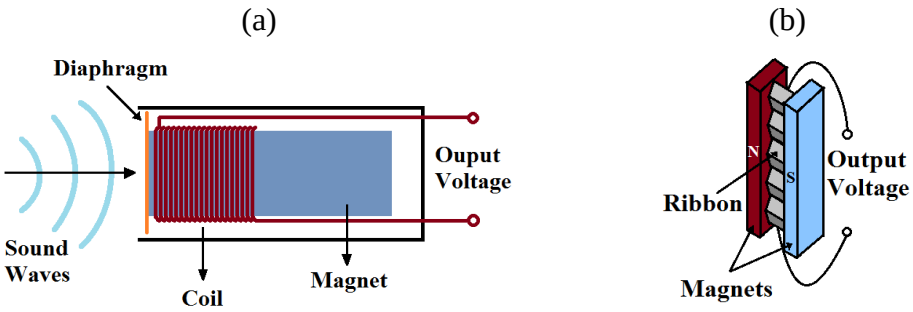

Fig. 2.8 Electrodynamic microphone (a) The moving-coil model (b) The ribbon model

bias voltage, the charge *Q* remains fixed. Therefore, the changes in the capacitance creates changes in the voltage across the plates, which is picked up by a following circuit for further amplification.

However, the polarized condenser microphone must be reverse-biased periodically if it is to be used for a long period of time. Therefore, in 1962, Gerhard M. Sessler and James E. West from Bell Lab built the first electret condenser microphone [6] which has no need for an external bias voltage source. For this kind of microphone, either the backplate or the diaphragm is coated with a pre-polarized material (e.g. polytetrafluoroethylene (PTFE)) which provides a permanent electrostatic charge. Due to its stable performance and low cost, electret microphones are still widely used today. Before the Micro-Electro-Mechanical-Systems (MEMS) microphones were applied commercially, the electret microphones were the majority of microphones used in mobile devices, hearing aids, and so forth.

The electrodynamic microphone works based on electromagnetic induction. It has a moving induction coil connected with the diaphragm and placed in a permanent magnetic field (see Fig. 2.8 (a) [7]). When the sound waves cause the vibration of the diaphragm, the coil moving across the magnetic field induces a voltage proportional to the strength of the magnetic field and the velocity of the coil. Another type of electrodynamic microphones is the ribbon microphone as shown in Fig. 2.8 (b) [8]. In its structure, a thin metal ribbon not only performs as the diaphragm forced by the sound waves, but also replaces the role of the moving coil introduced before. As the ribbon moves back and forth between the poles of the magnet, both the frontal and the rear surfaces of the ribbon are exposed to the transmission medium. Therefore, the ribbon microphone often has a bi-directional performance, and it is also the first type of directional microphone which is still commonly used today.

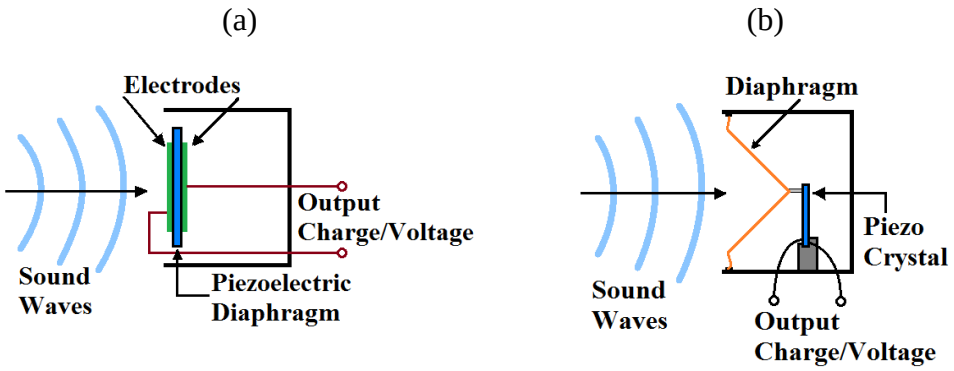

Fig. 2.9 Schematics of piezoelectric microphones: (a) Directly actuated: the diaphragm is made of piezoelectric material. (b) Indirectly actuated: the diaphragm is connected to a piezoelectric layer, of which movements cause the deformation of the piezoelectric layer.

Piezoelectric microphones, also called crystal microphones, were developed based on the phenomenon of piezoelectricity of specific crystal materials. This phenomenon was discovered in the late of 1800s. It was observed that when a certain material was compressed by a mechanical stress, it generates electrical charge or voltage captured by the output terminal placed on the surface of the material. Conversely, the material deforms when an electrical field is placed on it. The former phenomenon is called the direct effect of piezoelectricity, and the later one is called the inverse effect of piezoelectricity [9]. The operational theory of the piezoelectric microphone follows the direct effect of piezoelectricity. During the 1930s to 1960s, the piezoelectric microphones were quite popular as they have high output impedance which matched with the input impedance of vacuum tube amplifiers at that time. However, this also enlarges the noise both picked up from the microphone itself and the connecting cables. Therefore, after the low-cost electret condenser microphones were invented, the production of piezoelectric microphones declined shapely. Now, conventional piezoelectric microphones are applied in a lot of hydrophone products due to their high mechanical resonance. Figure 2.9 demonstrates schematics of two types of typical piezoelectric microphones.

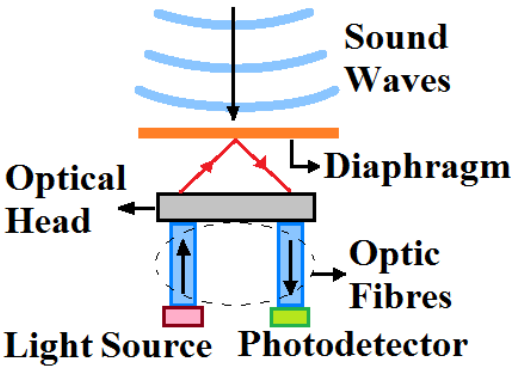

Fig. 2.10 Details of a typical optical microphone

However, all the microphones mentioned above are influenced by environmental effects, such as electrical and magnetic fields, temperature and humidity. In order to acquire acoustic signals in any dangerous environment, the optical microphone was invented to be applied in special applications. Figure 2.10 shows the details of an optical microphone. A light beam generated by a laser source travels through an optical fibre and illuminates the surface of the reflective diaphragm. The vibration of the diaphragm modulates the intensity and phase of the light and reflects the light. Then the light reflection is transmitted over the second fibre and finally captured by photodetectors or an interferometer to record phase variation [10]. Therefore, optical microphones have EMI/RFI immunity and are not affected by any environmental changes, so they have quite high SNR. However, this high-quality performance also brings high cost (e.g. the Sennheiser MO 2000 optical microphone [11]).

2.2.2 MEMS microphones

Since integrated circuit (IC) technology MEMS was developed in the 1960s [12], which brought a fundamental change to the computer market and led the world to the personal computer (PC) age, the growing requirements on computer capacity and stability doubled the density of the transistor integration in the processor every two years, as described in the Moore's law. However, people quickly recognized that this growth did have an end produced by the limitation of engineering capability and classical physics. Fortunately, the microfabrication technology gave a ray of light to the solution of this kind of problem when the first surface micro-machined resonant

gate transistor was invented in 1967 [13]. Several years later, the first silicon micromachining pressure sensor was built by James Angell et al., and was the beginning of the development of MEMS devices [14]. In 1982, the paper "Silicon as a Mechanical Material" written by Kurt Peterson [15] summarized the status of silicon micromachining technology at that time. In the year after, Royer et al. [16] introduced the first piezoelectric micro-machined microphone made by silicon and zinc oxide. Similar to the conventional microphones, nowadays MEMS microphones can still be roughly separated into different types according to their respective sensing technology. As this research involves building MEMS microphones driven by capacitive sensing and piezoelectric sensing, this section focuses on introducing the microphones using these two sensing techniques.

In terms of capacitive MEMS microphones, there are mainly two types: parallel-plate devices and comb-drive devices. The former one has the same working principle as the conventional condenser microphones described before. For this kind of microphone, the pull-in effect is a critical factor that should be considered in the design process. The pull-in effect is a phenomenon relating to the balance between the electrostatic force F_e produced by the bias voltage and the mechanical force F_m due to the supports and the stiffness of the diaphragm as shown in Fig. 2.11. Therefore, the electrostatic force equals [17]

$$F_e = \frac{d\left(\frac{1}{2}CU^2\right)}{d(x_0-x)} = \frac{\varepsilon A}{2(x_0-x)^2}U^2, \qquad [2.29]$$

where x_0 is the initial position of the diaphragm. When the mechanical force $F_m = F_e = k_m \Delta d$,

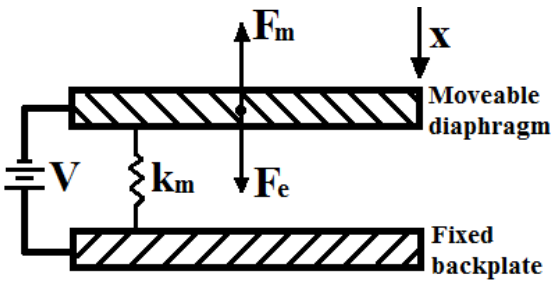

Fig. 2.11 The electro-mechanical mode of capacitive microphone with paralleled plates

$$U = \sqrt{\frac{2k_m x}{\varepsilon A}}(x_0 - x). \quad [2.30]$$

And when $\frac{dU}{dx} = 0$,

$$x = \frac{x_0}{3}. \quad [2.31]$$

This is the equilibrium position of the diaphragm under the bias voltage. It states that the maximum gap between two parallel plates is exactly one third of the original spacing. This critical gap is irrespective of the sound pressure and the applied bias voltage. The equilibrium position limits the acceptable sound pressure of this kind of microphone. When the displacement of the diaphragm exceeds this threshold distance, the attraction between the plates will permanently damage the device. Unlike how the parallel-plate microphone sensed the capacitive change between the electrodes facing with each other, the comb-drive capacitive microphone (i.e. interdigitated fingers microphone) generates capacitance between walls of electrodes. Generally, there are two groups of comb fingers in a comb-drive capacitive sensor as shown in Fig. 2.12 (a): the fixed comb fingers on the die and the floating comb fingers freely moving in one or multiple axes. According to the different types of relative movement between the fixed comb fingers and the floating ones, the comb-drive capacitive sensor can be roughly divided into three categories as illustrated in Fig. 2.12 (b) – (d). For a transverse comb-drive device, the set of floating fingers moves in a direction perpendicular to its longitudinal axis, and the change of capacitance depends on the

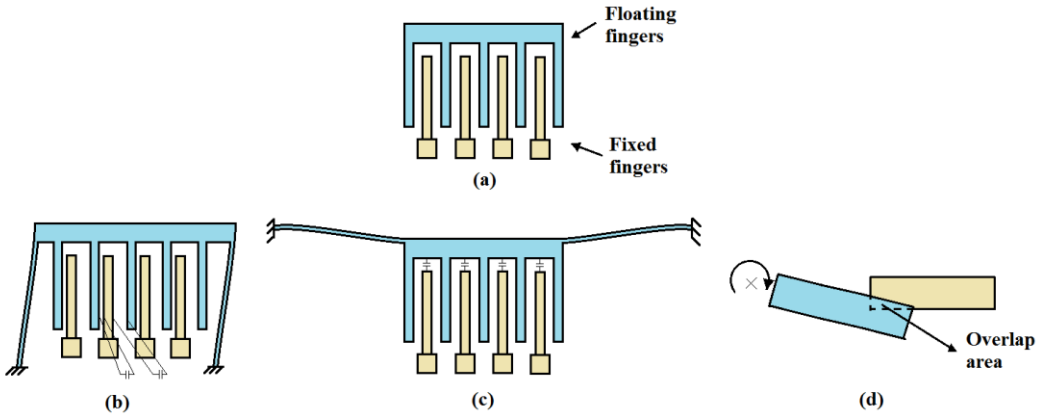

Fig. 2.12 (a) A comb-drive at initial state (no bias) (b) A transverse comb-drive (c) A longitudinal comb-drive (d) A torsional comb drive

varying distance between the side faces of the fingers; while for the longitudinal comb-drive, the floating fingers move along the longitudinal axis, and the capacitance changes over the gap between the end side of the floating fingers and the surface of the fixed fingers that the floating fingers face to; the comb fingers in the torsional comb-drive completely rotate along the longitudinal axis so that the variation in the overlap area between the two sets of fingers drives the change of capacitance.

The fabrication process of capacitive microphones can be bulk microfabrication, or surface microfabrication, or their combination. Here the bulk microfabrication deals with relatively large micromachining, such as etching a hole, removing a large area of the wafer, and constructing a complex structure. However, this technology cannot provide good performance when processing very thin films. On the other hand, surface microfabrication builds a structure from the thin layers deposited on the wafer, which requires high control techniques to avoid fracture, unexpected deformation, and thermal vibration occurring on the produced microstructures. For the parallel-plate microphone, the material of the backplate can be variable depending on different design purposes, such as single-crystalline silicon (SCS), polysilicon, doped silicon (e.g. boron or phosphorus doped), electroplated metal, silicon nitride (Si_3N_4), polyimide, etc. The diaphragm can also be made by SCS, Si_3N_4, platinum, aluminium and so on, Different diaphragms associating with different backplates and various layers providing diverse functions can yield MEMS

Author, Year	Diaphragm material, size ($\boldsymbol{mm^2}$)	Backplate material	Sensitivity (mV/Pa)	Equivalent noise level (dBA)	Resonance Frequency (kHz)
Hohm,1985 [18]	0.15μm Si_3N_4 0.8× 0.8	Silicon	4.3	54	20
Murphy, 1988 [19]	1.5μm Polyester 3× 3	silicon	4-8	30	>15
Voorthuyzen, 1989 [20]	2.5μm Mylar 2.45× 2.45	Silicon	19	60	15
Bergqvist, 1990 [21]	5μm doped Si 2× 2	Glass	13	31.5	4
Kuhnel, 1991 [22]	0.15μm Si_3N_4 0.8× 0.8	Silicon	0.44-10	43	>20
Scheeper, 2003 [23]	0.5μm silicon nitride 1.95× 1.95	p-type silicon	22.4	23	47-51
Martin, 2007 [24]	2.25μm Si_3N_4 0.23× 0.23	polysilicon	390	41	178

Table 2.3 Performance characteristics of parallel-plate microphones from academic literature

microphones with different resonance frequencies, sensitivity, damping and noise level as shown in Table 2.3 [18]–[24].

A piezoelectric microphone consists of either a single thin piezoelectric diaphragm or a diaphragm connected with a bimorph bender which is a cantilever beam of two piezoelectric layers having opposite polarization. As the sound wave exerts a pressure on the diaphragm, the diffraction of the diaphragm leads to a stress on the piezoelectric material that causes an electric voltage (i.e. direct piezoelectric effect). Most of the critical properties of a piezoelectric material are attributed to its internal crystal structure. By poling the piezoelectric material in a strong electric field at a temperature below the Curie point, the orientation of most crystallites in the material are aligned with the direction of the electric field. Therefore, a piezoelectric material can be made piezoelectric in any direction. Figure 2.13 shows the crystallographic axes of a piezoelectric crystal. Usually, the polarization direction coincides with the Z axis. The subscripts 1, 2, and 3 denote X, Y and Z axes and also represent the three directions of normal stress. The shear stress components are denoted by subscripts 4, 5, and 6. The direct effect of piezoelectricity can be described by a matrix-form equation referring to applied mechanical stress and external applied electric field as shown below,

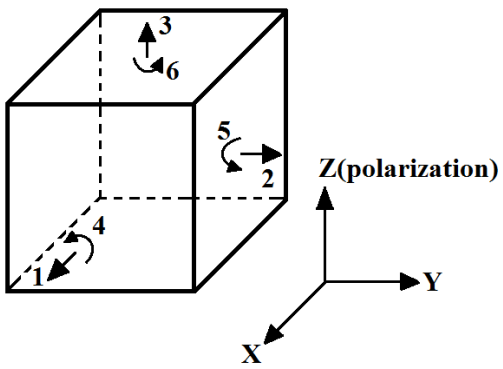

Fig. 2.13 Schematic diaphragm of a piezoelectric crystal in Cartesian coordinate

$$\begin{bmatrix} D_1 \\ D_2 \\ D_3 \end{bmatrix} = \begin{bmatrix} d_{11} & d_{12} & d_{13} & d_{14} & d_{15} & d_{16} \\ d_{21} & d_{22} & d_{23} & d_{24} & d_{25} & d_{26} \\ d_{31} & d_{32} & d_{33} & d_{34} & d_{35} & d_{36} \end{bmatrix} \begin{bmatrix} T_1 \\ T_2 \\ T_3 \\ T_4 \\ T_5 \\ T_6 \end{bmatrix} + \begin{bmatrix} \varepsilon_{11} & \varepsilon_{12} & \varepsilon_{13} \\ \varepsilon_{21} & \varepsilon_{22} & \varepsilon_{23} \\ \varepsilon_{31} & \varepsilon_{32} & \varepsilon_{33} \end{bmatrix} \begin{bmatrix} E_1 \\ E_2 \\ E_3 \end{bmatrix},$$

[2.32]

where D_i is the electrical displacement matrix, d_{ij} is the piezoelectric coefficient matrix, T_{ij} is the matrix of mechanical stress, ε_{ij} is electrical permittivity matrix, and E_i is the external applied electric field. Generally, for sensor designs, the external applied electric field is negligible. Quartz crystals, lead zirconate titanate (e.g. $PbZrTiO_3$ or PZT), zinc oxide (ZnO), aluminium nitride (AlN), polyvinlidenfluoride (PVDF) and barium titanate ($BaTiO_3$) are commonly used piezoelectric materials for MEMS devices nowadays.

The first piezoelectric MEMS microphone built by Royer et al. was constructed with a circular silicon diaphragm 3mm in diameter and 30 μm in thickness, and two aluminium electrodes sensing the stress variation of the ZnO piezoelectric film clamped between them. One of the electrodes is circular and attached on the front side of the ZnO layer while the other one is placed on the backside of the piezoelectric film is formed as a concentric configuration and isolated by a 1μm SiO_2 layer. This microphone has a measured sensitivity of 250 μV/Pa and a frequency response of 10 Hz to 10 kHz. In 1987, an IC-processed piezoelectric microphone working from 20 Hz to 4 kHz was designed by E. S. Kim et al [25]. It consisted of a square LPCVD (low pressure chemical vapour deposition) 2 μm thick silicon diaphragm and a 3mm×3mm deposited ZnO layer, having response about 500 μV/Pa at 1 kHz. Other piezoelectric microphones were also invented to achieve different purposes. In 1993, R. P Ried et al. integrated COMS circuit with piezoelectric microphone [26]. For the piezoelectric microphone with a cantilever as mentioned above, the microphone presented by S. S. Lee et al. in 1996 can be regarded as a good example [27]. After the technology of using PZT in a microfabrication process matured, a high-quality PZT-based piezoelectric microphone was yielded by H. J. Zhao in 2003 [28]. Furthermore, for specific demands such as aeroacoustic sensors, M. D. Williams et al. developed a

piezoelectric microphone using an AlN layer integrated in a thin-film composite diaphragm to increase bandwidth [29].

Compared to the traditional microphones, the benefit of MEMS microphones is not only providing high SNR against volume, but also consistent operation over temperature. In addition, MEMS microphones can withstand high temperature reflow during manufacturing, are immune to environmental vibration and create less unwanted sound when responding. Shipments of MEMS microphone is predicted to reach over 5 billion units in 2018, over 5 times larger than the shipments in 2010, and it is predicted to reach 5.8 billion unit in 2019 according to IHS report, which proves that MEMS microphones have an enormous market demand. In all demands, the leading enterprise of mobile products, Apple, increased its procurement of MEMS microphones to over 1.2 billion units in 2015 and became the world's largest consumer of MEMS microphones [30], [31].

Most MEMS microphone manufacturers provide both omnidirectional microphones and directional microphones (e.g. Knowles, AAC Technologies, STMicroelectronics, etc.). In order to pick up sound from a specific direction, unidirectional microphones are the type of MEMS microphones most requested to be applied in particular areas such as robotics, navigation and ocean exploration. For mobile applications, directional microphones could acquire much clearer speech signals and decrease the chance of getting unnecessary background information. One of the traditional ways of confirming sound source localization is to build a microphone array which combines at least two independent identical omnidirectional microphones [32]. In such a system, calculating the incident angle of sound waves depends on the separating distance between adjacent microphones and the time delay between the two microphones receiving the plane waves. This method requires an amount of signal processing, high match quality between microphones and complex external connected circuitry. The other method is to build a microphone whose activating diaphragm is exposed to the sound propagation medium on both sides. The time difference of sound arrivals between the two sides of the diaphragm is achieved by a well-designed route connecting the front and the back. However, these sorts of microphones usually have resonance frequencies high above the audio frequency range (i.e. > 20 kHz). In other words, the sensitivity of the microphones is relatively low in

the operating frequency range, and they need further signal processing to cancel noise due to low SNR. The main reason that leads to the issues for these microphones is the limitation of the dimensions of the diaphragm. If a microphone operating below 20 kHz does not suffer sound diffraction and phase interference, the radius of the diaphragm should be less than 2mm [33], which easily generates a high resonance frequency above 20 kHz.

During the same period of the investigation of MEMS microphones, a group of biologists found that an insect called *Ormia ochracea* has a surprising capability for sound localization, which is not limited by their body size. A few researchers have implemented the mechanical operation of *Ormia ochracea* external hearing organ with MEMS directional microphone designs and so guided it to new era. The new *Ormia*-inspired microphone does not require much further signal processing and reduces the size of the package product. However, this kind of microphone is still in the experimental stage. The anatomical details of the hearing organ of *Ormia ochracea*, its mechanical properties, and previous designed microphones inspired by *Ormia ochracea* will be discussed in the next section.

2.3 MEMS microphones inspired by *Ormia ochracea*

Similar to microphone arrays, many large animals including human beings have two ears distributed by a certain distance on their heads. When their eardrums are stimulated by sound waves, the interaural time difference (ITD) and interaural intensity difference (IID) are transformed into signals which are transferred to the brain and processed by the central nervous system eventually to determine the orientation of the sound source. However, as for the reasons mentioned previously, this kind of auditory system is hard to manufacture as sensors with smaller dimensions than the wavelength of interest. In other words, it cannot be applied to produce micro-scale devices. Therefore, scientists turned to the hearing systems of insects, to try to find the best ways to apply their advantages on MEMS microphones. *Ormia ochracea* is one of the insects that new generations of MEMS microphones have been inspired by.

2.3.1 Hearing system of Ormia ochracea

At the end of the last century, biologists found that *Ormia ochracea* has a great capability for detecting sound sources. The parasitic female *Ormia ochracea* uses

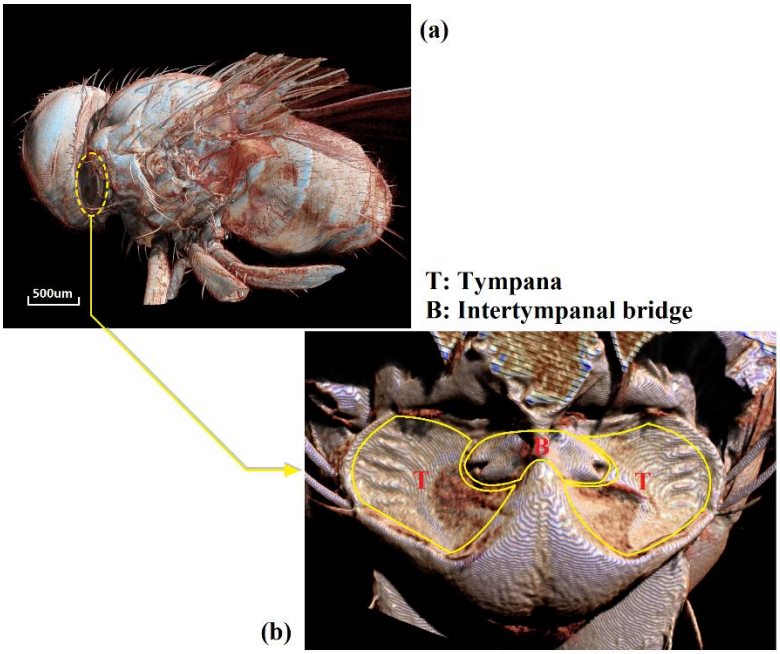

Fig. 2.14 MicroCT scanned images of Ormia ochracea (taken by colleague Andrew Reid) (a) The side view of Ormia's body (b) The frontal face of the hearing organ

auditory cues to localize the mating call of its host *Gryllus*, a genus of cricket, and then deposits its predaceous larvae on the host [34]–[42]. The cricket's mating call has a fundamental frequency around 5 kHz and therefore wavelength at approximately 70 mm, compared to the interaural distance of *Ormia* that is only around 520 μm. Despite of the extremely small distance that gives the original maximum ITD and IID are approximately 1.5 μs and 1 dB [43], respectively, experimental investigations show that it can localize the mating call with a resolution less than 2° [44]. This high accuracy is attributed to the mechanical coupling structure of the ear of *Ormia ochracea*, which enhances both ITD and IID by up to 40 times more than the original values at 5 kHz.

The hearing organ of *Ormia ochracea* is constructed by two small tympana (less than 1mm in radius) located on the frontal face of the prothorax, joined by a flexible intertympanal bridge (see Fig. 2.14). Dissections also confirmed that both tympana are backed by an undivided air-filled chamber connecting to the outside by a pair of tracheae. When the incident sound waves arrive at the tympana, the tympana will not fluctuate synchronously due to the vibration of the bridge. The tympanal pit far from the source (i.e. ipsilateral) gets as much as 20 dB higher response than the tympanal pit close to the sound source (i.e. contralateral). Then, the deflections at the tympanal pits are transferred to the deformation of bulba acustica. Each bulba acustica has approximately 70-75 auditory receptor cells, which are innervated by the auditory nerve. It was also discovered that the mechanical responses of the two tympana can be divided into two vibration mode shapes. One is a rocking mode in which the two eardrums move in opposite directions, like a see-saw. The other mode is a translational mode, also called bending mode, in which the eardrums deflect in-phase. The rocking mode is driven by the sound pressure gradient between the eardrums while the translational mode is controlled by the average pressure on the tympana. The movements of the tympana are superimposed in the frequency range beyond these two main resonance mode shapes [45].

2.3.2 Mechanical analysis of Ormia ochracea's hearing organ

In 1995, Miles et al. built a simplified mechanical structure to reveal the basic mechanical principles behind the motion of *Ormia*'s ears when deflecting incident

sound waves, which is a two-degree-of-freedom system (2-DOF) model as shown in Fig. 2.15 [39], [46]. In this model, the two plates represent the ispi- and contralateral eardrums at the ends of the intertympanal bridge with stiffness K_1 and K_2, and damping coefficient C_1 and C_2, respectively. The intertympanel bridge working as a coupling pivot is assumed to be a simple spring-mass model with stiffness K_3 and damping coefficient C_3. Based on the general equation for a 2-DOF system, the equation of motion for the vibration due to sound pressure waves acting on the two membranes are written as follows

$$[\boldsymbol{M}][\boldsymbol{x}(\ddot{\boldsymbol{t}})] + [\boldsymbol{C}][\boldsymbol{x}(\dot{\boldsymbol{t}})] + [\boldsymbol{K}][\boldsymbol{x}(\boldsymbol{t})] = [\boldsymbol{f}(\boldsymbol{t})]$$

$$\begin{bmatrix} m_1 & 0 \\ 0 & m_2 \end{bmatrix}[\boldsymbol{x}(\ddot{\boldsymbol{t}})] + \begin{bmatrix} C_1 + C_3 & C_3 \\ C_3 & C_2 + C_3 \end{bmatrix}[\boldsymbol{x}(\dot{\boldsymbol{t}})] + \begin{bmatrix} K_1 + K_3 & K_3 \\ K_3 & K_2 + K_3 \end{bmatrix}[\boldsymbol{x}(\boldsymbol{t})] = [\boldsymbol{f}(\boldsymbol{t})], \quad [2.33]$$

where the response matrix $[\boldsymbol{x}(\boldsymbol{t})] = \begin{bmatrix} x_1(t) \\ x_2(t) \end{bmatrix}$ and the applied force matrix $[\boldsymbol{f}(\boldsymbol{t})] = \begin{bmatrix} f_1(t) \\ f_2(t) \end{bmatrix}$. Since the mass of the sensory tympana is significantly greater than any other parts of the organ, it is reasonable to assume that the kinetic energy is concentrated on the tympana and ignore the mass of the bridge. In order to further facilitate the model, the mass, the surface area, the stiffness and the damping coefficient of the two tympana are assumed to be identical, i.e. $m_1=m_2=m$, $S_1=S_2=S$, $K_1=K_2=K$ *and* $C_1=C_2=C$. Hence,

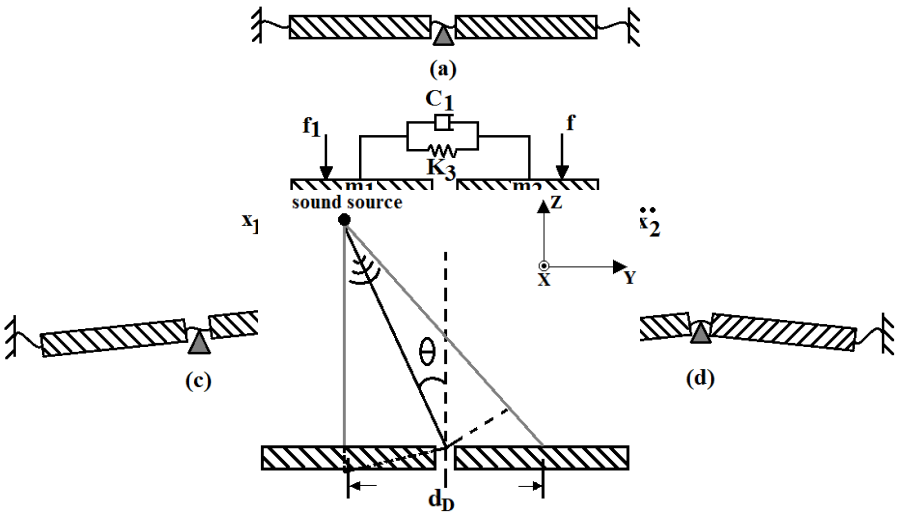

Fig. 2.16 Definition of sound incident angle

the displacement response in the frequency domain between the two forces applied on the two tympana can be derived using the Cramer rule,

$$x_1(\omega) = \frac{f_1(\omega)\left[-\omega^2 m+i\omega(C+C_3)+K+K_3\right]-f_2(\omega)(i\omega C_3+K_3)}{\left[-\omega^2 m+i\omega(C+C_3)+K+K_3\right]^2-(i\omega C_3+K_3)^2} \quad [2.34]$$

$$x_2(\omega) = \frac{f_2(\omega)\left[-\omega^2 m+i\omega(C+C_3)+K+K_3\right]-f_1(\omega)(i\omega C_3+K_3)}{\left[-\omega^2 m+i\omega(C+C_3)+K+K_3\right]^2-(i\omega C_3+K_3)^2} \quad [2.35]$$

The eigen-frequencies ω_r and ω_t at rocking mode and translational mode, respectively, be obtained under free vibration condition, which means that $|-\omega^2[\boldsymbol{M}]+[\boldsymbol{K}]|=0$. Thus,

$$\omega_r = \sqrt{\frac{K}{m}}, \omega_t = \sqrt{\frac{K+2K_3}{m}}. \quad [2.36]$$

The force placed on the frontal faces of the two membranes due to sound pressure is expressed in exponential form as $f_1(\omega) = SPe^{i\omega\tau/2}$ and $f_2(\omega) = SPe^{i\omega\tau/2}$ (i.e. the sound does not hit the back of the membranes), where τ is the time delay of the sound waves reaching to the two membranes, which is equal to $d_D \sin\theta\,/c$. Here, d is the distance between the centres of the two membranes and θ is the sound incident azimuth angle as shown in Fig. 2.16. To further analyse the relationship between the displacement response and sound incident azimuth angle, the modal analysis method [47] was applied on equation 1.33. Firstly, the displacement response matrix ***x(t)*** was rewritten as ***[X]q(t)***, where ***[X]*** is the modal matrix and ***q(t)*** is the modal participation coefficient matrix. Then, the motion equation was transformed into the modal form by pre-multiplying the transposed modal matrix $\mathbf{[X]^T}$. Therefore, the equation 1.33 can be rewritten in frequency domain as

$$\left[-\omega^2[\boldsymbol{X}]^{\boldsymbol{T}}[\boldsymbol{M}][\boldsymbol{X}]+i\omega[\boldsymbol{X}]^{\boldsymbol{T}}[\boldsymbol{C}][\boldsymbol{X}]+[\boldsymbol{X}]^{\boldsymbol{T}}[\boldsymbol{K}][\boldsymbol{X}]\right]\boldsymbol{q}(\boldsymbol{\omega}) = [\boldsymbol{X}]^{\boldsymbol{T}}\boldsymbol{f}(\boldsymbol{\omega}) \quad [2.37]$$

The modal matrix can be derived by substituting ω_r and ω_t into $\left[-\omega^2[\boldsymbol{M}]+[\boldsymbol{K}]\right][\boldsymbol{X}]=\mathbf{0}$, separately, so

$$[\boldsymbol{X}] = [X_r \quad X_t] = \begin{bmatrix} 1 & 1 \\ -1 & 1 \end{bmatrix}. \quad [2.38]$$

Once the modal matrix is known, q(t) can be calculated by substituting equation 1.38 into equation 1.37:

$$[\boldsymbol{q}(\boldsymbol{\omega})] = \begin{bmatrix} q_1(\omega) \\ q_2(\omega) \end{bmatrix} = \begin{bmatrix} \frac{f_1(\omega)-f_2(\omega)}{-2m\omega^2+2i\omega C+2K} \\ \frac{f_1(\omega)+f_2(\omega)}{-2m\omega^2+2i\omega(C+2C_3)+2(K+2K_3)} \end{bmatrix} \quad [2.39]$$

Hence the frequency response of the displacement

$$x(\omega) = \begin{bmatrix} x_1(\omega) \\ x_2(\omega) \end{bmatrix} = \begin{bmatrix} q_1(\omega) + q_2(\omega) \\ -q_1(\omega) + q_2(\omega) \end{bmatrix}$$

→

$$x_1(\omega) = \frac{f_1(\omega)+f_2(\omega)}{2m(\omega_t^2-\omega^2+2i\omega\xi_t\omega_t)} + \frac{f_1(\omega)-f_2(\omega)}{2m(\omega_r^2-\omega^2+2i\omega\xi_r\omega_r)}$$

$$= \frac{SP\cos\frac{\omega\tau}{2}}{m(\omega_t^2-\omega^2+2i\omega\xi_t\omega_t)} + \frac{iSP\sin\frac{\omega\tau}{2}}{m(\omega_r^2-\omega^2+2i\omega\xi_r\omega_r)} \quad [2.40]$$

$$x_2(\omega) = \frac{f_1(\omega)+f_2(\omega)}{2m(\omega_t^2-\omega^2+2i\omega\xi_t\omega_t)} - \frac{f_1(\omega)-f_2(\omega)}{2m(\omega_r^2-\omega^2+2i\omega\xi_r\omega_r)}$$

$$= \frac{SP\cos\frac{\omega\tau}{2}}{m(\omega_t^2-\omega^2+2i\omega\xi_t\omega_t)} - \frac{iSP\sin\frac{\omega\tau}{2}}{m(\omega_r^2-\omega^2+2i\omega\xi_r\omega_r)}. \quad [2.41]$$

$$\xi_r = \frac{C}{2\omega_r m}, \xi_t = \frac{C+C_3}{2\omega_t m}$$

When $\omega \to \omega_r$, the total response is mainly contributed to the terms that are proportional to $\sin\frac{\omega\tau}{2}$; when $\omega \to \omega_t$, the total response is driven by the terms that are proportional to $\cos\frac{\omega\tau}{2}$. Since τ is extremely small,

$$\sin\frac{\omega\tau}{2} = \sin\left(\frac{\omega d\sin\theta}{2c}\right) \approx \frac{\omega d\sin\theta}{2c},$$

$$\cos\frac{\omega\tau}{2} = \cos\left(\frac{\omega d\sin\theta}{2c}\right) \approx 1 - \left(\frac{\omega d\sin\theta}{2c}\right)^2 \approx 1. \quad [2.42]$$

Thus, at the rocking mode and the translational mode, respectively, the amplitude of displacement of two membranes

$$A_r = |x_1(\omega)| = |x_2(\omega)| \approx \frac{SP\sin\frac{\omega\tau}{2}}{m} \frac{1}{\sqrt{\left(\omega_r^2-\omega^2\right)^2+(2\omega\xi_r\omega_r)^2}} \propto \sin\theta \propto |f_1(\omega) - f_2(\omega)|, \quad [2.43]$$

$$A_t = |x_1(\omega)| = |x_2(\omega)| \approx \frac{SP\cos\frac{\omega\tau}{2}}{m} \frac{1}{\sqrt{\left(\omega_t^2-\omega^2\right)^2+(2\omega\xi_t\omega_t)^2}} \approx constant \propto |f_1(\omega) + f_2(\omega)|. \quad [2.44]$$

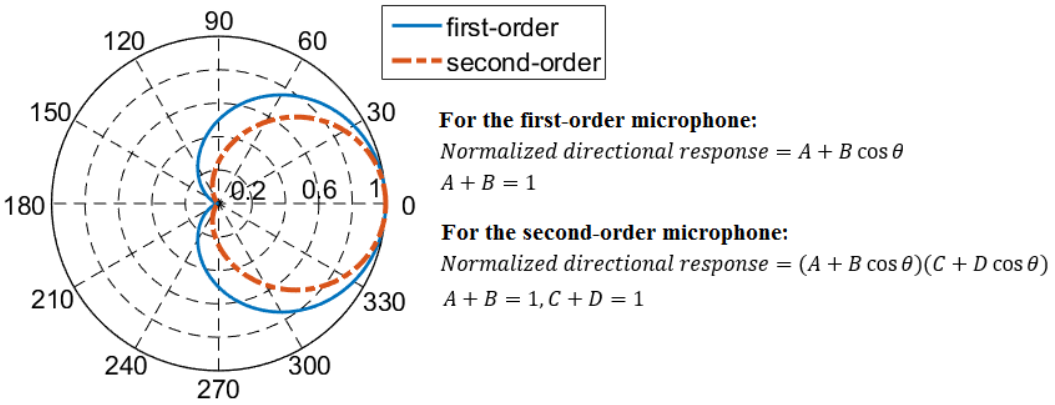

Fig. 2.17 Directional polar patterns of the first-order and the second-order microphones

In other words, the displacement amplitude of the two tympana of *Ormia ochracea*'s hearing organ has sine dependence on sound incident angle at rocking mode while it remains constant throughout sound incident angles at translational mode. This relationship is only valid when the sound waves do not arrive on the back of the two tympana as well as the activating rotating plates used in the MEMS microphones inspired by this kind of fly. Several *Ormia*-inspired MEMS microphones designed by other research groups during last decade will be introduced and discussed in the next section.

2.3.3 Previous designs

The published designs of *Ormia*-inspired MEMS microphones can be broadly separated into two main categories in terms of their directivity: the first-order and the second-order [2]. The response of the first-order microphones is proportional to the pressure gradient while the second-order microphones have directional responses that are proportional to the difference between the gradients. In other words, the highest order of the cosine term against the sound incident angle in the general equation of the directional response is the first order. In the equation for the second-order directional response, the highest order of the cosine term is the second order. The directional polar patterns of these two kinds of microphones are shown in Fig. 2.17.

a) The first order microphones

Two types of design models are assigned to the first-order microphones: the see-saw model and the clamped diaphragms model. Although both types are inspired by the same insect, they use different methods to locate a sound source.

1) See-saw models

A see-saw model consists of one unclamped diaphragm separated by a centred beam or two unclamped diaphragms placed side by side on the beam. This type of models follows the basic mechanical analysis of the 2-DOF system described above. It utilizes the sine function relationship between the displacement amplitude and sound incident angle to locate the source. Miles et al. [48]–[50] from State University of New York at Binghamton developed various pressure gradient microphones with this type of model. Instead of placing a single rigid beam in the centre of the diaphragm, they attempted to build a stiffened plate with a carefully re-designed hinge in order to provide a higher sensitivity than the previous design. The rotating polysilicon diaphragm was bonded on supports composed of well-distributed crossed stiffeners that not only increase the stiffness of the diaphragm but also control the entire mass. The whole diaphragm is surrounded by an extremely narrow slit, and the wafer is etched from the backside, leading to a low damping ratio. Although the reduced damping increases sensitivity, the design only produces a single narrow working band. More recently, W. Cui et al. [51]–[56] modified the stiffeners and the central hinge so that the design is close to an ideal rigid plate and so the first mode frequency is highly increased.

Three transduction methods were attempted by Miles and Weili et al.: paralleled-plate capacitive sensing [57], optical sensing [58]–[62], and comb-finger capacitive sensing [63], [64]. For parallel-plate sensing, the SNR is negatively influenced by electronic noise, meanwhile the viscous damping caused by the air between the diaphragm and the backplate leads to thermal noise. While the electrical sensitivity is proportional to the bias voltage, the diaphragm will collapse against the backplate if the voltage exceeds a critical value. Optical sensing based on a phase-sensitive diffraction grating structure can lower noise and power requirements compared to capacitive sensing. This method is achieved by incorporating inter-digitated comb fingers at the ends of the diaphragm. However, optical sensing is a

comparably high-cost transduction method, which is generally considered not suitable for commercial use. Capacitive comb, in contrast, can be fabricated in a single layer MEMS device and offers the benefits of extremely low noise at the trade-off of electrical sensitivity. In recent years PZT [65]–[70] or Aluminium Nitride [71] thin film layers have been used in combination with cantilevers connecting to the diaphragms to provide an alternative method of transduction.

In addition, researchers in the Sensor Research Laboratory (SRL) at the Naval Postgraduate School in the USA have also developed several biologically inspired directional microphones. Most of their designs can be divided into two major types. One has arrays of square holes etched onto two wings representing two tympana, while the other has vertical and horizontal beams intersecting at a pivot (like a bow-tie). The graduate student Shivok [72] built the former kind of microphone with $86\mu m$ square holes, and each wing has four rows of nine holes. These holes are proposed to release air damping and are produced via PolyMUMPs, a micro-fabrication process supplied by MEMSCAP [73]. This design supports both parallel-plate capacitive sensing and comb capacitive sensing. Two electrodes are added under the polysilicon membranes, grounded to the centre electrode connecting the wings. Additionally, a set of moveable diffraction grating are added to the wings and a set of stationary fingers attached at the substrate. However, experiments showed that the displacement amplitude was very low due to weak sound coupling caused by the relatively large holes on the wings. Another student, A. Dritsas [74] built a similar design to Shivok's work but using the SOIMUMPS fabrication process where the substrate is deep etched under the structure to reduce squeeze film damping. The alternative device has a $10\mu m$ layer thickness which is determined by SOIMUMPS design rules. Also, the width of the central beam was increased to $20\mu m$. However, because of the thermal stress during the processing, the edges of the wings touch the substrate underneath.

The bow-tie model contains a pair of cross beams at the centre connecting two membranes 'wings' surrounded by narrow slits and substrate. Muamad [75], Simsek [76] and Harrison [77] from the Naval School successively developed such directional microphones. Because the rocking mode response, driven by the moment originating from the acoustic pressure gradient, is vital to enlarge the interaural difference, the

dimension of the cross beams was designed to alter the moment acting on the structure by changing the length of the horizontal and vertical beams. Muamad devised 11 different designs with perforated wings and one with solid wings on a single chip manufactured by SOIMUMPS. His work indicated that the small holes on the wings do not reduce the sound coupling. On the basis of Muamad's work, Simsek developed capacitance readout circuitry for the sensor and introduced it into a network configuration. After that, Harrison included the substrate in computer simulations. The introduction of the substrate enhances the amplitude response since a larger pressure gradient is generated with the increase in the path length of the acoustic wave travelling to reach the back side of the diaphragms. An et al. [78] appended stiffeners under the wings and cross beams to strengthen the diaphragms and avoid unnecessary diaphragm deformation. When simulating the device, they found that the first eigen-frequency decreases as the length of vertical beam increases. The second eigen-frequency stays almost constant in the same process since the torsional stiffness of the vertical beam is inversely proportional to its length. On the other hand, the second eigen-frequency decreases as the length of the horizontal beam increases and the first eigen-frequency stays constant since the bending stiffness of the vertical beam is inversely proportional to its length. They also discovered that the amplitude of each diaphragm is reduced with increasing horizontal beam stiffness whereas the phase difference increases along with the increase of horizontal beam. More recently, Touse et al. [79], [80] added comb sensing elements into the design. From that, an asymmetric design was also later discussed [81]. The difference in area causes a greater effective pressure gradient to be placed on the two wings and the amplitude of the rocking mode is dramatically increased. In addition, with an open backside, the asymmetric design works with both rocking and bending modes.

Except for Mile's research group and the researchers from the Navel Graduate School, other research groups were also developing various microphone with see-saw type model but different design details [82]–[85].

2) Clamped diaphragms model

As the displacement amplitude of rotating plates in see-saw model is proportional to the surrounding sound pressure, such microphones are usually

packaged with an omnidirectional microphone side by side in order to measure the sound pressure near the frontal surface of the device if the application requires the determination of accurate sound direction, which enlarges the entire package size and brings errors caused by the offset between the pressure gradient microphone and the omnidirectional one. Yu et al. circumvented this problem by taking the ratio of amplitudes of the two diaphragms [43], [86], [87] and their phase difference which were termed the mechanical Interaural Intensity Difference (mIID) and mechanical Interaural Phase Difference (mIPD) respectively.

Re-write the Eq. [1.40] and [1.41] as:

$$\begin{bmatrix} x_1(\omega) \\ x_2(\omega) \end{bmatrix} = \frac{PS}{K} \frac{\cos\frac{\omega\tau}{2}}{1-\Omega^2+2i\Omega\xi_r} \begin{bmatrix} \Gamma + i\tan\frac{\omega\tau}{2} \\ \Gamma - i\tan\frac{\omega\tau}{2} \end{bmatrix} \quad [1.45]$$

$$\Gamma = \frac{1-\Omega^2+2i\Omega\xi_r}{\eta^2-\Omega^2+2i\eta\Omega\xi_r}, \Omega = \frac{\omega}{\omega_r}, \eta = \frac{\omega_t}{\omega_r},$$

where Γ, Ω and η are the relative contributions of the two modes subject to unit modal force, the normalized excitation frequency, and the eigen-frequency frequency ratio, respectively. The mIPD is defined as the phase ratio of the two amplitudes:

$$\text{mIPD} = \angle\frac{x_1(\omega)}{x_2(\omega)} = \angle\frac{\Gamma+i\tan\frac{\omega\tau}{2}}{\Gamma-i\tan\frac{\omega\tau}{2}}. \quad [1.46]$$

To more precisely determine the directional capability of using mIPD of *Ormia*'s hearing organ, another parameter, directional sensitivity (DS), is introduced as the gradient of the mIPD during the excitation, which is shown as

$$DS = \frac{\partial mIPD}{\partial\theta}. \quad [1.47]$$

As shown in equations 1.46 and 1.47, both values of mIPD and DS change with the modal response value Γ and time delay of sound arrival (TDSA). In addition, Γ is controlled by the natural frequency ratio η and normalized excitation frequency Ω. From the simulation results made by Yu et al. [88], with a 5 kHz plane wave in a $-30°$ to 30° incident angle range, the DS remains very flat and achieves a higher value than that at any other frequency, which also means that the mIPD is linear to the sound incident angle between $-30°$ to 30°. Based on the theory above, Yu's research group introduced Ormia-inspired microphones that determine sound incident angle by

detecting the mIPD between two coupled circular membranes mimicking the behaviour of two *Ormia*'s tympana [89]. So, this kind of microphones does not require an omnidirectional microphone for sound pressure sensing due to the mIPD detection method. In their latest report [90], the device consists of two polysilicon membranes (1.1 mm in diameter and 0.5 μm in thickness), and their boundary is clamped to the substrate. A 300μm wide SiO_2/Si_3N_4 bridge is pivoted in the centre, and the two ends are connected to the centres of two membranes. The backside of the membranes are firstly etched though deep reactive ion etching, and then a SOI wafer that has eight 60μm diameter perforated holes for tuning air damping and two 500μm diameter holes for guiding optical fibres to detect the vibration of the two membranes is bonded onto the bottom of the previous substrate. Underneath the SOI wafer, two circular air chambers are attached to increase the air damping and block the sound pressure from the backside. The device has its best performance at 8 kHz, which is slightly below the first resonance and just like what happens in *Ormia*'s hearing organ (i.e. the best performance of *Ormia*'s ear occurs at 5 kHz, however the first resonance frequency is slightly higher than that value, which is around 7 kHz). At 8 kHz excited frequency, the slope of the mIPD versus the azimuth sound incident angle (i.e. DS) of this device is about 1.69 deg/deg.

Another *Ormia*-inspired MEMS microphone with clamped circular membranes was designed by M. L. Kuntzman et al [71]. The device consists of two polysilicon membranes connected by a polysilicon bridge with different thickness. Two electrodes are placed underneath the membranes for capacitive sensing. It was designed for ultrasound measurement. However, unlike the designs from Yu et al., this ultrasonic transducer still uses a displacement amplitude detection method.

3) Others

The microphones presented here only permit the localization of sound on one axis, either the azimuth measured around the axis normal to the plane of the device, or the pitch, measured around the axis normal to the line between the two diaphragms. In any situation where either the azimuth or the pitch cannot be assumed to be zero there will be some ambiguity in the results, with the directional reading of the sensor describing a paraboloid surface in space. The simplest of these consists of three

mechanically linked diaphragms in a triangle formation around a central pivot [91]. Comparing the phase difference between any two diaphragms will yield a set of azimuth and pitch angles, which can then be correlated to the set produced by another pair of diaphragms to localize the sound source. Although this sensor is capable of resolving the ambiguity in pitch and azimuth angle it does so by triangulation and offers little improvement over a similarly spaced array of *Ormia*-inspired microphones. Other research groups also have shown their interest in designing *Ormia*-inspired 2D sound localizing sensors. N. Ono et al. [92], [93] built a model with a fixed centre region surrounded by a diaphragm. Between these two regions, two narrow torsional beams were provided to permit the diaphragm to vibrate in different directions. The model was fabricated using three different methods. The first one was using metal. The diaphragm is a chemical etched phosphor bronze foil that is surround by an aluminium pipe with a small gap and glued to a centre pole. The second way to make the device was by assembling three polysilicon and two phosphosilicate glass layers into the diaphragm. The back electrodes were divided into four parts performing as four measuring capacitors. The last method is using a Ni thin plate suspended on a SOI substrate with a back cavity. Only first fabrication method was chosen for characterization in the final experimental stage, and it gave a small sound localization error in the test results.

b) The second order microphones

As described above, a second-order directional microphone has better ability to reject off-axis noise since it detects the sound location through estimating the second spatial derivative of the pressure gradient. The first model of second-order *Ormia*-inspired MEMS microphone was designed by Liu [94], [95], which joins two single *Ormia*-inspired first-order polysilicon microphone built by Miles et al. mentioned above with an S-type beam in the middle. Developing Liu's work, another graduate, Albahri [96] optimized the model and replaced the S-type connection with a simple rectangular beam and added extra mass to the sides of the rotating plates to reduce the influence of any mismatch between the two single microphones. Meanwhile, Huo [97] changed the two diaphragms into a structure constructed with comb fingers, and the hinge between is removed in this model.

To summarize, the see-saw model suppresses the contribution of the bending mode and primarily applies a rocking mode driven by the sound pressure gradient acting on the two rigid plates. However, this model does require an omnidirectional microphone to get the sound pressure variation and bring full function to the final products that requires accurate sound incident angle definition. The clamped-diaphragm model uses mIPD to locate sound and solve the omnidirectional microphone problem. But the fixed ends boundary of the diaphragm in this model generates a reaction force and so degrades the effective force driving vibration. The small displacement of the membranes can only be measured using optical (fibre) techniques so far. To detect sound sources spatially, the gimbal diaphragm model was invented. It can locate the source from any direction and has a sensitivity-adjustment mechanism. Unfortunately, only the model made by bronze foil had been implemented and tested, which is not within a MEMS device. The second-order model contains two see-saw models. It provides better directional capability than a single model but does require larger dimensions.

However, after the centre-supported gimbal model was published, researchers found that its performance is greatly affected by gravity. Chen and Cheng [98] proposed a clover-stem-like gimbal structure to alleviate this influence. The entire mass of the diaphragm is supported by four pairs of centred beams that have one end clamped and the other end connected to a central floating joint, which performs as a freely suspended support. The effect of gravitational force or residual stress acting on the diaphragm can then be compensated by the concentrated moments resulting from

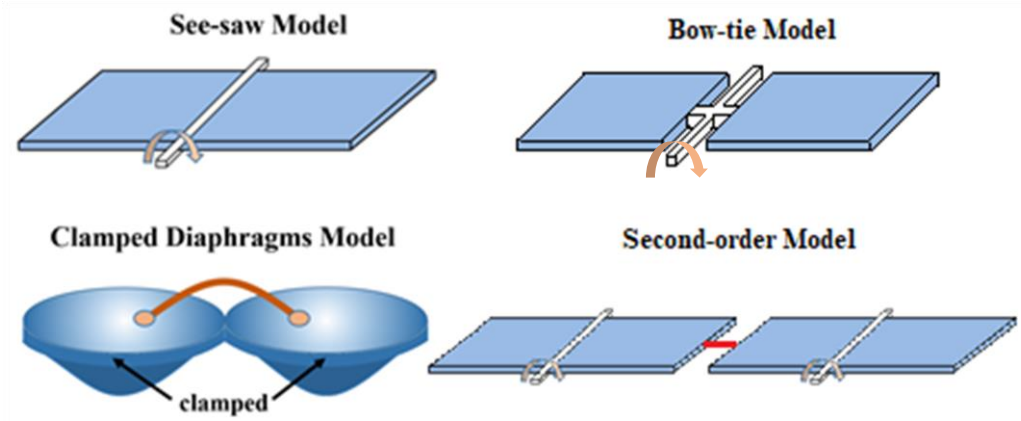

Fig. 2.18 Schematic sketches of see-saw, bow-tie, clamped diaphragms and second-order models

the reaction force applied on the joint when the diaphragm vibrates along the axis. However, all these designs are either on the meso-scale or are proposed models only.

Chapter 3

The First-Generation Design

This chapter presents the first generation of multi-band operational *Ormia*-inspired MEMS microphone design. The development of this device is a process of discovering and studying the procedure of designing and characterizing a MEMS microphone for the first time.

3.1 Introduction

The simplest way of introducing more resonance frequencies into a system is to include more vibrational elements. However, blindly adding more vibrational elements or increasing the size of the structure could cause an *Ormia* type microphone to lose its directivity or decrease the sensitivity. Therefore, in order to retain the advantages of an *Ormia*-inspired MEMS microphone and build a device operating in an audible range of frequencies, a novel microphone structure having four resonance frequencies was developed to meet the demands.

The concept of the design is based on two concentric diaphragms placed in the same plane. Depending on position, the structure can be divided into an outer diaphragm and an inner diaphragm that rotate along a two-end fixed beam parallel with one side of the outer diaphragm. These two parts are expected to have individual rocking modes and bending modes, not impacted by the mechanical coupling between them. In addition, the introduced resonance frequencies should be below the maximum auditory frequency. This value could reach to 20 kHz for a healthy young adult. But, for a middle-aged or elder adult, the maximum auditory frequency is only about 15 kHz since the ability to hear high frequency can decrease with age [99]. The wavelength for a 15 kHz sound wave is 22.87mm. The reason of calculating the wavelength is that the critical size of the MEMS microphone is derived from this value.

According to Kinsler L. et al.'s book [33], if a microphone is required to work in a non-diffractive sound environment throughout the audible range of frequencies, the size of it should meet the following rule: $k_w \times r < 1$, where k_w is the wave number and r is the radius of the microphone. In this case, the critical radius of the microphone is 3.6 mm.

In this chapter, a device designed to match the above requirements and expectations is introduced. As this is the first design for this thesis, another aim of this design is gain familiarity with the process of developing a MEMS device, including simulation using finite element modelling software, drawing a layout for MEMS fabrication and using exclusive experimental equipment to test the prototypes. The experimental results may not be ideal, but they act as a reference for further device development.

3.2 Analytical model

The first generation *Ormia*-inspired microphone design is drawn using Tanner EDA L-edit software. The new design comprises an inner circular thin plate with 1mm radius, an outer square thin plate $2.6mm \times 2.6mm$ with a circular hole (1.084 mm in radius) placed in the centre, and a rectangular beam ($2.7mm \times 50\mu m$) working as a pivot. The other details of the structure are shown in Fig. 3.1. The whole model is designed to be made using single-crystal silicon, with thickness of 10 µm. As the

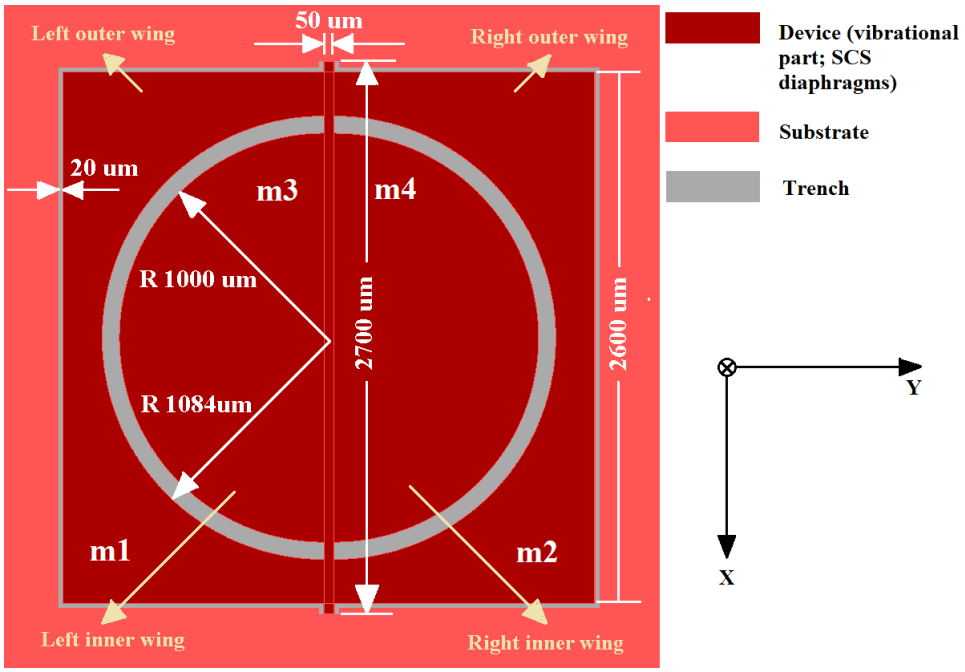

Fig. 3.1 The L-Edit drawing of the first-generation device

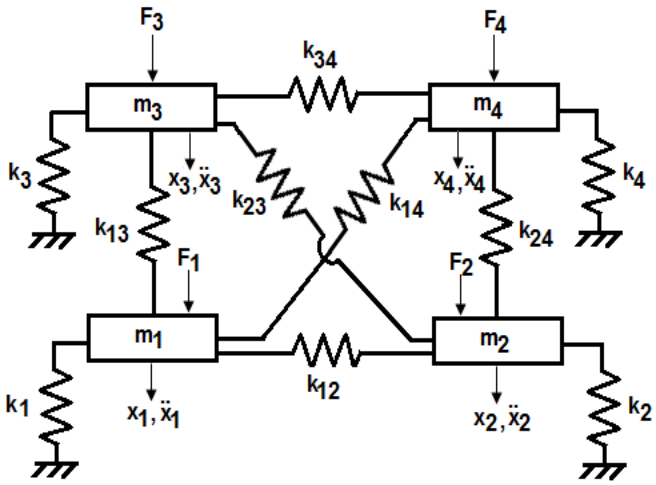

Fig. 3.2 Equivalent lumped model of the first-generation design

model contains two diaphragms (four wings) rotating along the pivot, it can be considered as a four-degree-of-freedom-system. The equivalent mechanical model (see Fig. 3.2) gives out the governing equation of the system.

$$[\boldsymbol{M}]\left[\boldsymbol{x}(\boldsymbol{t})\right] + [\boldsymbol{C}]\left[\boldsymbol{x}(\boldsymbol{t})\right] + [\boldsymbol{K}][\boldsymbol{x}(\boldsymbol{t})] = [\boldsymbol{f}(\boldsymbol{t})] \qquad [3.1]$$

where,

$$[\boldsymbol{M}] = \begin{bmatrix} m_1 & 0 & 0 & 0 \\ 0 & m_2 & 0 & 0 \\ 0 & 0 & m_3 & 0 \\ 0 & 0 & 0 & m_4 \end{bmatrix}, [\boldsymbol{C}] = \begin{bmatrix} C_a & c_{12} & -c_{13} & c_{14} \\ c_{12} & C_b & c_{23} & -c_{24} \\ -c_{13} & c_{12} & C_c & c_{34} \\ c_{14} & -c_{24} & c_{34} & C_d \end{bmatrix},$$

$$[\boldsymbol{K}] = \begin{bmatrix} K_a & k_{12} & -k_{13} & k_{14} \\ k_{12} & K_b & k_{23} & -k_{24} \\ -k_{13} & k_{12} & K_c & k_{34} \\ k_{14} & -k_{24} & k_{34} & K_d \end{bmatrix},$$

$$\left[\boldsymbol{x}(\boldsymbol{t})\right] = \begin{bmatrix} \ddot{x}_1(t) \\ \ddot{x}_2(t) \\ \ddot{x}_3(t) \\ \ddot{x}_4(t) \end{bmatrix}, \left[\boldsymbol{x}(\boldsymbol{t})\right] = \begin{bmatrix} \dot{x}_1(t) \\ \dot{x}_2(t) \\ \dot{x}_3(t) \\ \dot{x}_4(t) \end{bmatrix}, [\boldsymbol{x}(\boldsymbol{t})] = \begin{bmatrix} x_1(t) \\ x_2(t) \\ x_3(t) \\ x_4(t) \end{bmatrix}$$

$C_a = c_1 + c_{12} + c_{13} + c_{14}, C_b = c_2 + c_{12} + c_{23} + c_{24},$

$C_c = c_3 + c_{13} + c_{23} + c_{34}, C_d = c_4 + c_{14} + c_{24} + c_{34},$

$K_a = k_1 + k_{12} + k_{13} + k_{14}, K_b = k_2 + k_{12} + k_{23} + k_{24},$

$K_c = k_3 + k_{13} + k_{23} + k_{34}, K_d = k_4 + k_{14} + k_{24} + k_{34}.$

$[\boldsymbol{M}]$, $[\boldsymbol{C}]$ and $[\boldsymbol{K}]$ in the equations here are the mass matrix, damping coefficient matrix and stiffness matrix, separately. Since the system is regarded as a system of particles, the m_i, c_i, and k_i shown in the matrices are the participating mass concentrated on the centroid, the damping coefficient around each wing (e.g. the structural damping in the central torsional beam, air damping in the surrounding silts and underneath the wings), and the stiffness transferred from the torsional stiffness of the central beam that is distributed on each wing. $x_i(t)$ is the structural displacement response in time domain, while c_{ij} and k_{ij} are the damping coefficient and stiffness coefficient between two adjacent wings (i = 1, 2, 3, 4, j = 2, 3, 4, $i \neq j$). To find out the resonance frequencies

of the system and other factors affecting the motions of the vibrating wings, the Fourier Transform is applied to Eq. 2.1 and system response in the frequency domain is shown as follows

$$\begin{bmatrix} -\omega^2 m_1 + i\omega C_a + K_a & c_{12} + k_{12} & -c_{13} - k_{13} & c_{14} + k_{14} \\ c_{12} + k_{12} & -\omega^2 m_2 + i\omega C_b + K_b & c_{23} + k_{23} & -c_{24} - k_{24} \\ -c_{13} - k_{13} & c_{23} + k_{23} & -\omega^2 m_3 + i\omega C_c + K_c & c_{34} + k_{34} \\ c_{14} + k_{14} & -c_{24} - k_{24} & c_{34} + k_{34} & -\omega^2 m_4 + i\omega C_d + K_d \end{bmatrix} \begin{bmatrix} x_1(\omega) \\ x_2(\omega) \\ x_3(\omega) \\ x_4(\omega) \end{bmatrix} = \begin{bmatrix} F_1(\omega) \\ F_2(\omega) \\ F_3(\omega) \\ F_4(\omega) \end{bmatrix}. \quad [3.2]$$

The eigen-frequencies of the mode shapes are derived by calculating the eigenvalue of Eq. 2.2. The basic form of an eigenvalue problem is

$$[\boldsymbol{A} - \lambda \boldsymbol{I}]\boldsymbol{x} = 0, \quad [3.3]$$

where $\boldsymbol{A}$, λ, $\boldsymbol{I}$ and $\boldsymbol{x}$ are a square matrix, eigenvalues, identity matrix and eigenvalue vectors, respectively. Compared to Eq. 2.2, $\boldsymbol{A} = [\boldsymbol{K}]$, $\lambda = \omega^2$ and $\boldsymbol{I} = [\boldsymbol{M}]$. As $x_i(\omega)$ is a non-zero vector, the general mathematical eigenvalue problem can be simplified by solving the following determinate

$$|-\omega^2[\boldsymbol{M}] + [\boldsymbol{K}]| = 0. \quad [3.4]$$

Applying Ferrari's method [100] of solving quadratic equations on Eq. 2.4, the general solution of the eigen-frequencies of this 4DOF system could be expressed as follows

$$f_{n1} = \frac{1}{2\pi} \times \sqrt{-\frac{b}{a} + \frac{\sqrt{\alpha+2y} - \sqrt{-\left(3\alpha+2y+\frac{2\beta}{\sqrt{\alpha+2y}}\right)}}{2}} \quad [3.5]$$

$$f_{n2} = \frac{1}{2\pi} \times \sqrt{-\frac{b}{a} - \frac{\sqrt{\alpha+2y} + \sqrt{-\left(3\alpha+2y-\frac{2\beta}{\sqrt{\alpha+2y}}\right)}}{2}} \quad [3.6]$$

$$f_{n3} = \frac{1}{2\pi} \times \sqrt{-\frac{b}{a} - \frac{\sqrt{\alpha+2y} - \sqrt{-\left(3\alpha+2y-\frac{2\beta}{\sqrt{\alpha+2y}}\right)}}{2}} \quad [3.7]$$

$$f_{n4} = \frac{1}{2\pi} \times \sqrt{-\frac{b}{a} + \frac{\sqrt{\alpha+2y} + \sqrt{-\left(3\alpha+2y+\frac{2\beta}{\sqrt{\alpha+2y}}\right)}}{2}} \quad [3.8]$$

where

$$y = -\frac{5}{6}\alpha - U + \frac{P}{3U}, (U \neq 0)$$

$$\gamma = -\frac{3}{256}\left(\frac{b}{a}\right)^4 + \frac{b^2 c}{16a^3} - \frac{bd}{4a^2} + \frac{e}{a}, P = -\frac{\alpha^2}{12} - \gamma,$$

$$\mathrm{Q} = -\frac{\alpha^3}{108} + \frac{\alpha\gamma}{3} - \frac{\beta^2}{8}, R = \frac{Q}{2} - \sqrt{\frac{Q^2}{4} + \frac{P^3}{27}}, U = \sqrt[3]{R},$$

$$\alpha = -\frac{3}{8}\left(\frac{b}{a}\right)^2 + \frac{c}{a}, \beta = \frac{1}{8}\left(\frac{b}{a}\right)^3 - \frac{cb}{2a} + \frac{d}{a},$$

$$\frac{b}{a} = -\left(\frac{K_a}{m_1} + \frac{K_b}{m_2} + \frac{K_c}{m_3} + \frac{K_d}{m_4}\right),$$

$$\frac{c}{a} = \frac{K_a K_b - k_{12}^2}{m_1 m_2} + \frac{K_a K_c - k_{13}^2}{m_1 m_3} + \frac{K_a K_d - k_{14}^2}{m_1 m_4} + \frac{K_b K_c - k_{23}^2}{m_2 m_3} + \frac{K_b K_d - k_{24}^2}{m_2 m_4} + \frac{K_c K_d - k_{34}^2}{m_3 m_4},$$

$$\frac{d}{a} = \frac{K_b k_{34}^2 + K_c k_{24}^2 + K_d k_{23}^2 + 2k_{23}k_{24}k_{34} - K_b K_c K_d}{m_2 m_3 m_4} + \frac{K_a k_{34}^2 + K_d k_{13}^2 + K_c k_{14}^2 + 2k_{13}k_{14}k_{34} - K_a K_c K_d}{m_1 m_3 m_4} +$$

$$\frac{K_a k_{24}^2 + K_b k_{14}^2 + K_d k_{12}^2 + 2k_{12}k_{14}k_{24} - K_a K_b K_d}{m_1 m_2 m_4} + \frac{K_a k_{23}^2 + K_b k_{13}^2 + K_c k_{12}^2 + 2k_{12}k_{13}k_{23} - K_a K_b K_c}{m_1 m_2 m_3},$$

$$\frac{e}{a} = \frac{(K_a K_b - k_{12}^2)(K_c K_d - k_{34}^2)}{m_1 m_2 m_3 m_4} - \frac{(k_{12}k_{13} + k_{23}K_a)(k_{24}k_{34} + k_{23}K_d)}{m_1 m_2 m_3 m_4} -$$

$$\frac{(k_{12}k_{14} + k_{24}K_a)(k_{23}k_{34} + k_{24}K_c)}{m_1 m_2 m_3 m_4} - \frac{(k_{12}k_{23} + k_{13}K_b)(k_{14}k_{34} + k_{13}K_d)}{m_1 m_2 m_3 m_4} -$$

$$\frac{(k_{12}k_{24} + k_{14}K_b)(k_{13}k_{34} + k_{14}K_c)}{m_1 m_2 m_3 m_4} + \frac{(k_{13}k_{24} - k_{14}k_{23})^2}{m_1 m_2 m_3 m_4}.$$

When the device is symmetric, where $m_O = m_1 = m_2, m_I = m_3 = m_4, k_O = k_1 = k_2, k_I = k_3 = k_4, k_{c1} = k_{13} = k_{24}, k_{c2} = k_{14} = k_{23}, k_{t1} = k_{12}, k_{t2} = k_{34}$, the eigen-frequencies can be simplified as

$$f_{n1,3} = \frac{1}{2\pi}\sqrt{\frac{k_{total\_I}}{2m_I} + \frac{k_{total\_O}}{2m_O} \mp \sqrt{\frac{\Omega^2}{4{m_O}^2{m_I}^2} + \frac{k_{sum\_c}^2}{m_O m_I}}}, \quad [3.9]$$

$$f_{n2,4} = \frac{1}{2\pi}\sqrt{\frac{k_{total\_i} + 2k_{t2}}{2m_i} + \frac{k_{total\_o} + 2k_{t1}}{2m_o} \mp \sqrt{\frac{[\Omega - 2\kappa]^2}{4{m_o}^2{m_i}^2} + \frac{k_{diff\_c}^2}{m_o m_i}}}, \quad [3.10]$$

where

$$k_{sum\_c} = k_{c1} + k_{c2}, k_{diff\_c} = k_{c1} - k_{c2}, k_{total\_O} = k_O + k_{sum\_c},\ k_{total\_i} = k_I + k_{sum\_c},$$

$$\Omega = (m_I - m_O)k_{sum\_c} + k_I m_I - k_O m_O,$$

$$\kappa = k_{t1} m_O - k_{t2} m_I.$$

Further analysing Eq. [3.9] and Eq. [3.10], it is easy to discover that the 1st and the 3rd eigen-frequencies are related to the sum of the coupling stiffness between the inner disc and outer frame, and also the torsional stiffness provided by the rotational beam. Compared to the equations of eigen-frequency of *Ormia*'s ears, it could be imagined that the outer and the inner plates mainly rotate in the same or in the opposite directions at the 1st and the 3rd eigen-frequencies. However, these two eigen-frequencies are independent of the interior coupling stiffness of either inner disc or outer frame (i.e. k_{t1} and k_{t2}). On the other hand, for the 2nd and the 4th eigen-frequencies, the interior coupling stiffness greatly affects these two values. So conceivably, the wings of both inner disc and outer frame would vibrate in phase at the 2nd and the 4th eigen-modes. They would move just like the *Ormia*'s ears at the bending mode, individually.

In this design, the mass of the outer frame ($\approx 3.54 \times 10^{-8} m^2$) is in close proximity to the value of inner disc ($\approx 3.55 \times 10^{-8} m^2$), i.e. $m_O \approx m_I = m$, therefore the Eq. [3.9] and [3.10] are re-written as

$$f_{n1,3} = \frac{1}{2\pi}\sqrt{\frac{k_O + k_I}{2m} + \frac{k_{sum\_c}}{m} \mp \frac{1}{2m}\sqrt{(k_i - k_o)^2 + 4k_{sum\_c}^2}}, \quad [3.11]$$

$$f_{n2,4} = \frac{1}{2\pi}\sqrt{\frac{k_O + k_I}{2m} + \frac{k_{sum\_t} + k_{sum\_c}}{m} \mp \frac{1}{2m}\sqrt{\left[(k_I - k_O) - 2k_{diff\_t}\right]^2 + 4k_{diff\_c}^2}}, \quad [3.12]$$

where

$$k_{sum\_t} = k_{t1} + k_{t2}, k_{diff\_t} = k_{t1} - k_{t2}. \quad [3.13]$$

Because of the complexity of the device geometry, the mechanical stiffness matrix $[\boldsymbol{K}]$ and the eigen-frequencies are confirmed using COMSOL finite element modelling which will be introduced in the next section.

3.3 COMSOL simulation

COMSOL Multiphysics is a finite element modelling (FEM) software allowing users to analyse the physical phenomenon of a structure in multiple physics conditions. The structure can either be drawn using a built-in simple CAD function or be imported from other CAD software (e.g. AutoCAD, Solidworks, etc.). To simulate the performance of the design operating in air, the Solid Mechanics interface in the Structural Mechanics Module and the Acoustic-Solid Interaction in the Acoustic Module were utilized. The Solid Mechanics interface is used to study the eigen-values and the stationary structural displacement of the design. The Acoustic-Solid Interaction, combining the Acoustic interface and the Solid Mechanics interface, is used to analyse the mechanical and acoustic properties when a sound field is applied to the structure, such as the mechanical vibration of the design, the stress occurring in the structure, the near and far-field acoustic pressure field, etc. The method of simulation described in this section is also the basic process for investigating subsequent designs at an early stage.

To estimate the resonance frequencies of the planning manufactured device and to calculate the structural stiffness matrix $[K_{stiffness}]$, the two-dimensional foot-print of the device is first drawn and then extruded by 10 μm in the z-direction. Since the design was later fabricated using SOIMUMPS provided by MEMS foundry service company, MEMSCAP, the material is set to be single-crystal silicon (SCS). The density of the material is 2330 kg/m^3. According to M. A. Hopcroft et al.'s discovery [101], that the primary flat of a (100) SCS wafer is generally aligned with the [110]

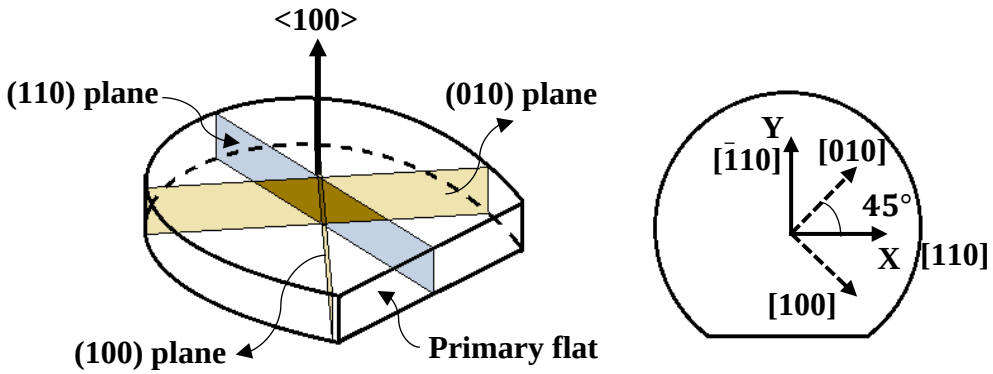

Fig. 3.3 (a) Crystal orientation of a (100) wafer, (b) Directions and axes in a (100) wafer

direction which is also the flat for orientation used by common microfabrication tools, the X-Y axes used in the designing or computing software are practically aligned with the <110> crystal direction of a (100) SCS wafer as illustrated in Fig. 3.3 (b). They also compared the resonance frequency of a resonator sample computed by COMSOL when the SCS is regarded as an isotropic and an anisotropic material. The simulated results recommend using the anisotropic elasticity properties for SCS in COMSOL FEM work as they are much closer to the measured resonance frequencies. Therefore, the material used for this device was set to be anisotropic and the simulated model was rotated 45 degrees in the XY plane. The stiffness matrix of the material with three axes at [100], [010] and [001] is given in Eq. 2.14. Last but not least, to ensure accurate modelling, the two ends of the central beam in the simulated model were set to be fixed.

$$[\boldsymbol{S_{stiffness}}] = \begin{bmatrix} 166 & 64 & 64 & 0 & 0 & 0 \\ 64 & 166 & 64 & 0 & 0 & 0 \\ 64 & 64 & 166 & 0 & 0 & 0 \\ 0 & 0 & 0 & 80 & 0 & 0 \\ 0 & 0 & 0 & 0 & 80 & 0 \\ 0 & 0 & 0 & 0 & 0 & 80 \end{bmatrix} [GPa]. \qquad [3.14]$$

First of all, assuming the device is a mechanically balanced system (i.e. no velocity and no acceleration) and placing a uniform specified force load on each wing of the device, the matrix $[\boldsymbol{K}]$ could be derived from a matrix of simulated structural displacement field values, which can be expressed as follows

$$k_O = 4.6906\, N/m\,, k_I = 14.4512\, N/m,$$

$$k_{c1} = 7.8875\, N/m\,, k_{c2} = 0.4472\, N/m,$$

$$k_{t1} = 5.5554\, N/m\,, k_{t2} = 19.5944\, N/m,$$

$$[\boldsymbol{K}] = \begin{bmatrix} 18.5807 & 5.5554 & -7.8875 & 0.4472 \\ 5.5554 & 18.5807 & 0.4472 & -7.8875 \\ -7.8875 & 0.4472 & 42.3803 & 19.5944 \\ 0.4472 & -7.8875 & 19.5944 & 42.3803 \end{bmatrix} [N/m]. \qquad [3.15]$$

Substituting the matrix into the analytical model, the analytical resonance frequencies are derived as 2425 Hz, 4027 Hz, 4430 Hz, and 6713 Hz.

The more precise estimation of the resonance frequencies is implemented by the built-in eigen-frequency study option. Figure 2.4 shows the first four simulated

mode shapes, and their corresponding eigen-frequencies are 2220 Hz, 3646 Hz, 3977 Hz and 6438 Hz separately. The outer plate drives the first two mode shapes. The two wings of the outer plate vibrate out of phase at the 1st eigen-frequency while they move in phase at the 2nd eigen-frequency. Compared to the outer plate, the average structural displacement of the inner plate is much smaller and even zero at the 2nd eigen-frequency. At the 3rd and the 4th eigen-frequencies, the exact opposite situation happens. The structural displacement of the inner plate is much higher than the outer plate, and it has rocking and bending movement at the 3rd and the 4th eigen-frequencies respectively. In other words, the mechanical coupling between the inner and the outer structure does not affect their behaviour as the *Ormia*'s tympana.

In order to analyse the physical phenomenon when the structure is exposed to a sound pressure field, the main device was built to connect to a 400 μm thick substrate with a fixed backside at the hinge, similar to the planned manufactured prototype and experimental setup. The air domain was defined to surround the main device and induce a 1 Pa sound plane wave propagating along the plane normal to the surface of

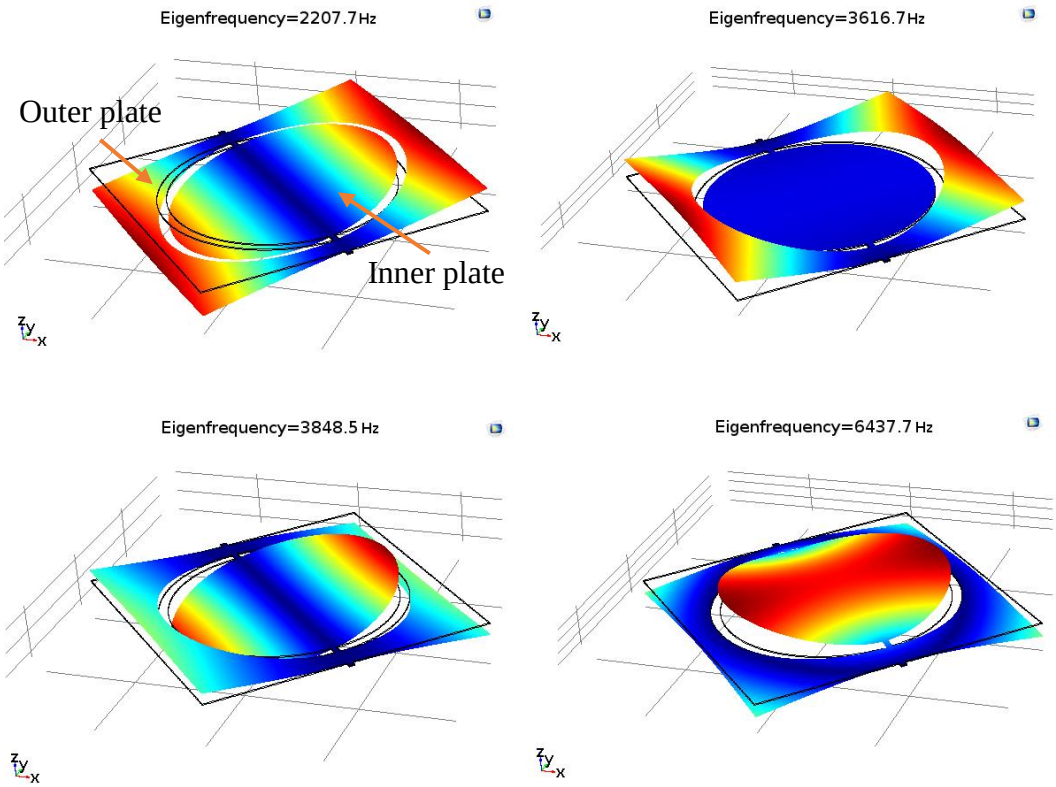

Fig. 3.4 The first four mode shapes and their corresponding resonance frequencies simulated by COMSOL

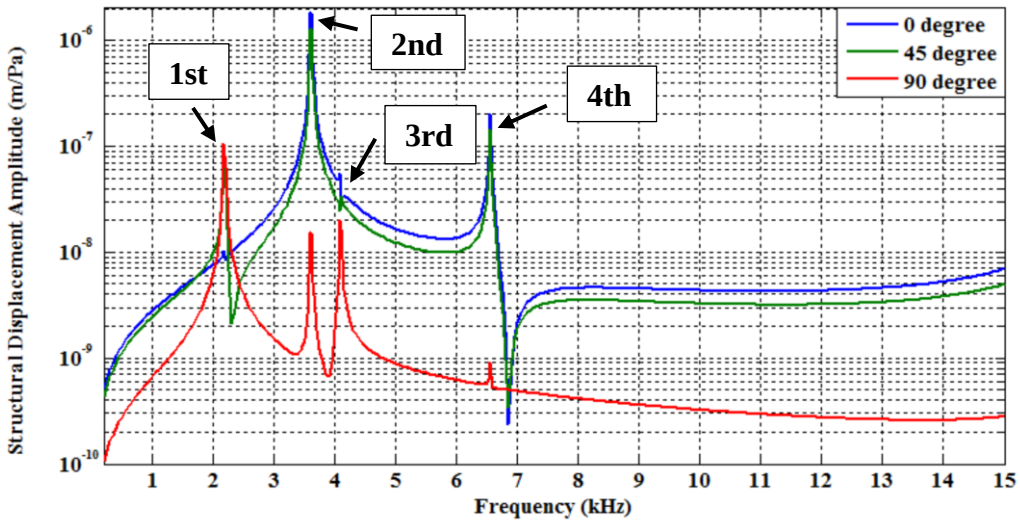

Fig. 3.5 Simulated mechanical frequency response of the outer plate

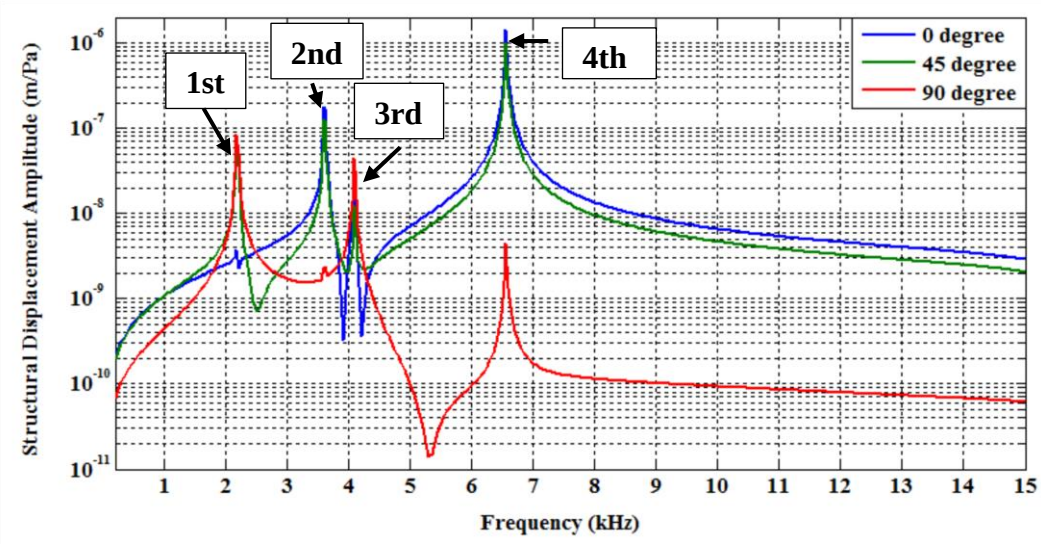

Fig. 3.6 Simulated mechanical frequency response of the inner plate

plate and vertical to the central beam as shown in Fig. 3.2. Since the backside of the substrate was set to be exposed to the air, the air damping in the silts between the outer frame and the inner plate, the outer plate and the substrate, are negligible. Then a parametric sweep of frequencies was conducted across a frequency range below 15 kHz. Figure 3.5 and Fig. 3.6 show the structural displacement response exported at the ends of both inner and outer plates of the structure when the sound incident angle θ was set to 0 degree, 45 degrees and 90 degrees. In this case, only the bottom side of the substrate was set to be fixed, the eigen-frequencies are approximately 200 Hz

higher than the results obtained only using the Solid Mechanics interface. In terms of the outer plate, its maximum structural displacement amplitude appears when the sound wave strikes the front surface of the device perpendicularly (i.e. $\theta = 0°$) at the 2nd resonance frequency, which is 1.81 μm/Pa. For the inner plate, it has a maximum vibration of about 1.41 μm/Pa at the 4th resonance mode when $\theta = 0°$. Both plates have larger mechanical vibration at the bending modes than at the rocking modes, which agrees with the mechanical phenomenon that happens on an *Ormia*-inspired microphone with just a single rotating membrane. The mechanical coupling between the two plates not only introduce two more resonance frequencies to each other but also provides the possibility of increasing the total signal output and SNR by summing and differentiating the output captured from each wing of each plate.

Furthermore, a parametric sweep of sound incident angle with 10 degrees per step was computed at each resonance frequencies to figure out the directivity of the designed structure. Figure 3.7 illustrates the directional polar patterns of both outer square frame and inner circular plate excited by frequencies around the resonance frequencies. It is observed that instead of capturing most acoustical energy from exactly the front, this microphone structure collects much more energy when the sound waves propagate to the device from the side face and firstly hit the edge of the entire structure at the 1st and the 3rd resonance frequencies. This phenomenon is mainly caused by the superposition of sound diffraction and reflection produced by the substrate when the sound waves travel to its bottom and meanwhile passes through the silts between it and the main vibrational structure. The thickness of the substrate strongly affects the degree of deflection of the directional polar patterns for the *Ormia*-inspired MEMS microphones with a symmetric geometry at the rocking modes, which will be described in detail in Chapter 5.2. In this case, the degree of deflection of the directional polar patterns is around 95 degrees and 60 degrees at the 1st and the 3rd resonance modes, respectively. However, the microphone structure is still able to reject the incident sound energy from the side and pick up much more energy from the front when the device is operating at the 2nd and the 4th resonance frequencies.

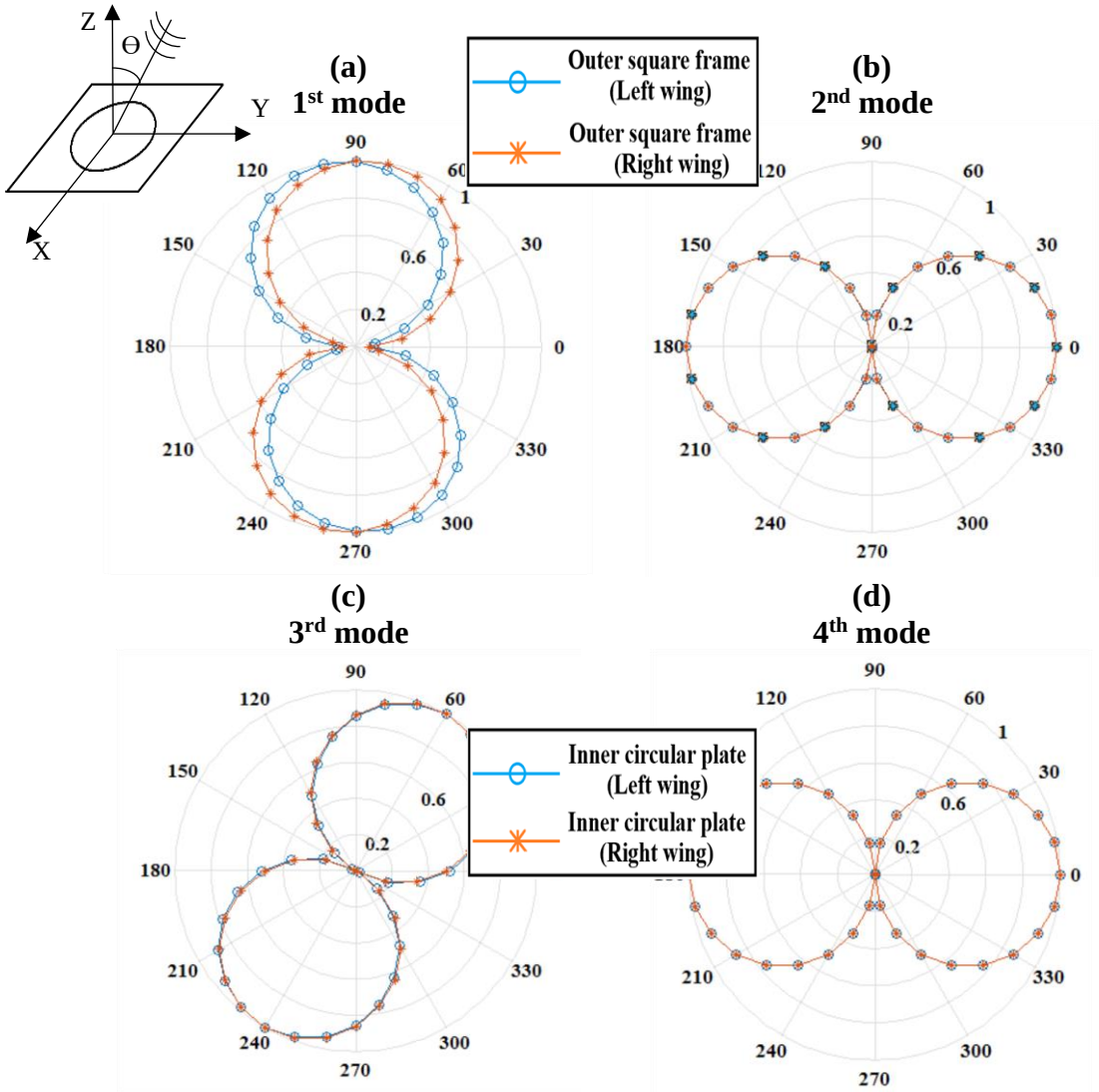

Fig. 3.7 The simulated directional polar patterns of the designed structure in XY plane

3.4 Fabrication

3.4.1 Microfabrication process

As mentioned previously, the MEMS manufacturing service used in the dissertation is provided by MEMSCAP [5]. Depending on different material and sensing demands from its customers, the company supplies SOIMUMPs (a SOI micromachining process), PolyMUMPs (a three-layer polysilicon surface micromachining process), and PiezoMUMPs (SCS + Aluminium Nitride for piezoelectric transducer fabrication). The suffix 'MUMPs' here is the abbreviation of "Multi-User MEMS Processes", which means different projects can share a single wafer using the same documented process design rules. This sort of foundry service reduces the manufacturing cost and increases the production quality and yield. They also have additional post processing services, such as laser sub-dicing, HF (hydrogen fluoride) release, supercritical CO_2 dry, and atomic layer deposition. The fabrication service used in this dissertation includes SOIMUMPs and PiezoMUMPs. Since the device being introduced in this chapter is a trial (or test) version, only the mechanical performance of the device is reported. It is unnecessary to integrate any electrical sensing part into the design, and so a SOIMUMPs process meets the requirements. As the sub-dicing service was not launched when this first generation was being fabricated, the device described in this chapter shares an 11.15mm × 11.15 mm die with other three designs.

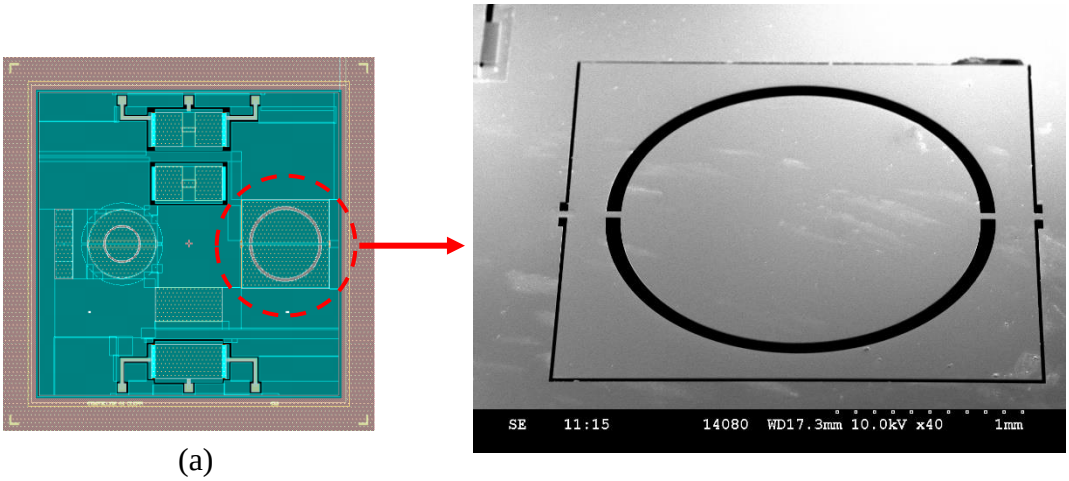

(a) (b)

Fig. 3.8 (a) The layout of the entire die; (b) The zoom out device image taken by scanning electron microscope (SEM)

For the SOIMUMPs, the company has SOI wafers with two thickness values of SCS layer: 10µm and 25µm. Considering the stiffness and lower frequency operation condition, the SOI wafer combining with a 10µm thick SCS layer doped on a 1µm thick oxide layer and a 400µm handle substrate was chosen. To lithographically pattern the silicon mechanical structure, the wafer is coated with positive photoresist. The area that has not been covered by the mask is laterally exposed to UV light and becomes soluble, leaving a photoresist mask behind. After that, deep reactive ion etching (DRIE) is applied to etch the region not protected by photoresist, and the silicon pattern is formed. The wafer is then reversed, and a similar process is done to the substrate, so that the trench is built, and the mechanical structure is released. Reference [6][102] affords the details of SOIMUMPs.

3.4.2 Prototype

The final prototype of the design is shown in Fig. 3.8 taken with a Hitachi S-3000N Scanning Electron Micrograph (SEM). To investigate the material properties of the SCS provided by SOIMUMPs, the prototype was tested with a Veeco NT1100

	Diameter (l)	Hight difference (M)	Radius of curvature (R)
Inner plate	2 mm	5.4 µm	91 mm
Outer plate	2.6 mm	> 9.2 µm	> 91 mm

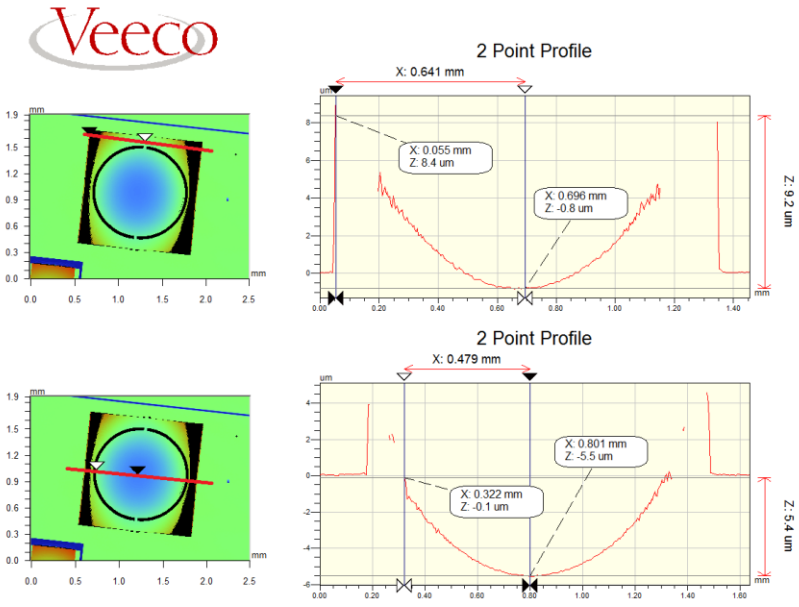

Fig. 3.9 The 2D contour plots (Left) of the measured data obtained from the optical profilometer and their corresponding 1D line plots

optical profilometer with 2.5X objective lens and 0.5X field-of-view (FOV) lens using Vertical Scanning Interferometry (VSI) mode. The optical profilometer is an interference microscope that measures height variation by comparing the optical path difference between the test surface and the reference surface. Using the two-point cursor type, it is easily to get the curvature of the surface finish between two defined points in a 1D line plot as shown in Fig. 3.9 (Notice: The FOV value was set as 1.0X when doing the surface measurement, so the plot scale is half of the actual scale). The height difference between the centre to the edge of the inner circular is about 3.9 µm, while the height difference from central beam to the edge of square frame is 9.2 µm. Due to the intrinsic stress of the SCS layer, the radius of curve from the centre to the edge of inner disc approaches to approximately 9.1cm (the calculation is given by Fig. 3.10). The device centre is 5.5µm below the zero baseline (i.e. the top surface of the substrate). The missing measured data (i.e. the black region in the 2D contour plots) is caused by insufficient interference fringes generated in these regions due to large geometry and curvature. By adding an initial stress into the COMSOL FEM model to imitate the intrinsic stress and matching height difference values using a stationary study, the calculated intrinsic stress gradient of the SCS layer used in this fabrication round is about 1.8 [MPa/µm]. The curvatures can cause measurement error and the device fracture.

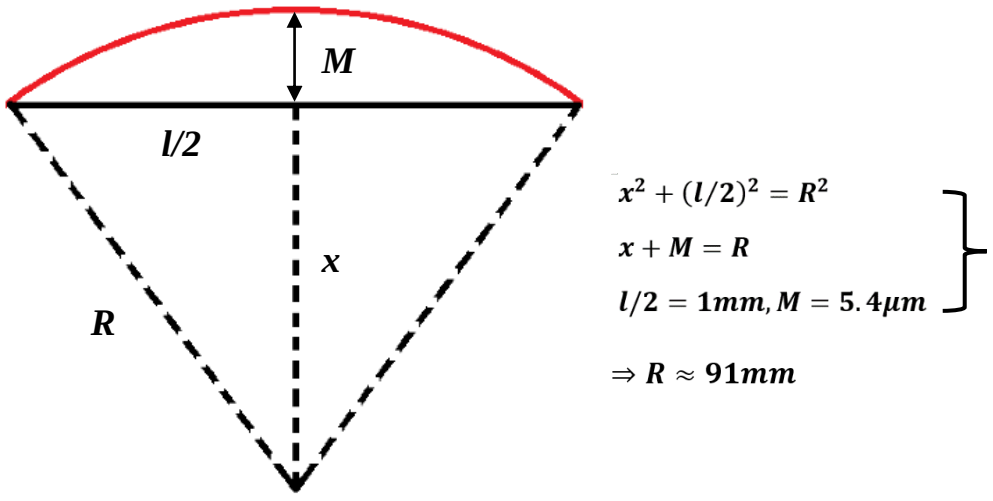

Fig. 3.10 Calculate the radius of curve occurring on the fabricated prototype

As shown in Fig. 3.5 (b), the device is located just beside the edge of the die, which results in different length of sound travelling paths, which was forecast to

influence the experimental results of the directional polar patterns. Figure 3.11 demonstrates the simulated directional polar patterns of the device when allocated beside the edge of the die to support this prediction. Comparing Fig. 3.11 with Fig. 3.7, the directional polar pattern of the inner fabricated circular disc at the 3rd resonance mode shifts 90 degrees. In other words, it acquires more energy from the front than from the side around the 3rd resonance frequency, which is far away from the previous expectation.

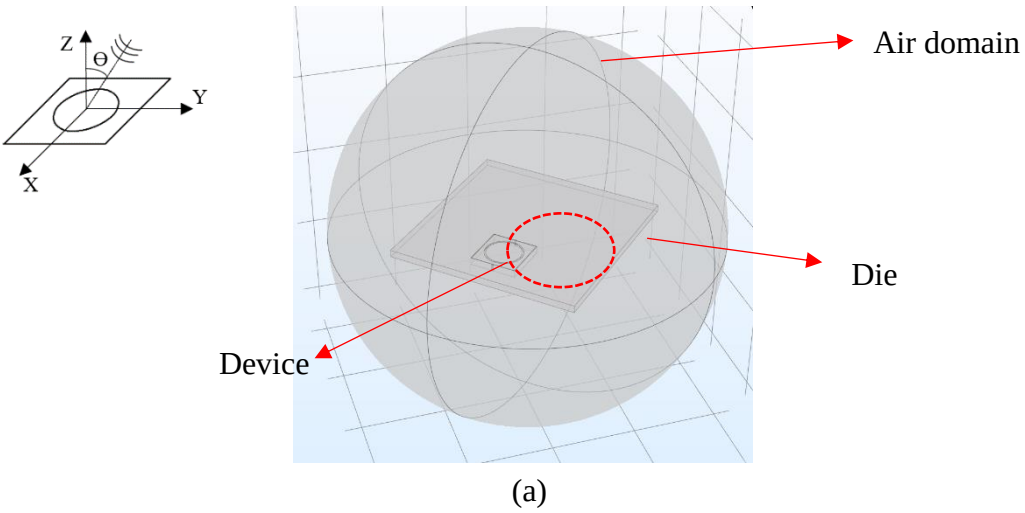

(a)

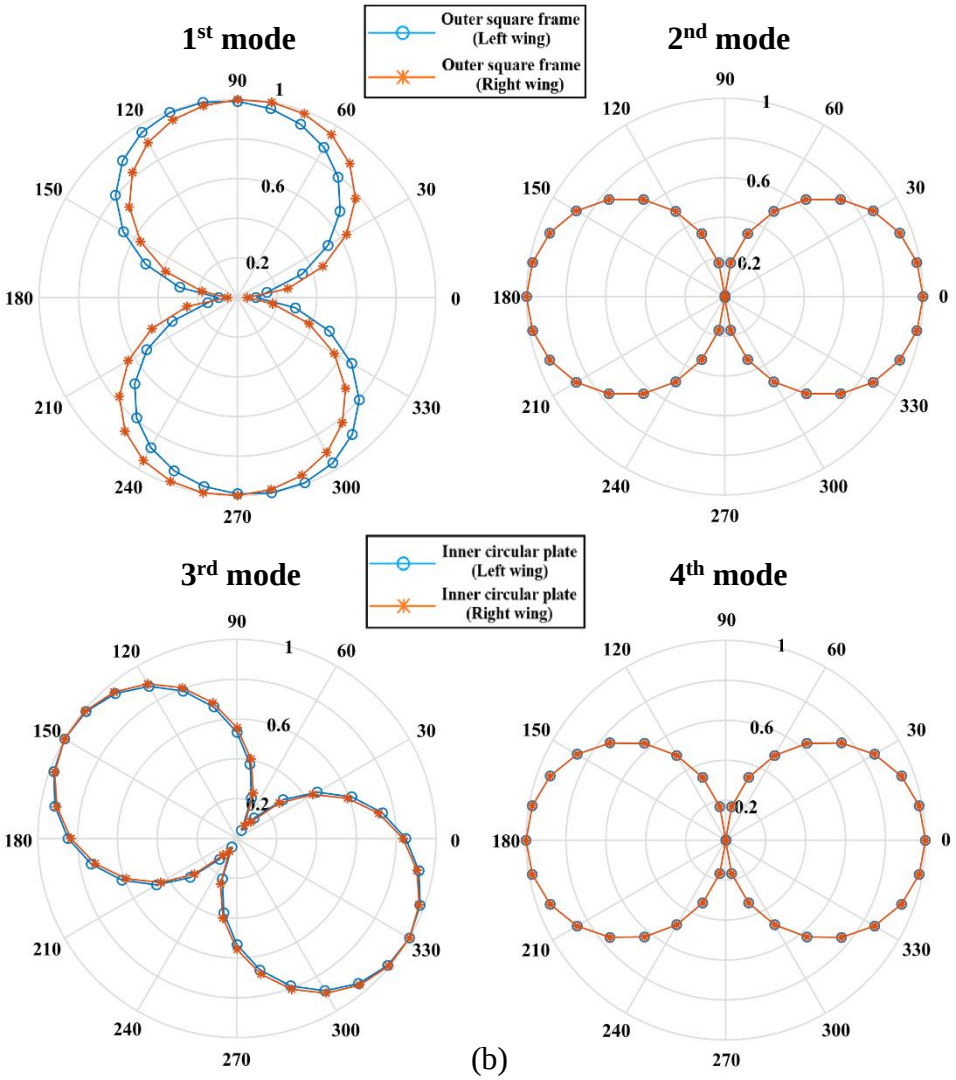

(b)

Fig. 3.11 Directivity simulation of the fabricated prototype when the device is close to the edge of the die: (a) COMSOL geometry model; (b) Simulated directional polar patterns taken at four resonance modes

3.5 Characterization of mechanical properties

3.5.1 Setup for mechanical measurement

The mechanical performance of the first prototype was characterized using a Poleytec PSV-300-F Laser Doppler Vibrometer (LDV) with a close-up scanning head unit. The principle of LDV is based on Doppler effect and interferometry. In detail, a f_0 Hz laser beam is split into a reference beam and a test beam. The test beam has a frequency shift f_b added when passing through a Bragg cell and then hits the surface of the MEMS sample as shown in Fig. 3.12 [7][103]. Due to the motion of the surface, a Doppler frequency shift is added into the beam reflected by the sample surface. After that the reflected beam interferes with the reference beam and is collected by the photodetector. The vibration velocity of the surface is computed by demodulating the output signal of the photodetector and compare the frequency difference between the reference and the reflected beam.

The MEMS prototype die was mounted onto a $7.5cm \times 2.5cm \times 1.5cm$ rectangular dielectric board with a hole for air exposure drilled in the centre to give a path for sound waves approaching the backside. A loudspeaker (ESS Heil Air-motion Transformer) driven by a chirp signal with 10 kHz bandwidth generated by the LDV built-in waveform generator, was placed 1 meter away from the centre of the microphone as shown in Fig. 3.13. A large protractor, with 0 degree aligned with the direction normal to front surface of the die, was laid on the floor as an angle changing

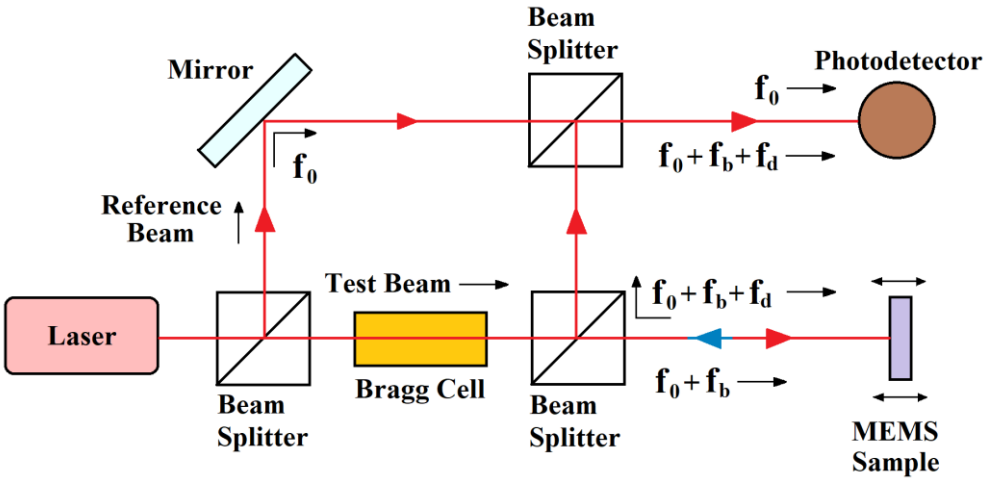

Fig. 3.12 The interior schematic of Laser Doppler Vibrometer

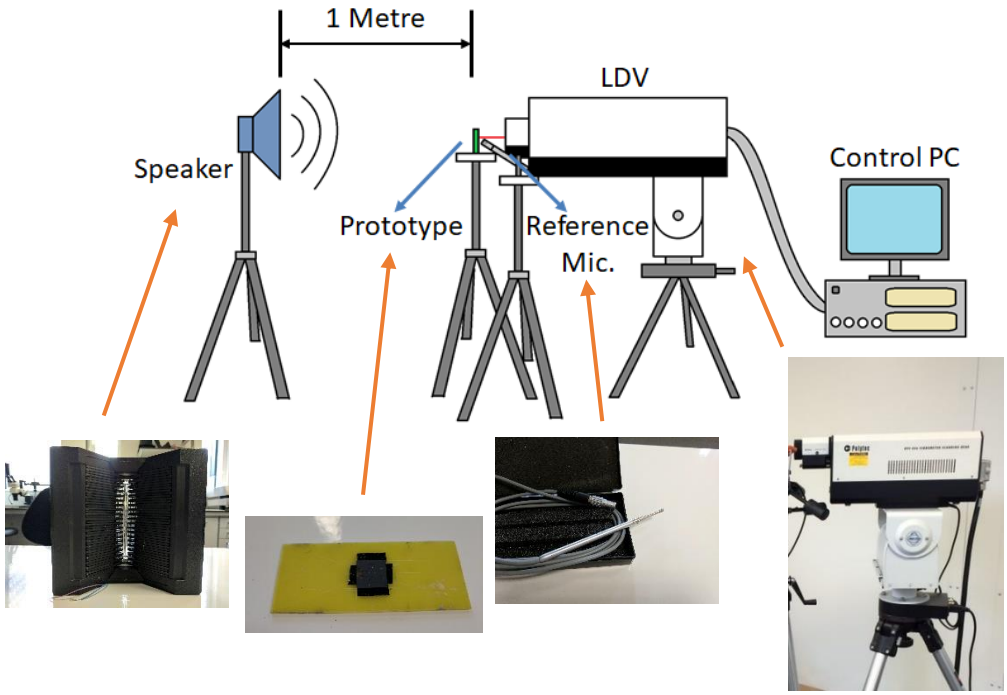

Fig. 3.13 Experimental setup for measuring mechanical vibration of the device

reference. Then the speaker could be manually moved to new positions with respect to the sample to change the sound incident angle. In addition, a Brüel & Kjær (B&K) 4128 pressure-field microphone connected to a dedicated Nexus conditioning preamplifier was fixed on a tripod, acting as a sound pressure reference.

3.5.2 Experimental results

As previously explained, the inner circular plate has minimum mechanical displacement when the sound waves are vertically incident on its front or back surface. Therefore, to gain clearer mode shape information, the sound incident angle θ was adjusted to 70 degrees. The four resonance mode shapes (shown in Fig. 3.14) were then found at 1975 Hz, 3594 Hz, 3738 Hz, and 7031 Hz, respectively. Table 2.1 compares the four resonance frequencies obtained by analytical model, COMSOL simulation and experiments. Apparently, the measured resonance frequencies are well matched with the simulated results. The errors occurring at the 4^{th} resonance mode are mainly attributed to the tolerance in size and the position offset of the device. When the device in the centre of the die, the length of sound paths (i.e. sound arrival time) travelling from the sound waves applied on the front surfaces to the backside surfaces

Methods	Resonance Frequencies (Hz)			
	1st	**2nd**	**3rd**	**4th**
Analytical (Eq. 3.11-12)	2425	4027	4430	6713
Simulated	2207	3617	3849	6438
Measured	1975	3594	3738	7031

Table 3.1 Comparison of Resonance Frequencies

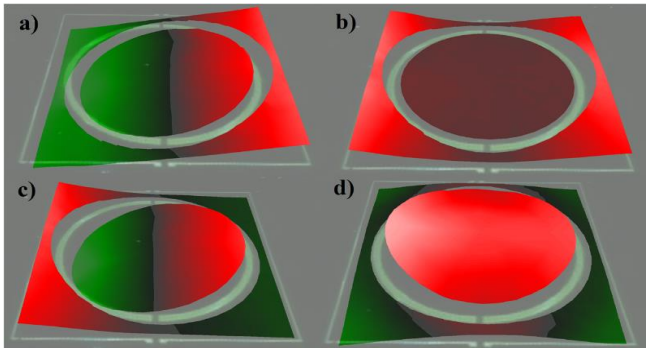

Fig. 3.14 Experimental mode shapes of the first design get at an incident angle of 70 degrees.

of the left wing and the right wing of the device are almost identical. When the device deviates the centre of the die, the length of sound travelling paths are different so that it reduces the amplitude of applied sound gradients at the left and right wings when sound incident in certain angles.

In order to measure the mechanical frequency response of the prototype, the speaker was turned back to the position where the sound wave could vertically hit the front surface of the prototype (i.e. $\theta = 0°$). As shown in Fig. 3.12, the experimental displacement response is consistent with the simulated results. The maximum measured displacement response of the outer square frame when $\theta = 0°$ is 2.33μm/Pa, appearing around the second resonance frequency. Similar to the simulated results, the displacement response is almost invisible near the 1st and the 3rd resonance mode due to the directivity. Its average displacement response is about 0.05 μm/Pa. In terms of

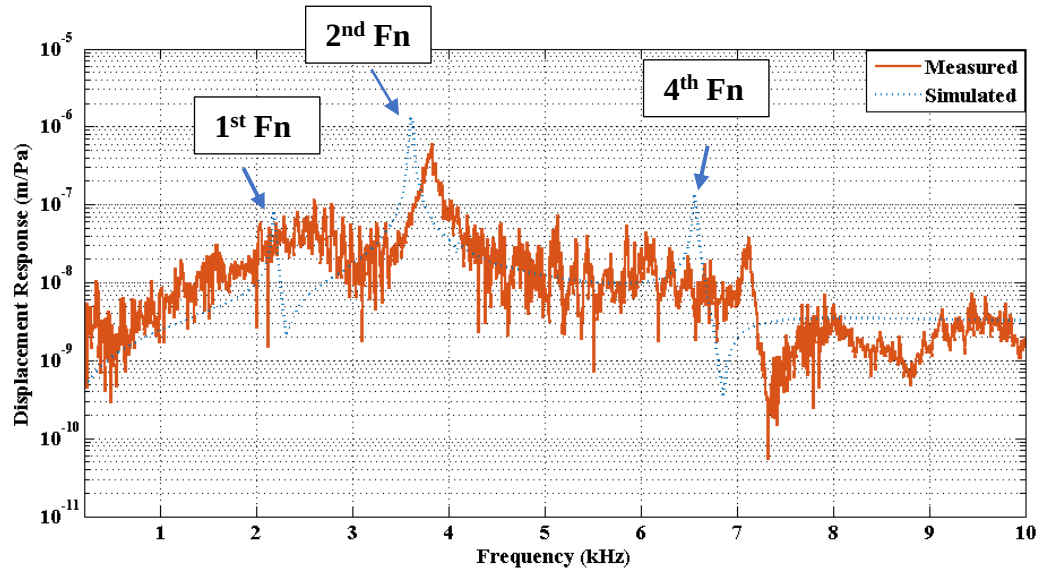

(a)

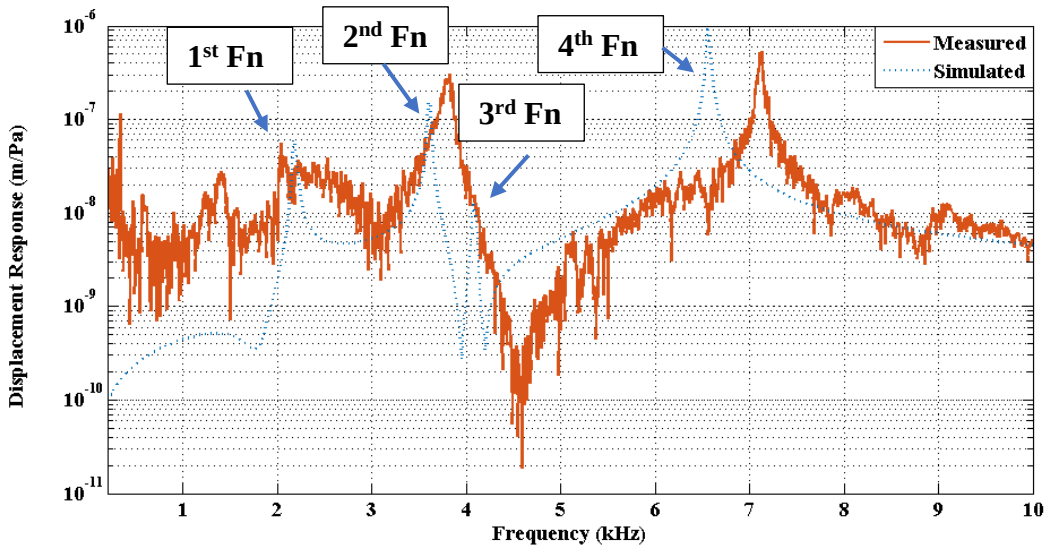

(b)

Fig. 3.16 Mechanical frequency response of the prototype at 45 degrees: (a) Outer square frame (b) Inner circular plate

the inner circular plate, the maximum response reaches to 0.62 µm/Pa, and the average response is approximately 0.015 µm/Pa. Because of the narrow frequency gap between the 2nd and the 3rd resonance frequencies, there is a frequency response overlap between these two mode shapes (see Fig. 3.15 (b)).

By adjusting the sound incident angle to 45 degrees, the maximum response of the outer plate falls to one-fourth of the value gained at $\theta = 0°$ (i.e. $\approx$ 0.61µm/Pa) and its average response decreases to 0.02 µm/Pa as illustrated in Fig. 3.16 (a). Meanwhile,

the maximum displacement response of the inner plate at 45 degrees is about 0.53 μm/Pa, but the average response increases by 5 nm/Pa.

When the sound incident angle is increased to 90 degrees, the displacement response at the 1st resonance mode becomes obvious. However, unlike the COMSOL simulation, the frequency response of the outer frame at the 2nd resonance mode is 0.46

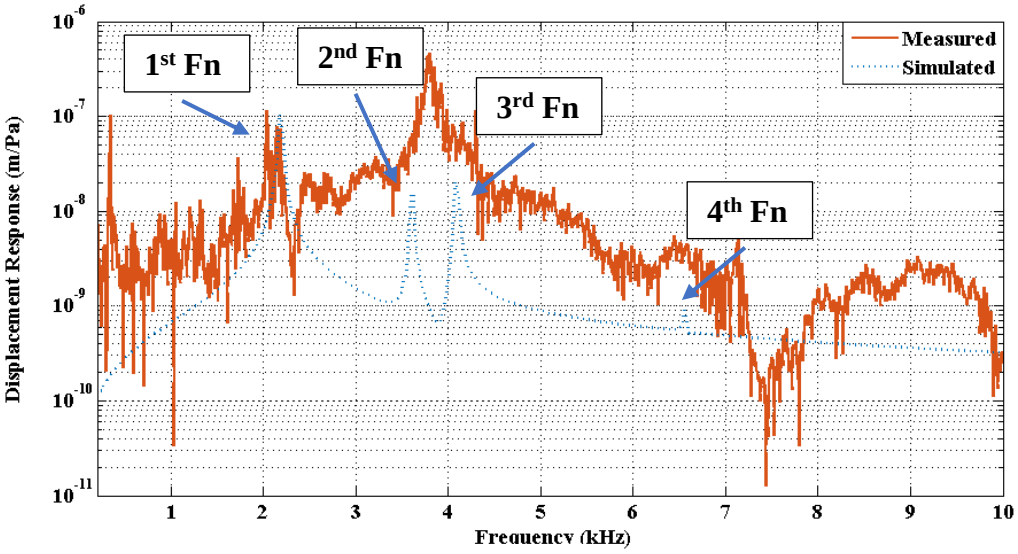

(a)

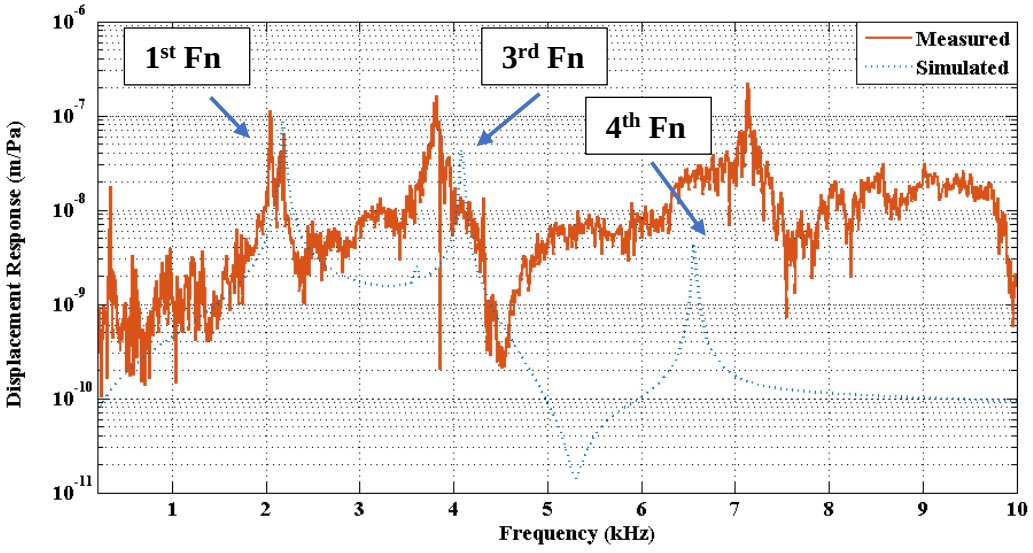

(b)

Fig. 3.17 Mechanical frequency response of the prototype at 90 degrees: (a) Outer square frame (b) Inner circular plate

μm/Pa, which is 0.34 μm/Pa higher than the response at the 1st resonance frequency (see Fig. 3.17). For the inner plate, despite that the maximum displacement response when $\theta = 90°$ is 0.22 μm/Pa at the 4th resonance frequency, it is still almost 100 times higher than the simulated result due to the layout offset and sound incident angle error in experimental setup.

These kinds of errors become more apparent in the experimental data relating to directivity measurement. As the displacement response around the 3rd resonance frequency is superposed with the response near the 2nd resonance frequency, it is barely possible to distinguish the resonance frequencies. Also, since the displacement response around the 2nd resonance frequency is much higher than the rest of the frequencies of interest as a whole, the response at the 3rd resonance frequency is masked by the background noise, and it is almost impossible to extract sufficient data for the corresponding directivity patterns. Figure 3.18 shows the normalized displacement response (NDR) with respect to the sound incident angle from 0 degree

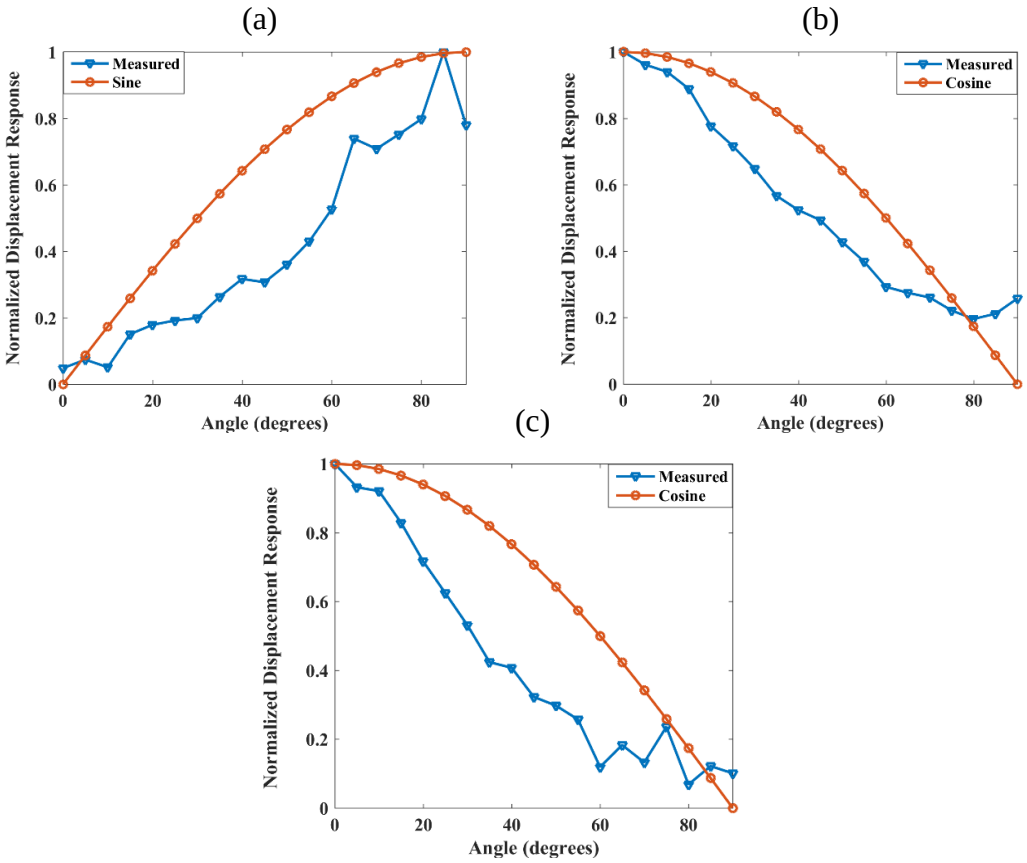

Fig. 3.18 Normalized Displacement Response obtained at: (a) the 1st, (b) the 2nd, and (c) the 4th resonance frequencies

to 90 degrees due to the symmetric geometry of the prototype. According to the simulation, the directivity of the device should be proportional to the sine function at the 1st resonance frequency, and it depends linearly on the cosine function at the 2nd and the 4th resonance frequencies. However, although the varying tendencies of the NDR conform to these trigonometric functions, it is clear that there is an incredibly large difference between the measurement results and the simulation. Due to the limitation of the technique of measuring the directivity through mechanical displacement response, all the future designs include electric sensing parts. The method of measuring directivity through electric output signals replaces the method of measuring displacement response when investigating the later devices.

3.6 Discussion and conclusion

Earlier *Ormia*-inspired MEMS directional microphone designs can detect sound direction in no more than two frequency bands. The design model presented in this chapter introduces two more working frequency bands by using two concentric diaphragms. These two diaphragms are placed in the same plane and rotate along the same rectangular beam fixed to the substrate at the ends. Due to the use of SOIMUMPs, the main vibrational part of the device is built with a 10μm-thick single crystal silicon layer. The documented design rules and optimized fabrication process reduces the cost and guarantees the quality of manufacture.

This 2.7mm×2.6mm device was expected to have four individual resonance frequencies. Each diaphragm drives two resonance mode shapes. Except for the 3rd resonance mode, it responds directionally with sine functions at the 1st resonance frequencies, and with cosine functions at the 2nd and the 4th resonance frequencies, as verified by COMSOL finite element modelling software. When the device operates at the 3rd resonance frequency, it should collect maximum sound energy when the sound waves incident from 30 degrees. However, the device is placed just beside one of the edges of the entire die, which causes a larger angle deflection in directional polar patterns.

The measured results prove part of the prediction. The first four experimental resonance frequencies are 1975 Hz, 3594 Hz, 3738 Hz, and 7031 Hz, respectively. The maximum displacement response occurs when the outer diaphragm is excited by the sound waves at the 2nd resonance frequency that also vertically hit its front surface, which is about 2.33μm/Pa. Overall, the plots of experimental displacement response are closely matched with the COMSOL simulation. However, as the frequency gap between the 2nd and the 3rd resonance frequencies is less than 200 Hz, the response around the 3rd resonance frequency almost totally overlapped with the response near the 2nd resonance frequency. In addition, the response around the 1st resonance frequency is covered by background and laser noise most of the time when changing the sound incident angle. The plots of normalized displacement response against the sound incident angle that were measured by LDV suggest that, in order to increase the

accuracy, the directivity in this case should be measured using other parameters rather than structural displacement response.

Therefore, in subsequent designs, the size will be reduced to make the device more appropriate for future packaging. The 2nd and the 3rd resonance frequencies will be moved further apart. The four resonance frequencies will be distributed evenly in the audible range of sound. A piezoelectric layer will be deposited for each diaphragm of the device to generate sufficient electric output signal for directivity tests and results.

Chapter 4

Development of Multi-Band Operational *Ormia*-inspired MEMS Microphones

Based on the concept of the design from last chapter, two multi-band operational *Ormia*-inspired MEMS microphones with different directional properties were designed, fabricated, and tested shortly afterwards. To make the microphones fully functional, an aluminium nitride piezoelectric layer is attached on the activating diaphragms to transfer their mechanical vibration into electrical signals. A customized read-out circuit amplifies the piezoelectric output signals and allows the tester to get more accurate electrical specifications of the prototypes such as the frequency response and directional polar patterns.

4.1 Introduction

The idea of a dual-plate *Ormia*-inspired MEMS microphone that could operates in multiple frequencies has been introduced in Chapter 2, and new shortcomings, such as overlapped resonance peaks and large angle shift in directional polar patterns of fabricated device, also have been subsequently discovered. In this chapter, the frontal activating surface area of the multi-band operational device will be firstly reduced without sacrificing the advantages of high mechanical sensitivity and low resonance frequencies. Additionally, the device shown in the last chapter cannot be regarded as a fully functional microphone due to the lack of a sensing unit that is integrated into the system followed by a carefully designed readout circuit to convert the mechanical vibration energy of the diaphragms into electrical signals, which has been accomplished in this chapter.

Except of improving previous model and adding sensing units, the asymmetric dual-plate model with torsional beam shifted with a certain distance in the direction normal to the beam that leads to unequal mass distribution of diaphragms has also been developed to resolve the problem of irregularity directional behaviour between the resonance frequencies. The new model is also compared with the symmetric design in the fields of mechanical and electrical sensitivities against the sound pressure.

4.2 The Piezoelectric *Ormia*-inspired MEMS Microphone working in the multiple frequency bands (with symmetric geometry)

4.2.1 The structure of the design

Like the first-generation design, this new device is built to perform throughout the audio frequency range, such that the radius of the microphone is controlled below 3.6 mm. The inner plate geometry is changed from round to rectangular to reduce the entire dimension of the moving area. In addition, 10 μm wide slits surround both the outer frames and the inner plate, releasing the microphone from the 400 μm SOI substrate that is deeply etched from the backside and separating the entire silicon membrane into two plates. As shown in Fig. 4.1, the microphone has a symmetric structure. The outer plate of the design has a dimension of 2.4 mm × 1 mm × 10 μm

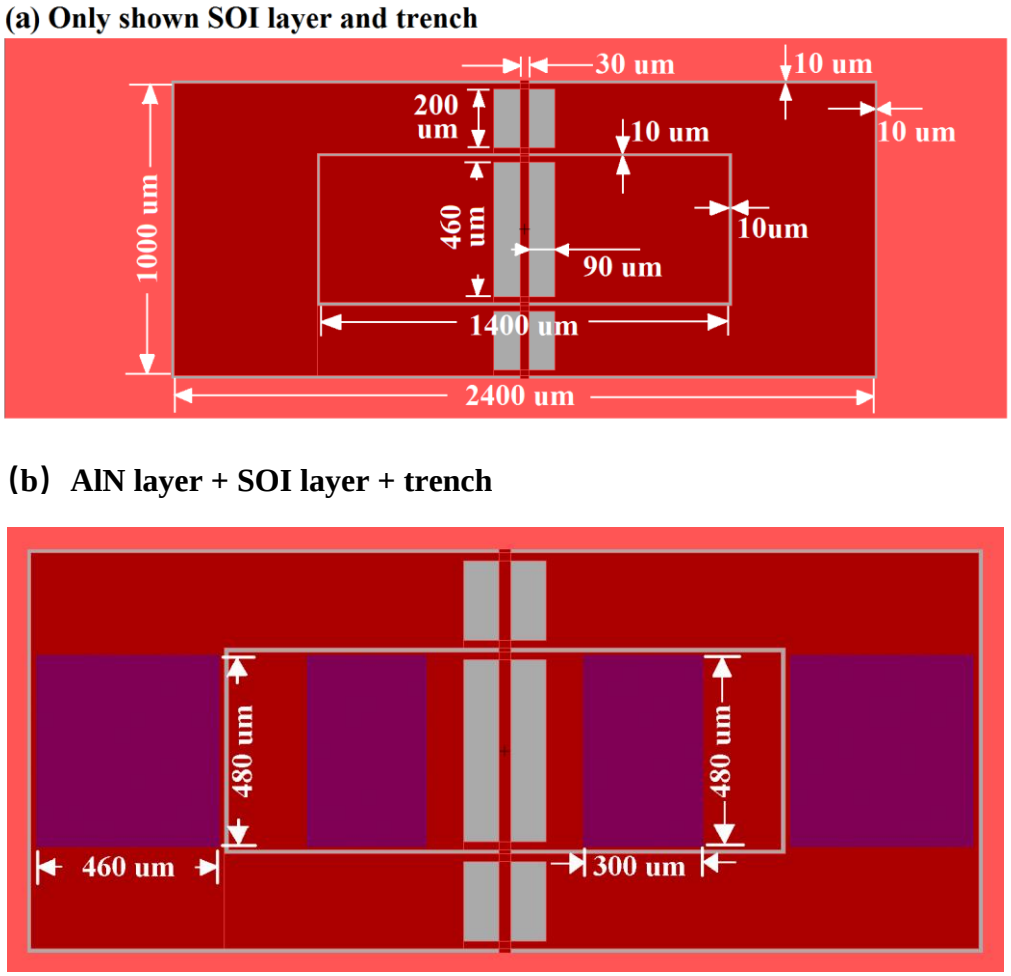

Fig. 4.1 The design layout of the symmetric microphone drawn by L-edit

with a sound active area of 1.58 mm^2, while the inner plate has a size of 1.4 mm × 0.5 mm × 10 μm with an active area about 0.6 mm^2. If taking the central torsional beam as the reference, the microphone can be regarded as a group of four rectangular diaphragms rotating along the 30 μm wide central beam fixed to the substrate. In the last chapter, the 2nd and the 3rd resonance frequencies are too close to provide distinguishable working bands. Theoretically, the directional polar patterns at the 2nd and the 3rd resonance frequencies are both bi-directional, but there is a 90-degree shift between the patterns. As explained in Chapter 3, the overlapped response can cause unclear directional behaviour between the resonance frequencies and even at the resonance. The rectangular holes close to the torsion bean are designed to accomplish the expected resonance frequencies. The mechanical vibration of each diaphragm is transduced to electrical signals due to the strain variation in a 500 nm thick Aluminium Nitride (AlN) layer deposited on the mass of the diaphragms as shown in Fig. 4.1 (b). In addition, four 1 μm thick aluminium (Al) metal pads isolated by the thermal oxide from the ground are attached on the end of the piezoelectric area on each diaphragm, transmitting electrical signals to the output terminals placed on the substrate. The fabrication process of this piezoelectric device is called PiezoMUMPs that also supplied by MEMSCAP.

4.2.2 Fabrication

(a) PiezoMUMPs

In terms of the piezoelectric material, MEMSCAP only provides AlN with a piezoelectric strain coefficient d_{33} on the order of 3.4 to 6.5 (pC/N). Comparing the d_{33} shown in the document of PiezoMUMPs' design rules and the data provided by the material library of COMSOL, the piezoelectric confident matrix of the AlN used in PiezoMUMPs is assumed as

$$[d_{ij}] = \begin{bmatrix} 0 & 0 & 0 & 0 & -3.84 & 0 \\ 0 & 0 & 0 & -3.84 & 0 & 0 \\ -1.92 & -1.92 & 4.96 & 0 & 0 & 0 \end{bmatrix} [pC/N] \qquad [4.1]$$

Before depositing the AlN layer by reactive sputtering, a 0.2 μm thermal oxide layer is grown on the SOI wafer and lithographically patterned to build the insulation for the circuit paths on the die. The circuit paths are implemented by a metal layer combined

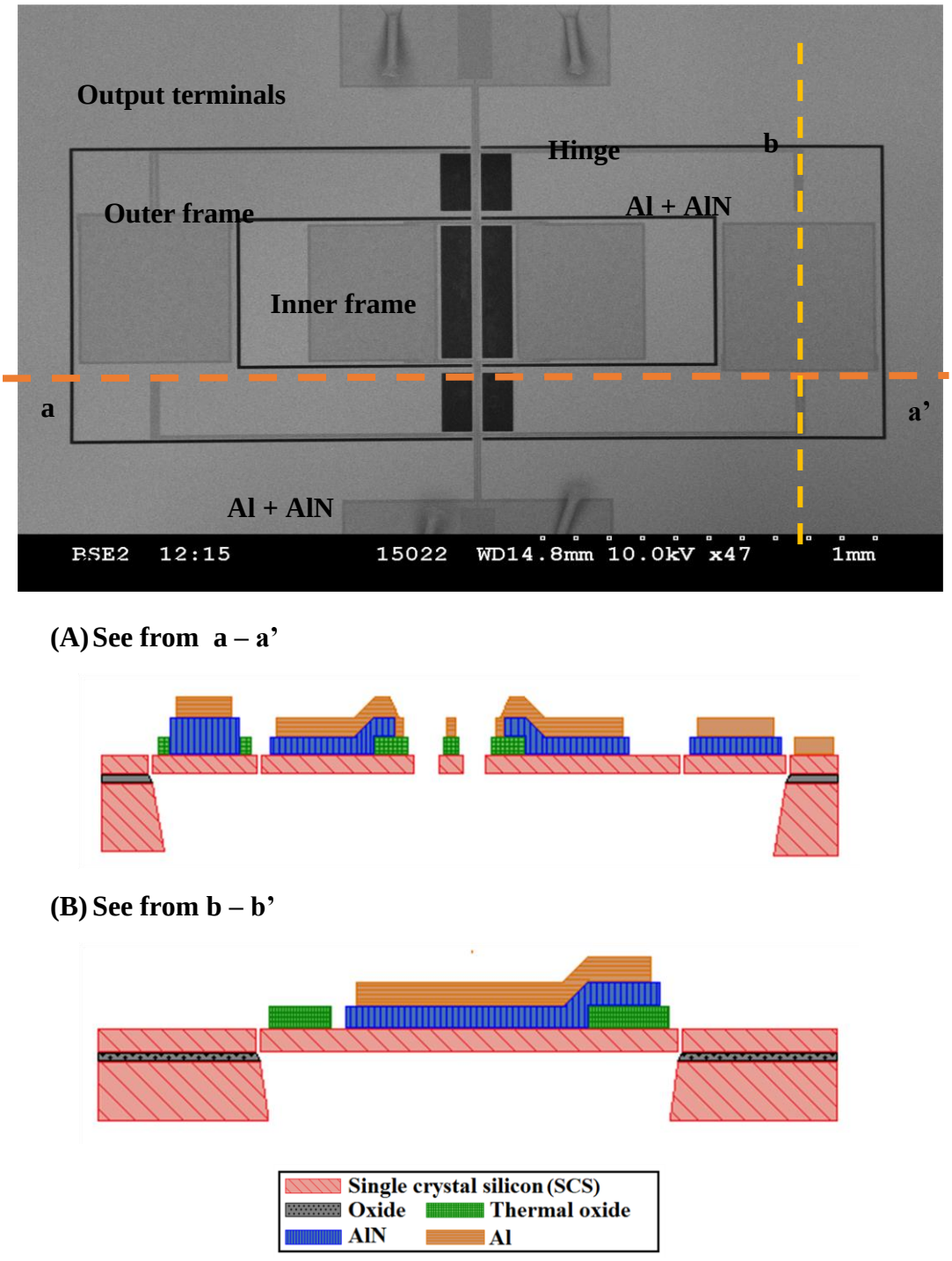

Fig. 4.3 The cross-section views of the symmetric model taken from (A) the dashline a-a' (B) dashline b-b'

with 20 nm chrome (Cr) and 1µm aluminium (Al) layers. Similar to the SOIMUMPs when releasing the main vibrational part of the device, DRIE is applied to etch the SCS

down to the oxide of the SOI. Then the wafer is held together using polymide, and the backside of the device is then opened with the trench etching process. The SEM image of the prototype is illustrated in Fig. 4.2. Figure 4.3 gives the cross-section views of the prototype taken from the cutting lines shown in Fig. 4.2, explaining the distribution of the layers in a device fabricated by the PiezoMUMPs. More details of fabrication can be found in reference [104]. Except for using the PiezoMUMPs foundry service, the post-processing service - laser sub-dicing is also utilized on the device fabricated for this design round. A different approach from the first-generation device that shares the space with other designs on the same chip is taken. The new prototypes are separated from the other designs by cross dicing from the centre of the chip, hence the entire device including the substrate is almost symmetric in the new design (i.e. For each diaphragm, the sound paths from the frontal to their backside are equal).

(b) Optical profiles

With the piezoelectric AlN layer, the diaphragms are likely to bend due to the intrinsic stress and the thermal stress which are often referred to as residual stresses. The intrinsic stresses arise during the deposition process. The deposition temperature is variable depending on the steps of the process, and the intrinsic stresses are the stresses presenting at the deposition temperature. Different from the intrinsic stresses, the thermal stresses are produced due to the different coefficients of thermal expansion between layers. As the testing temperature may be different from the deposition temperature, the device can suffer both intrinsic and thermal stresses. The results of surface measurement taken by the optical profiler shown in Fig. 4.4 shows the anticipated effect.

From the top to the bottom of Fig. 4.4, each 2-point plot on the right column shows the surface profile at the red line across different areas of the device. For the outer plate, the average elevation of the diaphragms measured at their two outermost ends is about 7 μm relative to the central beam. The inner two diaphragms also bend at a curvature coefficient almost the same as the value for the outer plate, reaching up to 0.15 m (averaged). Moreover, from the central line to the longer edge of the inner plate, the curvature coefficient is approximately 36.35 mm, revealing that the device curves in three dimensions. Moreover, the silicon area not covered by the AlN material

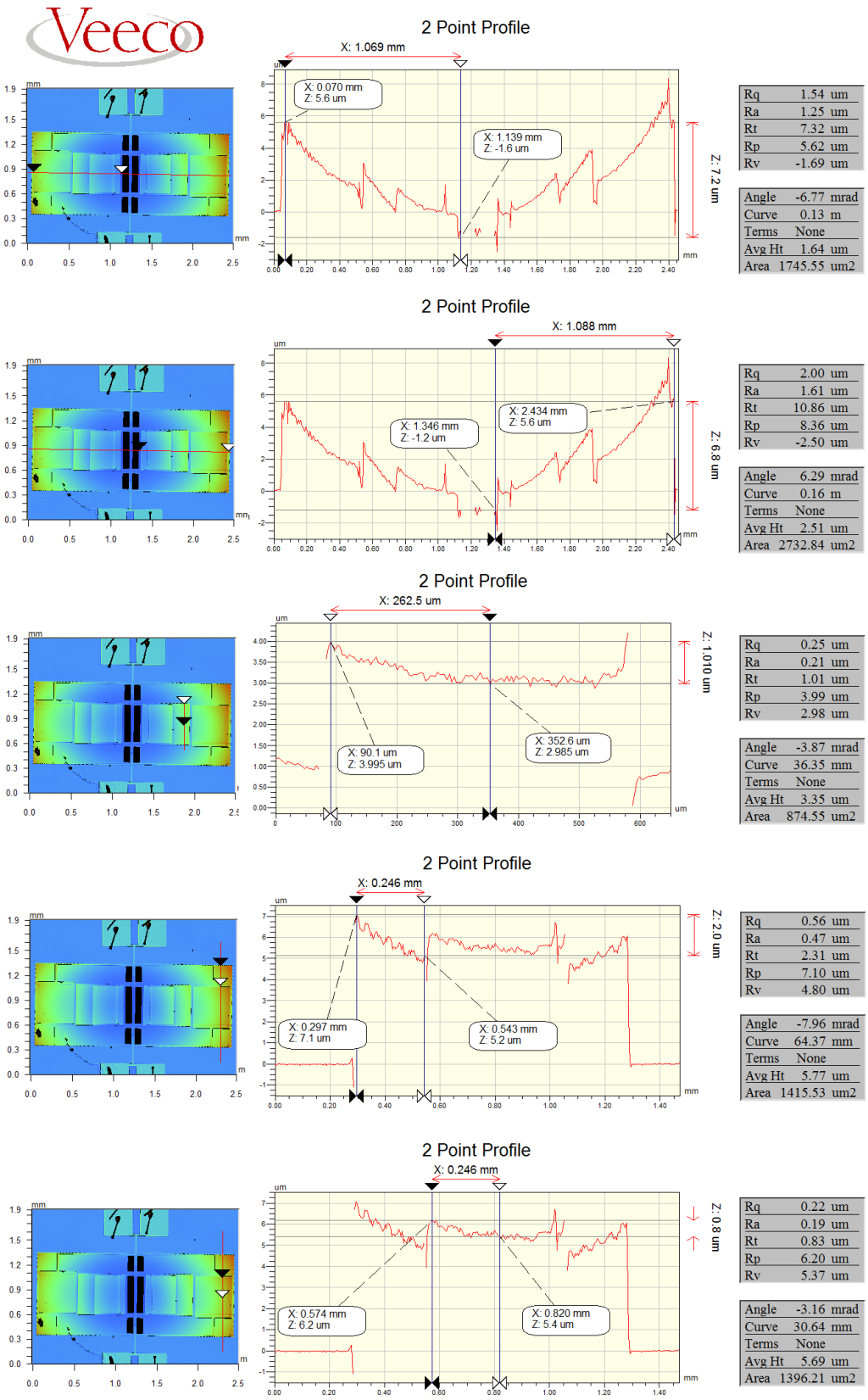

Fig. 4.4 The surface measurement results of the symmetric multi-band operational microphone obtained by the optical profiler

has a larger curvature than the area covered by the piezoelectric material. For example, as shown in the third 2D contour plot of Fig. 4.4, the radius of curvature measured from the edge of the AlN pad to the longer edge of the outer frame is about 64.37 mm, which doubles the value captured from the central line to the edge of the AlN pad as illustrated in the last plot of the figure. This proves that thermal stress exists between the layers.

4.2.3 Simulation model

The method of simulating the mechanical behaviour of the *Ormia*-inspired MEMS microphone has already been covered in the last chapter. Since the piezoelectric sensing method is applied here, the study of piezoelectric and solid mechanical coupling is introduced into the simulation model. In the COMSOL software, the Acoustic-Piezoelectric Interaction interface that combines the acoustic-structure interaction and the piezoelectric effect-structure is used to implement the analysis.

As the metal layer is much thinner than the silicon film, it is neglected in the simulation model when calculating the mechanical performance of the device, such as

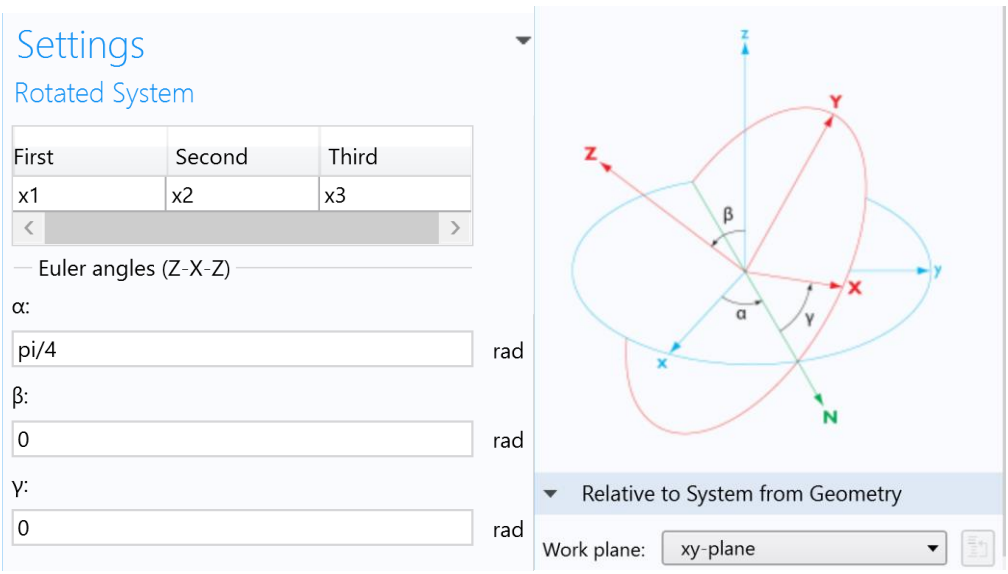

Fig. 4.5 The detail of the reference coordinate settings for simulating the piezoelectric effect in COMSOL. The blue coordinate is the coordinate for the SCS diaphragms and the red coordinate is for the piezoelectric material.

the resonance frequency and the mechanical frequency response. The entire device including the piezoelectric structure is surrounded by a spherical air domain. The settings of geometry and material properties of the silicon film and the substrate are similar to the settings described in Chapter 3. However, as generally the piezoelectric material is isotropic, and the device is rotated by 45 degree (the reason of rotation is explained in Chapter 3), the analysis of the piezoelectric effect should be carried out in a different reference coordinate system. With the origin of the coordinate system used by the remaining structure of the device as the centre, the reference coordinate system used by the piezoelectric material is 45 degrees rotated in the plane parallel to the frontal surface of the diaphragms, as shown in Fig. 3.5, in order to match with the reference coordinate used by the piezoelectric confidence matrix. Also, in the piezoelectric settings, the boundaries of the piezoelectric material that contacts with the silicon film are set to the physical ground while the upside surfaces of the material are assumed to be connected to an output circuit.

4.2.4 Signal readout circuit

The piezoelectric material generates charges due to its strain change. Meanwhile, because of the output circuit, these charges flow in the opposite direction of the external current flow and form a voltage field. As it produces both a current and voltage field in a short time, the signal conditioning of a piezoelectric sensor can be fulfilled by either a current amplifier or a voltage amplifier. Generally, a piezoelectric sensor has a high output impedance over MΩ while the measuring device, such as oscilloscope, has an input impedance on the order of several MΩ. Therefore, the ideal readout circuit should have a high input impedance to match with output impedance of the sensor, and a low output impedance. The following content discusses the features of different types of amplifier circuits designed for piezoelectric sensors, their individual merits and shortcomings, and the conditions for applications.

(a) Different signal conditioning methods for Piezoelectric Sensing

Charge amplifier

A piezoelectric sensor can usually be modelled as a charge source Q_p in parallel with an insulation leakage resistor R_p causing the generated charge to leak off and the

shunt capacitor C_p of the sensor as depicted in Fig. 4.6. C_c is the capacitance of the interface cable. One of the pre-amplifiers commonly used for piezoelectric sensors is the charge amplifier which meets the requirements of high input impedance and low output impedance. R_i represents the total resistance of the interface cable and the added resistor to control the high corner frequency of the amplifier. The charge amplifier has several advantages. First of all, as the charges generated by the sensor transfer onto the feedback capacitor C_f due to the potential difference between the output and the inverting input of the operational amplifier, the gain of the amplifier is a value reversing to the feedback capacitor. This means that once the value of C_f is fixed, the gain of the amplifier is known and irrespective of the capacitance of the sensor. Secondly, with a feedback resistor R_f that is used to prevent the amplifier from drifting into saturation by releasing the charges on the feedback capacitor at a slow rate, the dynamic range of the charge amplifier can be selected. The low cut-off frequency of the amplifier is set by R_f and C_f while the combination of C_P, C_c and R_i provides electrostatic discharge protection and produces a roll-off at high frequency. Assuming that the sensor operates at low frequency, the resistive reactance is ignored compared with the capacitive reactance of C_p. The equations of output voltage V_O and cut-off frequencies of the charge amplifier are expressed as below [2][105]

$$V_O = -\frac{1}{R_i C_f}\int_0^t V_p dt = -\frac{Q_p}{C_f}, \qquad [4.2]$$

$$f_L = \frac{1}{2\pi R_f C_f}, \qquad [4.3]$$

$$f_H = \frac{1}{2\pi R_i (C_p + C_c)}, \qquad [4.4]$$

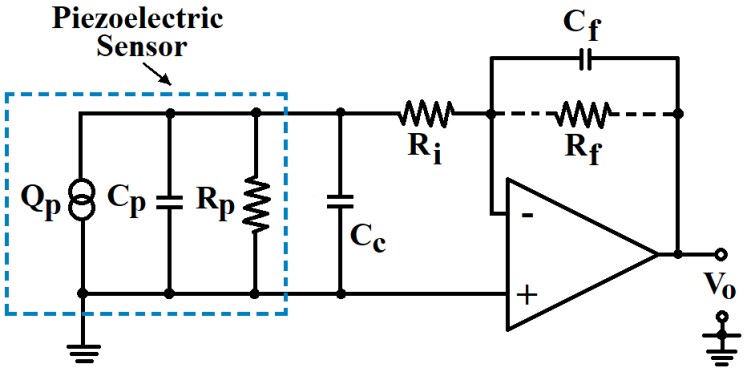

Fig. 4.6 Charge amplifier circuit dedicated for use with piezoelectric sensor

where V_p is the voltage generated by piezoelectric sensor. Thus, the gain of a charge amplifier, also called "charge gain", is expressed as $1/C_f$. As shown in Eq. [4.2], the gain of the circuit is not affected by the capacitance of the interface cable. However, a charge amplifier has its limitations. With a high output impedance, the C_p of a piezoelectric sensor can be below 100 pf in some cases, leading to the requirement of a feedback capacitor with an extremely low capacitance when the charge generated by the piezoelectric material is very small, which s impractical. For example, the AlN used in the presented device is assumed to have d_{31} = 1.92 pC/N = 1.92 pm/V and the measured C_p is about 51 pF. If the deflection in the same direction of d_{33} is about 10 pm and considering the high aspect ratio of the cantilevers, the movement in d_{31} directional could be below 0.1 pm. Then C_f is required to be below 10 pF to get an output voltage with an amplitude roughly around 200 mV. As the application is designed for operating in the audio frequency range, f_L should be below 20 Hz. Therefore, R_f has to be over 0.8 GΩ, which would introduce extremely high thermal noise into the circuit. Trying to get an ideal charge amplifier is a process of finding the balance between achieving high gain and controlling the noise, which is hard to implement on a piezoelectric audio MEMS microphone with only a small charge generated. It is also the reason that charge amplifiers are generally used for ultrasonic sensors.

Voltage amplifier

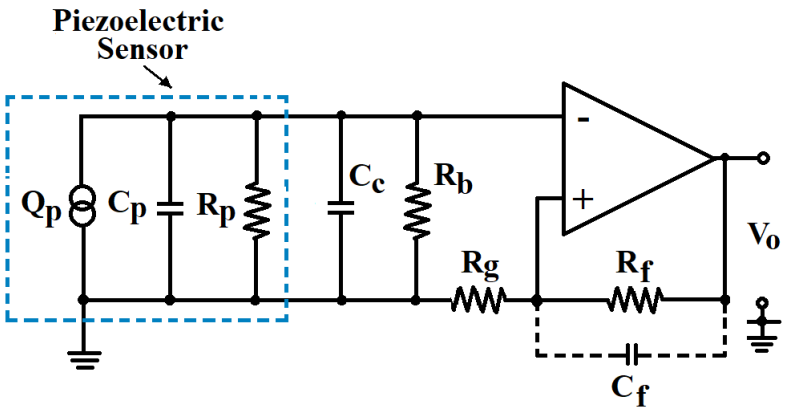

Fig. 4.7 Voltage amplifier circuit (non-inverting) dedicated for use with piezoelectric sensor

The non-inverting voltage amplifier circuit as shown in Fig. 4.7 is another solution for amplifying small piezoelectric signals. In this case, the equivalent circuit of a piezoelectric sensor is as same as the circuit used when deriving output gain of a charge amplifier circuit. R_b provides a DC bias path for the input stage of the amplifier, which should be as high as possible. The action of the amplifier maintains the same voltage potential at its input terminals so that the output voltage V_O is derived as follows

$$\frac{V_O - V_p}{R_f} \times R_g = V_p,$$

thus

$$V_O = V_p \left(1 + \frac{R_g}{R_f}\right) = \frac{Q_p}{C_p + C_c}\left(1 + \frac{R_g}{R_f}\right). \quad [4.5]$$

where R_g is usually defined as the resistor for the gain. Ideally, as there is no current following through the non-inverting terminal, the input impedance of a non-inverting voltage amplifier approximately equals the input impedance of the operational amplifier applied in the circuit, which can be over 10 MΩ. Meanwhile, the output impedance of a non-inverting amplifier is very small since an ideal operational amplifier condition is assumed. According to Eq. [4.6], the output voltage depends on the capacitance of the interface cable which means that a change of measuring cables can cause errors. Hence, the interface cable should be as short as possible. The low and the high corner frequencies of the circuit are calculated by [2][105]

$$f_L = \frac{1}{2\pi(R_p \| R_b)(C_p \| C_c)}, \quad [4.6]$$

$$f_H = \frac{1}{2\pi R_f C_f}. \quad [4.7]$$

Unlike the charge amplifier, since the resistance of $R_p \parallel R_b$ is high as well as the capacitive reactance of $C_p \parallel C_c$, f_L can be controlled under 20 Hz. With a specified feedback capacitor C_f, the circuit will filter out high frequency noise beyond the frequency range of interest.

Instrumentation amplifier

As shown in Fig. 4.8, an instrumentation amplifier is a special type of differential amplifier that introduces two input buffers in front of the input terminals of a typical differential amplifier that is constructed with four resistors and an

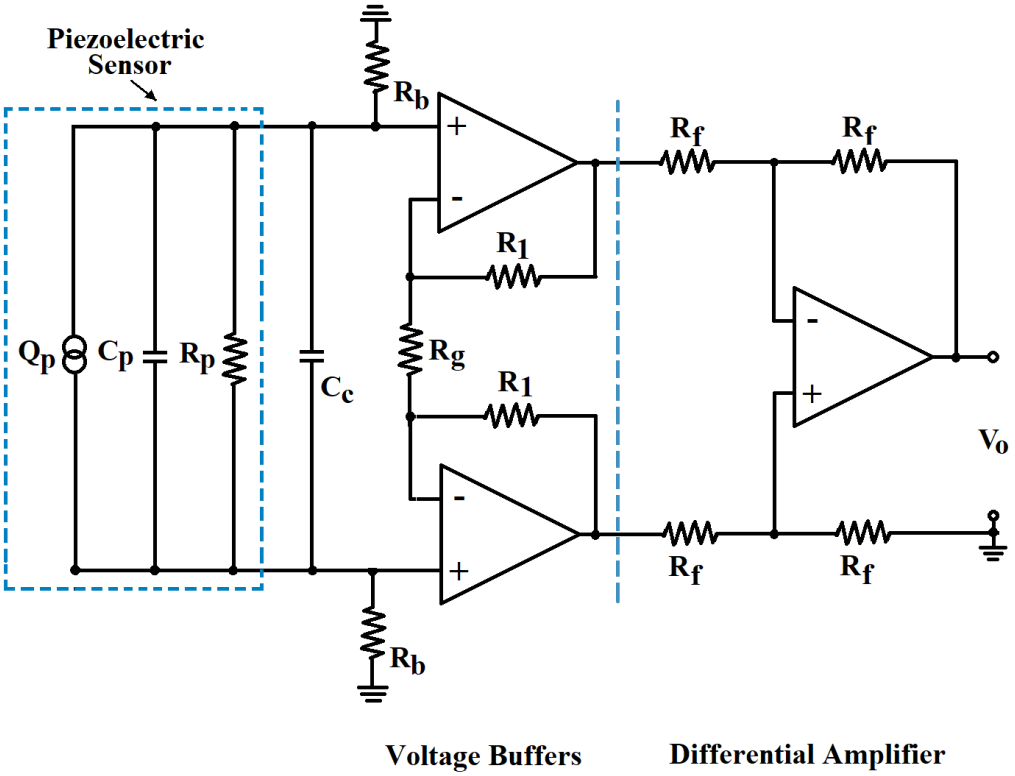

Fig. 4.8 Instrumentation amplifier circuit dedicated for use with piezoelectric sensor

operational amplifier. For most analogue-controlled instrumentation amplifiers available on the market (e.g. INA126, AD8220, etc.), the four resistors at the differential stage are pre-set as identical. Therefore, the output voltage of an instrumentation amplifier is

$$V_O = \left(1 + \frac{2R_1}{R_g}\right) V_p = \left(1 + \frac{2R_1}{R_g}\right) \frac{Q_p}{C_p + C_c}, \qquad [4.8]$$

where R_1 is the feedback resistor in the input buffers and generally pre-defined in the datasheet of a commercial amplifier, hence the gain of an instrumentation amplifier is driven by the gain resistor R_g.

An instrumentation amplifier not only has the merits of a non-inverting voltage amplifier (i.e. lower high corner frequency compared with charge amplifiers) for piezoelectric sensing in the audio frequency range, but also acts as a natural common-mode noise filter, especially for reducing electro-magnetic noise, owing to the built-in differential stage. Furthermore, due to the input buffers, an instrumentation amplifier

has a high input impedance, typically greater than 1GΩ. Although the capacitance of interface cables may affect the measured results, this can be solved by designing exclusive printed circuit board (PCB) for the final prototype package in the future. Therefore, an instrumentation amplifier is chosen as the fundamental part of the readout circuit for the piezoelectric microphones presented in this manuscript.

(b) Experimental setup for measuring piezoelectric signals and characterizing the directionality of the microphone

Fig. 4.9 shows the experimental setup for acquiring an electrical response of the prototype and obtaining its directional polar patterns. In order to fully analyse the electrical response from each terminal of the device, no differential output testing (i.e. the non-inverting input terminal is connected to the piezoelectric pad and the inverting terminal is connected to the GND) is executed at this experimental stage so that the measured response does not get the benefit from the high CMRR of instrumentation amplifier. However, it will be implemented in a later device (see Chapter 5). Also, as the device is in symmetric geometry, only output terminals of diaphragms on one side are characterized. The electrical output signals are measured using the instrumentation amplifier, INA128, with a gain of 15. Two 1 MΩ bias resistors connect the input

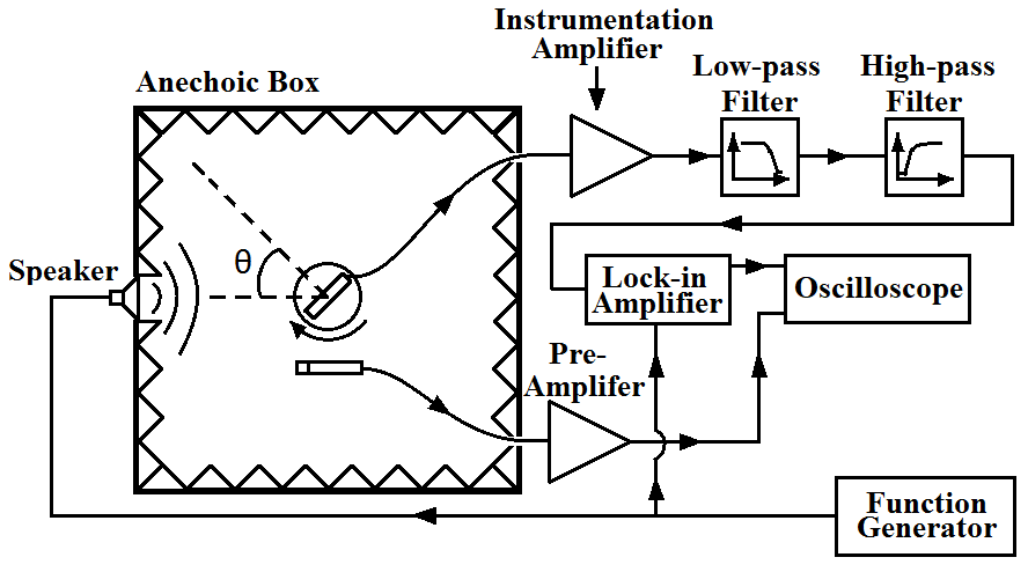

Fig. 4.9 The experimental setup for characterizing the electrical response of the piezoelectric microphone and its directionality

terminals of the amplifier to the ground to prevent saturation. Due to the common mode noise, the amplifier is followed by a fourth order Butterworth high-pass filter with a corner frequency at 50 Hz and a fourth order Butterworth low-pass filter with a corner frequency at 15 kHz, combining into a pre-amplifier of the microphone. Moreover, to achieve more accurate measurements, a SR850 lock-in amplifier is used with time constant of 100 ms. Its input is connected to the output of pre-amplifier and output is connected to a digital oscilloscope, Tektronix TBS1032B. The microphone under test is wire-bonded onto a 7cm×2.5cm×1.5mm PCB. The board is then mounted on an automatic rotation stage controlled by Arduino Due and is placed at the centre of an anechoic box sitting in an acoustic booth. The B&K 4138 pressure field microphone connected to a dedicated preamplifier is placed closed to the sample, acting as a sound pressure reference. A loudspeaker (VISATON 2-inch speaker) is set about 80 cm away from the centre of the die, driven by a sine signal sweeping from 100 Hz to 15 kHz. The step motor driving the rotation stage has a step resolution of 1.8 degree. It rotates the device with 5 steps per turn when measuring the directionality.

4.2.5 Experimental results

(a) Mechanical performance

To characterize the mechanical response of the microphone, the experimental setup is similar to the one for the first-generation prototype shown in Chapter 2, except that the loudspeaker was placed in a 45° sound incident angle relative to the centre of frontal surface of the device. The resonance mode shapes of the prototype are proven to be the same as the mode shapes of the first-generation device, which also closely matches with the COMSOL simulated results illustrated in Fig. 4.10. As listed in Table 4.1, the measured resonance frequencies are just slightly higher or lower than expected, which is acceptable. Compared to the first-generation design, all four resonance frequencies of the new device with symmetric geometry are higher than the values of the first-generation model. The frequency gap between the 2nd and the 3rd resonance frequencies increases from the previous design's 200 Hz to 2500 Hz in the current model, bringing more clearly separated resonance peaks and providing more possibilities of showing clear bi-directional behaviour around its resonances. The maximum measured mechanical response of the outer plate is about 0.97 μm/Pa when

Mode Shapes	Simulation (Hz)	LDV (Hz)
First	3310	2897
Second	4193	3943
Third	7679	7755
Fourth	10118	9860

Table 4.1 Comparison of simulated and measured resonance frequencies of the piezoelectric multi-band operational MEMS microphone (with symmetric geometry) inspired by Ormia ochracea

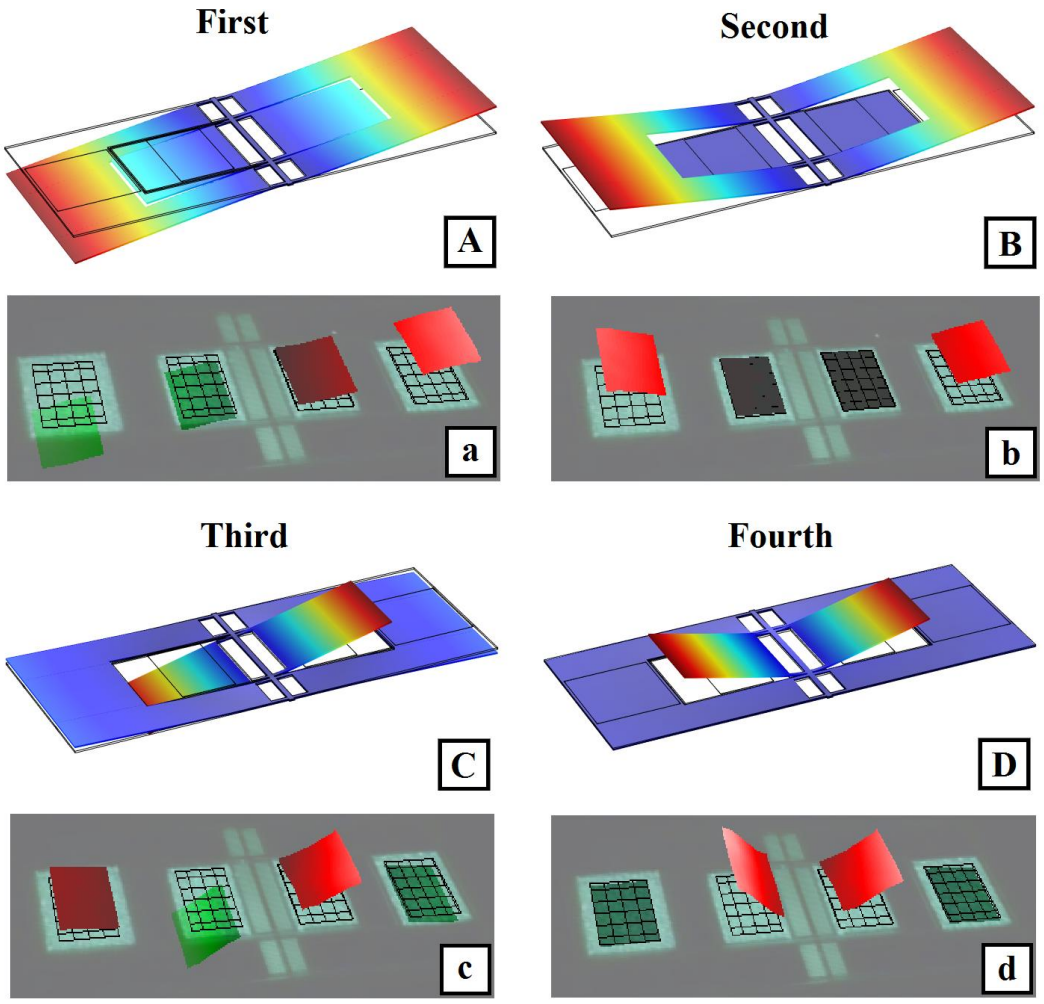

Fig. 4.10 Mode shapes of the symmetric device: (A) – (D) The COMSOL simulation; (a) – (d) Results captured by Polytec laser Doppler vibrometer

the sound incident angle $\theta = 45°$, occurring at the 2nd resonance frequency, which is about 20 times higher than the response at the 1st resonance frequency. Compared to the response at the first two resonance frequencies, the response at the 4th resonance for the outer plate is much lower and in the order of $10^{-8}\mathrm{m/Pa}$. On the contrary, the

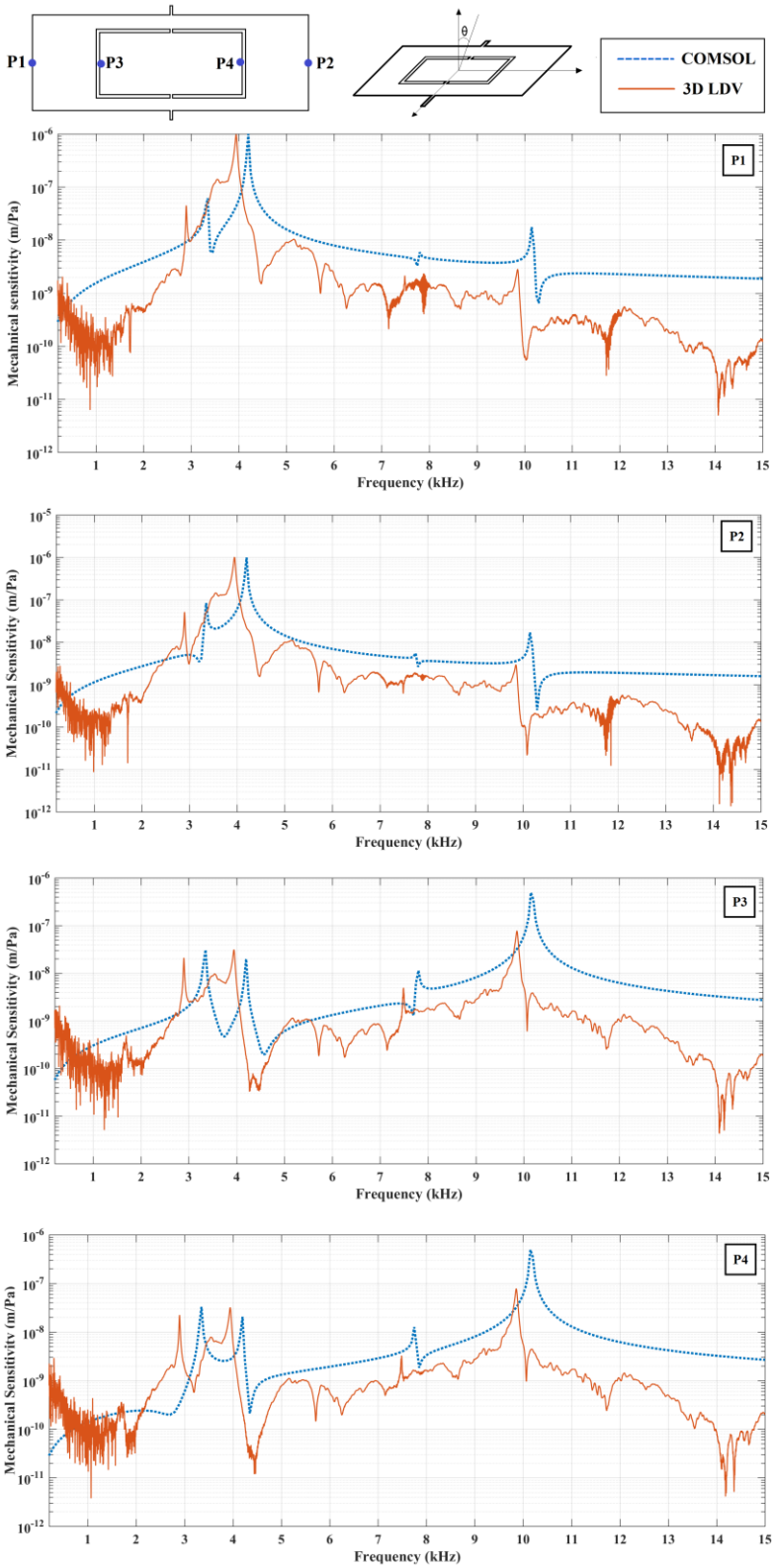

Fig. 4.11 Mechanical sensitivity of the piezoelectric multi-band operational microphone inspired by Ormia, obtained at the two ends of inner plate (P1 and P2) and outer plate (P3 and P4).

mechanical sensitivity at the 4th resonance frequency is about 3 times higher than the

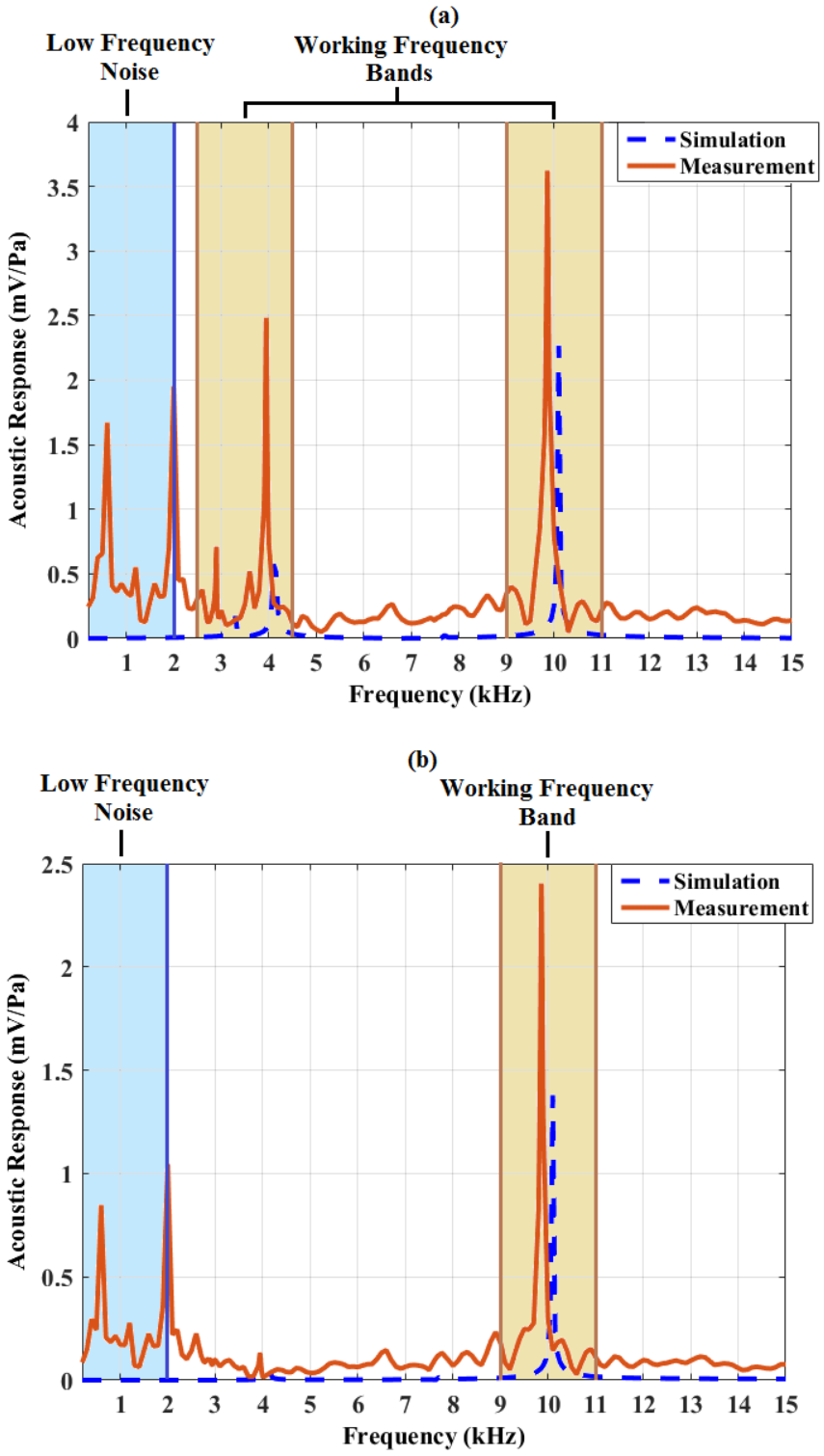

Fig. 4.12 Acoustic response of the microphone using piezoelectric sensing measured at the port corresponding to (a) outer plate (b) inner plate. The measured results are against with COMSOL simulated results

one at the 1st and the 2nd for the inner plate, reaching to 0.08 μm/Pa. However, whether for the outer plate or the inner plate, the mechanical response around the 3rd resonance frequency is too small to be defined and is almost covered by mechanical-thermal noise during the experiments. As the 3rd resonance mode is a rocking mode, the displacement is proportional to pressure difference between the total pressures applied on each diaphragm of the plate according to Eq. [2.40] and [2.41], instead of the sum of pressure. Also, the size of the inner plate is smaller than the outer plate, and so the combination of these characteristics causes this phenomenon.

(b) Electrical performance and directionality

The port corresponding to outer plate of the new piezoelectric microphone was measured to generate an open-circuit acoustic sensitivity (excluding the gain of the readout circuit) about 1.75 mV/Pa at around 3 kHz when $\theta = 45°$, as shown in Fig. 4.12. Then the sensitivity increases to a higher level at 2.5 mV/Pa at around 4 kHz and finally approaches to 3.65 mV/Pa at around 10 kHz. For the inner plate, the acoustic response is easily obtained around 10 kHz, which is 2.44 mV/Pa. However, the acoustic responses of the inner plate at the 1st, the 2nd and the 3rd resonance frequencies almost vanish in the common mode noise, which is predictable. Since the whole dimensions of the device are smaller than the first-generation model, the bridges linking the diaphragm to the central torsional beam were set to be narrow enough to follow the design rules. Therefore, the piezoelectric material was finally decided to be placed on the diaphragm rather than on the bridges that have more strain variation during the vibration. In addition, as the inputs are grounded signal sources, common noise is not cancelled from the output, which results in the low frequency noise below 2 kHz.

Although a clear peak of acoustic sensitivity has not been found around the 3rd resonance frequency, the directionality measurement still reveals that the device has directional behaviour with a supercardioid directional polar pattern as demonstrated in Fig. 4.13 (c) that shows the device rejects most of sound power when sound incident angle $\theta = 240°$ and $295°$ and has maximum response when $\theta = 90°$. When working at the 2nd resonance frequencies, the device is a bi-directional device that picks up most of sound power when $\theta = 0°$ and has minimum acoustic response when $\theta =$

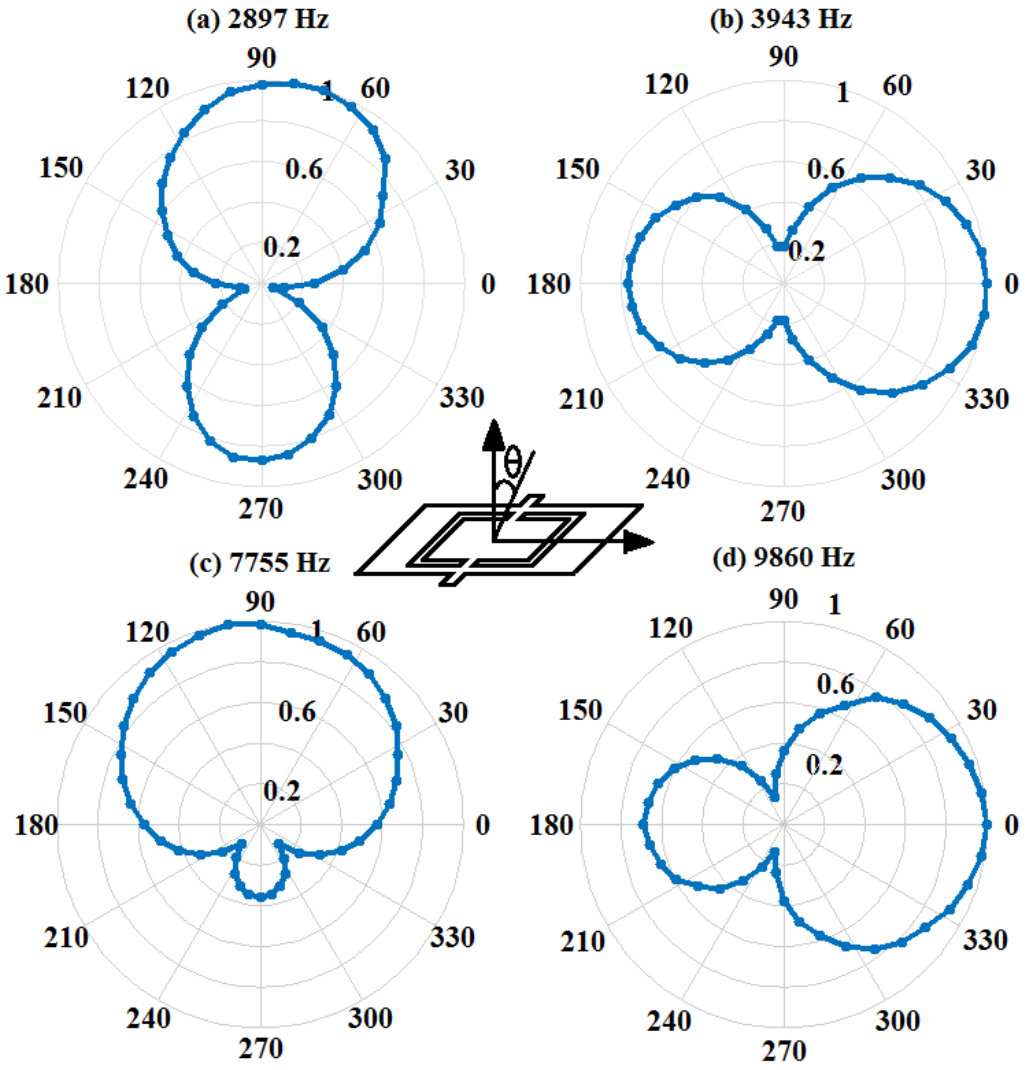

Fig. 4.13 The directional polar patterns of the symmetric microphone obtained at the four resonance frequencies

90° and 270°. Also, at the 4th resonance frequency, the device has maximum acoustic response when $\theta = 0°$ and has minimum response when $\theta = 108°$ and $252°$. Conversely, the microphone concentrates on collecting the sound power incident from the direction of $\theta = 90°$ and $270°$ but has much less response to the sound coming from the direction of $\theta = 0°$ and $180°$ when operating at the 1st resonance frequency. To summarize, the measured results show that the new piezoelectric microphone is more sensitive to the sound incident from directly in front of the frontal and back surfaces of the device when it works at the 2nd and the 4th resonance frequencies and the incoming sound from the edges of the device plate when it works at the 1st and the

3rd resonance frequencies, which matches with the initial concept of the first-generation model.

4.3 The Piezoelectric *Ormia*-inspired MEMS Microphone working in the multiple frequency Bands (with asymmetric geometry)

The main purpose of developing a dual-plate multi-band operational *Ormia*-inspired MEMS directional microphone is to broaden the working frequency bands of this kind of microphones, which means that the device should be optimized to meet two requirements: 1) Having flat and high acoustic sensitivity throughout the frequency range of interest; 2) Giving uniform directional behaviour in all working frequency bands. The previously introduced dual-plate microphone with a symmetric geometry satisfies the first requirement. Despite that the acoustic response is not nearly flat across all working frequency bands since the fundamental structure of the device mimics the mechanical structure of *Ormia*'s hearing organ that gives high Q-factor response only around its resonance frequency, the dual-plate structure introduces more resonance frequencies into the model and thus builds more overlaps between resonance frequency to increase the acoustic sensitivity between the resonances. However, the previously introduced dual-plate device has different directional behaviour throughout the frequency of interest – the directional polar patterns around the 2^{nd} and the 4^{th} resonance frequencies shift 90° in polar coordinate to the directional patterns around the 1^{st} and the 3^{rd} resonance frequencies. In other words, the device picks up most of sound energy incident from the frontal surface than from the sides at the 2^{nd} and the 4^{th} resonance frequency, and this kind of directional behaviour is opposite at the 1^{st} and the 3^{rd} resonance frequency, which runs counter to the second requirement on a desirable multi-band operational directional microphone. In this section, the dual-plate microphone will remain having four resonance modes to pull up sensitivity, and it will also be improved to achieve uniform directional across the audio frequency range.

4.3.1 The structure of the design

Like the previous designs, the new microphone is also comprised of two coaxial plates which rotate about a combined off-centre torsional beam fixed to the substrate. Thus, the new device follows analytical results described in Section 3.2, which was also expected to have four separated resonance frequencies. The overall external dimensions of the microphone are 2.4 mm×1.06 mm×10 μm, with a sound active area

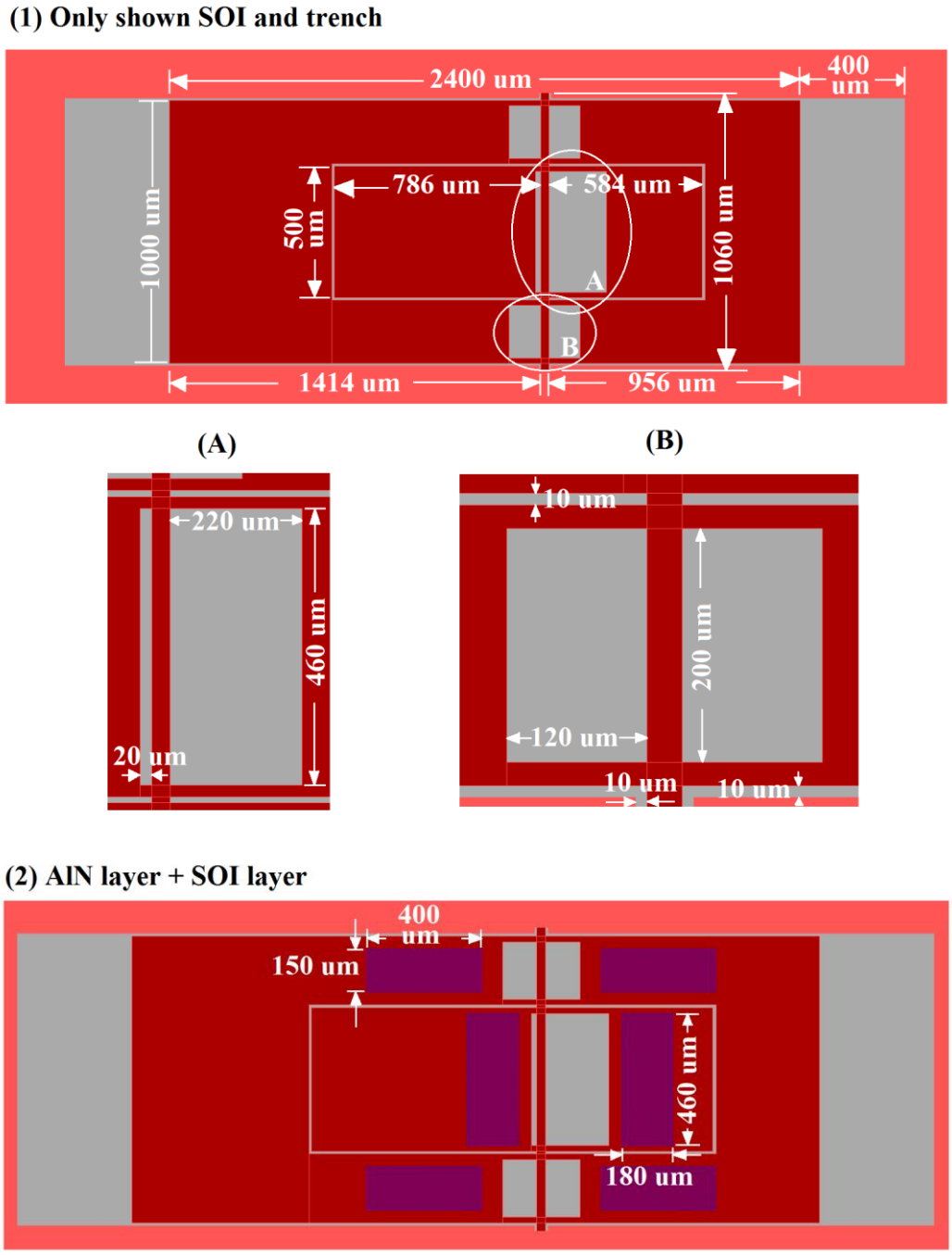

Fig. 4.14 The design layout of the asymmetric microphone drawn by L-edit

of the outer frame of 1.1mm^2 and of the inner frame of 0.58mm^2. The biggest difference from the previously built dual-plate device is the position of the torsional beam, which has a 214 µm bias to the centre of the plates and turns the structure into an asymmetric geometry and thus results in an unequal mass distribution of the diaphragms in both the outer and inner plates. The bias value of torsional beam is

determined by the prospective resonance frequencies. Expect for shifting the torsional beam, in order to uniformly distribute resonance frequencies below 15 kHz, the beams that connect the inner diaphragms to the torsional beam are not identical in length, which leads to a variation of the coupling stiffness between them. In addition, instead of just leaving 20 μm slits between the edges in longitudinal and the substrate, this value was increased to 400 μm in the new design to reduce the impact of diffraction sound field on total sound pressure applied on the both sides of the device. The dimension details of each part are labelled in Fig. 4.14. By using the same simulation steps mentioned in Section 3.3, it can be predicted that the directional behaviour of the new model is similar at all four resonance frequencies as shown in Fig. 4.15, where the new device focuses on responding to the sound waves incoming directly from the front. The principles that that supports the uniform directionality of a dual-plate *Ormia*-inspired microphone presented in this section will be explained in Chapter 4, including establishing analytical model with respect to an *Ormia*'s inspired microphone with asymmetric structure and analysing design factors that fundamentally alter the sound field surrounding the device and hence change its directionality.

As same as the fabricating the dual-plate device presented in the last section, the asymmetric device also uses PiezoMUMPs foundry service. However, the distribution of piezoelectric AlN sensing pads attached on the outer plate was changed to the regions that are closer to the torsional beam in order to increase the strain variation thus improving the level of output signal at rocking mode, which was predicted to remedy the shortcoming of weak output signal at rocking mode happening on the last dual-plate design. To be specific, there are two 400 μm × 150 μm AlN pads placed on each sides of the outer plate and two 180 μm × 460 μm AlN pads attached on the inner plate. In terms of the outer plate, the AlN pads on the same diaphragm are connected by the upper metal layer, thus providing same voltage potential. Scanning electron microscope images of the fabricated MEMS microphone design are shown in Fig. 4.16. As before, the active device area is released through a full backside etch step of a 400μm thick substrate.

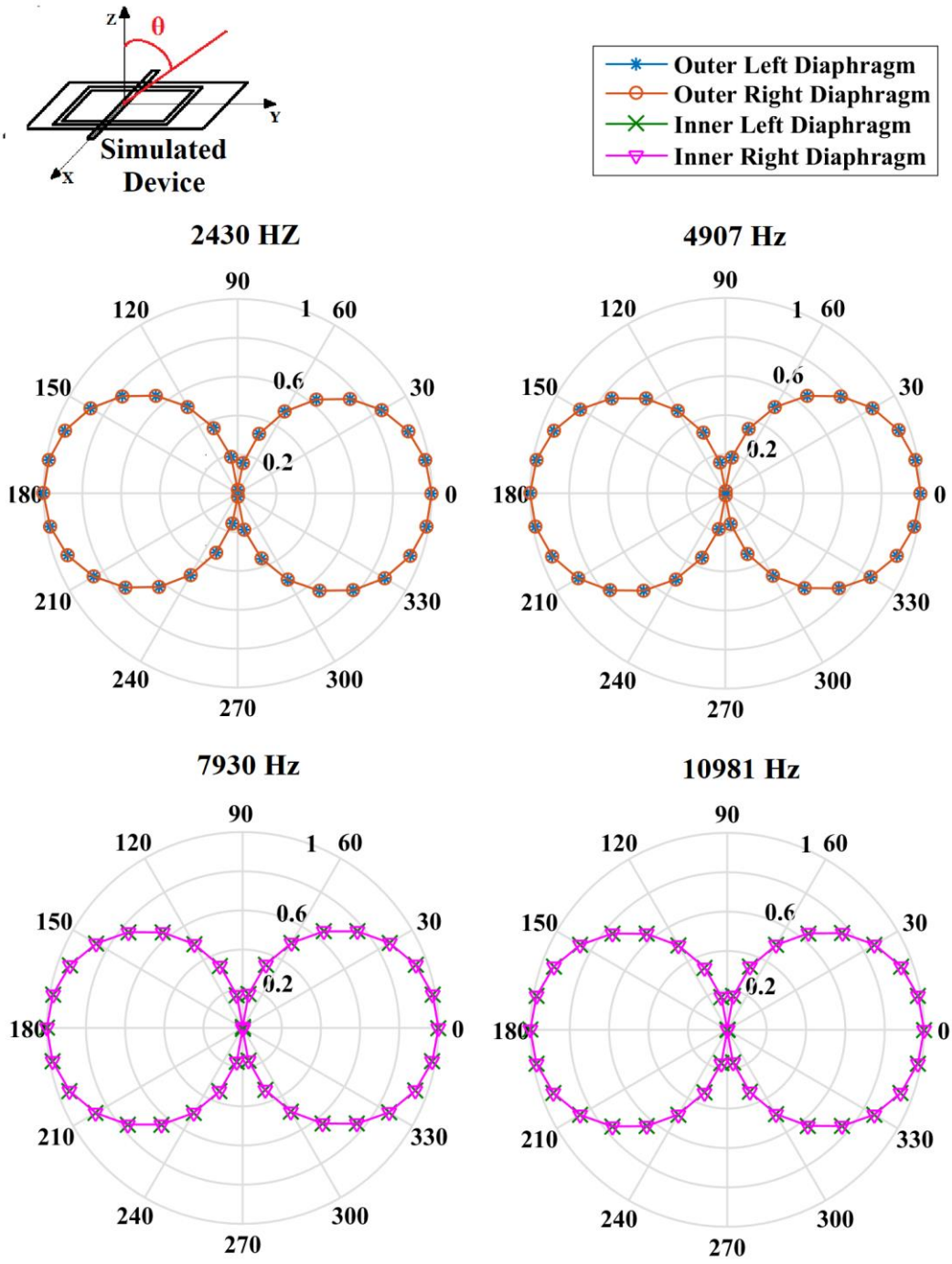

Fig. 4.15 Directional polar patterns of the new dual-plate Ormia-inspired MEMS microphone at four resonance frequencies – 2430 Hz, 4907 Hz, 7930 Hz and 10981 Hz, obtained by COMSOL simulation

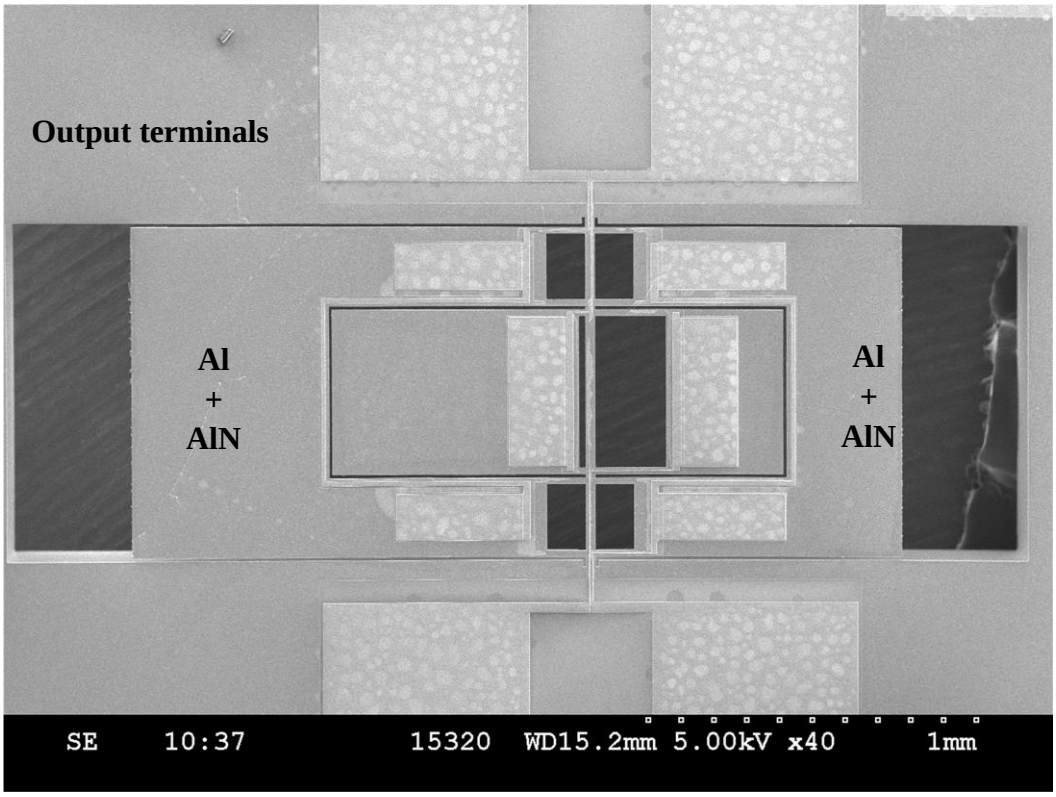

Fig. 4.16 SEM images of asymmetric piezoelectric Ormia-inspired Microphone operating in the multiple frequency bands

4.3.2 Optical Profiles

The same surface measurement that was executed on the previous designs using optical profiler was also carried out on the new fabricated design. As shown in Fig. 4.17, the elevation from the centre of the torsional beam to the end of the inner and the outer diaphragms with smaller area size in the longitudinal direction is about 3.2 µm and 8.5 µm, respectively. In the directional along the torsional beam, the elevation from the centre of narrow edges of these two diaphragms to the ends of the edges reach to 1.27 µm and 1.3 µm, respectively. For the inner and outer diaphragms with larger area size, the values of elevation in the longitudinal direction are as twice as the values for the smaller diaphragms (see Fig. 4.18), which are almost linear to the area ratios between the larger and the smaller diaphragm in the same plate. Compared to the previously designed piezoelectric dual-plate device, the curvature of the new device is much larger in despite that the area covered by piezoelectric material on the outer plate in the current design is over three times less than before. This reveals that

the higher elevation is mainly caused by the change of positions that the piezoelectric material attached on and the geometry of silicon diaphragm underneath rather than the size of the piezoelectric pads. However, since using the same fabrication method, the ferroelectric, dielectric and piezoelectric properties are almost the same in the current fabricated device and the previous device. Therefore, the electrical output will not be largely affected by the mechanical elevation of the diaphragms and only relate to the size of the piezoelectric pads and their positions.

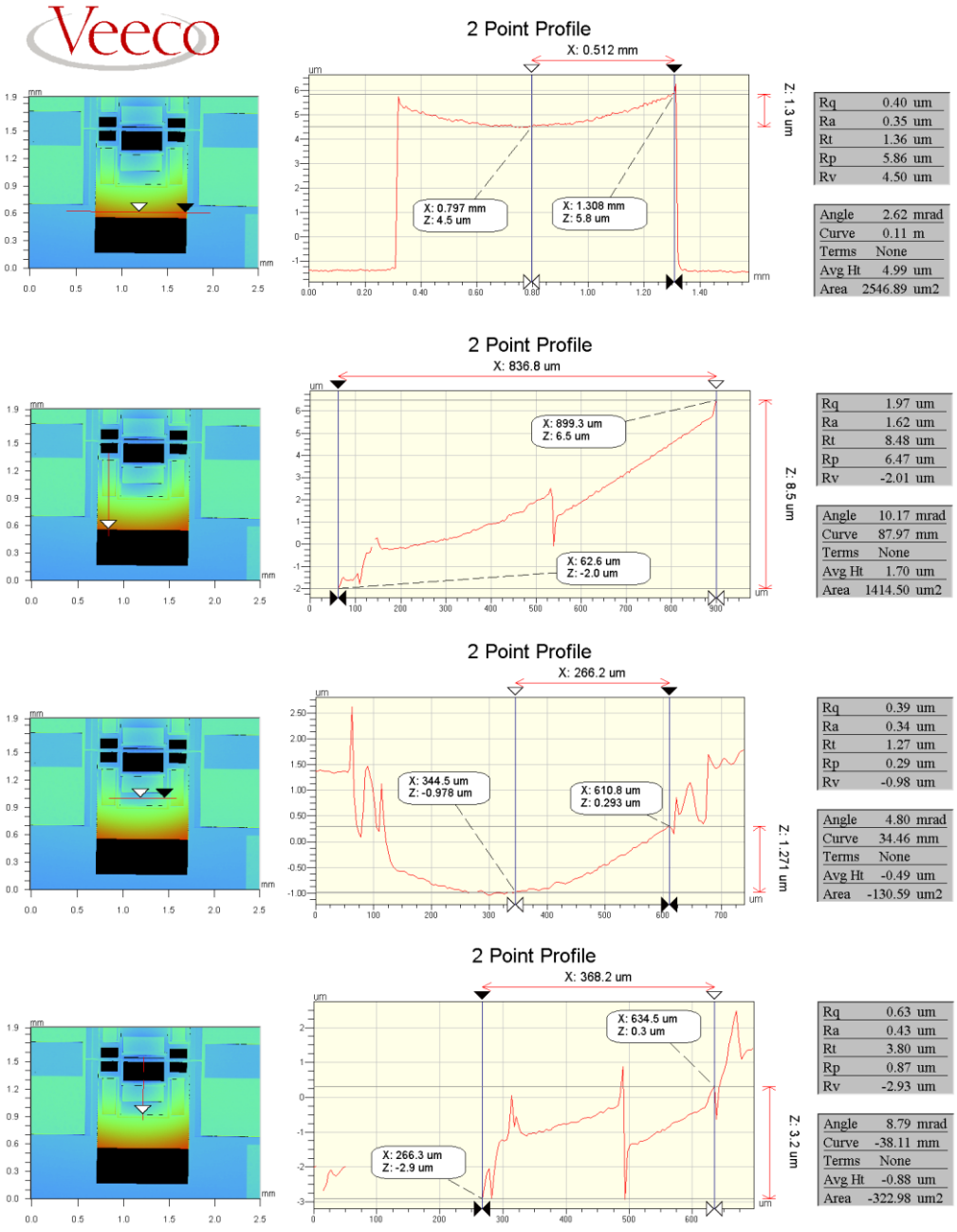

Fig. 4.17 The surface results of the symmetric multi-band operational microphone measured at the outer and the inner diaphragms with smaller area size, obtained by the optical profiler

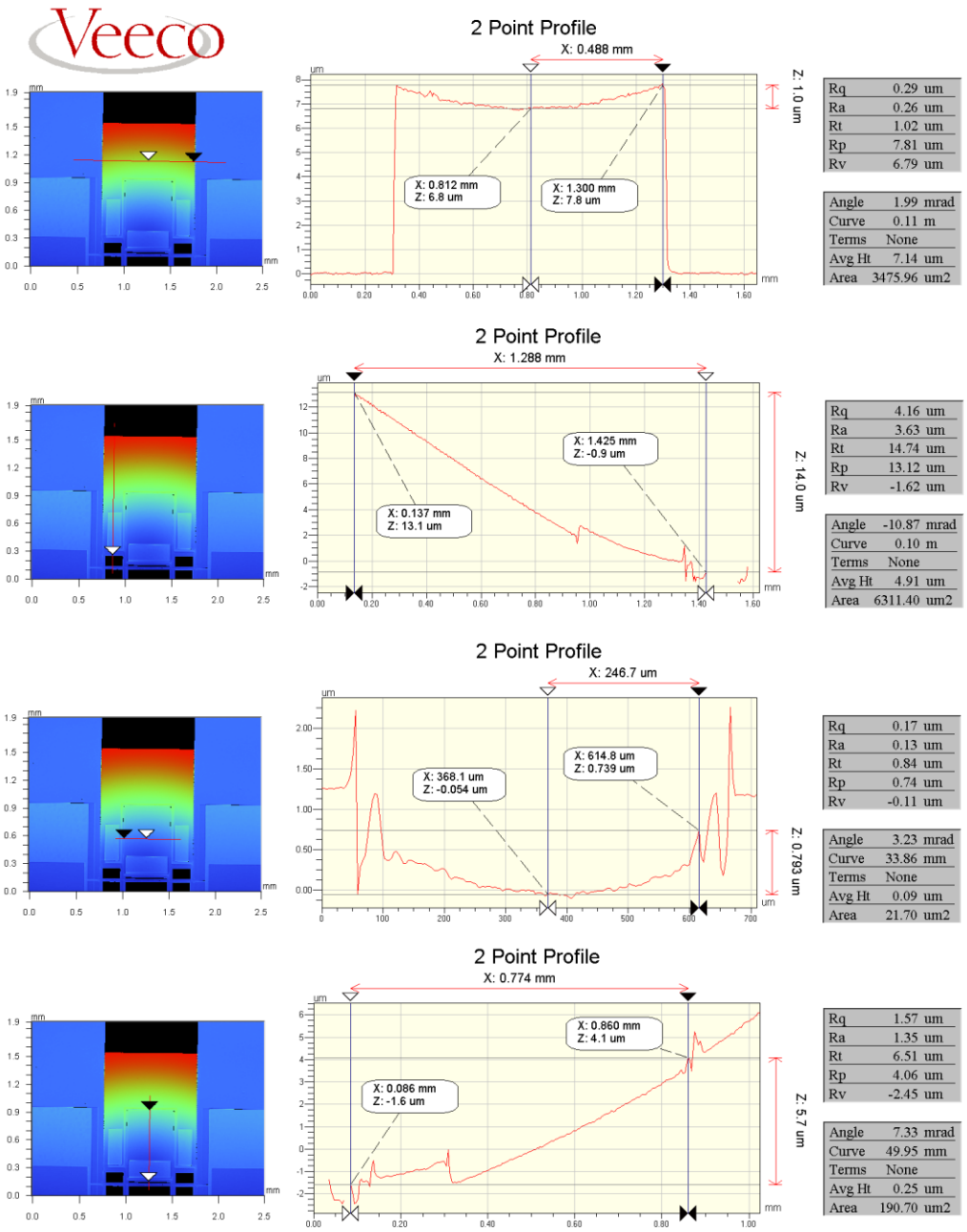

Fig. 4.18 The surface results of the symmetric multi-band operational microphone measured at the outer and the inner diaphragms with larger area size, obtained by the optical profiler

4.3.3 Simulated and Experimental Results

(a) Mechanical Performance

As same as the experimental process described in Chapter 3 and Section 4.1, the first task is to confirm if the fabricated device has the mechanical behaviour that is closely matched with the simulated results, which can be divided into two steps: 1) Measuring the mode shapes; 2) Characterizing the mechanical frequency response. Both steps were accomplished using the same experimental setup for measuring mechanical behaviours described in Section 3.5.1. As shown in Fig. 4.19, it can be confirmed that although there is a certain distance between the centre of the asymmetric device and its torsional beam, its resonance mode shapes are still similar to the ones of the symmetric device, where the outer and the inner diaphragms rotate out of phase at the 1st and the 3rd resonance frequencies, respectively, and move in phase at the 2nd and the 4th resonance frequencies, respectively. The mode shapes measured by LDV are consistent with the COMSOL simulation, and their corresponding resonance frequencies are also closely matched with predictions as listed in Table 4.2. Except that the 1st resonance frequency is approximately 1 kHz low than the value of the symmetric device presented in the last section to improve its performance at the low frequency range, other resonance frequencies were set close to the previous values. In terms of the mechanical frequency response, the maximum mechanical sensitivity is about 1.31 μm/Pa, occurring on the smaller diaphragm of the outer plate at the 2nd resonance frequency as shown in Fig. 4.21. Furthermore, the mechanical sensitivity at the 1st resonance frequency reaches up to 1.02 μm/Pa which is about 78 % of the maximum value, measured at the edge of the larger diaphragm of the outer plate. When working at the 3rd resonance frequency, the larger diaphragm of the inner plate has a mechanical response about 0.93 μm when sound pressure applied equals to 1 Pa. Compared to the mechanical performance of the symmetric device driven by the 3rd resonance frequency, the response has a dramatically increase. When the device is excited by 1 Pa sound pressures at the 4th resonance frequency, the smaller diaphragm of the inner plate will vibrate at the amplitude of 0.29 μm. As the device has very low damping, most of the measurement noise at low frequencies is background noise.

Mode Shapes	Simulation (Hz)	LDV (Hz)
First	2438	2362
Second	4909	4884
Third	7923	7972
Fourth	10946	11028

Table 4.2 Comparison of simulated and measured resonance frequencies of the piezoelectric multi-band operational MEMS microphone (with asymmetric geometry) inspired by Ormia ochracea

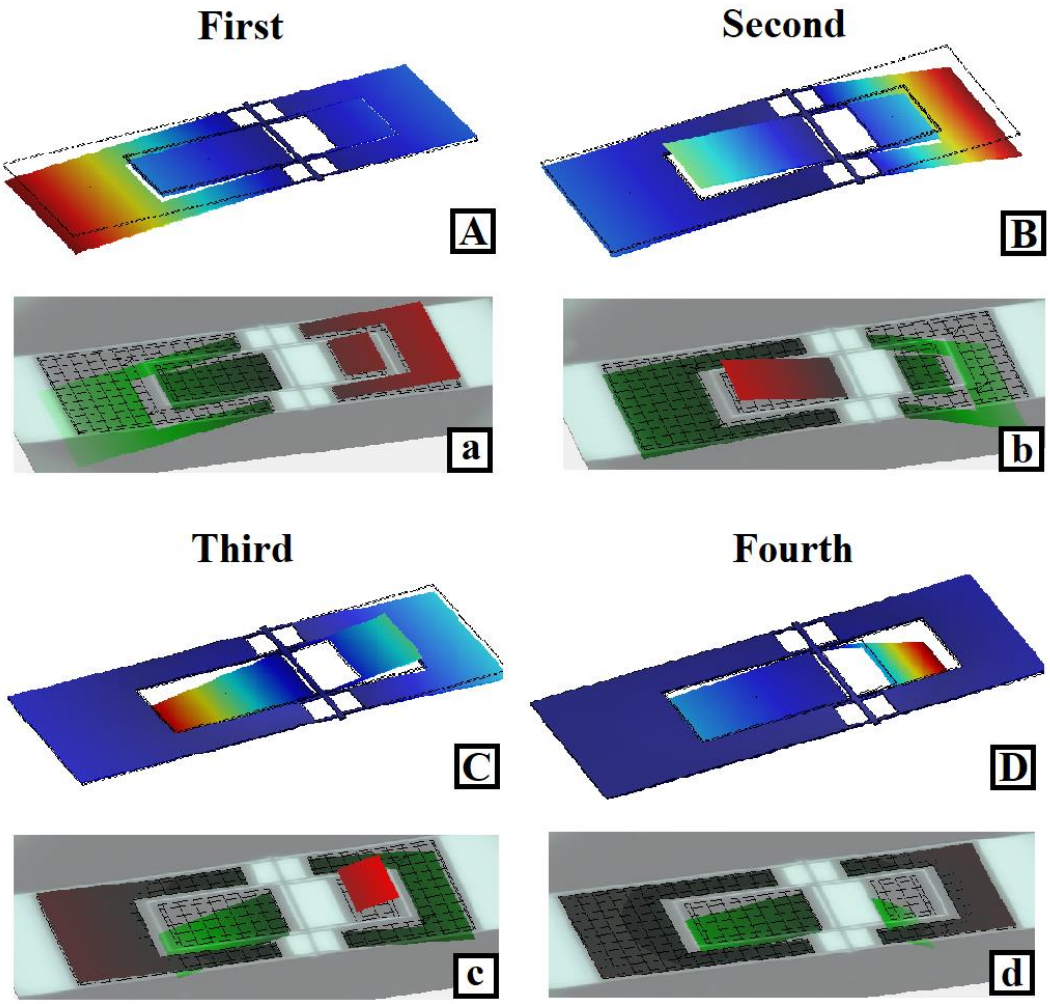

Fig. 4.19 Mode shapes of the symmetric device obtained by: (A) – (D) The COMSOL simulation; (a) – (d) LDV measurement

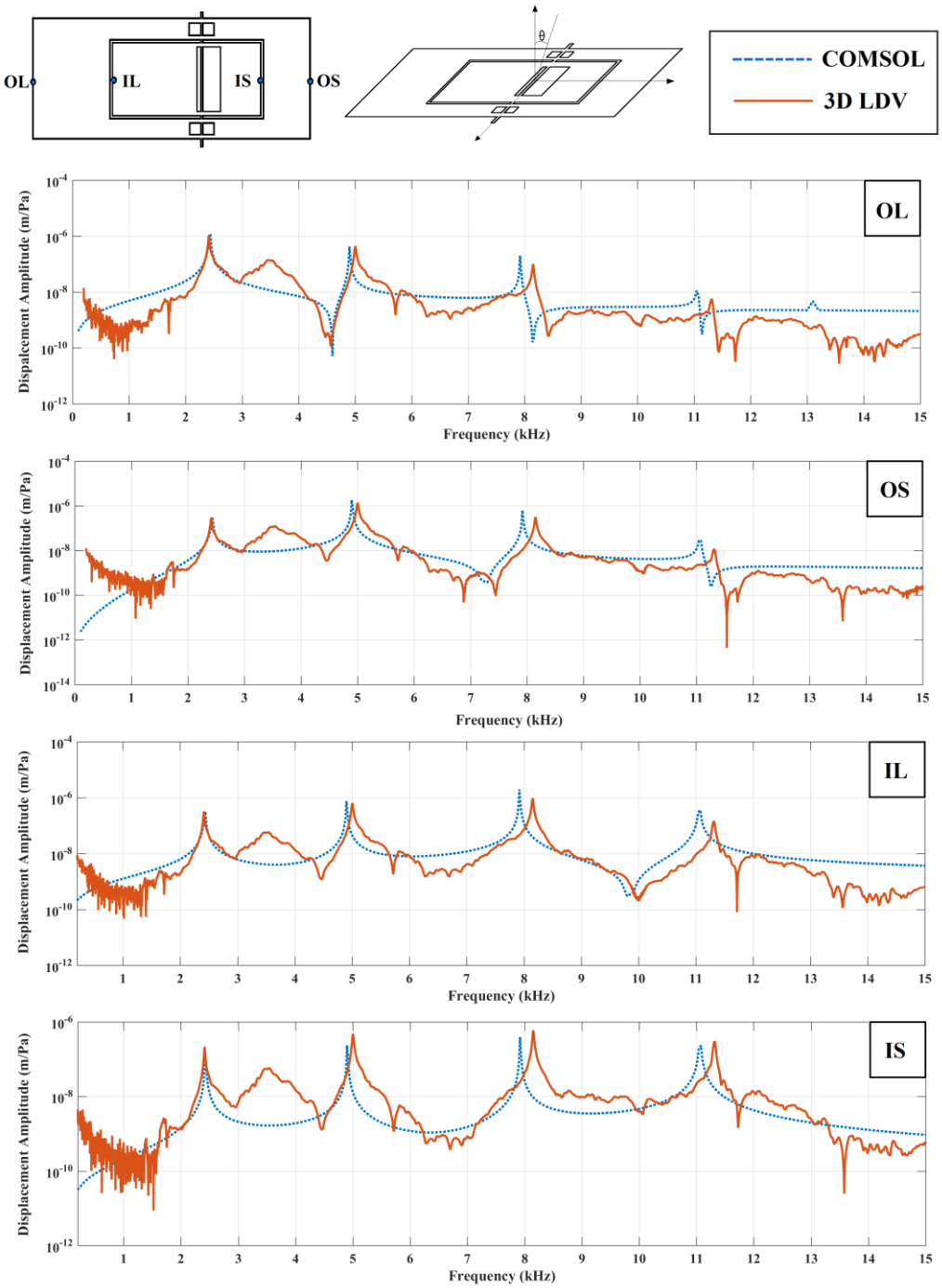

Fig. 4.20 Mechanical sensitivity of the asymmetric dual-plate piezoelectric Ormia-inspired MEMS microphone when $\theta = 45°$.

(b) Electrical Signals and Directionality

The experimental setup for acquiring the electrical signals of the new asymmetric device is as same as described in Section 4.2.4 (b). Figure 4.21 illustrates the electrical signals picked up from all four diaphragms at sound incident angle $\theta = 45°$ – from both inner and outer plates. The measured open-circuit acoustic sensitivity of the outer larger diaphragm reaches its maximum value about 4.61 mV/Pa at the 1st resonance frequency, and as simulation this value decreases to 3.08 mV/Pa. However, for the smaller diaphragm of the outer plate, the acoustic sensitivity captured at the 2nd resonance frequency is 3.82 mV/Pa whereas its acoustic sensitivity at the 1st resonance frequency is about 20 times lower than its sensitivity at the 2nd resonance frequency according to simulated results. Although its response is covered by the background noise in the experiment at the 1st resonance frequency, the overall acoustic response of the device is still beyond the noise floor and can be effectively captured by the output circuit. In addition, as the asymmetric design not only gives a better mechanical performance than the symmetric design at the 3rd resonance frequency, it generates higher acoustic sensitivity which attains 5.41 mV/Pa, collected from the port corresponding to the larger diaphragm of the inner plate. When the device operates at the 4th resonance frequency, the inner larger diaphragm can provide an acoustic sensitivity around 3.26 mV/Pa.

Figure 4.22 presents the measured normalized voltage outputs from the outer frame and the inner angle with varying sound incident angle. The experimental measurement show that the new device has an almost uniform bi-directional pattern at all four resonance frequencies as predicted from the previous finite element simulation. However, while the simulation shows an ideal figure-8 pattern, the experimental results show a reduced sound response at the back of the device. To be specific, its behaviour is a bi-directional at all four resonance frequencies, especially at the 3rd, 2nd and the 4th resonance. The reduced backside response potentially originates from the sound energy reduction at the backside of the chip due to sound reflection and diffraction occurring in the hole of the PCB. The pressure gradient between the two surfaces of the device is smaller when the rear surface faces to the speaker than the front surface does.

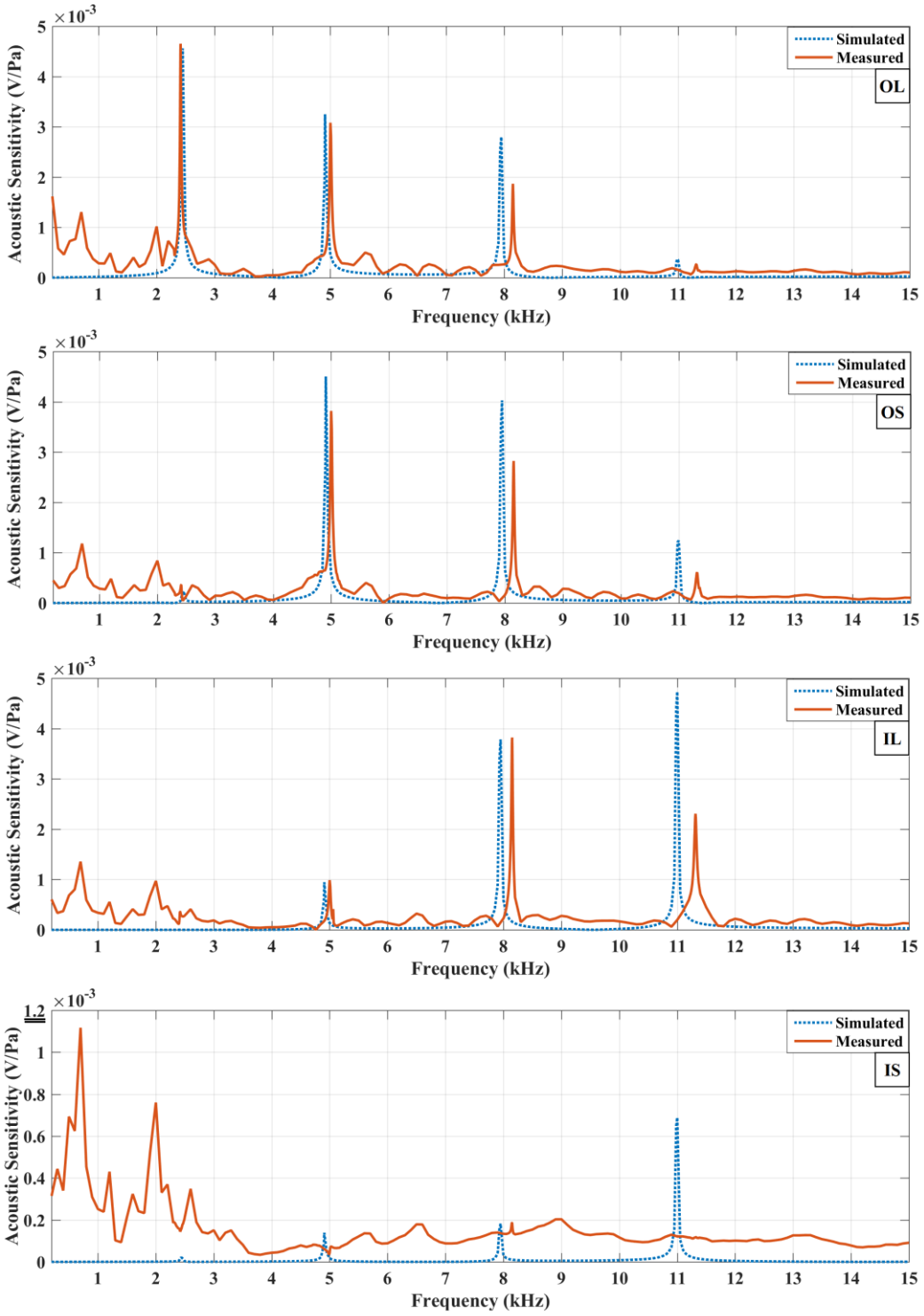

Fig. 4.21 Acoustic response of the microphone using piezoelectric sensing measured when $\theta = 45°$ at the port corresponding to (a) outer plate (b) inner plate. The measured results are against with COMSOL simulated results.

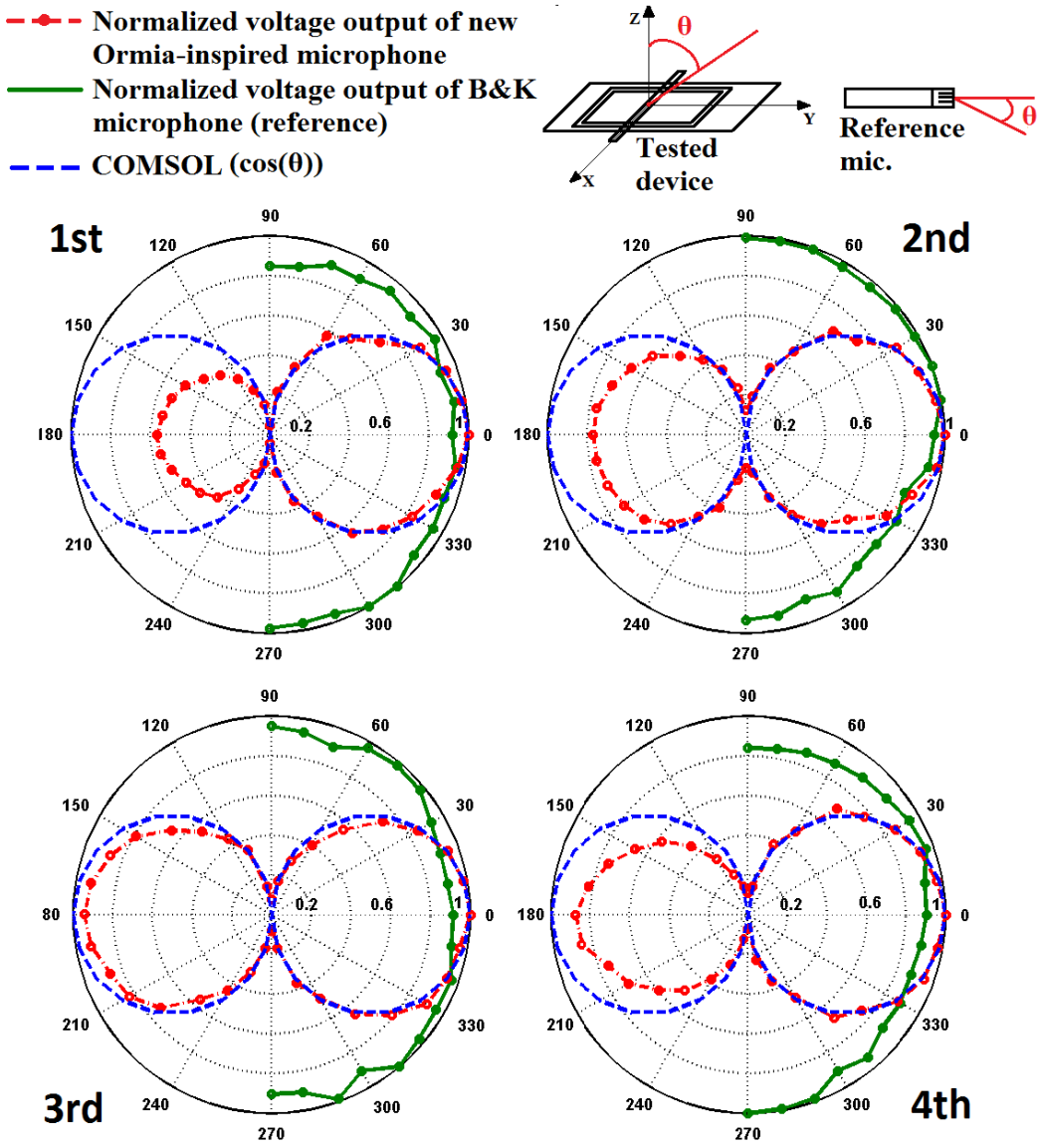

Fig. 4.22 Directional polar patterns of the symmetric microphone obtained at the four resonance frequencies.

4.4 Comparison between the symmetric and the asymmetric designs

This section will summarize the characteristics of both two generation piezoelectric microphones with symmetric and asymmetric geometry respectively, discuss the difference between them, and show the improvement of the asymmetric design compared to the symmetric design.

4.4.1 Structure and Surface Profile of Prototype

The total frontal surface area of the outer and inner plate of both the symmetric and asymmetric designs are almost the same. In addition, both devices have a 400 μm trench etched underneath the vibrational plates and hence building the path for sound pressure applied on both frontal and back surface of the plates. Except for the above similarities, the width of the torsional beams is identical, which is 30 μm. Although the length of the torsional beam of the asymmetric device is 20μm longer than the one of the symmetric devices, it is almost negligible if compared to an average total length of 1050 μm. The largest difference between the two designs concentrates on the position of their torsional beam and the length of the bending beams that connect four diaphragms to the torsional beam. Both two distinctions influence values of resonance frequencies, frequency response, and directionality of the devices. The torsional beam shifts about 200 μm from the centre of the entire geometry of the symmetric design to the current position in the asymmetric design. Other details of the difference are given in Section 4.2.1. Except for the structure change of silicon plates, the piezoelectric material attached on the outer plate was moved from the mass to the area that is close to the torsional beam to increase the piezoelectric output signals. Despite that the area covered by piezoelectric material on the outer plate of the asymmetric device has been reduced to one-third of the piezoelectric area applied on the outer plate of the symmetric device, the acoustical response shown in the subsequent electrical measurement is not affected despite of the reduction on the area of piezoelectric material.

Surface measurement is a useful tool to estimate the impact of adding piezoelectric material on the structure of the fabricated devices. For the symmetric device, according to Fig. 4.4 and Fig. 3.10, the average radius of curvature of outer plate is calculated about 82.20 mm while the average radius of curvature of inner plate

is 33.32 mm. The average curvature radius of outer plate declines to 50.22 mm (the curvature radius of larger diaphragm of outer plate is 59.26 mm, and it is 41.19 mm for the smaller diaphragm) for the asymmetric design, while the average curvature radius of the inner plate slightly smaller than the one of the symmetric device, which is about 36.87 mm (the curvature radius of larger diaphragm of inner plate is 52.55 mm, and it is 21.18 mm for the smaller diaphragm), based on the data collected from Fig. 4.17 and Fig. 4.18, respectively. It is easily to be explained by the change regarding to the position of AlN pads on the outer plate.

4.4.2 Mechanical Response

First of all, as mentioned in Section 4.2.3, the 1st resonance frequency of this four-resonance asymmetric device is about 1 kHz lower than the one of the symmetric devices, which is mainly caused by the shift of torsional beam that increases the total mass moment of inertia at the 1st mode shape. The change of mass distribution and length (i.e. stiffness) of bending beams also increase the resonance frequencies of bending modes (i.e. the 2nd and the 4th resonance frequencies). Table 4.3 compares the measurement of resonance frequencies of both fabricated symmetric and asymmetric devices, captured by LDV.

The major change of mechanical performance occurs on the frequency response. Table 4.4 shows the measured mechanical sensitivity at resonance frequencies of both the symmetric and the asymmetric devices so as to comparison. Both measurements of mechanical response were taken at $\theta = 45°$.The maximum mechanical sensitivity that is obtained from the narrow edge of the smaller outer diaphragm of the asymmetric device when operating at the 2nd resonance frequency is

Mode Shapes	Symmetric Device	Asymmetric Device
1st	3310	2362
2nd	4193	4884
3rd	7679	7972
4th	10118	11028

Table 4.3 Comparison of measured resonance frequencies between the Ormia-inspired piezoelectric multi-band operational MEMS microphone with symmetric and asymmetric geometry (extracted from Fig. 4.23)

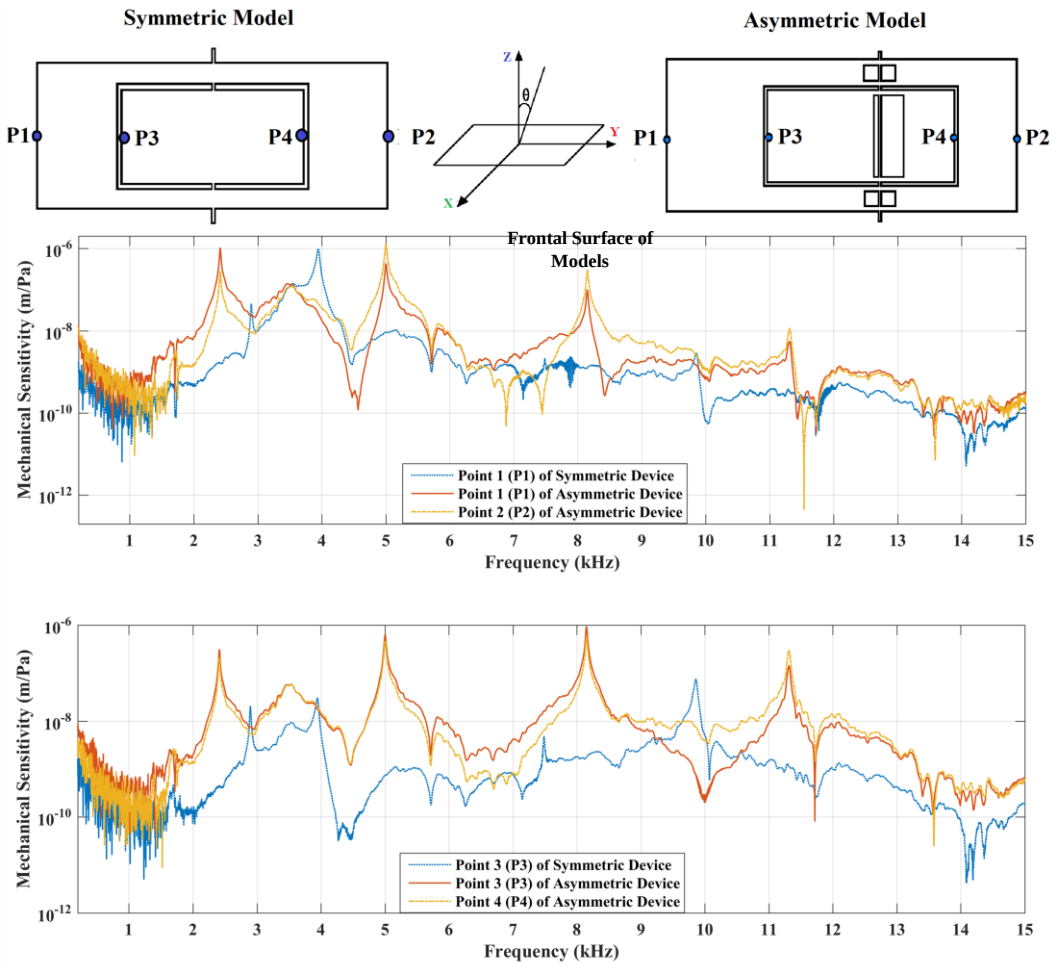

Fig. 4.23 Comparison of mechanical sensitivity between the symmetric and asymmetric dual-plate multi-band operational piezoelectric Ormia-inspired MEMS microphones.

36% higher than the maximum mechanical sensitivity of the symmetric device which is acquired from the narrow edge of the outer plate. Moreover, the average of four sensitivity peaks obtained from the outer plate of the asymmetric device is about 24.5% higher than the value of the symmetric one (without regard to the mechanical sensitivity at the 3rd resonance frequency of the symmetric device), whereas the average of four sensitivity peaks obtained from the inner plate of the asymmetric device is nearly 13 times higher than the value of the symmetric device. Expect for comparing the maximum mechanical sensitivity between the two types pf microphones, a new characterizing parameter mSD_{ij} (Mechanical Sensitivity Difference) is introduced to express the ratio of mechanical sensitivity between two

	Symmetric Device (nm/Pa)		Asymmetric Device (nm/Pa)			
f_n	Outer Plate	Inner Plate	OL Diaphragm	OS Diaphragm	IL Diaphragm	IS Diaphragm
1st mode	44.02	20.83	1017	277.2	309	207.3
2nd mode	966	30.74	426	1311	630	471
3rd mode	n/a	4.89	97.80	300	936	588
4th mode	27.72	76.10	5.49	11.31	141	298.2

Table 4.4 Mechanical Sensitivity acquired from the edge of vibrational diaphragms of both the symmetric and asymmetric devices (extracted from Fig. 4.11 and 4.20)

arbitrary resonance frequencies represented by subscripts *i* and *j* in this parameter. It is obtained by the mechanical sensitivity shown in Fig. 4.23 that combines the measured mechanical response of the symmetric device with the response of the asymmetric device and listed in Table 4.4. The values of mSD_{13} and mSD_{23} shown in Table 4.5 (a) and (d) are at least as twice as larger than the values shown in Table 3.5 (b)-(c) and Table 3.5 (e)-(f), respectively. The mSD_{23} shown in Table 4.5 (b) even

(a)

mSD_{ij}	$j = 1$	$j = 2$	$j = 3$	$j = 4$
$i = 1$	1	4.55×10^{-2}	20.80	15.85
$i = 2$	21.96	1	456.81	348.05
$i = 3$	4.81×10^{-2}	2.19×10^{-3}	1	0.76
$i = 4$	6.31×10^{-2}	3.01×10^{-2}	1.31	1

(b)

mSD_{ij}	$j = 1$	$j = 2$	$j = 3$	$j = 4$
$i = 1$	1	2.39	10.40	185.24
$i = 2$	0.42	1	5.39	77.60
$i = 3$	9.62×10^{-2}	0.23	1	17.81
$i = 4$	5.40×10^{-3}	1.29×10^{-2}	5.61×10^{-2}	1

(c)

mSD_{ij}	$j = 1$	$j = 2$	$j = 3$	$j = 4$
$i = 1$	1	0.21	0.92	24.50
$i = 2$	4.73	1	4.37	115.92
$i = 3$	1.08	0.2288	1	26.52
$i = 4$	4.08×10^{-2}	8.63×10^{-3}	3.77×10^{-2}	1

(d)

mSD_{ij}	$j = 1$	$j = 2$	$j = 3$	$j = 4$
$i = 1$	1	0.68	4.26	0.27
$i = 2$	1.47	1	6.27	0.40
$i = 3$	0.23	0.16	1	0.64
$i = 4$	3.65	2.48	15.56	1

(e)

mSD_{ij}	$j = 1$	$j = 2$	$j = 3$	$j = 4$
$i = 1$	1	0.49	0.33	2.20
$i = 2$	2.03	1	0.67	4.47
$i = 3$	3.01	1.49	1	6.64
$i = 4$	0.45	0.22	0.15	1

(f)

mSD_{ij}	$j = 1$	$j = 2$	$j = 3$	$j = 4$
$i = 1$	1	0.44	0.35	0.69
$i = 2$	2.27	1	0.80	1.58
$i = 3$	2.84	1.25	1	1.97
$i = 4$	1.44	0.63	0.51	1

Table 4.5 Mechanical Sensitivity Difference (mSD_{ij}) calculated from the mechanical sensitivity acquired at (a) Point 1 of the symmetric device; (b) Point 1 of the asymmetric device; (c) Point 2 of the asymmetric device; (d) Point 2 of the symmetric device; (e) Point 3 of the asymmetric device; (f) Point 4 of the asymmetric device

reaches up to over 100 times as the value shown in Table 4.5 (a). This big gap further demonstrates that the sensitivity peak of the symmetric device at 3rd resonance frequency is much lower than the sensitivity measured at other resonance frequencies, and it is easily to be covered by the self-thermal noise of the microphone and the background noise. Conversely, as shown in Fig. 4.24, all the sensitivity peaks of the

asymmetric device acquired at resonance frequencies are obvious and much higher than the noise flow nearby.

4.4.3 Electrical Response

If comparing the acoustic sensitivity of the symmetric device with the asymmetric device in the same figure (see Fig. 4.24), it is obvious that the maximum acoustic sensitivity obtained from the asymmetric device is about 30% higher than the value captured from the symmetric device. Moreover, like its mechanical behaviour,

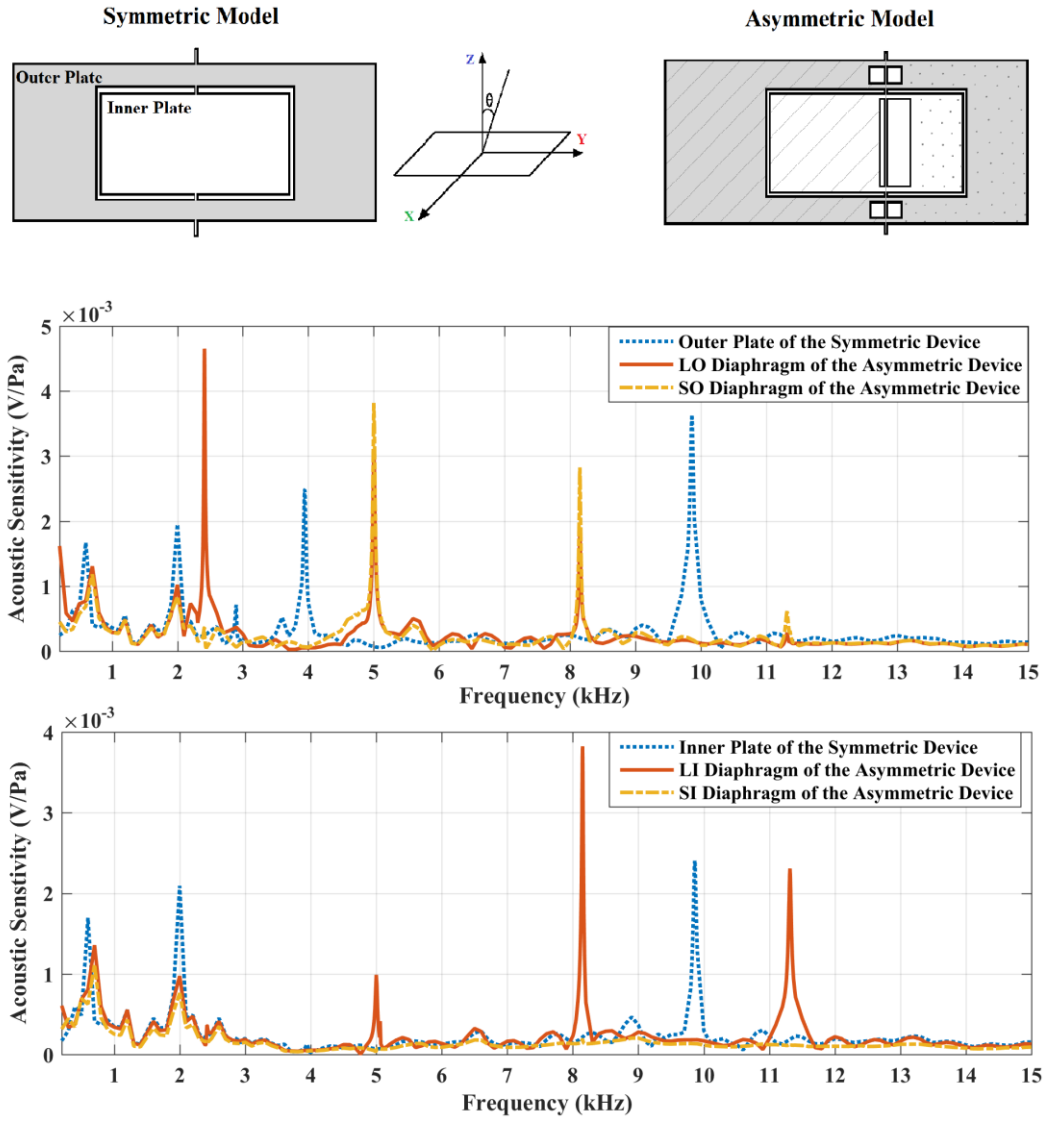

Fig. 4.24 Comparison of mechanical sensitivity between the symmetric and asymmetric dual-plate multi-band operational piezoelectric Ormia-inspired MEMS microphones when $\theta = 45°$.

	Symmetric Device (mV/Pa)		Asymmetric Device (mV/Pa)			
f_n	Outer Plate	Inner Plate	OL Diaphragm	OS Diaphragm	IL Diaphragm	IS Diaphragm
1st mode	0.71	n/a	4.61	0.36	0.36	n/a
2nd mode	2.48	0.13	3.08	3.82	0.99	n/a
3rd mode	n/a	n/a	1.87	2.83	3.80	n/a
4th mode	3.62	2.40	0.27	0.61	2.31	n/a

Table 4.6 Acoustic Sensitivity acquired from the ports corresponding to piezoelectric pad deposited on each vibrational diaphragm of both the symmetric and asymmetric devices (extracted from Fig. 4.24)

the electrical response of the symmetric device almost vanishes at the 3rd resonance frequency for either the inner or the outer plate while the larger inner plate of asymmetric device illustrates a 3.80 mV/Pa acoustic-electrical response at the 3rd resonance frequency, which is even about 5% higher than the maximum response acquired from the symmetric device so that enhances the average response in the frequency range between 7-9 kHz and improves the overall sound recording quality [106]. In addition, compared to the symmetric device, the asymmetric device owns more than 6 times higher sensitivity at the 1st resonance frequency, dramatically increasing the average sensitivity at low frequency range, which benefits human speech recording. At the 4th resonance frequency, the mean of acoustic sensitivity collected from both the inner and the outer plates of the symmetric device is higher than the value of the asymmetric device. However, for the asymmetric device, since the 4th resonance frequency is over 10 kHz the low response does not influence quality of recording tuning characteristics of human speech. Table 3.6 illustrates the acoustic sensitivity values picked up at the four resonance frequencies of both the symmetric and the asymmetric devices.

4.4.4 Directionality

The biggest difference occurs on the directionality behaviour as expected. At the 1st and the 3rd frequency, the maximum acoustic response is picked up by the symmetric device when incident sound waves travel along the longitudinal axis of the diaphragms, while the diaphragms of the asymmetric device get the most excitation when the sound waves propagate normal to the surface of the diaphragms. But different from operating at the 1st resonance frequency where the diaphragms of symmetric device have close measure acoustic response when sound hits either of the edges, the acoustic response is much higher when sound hit one side than the other at the 3rd resonance frequency. On the other side, the measured acoustic response is closer to a typical figure-8 polar patterns for the asymmetric device when operating at either the 1st or the 3rd resonance frequency. This is meanly due to the low acoustic response at

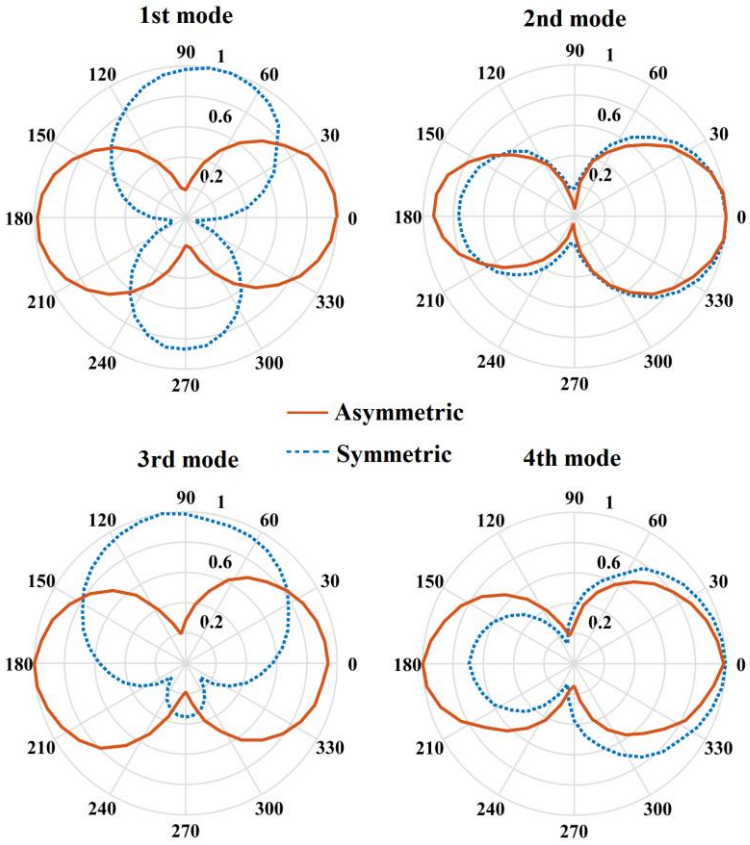

Fig. 4.25 Directional polar patterns of the fabricated symmetric microphone (blue dot line) and asymmetric microphone (red solid line) obtained at the four resonance frequencies

the 3rd resonance frequency. While at the 2nd and the 4th resonance frequency, both the symmetric and the asymmetric devices illustrate similar directional behaviour as shown in Fig. 4.25. Specifically, the asymmetric device owns a bit higher acoustic response when sound incident from the backside of the diaphragm than the symmetric device has.

4.5 Conclusion

In this chapter, two types of dual-plate multi-band operational *Ormia*-inspired microphones are developed. One is built in symmetric geometry while the other has an asymmetric geometry. Both fabricated devices contain piezoelectric sensing units and successfully transfer mechanical movement into electrical signals. Compared to the first-generation model introduced in Chapter 2, the frontal surface area of the new symmetric device is less than 65% of the value of the previous model given Chapter 3. Therefore, in general, the four resonance frequencies of the new fabricated symmetric device are higher than the values of the previous design as expected, especially for the 1st resonance frequency which is about two-third higher. However, the mechanical sensitivity levels at the resonance of the latest symmetric device are not affected by the mass reduction at all but beneficial from it. When sound incident angle $\theta = 45°$, the maximum mechanical response of the latest symmetric device is five times higher than the value of the first-generation device which is collected from the outer plate of both devices. In addition, according to the COMSOL simulated mechanical response, the 2nd and the 3rd resonance peaks are clearly separated mainly owing to the structure alternatives between the participated mass of the diaphragms and the torsional beam as well as the size of the inner diaphragms.

However, it still cannot remedy the low mechanical response of the latest fabricated symmetric device at the 3rd resonance frequency in experiment owing to the phase shift of the directional polar patterns between each resonance frequencies. This also affects the electrical response, and the device with activating area in asymmetric geometry is designed for remitting this problem. It is proved owns higher electrical sensitivity (see Fig 4.24) and more uniform directional behaviour (see Fig. 4,25) thus conforming the criterion of broaden band microphone operating in audio range.

Chapter 5

Low Frequency Band MEMS Microphone

In this chapter, an *Ormia*-inspired MEMS microphone developed for low frequency band operation is introduced. It is designed for hearing aid applications appropriate to low frequency hearing loss and inspired by the hearing mechanism of *Ormia ochracea*.

5.1 Introduction

The research described in this chapter concentrates on developing a directional microphone as a part for hearing aids designed for low frequency (or reverse-slope) hearing impairment people, which has enhanced sensitivity and obvious directional patterns in the low frequency audio range. With low frequency hearing loss, people are generally unable to hear frequencies below 2 kHz, which can be caused by Meniere's Disease, a genetic mutation, and other unknown or unexpected reasons [107], [108] Unlike most patients with high frequency hearing loss, low frequency hearing loss patients can clarify the pitch of words and sentences, so they are more comfortable in individual conversation. However, they usually have difficulty hearing in a group conversation and in some noisy environments. As low frequency impairment is much rarer than the high frequency hearing loss that usually happens to elderly people, most commercial hearing aids for low frequency hearing impairment are typically those pre-programmed for high frequency loss.

Unlike the four-band operational microphones presented in the last two chapters, this chapter is going to introduce a microphone built in see-saw structure that only adds one more resonance frequency compared to the similar designs mentioned

in the literature review. The two resonance frequencies in this case were designed to be below 2 kHz via replacing the straight rotating beam with serpentine springs and increasing the aspect ratio of the bending beams connecting the two mass to the rotating beam, in order to broaden the low frequency response. The piezoelectric material covers the area of the vibrating membrane with high strain to produce sensing elements, similar to the piezoelectric distribution of the asymmetric device described in Chapter 3. In addition, the capacitive sensing unit – comb fingers – were for the first time physically integrated into a piezoelectric *Ormia*-inspired MEMS microphone. Investigating the possibility of combining these two sensing mechanisms and bringing more functionalities and customized options for frequency response to the device is one of the plans in the future. Furthermore, as the theoretical support of the directional capability of the asymmetric microphone has been reserved in the previous chapter, this chapter will continuously discuss this topic.

5.2 Design concept

5.2.1 Analytical Model

In the previous two chapters, the mechanical principles of the dual-plate microphones have been analyzed, but not the reason of achieving their directivity. One point that should be noted is that the devices introduced in the last two chapters remove the air cavity which is included in the basic structure of *Ormia ochracea*'s hearing system and other subsequent symmetric microphones developed by other research groups [80], [81] This section will not only discuss the main factors that affect the directivity of the *Ormia*-inspired microphone built in the see-saw like structure model, but also the impact of the opened and closed substrate on the directional performance of the microphones. The experimental mechanical results demonstrated in Chapter 3 show that although the dual-plate structure rotates along the same axle, there is less mechanical coupling between the inner and he outer plates. Therefore, in this Chapter, the investigation about the directivity of the microphones with dual-plate structure is simplified to the study of the directivity of a single plate microphone.

The mechanical vibration model of *Ormia ochracea*'s hearing system, as well as the microphone developed with see-saw like structure and close-backside substrate, has previously been reported in Chapter 2. This assumes that the mass of the two tympana, as well as the stiffness of the tympana and the damping caused by the air cavity underneath, are identical, and thus infers the Eigen-frequencies and mechanical frequency response of the system. In order to fully analyze the factors influencing the directivity of the *Ormia*-inspired MEMS microphone, a simple asymmetric device

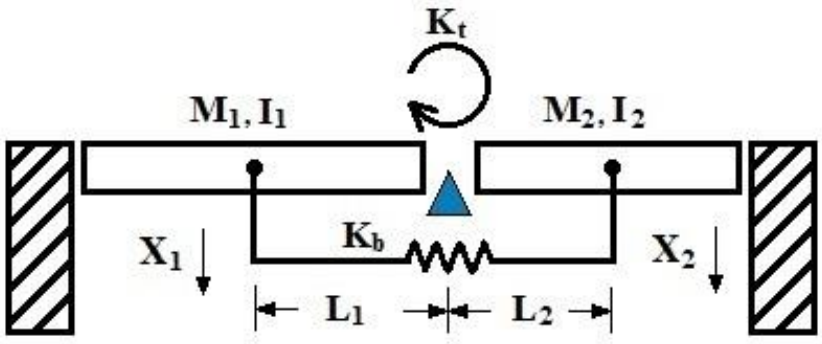

Fig. 5.1 The equivalent mechanical vibration model for the design

structure with open backside substrate is assumed – the rotation beam shifts in some distance from the centre on the membrane, and the mass *M* of the two diaphragms and the distance between the rotation beam and each diaphragm centroid are different. Figure 5.1 shows the two-degree-of-freedom equivalent mechanical vibration model of the asymmetric design. Ignoring the air damping between the comb fingers and generated in the gap between the membrane and the substrate, the equations of motion in the frequency domain can be expressed as

$$I\ddot{\theta}(\omega) + K_t\theta(\omega) = F_1(\omega)L_1 - F_2(\omega)L_2, \quad [5.1]$$

$$\begin{bmatrix} -\alpha M\omega^2 & 0 \\ 0 & -M\omega^2 \end{bmatrix}\begin{bmatrix} \ddot{X_1}(\omega) \\ \ddot{X_2}(\omega) \end{bmatrix} + \begin{bmatrix} K_b & K_b \\ K_b & K_b \end{bmatrix}\begin{bmatrix} X_1(\omega) \\ X_2(\omega) \end{bmatrix} = \begin{bmatrix} F_1(\omega) \\ F_2(\omega) \end{bmatrix}. \quad [5.2]$$

where $M = M_2$ and $\alpha = \frac{M_1}{M_2}$; K_t is the torsional stiffness of the rotation beam; K_b is the total bending stiffness of the bridges; I is the mass moment of inertia of the entire membrane about the rotational beam; L is the distance between the centroid of each diaphragm and the rotation beam; ω is the driving frequency; $\theta(\omega)$ and $X(\omega)$ represents the angular displacement about the rotation beam and the mechanical displacement after a Fourier transform; $F(\omega)$ is the effective forces placed on the diaphragms in frequency domain. The subscripts 1 and 2 represent the diaphragm with larger mass and the diaphragm with smaller mass, respectively. Equation [5.1] describes the motion of the device around the rocking mode while Eq. [5.2] is the motion equation near the bending mode. Re-arranging Eq. [5.1] and [5.2], the angular displacement and the mechanical displacement are then given by

$$\theta(\omega) = \frac{F_1(\omega)L_1 - F_2(\omega)L_2}{I(\omega_r^2 - \omega^2)}, \quad [5.3]$$

$$X_1(\omega) = \frac{F_1(\omega)(M\omega^2 - K_b) + F_2(\omega)K_b}{\alpha M^2\omega^2(\omega_b^2 - \omega^2)}, \quad [5.4]$$

$$X_2(\omega) = \frac{F_2(\omega)(\alpha M\omega^2 - K_b) + F_1(\omega)K_b}{\alpha M^2\omega^2(\omega_b^2 - \omega^2)}, \quad [5.5]$$

where ω_r and ω_b are the eigen-frequencies of the rocking and bending modes, respectively, that can be expressed as

$$\omega_r = \sqrt{\frac{K_t}{I}},\ \omega_b = \sqrt{\frac{(1+\alpha)K_b}{\alpha M}}. \quad [5.6]$$

Here the mechanical vibration model is regarded as a system of particles, hence the mass moment of inertia of each diaphragm is relative to the mass concentrating on its central of mass, i.e. $I_1 = L_1^2 M_1$ and $I_2 = L_2^2 M_2$. As the mechanical response at the centroid of each diaphragm is the superposition of the two main modes shapes, Equation [5.3], [5.4], and [5.5] enable the total displacement $x(\omega)$ to be written as

$$x_1(\omega) = X_1(\omega) + \theta(\omega)L_1 = \frac{\left[\frac{F_1(\omega)}{\alpha} + \frac{F_2(\omega)-F_1(\omega)}{\Omega^2(1+\alpha)}\right]/M}{\omega_b^2-\omega^2} + \frac{\frac{\beta[F_1(\omega)\beta-F_2(\omega)]}{M(\beta^2\alpha+1)}}{\omega_r^2-\omega^2}, \quad [5.7]$$

$$x_2(\omega) = X_2(\omega) - \theta(\omega)L_2 = \frac{\left[F_2(\omega) + \frac{F_1(\omega)-F_2(\omega)}{\Omega^2(1+\alpha)}\right]/M}{\omega_b^2-\omega^2} - \frac{\frac{F_1(\omega)\beta-F_2(\omega)}{M(\beta^2\alpha+1)}}{\omega_r^2-\omega^2}, \quad [5.8]$$

where $\beta = \frac{L_1}{L_2}$ and $\Omega = \frac{\omega}{\omega_b}$. When $\alpha = \beta$ (mostly happening in the case of a rectangular membrane), Eq. [5.7] and [5.8] can be simplified and shown as

$$x_1(\omega) = \frac{\left[\frac{F_1(\omega)}{\alpha} + \frac{F_2(\omega)-F_1(\omega)}{\Omega^2(1+\alpha)}\right]/M}{\omega_b^2-\omega^2} + \frac{\left[\frac{\alpha}{\alpha^3+1}(\alpha F_1(\omega)-F_2(\omega))\right]/M}{\omega_r^2-\omega^2}, \quad [4.9]$$

$$x_2(\omega) = \frac{\left[F_2(\omega) + \frac{F_1(\omega)-F_2(\omega)}{\Omega^2(1+\alpha)}\right]/M}{\omega_b^2-\omega^2} + \frac{\left[\frac{1}{\alpha^3+1}(\alpha F_1(\omega)-F_2(\omega))\right]/M}{\omega_r^2-\omega^2}. \quad [4.10]$$

In this case, if the driving frequency is close to the 1st resonance frequency (i.e. $\omega \approx \omega_r$), then as most kinetic energy accumulates in the torsional serpentine springs, the displacement amplitude of two diaphragms A_{r1} and A_{r2} has the following relationship,

$$A_{r1} = \alpha A_{r2} \propto |\alpha F_1(\omega) - F_2(\omega)|. \quad [4.11]$$

When the exciting frequency continuously increases and finally approaches the 2nd resonance frequency (i.e. $\omega \approx \omega_b$), most of the kinetic energy transfers from the torsional springs to the bending bridges. The amplitude of the two diaphragms A_{b1} and A_{b2} in this situation are linearly related, which can be expressed as

$$A_{b1} = \frac{1}{\alpha} A_{b2} \propto |F_1(\omega) + \alpha F_2(\omega)|. \quad [4.12]$$

If $\alpha = \beta = 1$ (i.e. the structure of the device is symmetric),

$$A_{r1} = A_{r2} \propto |F_1(\omega) - F_2(\omega)| \quad [4.13]$$

$$A_{b1} = A_{b2} \propto |F_1(\omega) + F_2(\omega)|, \quad [4.14]$$

which matches with the derivation results of displacement amplitude of the symmetric designs shown in Chapter 2. Through Eq. [5.11] and [5.12], it is apparent that the displacement amplitude of the diaphragms heavily depends on two main factors: the ratio of mass and the sound pressure field acting on the diaphragms. The former factor is relative to the bias of the torsional beam to the center of the entire active device. The latter factor is associated with the sound pressure gradient between the front and back surfaces of the diaphragms that is determined by the structure of the substrate. The next section will discuss the impact of the bias of the torsional beam on the directional behavior of the device.

5.2.2 Factors Affecting the Directional Behaviour

(a) Influence from the bias torsional beam

The bias torsional beam adjusts the surface and mass distribution of the entire rotational plate for the vibrational wings mimicking the tympana of the *Ormia*'s ears, thus the two wings suffers different force levels generated by sound pressure. To further investigate the two main factors that affect the directivity of an *Ormia*-inspired MEMS microphone with a see-saw structure, a simplified model was built and simulated in COMSOL. It consists of a single rectangle plate with open backside and a torsional bar as shown in the top left corner of Fig. 5.2. The whole model is enclosed in a spherical air domain enfolded by a perfect acoustic matching layer to simulate an infinite domain for sound waves. It is assumed that the substrate is 5.5 mm × 5.5 mm, of which thickness is a constant equal to the thickness of the diaphragm – 10 μm. The dimensions of the vibrational part of the microphone are also a constant. By changing the bias value of the torsional beam d_{bias} relative to the centre of the plate, the variation of the displacement amplitude of the device against the sound incident angle θ at the 1st and the 2nd resonance frequencies are obtained as illustrated in Fig. 5.2(a) and 5.2(b). As can be seen in Fig. 5.2(a), the displacement amplitude of the plate excited at the 1st resonance frequency is proportional to $|\sin 2\theta|$ when the device is symmetric. If increasing d_{bias} from 0 μm to 50 μm, the displacement amplitude gradually turns to a

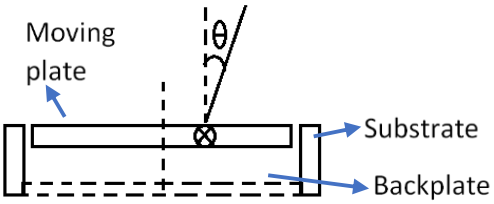

(a)

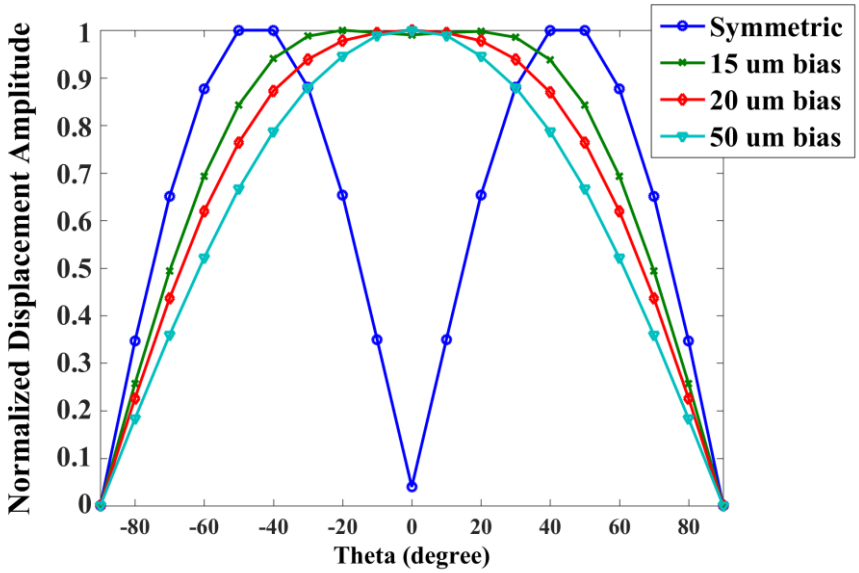

(b)

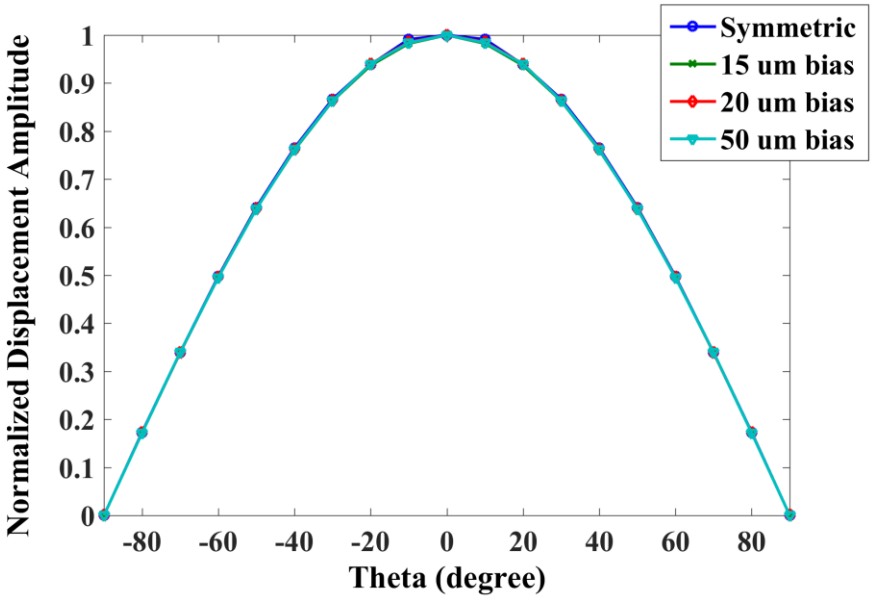

Fig. 5.2 Directivity of the device with a 10 µm thick substrate and an open backside when d_{bias} = 0 µm, 15 µm, 20 µm, and 50 µm at (a) The 1st resonance frequency (i.e. rocking mode) and (b) The 2nd resonance frequency (i.e. bending mode)

cosine function of θ. However, the bias of the torsional beam does not affect the directional behaviour of the model when it operates at the 2nd resonance frequency, which remains as a cosine function of the sound incident angle. In other words, when the bias of the torsional beam increases to a certain high value, the directional behaviour of a device excited at the 1st resonance frequency is similar to the behaviour at the 2nd resonance frequency. This phenomenon only occurs on the see-saw like *Ormia*-inspired MEMS microphone with open-backside substrate.

(b) Influence from the substrate

When a sound plane wave travels to a boundary with different density or speed of sound, it will change its original travelling path and deflects in other directions depending on the geometry and the surface condition of the boundary and its acoustic properties. This phenomenon is called sound scattering. If the substrate is assumed to be a short rigid pipe with one end closed at the backside of a rotational plate, the sound scattering happening at the edge of the bottom of substrate and the cavity of the pipe will change the sound pressure field underneath the vibrational plate. To study the relationship between the thickness of the substrate and the directivity, the model is initially regarded as symmetric. When the thickness of the substrate changes from 10 μm to 400 μm, the displacement amplitude of the model at the 1st resonance mode changes from a $|\sin 2\theta|$ function to a function close to $|\sin \theta|$, while it stays as a cosine function of θ at the 2nd resonance mode (see Fig. 5.3(a)). However, the directivity of the simplified model with a somewhat larger d_{bias}, such as 300 μm, is independent of the thickness of the substrate and the driving frequency as shown in Fig. 5.3(b).

When the substrate has a backplate, the device encloses an air cavity and blocks the sound waves hitting the backside of the vibrational plate, except for the diffracted waves from the slits. To discuss the impact of a backplate on the directivity, two states are simulated: a symmetric microphone and an asymmetric device with a 300 μm biased torsional beam. Both models include a backplate. The rest of the assumptions are the same - the thickness of the substrate sweeps from 50 μm to 400 μm. For the microphone with a symmetric geometry, the directivity of the device mostly follows the directional behaviour of the *Ormia*'s ears. It remains as a sine function of the sound

(a)

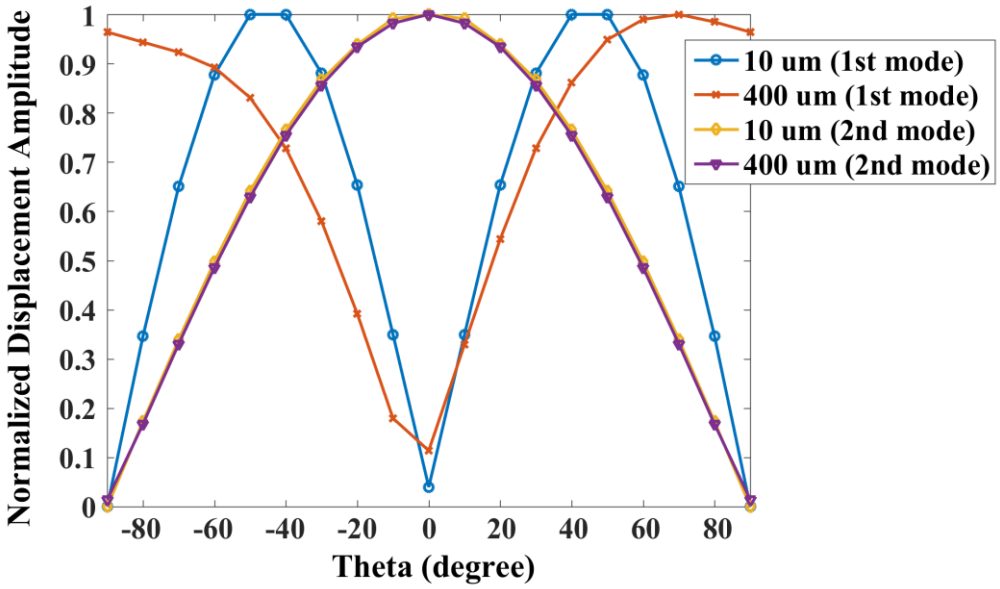

(b)

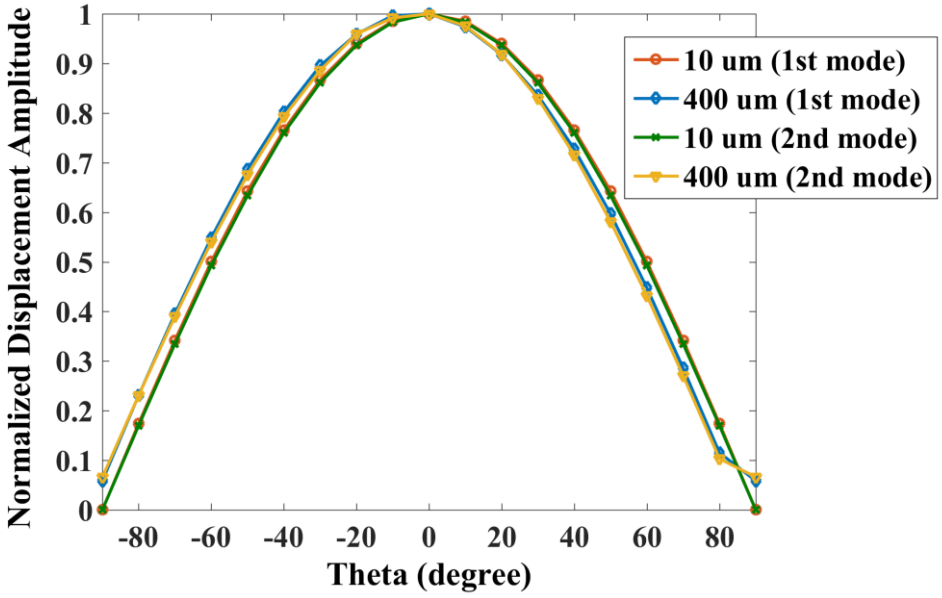

Fig. 5.3 Directivity of the device with a 10 µm or 400 µm thick substrate and an open backside at the 1st and the 2nd resonance frequencies when d_{bias} equals to (a) 10 µm (b) 300 µm.

incident angle at the 1st resonance mode, as shown in Fig. 5.4(a). However, there are some exceptions. As presented in Fig. 5.4(b), when the symmetric device is excited at the 2nd resonance frequency, it does not have an omni-directional mechanical response if the thickness of the air cavity underneath is equal to 50 μm, which has a $|\cos 2\theta|$ function instead. When the air cavity gets thicker, the variation of the displacement amplitude of the vibrational plate is progressively smaller across θ. As the air cavity is regarded to have solid boundaries, the sound field below the vibrational plate is the sum of the sound diffraction generated by the narrow slits between the membrane and the substrate, and the sound waves reflected from the bottom of the air cavity. With the thickness of the air cavity increasing, the reflected sound energy attenuates and reflected waves comprise a smaller portion of the sound field at the backside of the membrane. The symmetric device will eventually show omni-directional behaviour at the 2nd resonance frequency if the thickness of the air cavity is infinite. In this case, the membrane is treated as being embedded into an infinite rigid boundary parallel with the front surface of the membrane. On the other hand, for the asymmetric microphone with $b_{bias} = 300\,\mu m$, there is an angular offset on the function of directionality compared to the one of the symmetric device at both the 1st and the 2nd resonance frequencies (see Fig. 5.5 (a) and (b)). When increasing the thickness of the air cavity, the angular offset occurring at the 1st resonance frequency gradually approaches 10° while it reaches 90° when the device operates at the 2nd resonance frequency. In addition, despite the fact that the amplitude of variation of mechanical response decreases when the air cavity gets thicker, it still retains approximately 25 % variation across the sound incident angle when the air cavity deepens up to 400 μm at the 2nd resonance frequency. As mentioned before, the vibration of the membrane off the main resonance frequencies is the superposition of the mode shapes, hence the closed-back *Ormia*-inspired microphone structure with two different-size membranes is rarely applied as a directional microphone. Table 5.1 summarizes the factors for the directionality of the see-saw like *Ormia*-inspired microphone with combinations of various bias value of central torsional bar and different thickness of the substrate (or air cavity).

Since this type of biological-inspired devices are developed as directional microphones that requires uniform directionality in the frequency range of interest,

generally, only two structure combinations meet the requirement: the symmetric membranes structure with backplate and the asymmetric membranes structure without backplate. The former one places the 1st resonance frequency below the frequency range of interest and sets the 2nd resonance frequency beyond the frequency range of interest. The reason of this deliberate setting is to make the acoustic-electrical frequency response below the frequency range of interest as flat as possible and maintains the uniform directionality across the frequency range. However, this improvement is based on the sacrifice of the response level as the displacement amplitude at the 1st resonance frequency is proportional to the applied pressure gradient between the left and right membranes. On the other hand, the advantage of the asymmetric membranes structure without the backplate is that it has close response level at the two resonance frequencies. The high resonance peaks also increase the entire acoustic-electrical frequency response. However, the shortcoming of this structure is the uneven frequency response across the frequency range of interest, which can be solved by adding an application specific integrated circuit (ASIC). Therefore, in this Chapter, the asymmetric membrane structure without backplate is chosen as the foundation of the design structure, which has a torsional beam with nearly 400 μm bias relative to the central and a 400 μm thick open-backside substrate, its directional behaviour is predicted as that in the plot in Fig. 5.3(b).

(a)

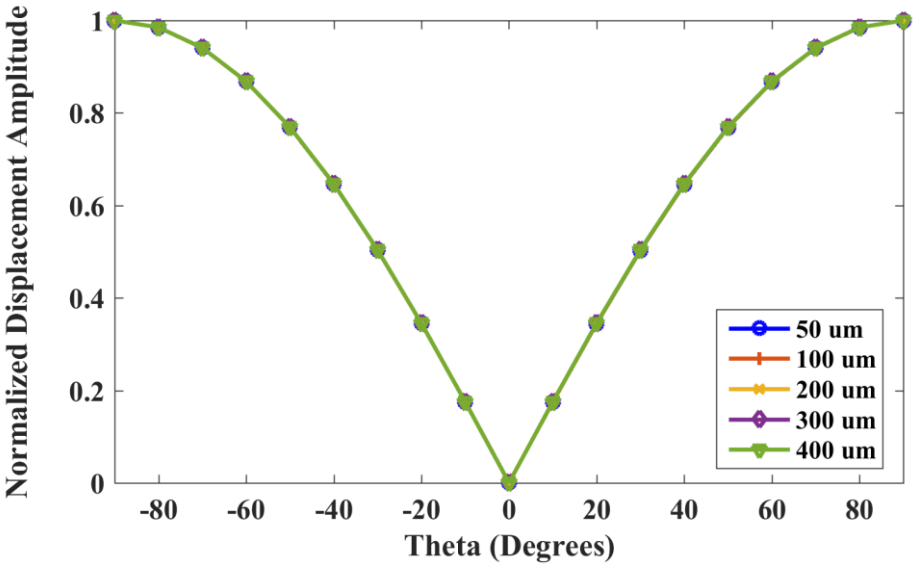

(b)

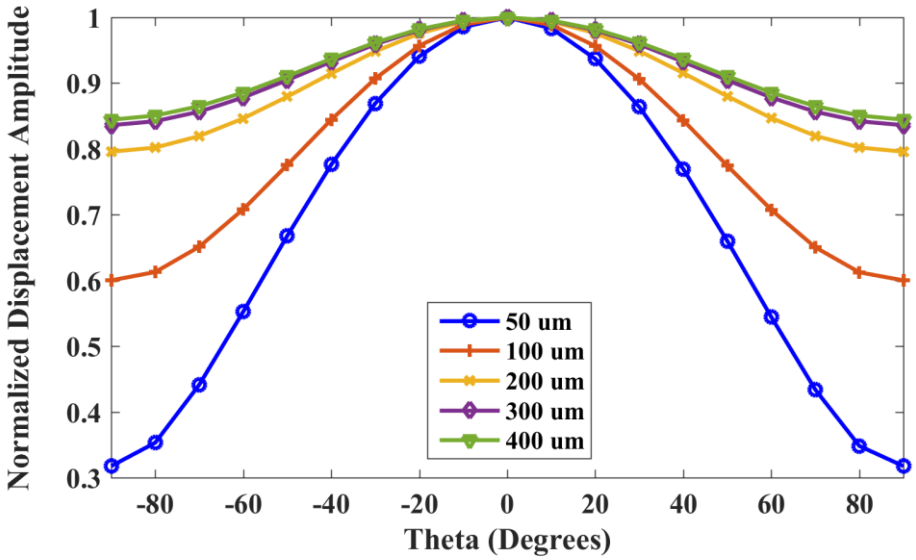

Fig. 5.4 Directionality of a symmetric device with a backplate, enclosing an air cavity with different thickness and working at (a) the 1st resonance frequency and (b) the 2nd resonance frequency

(a)

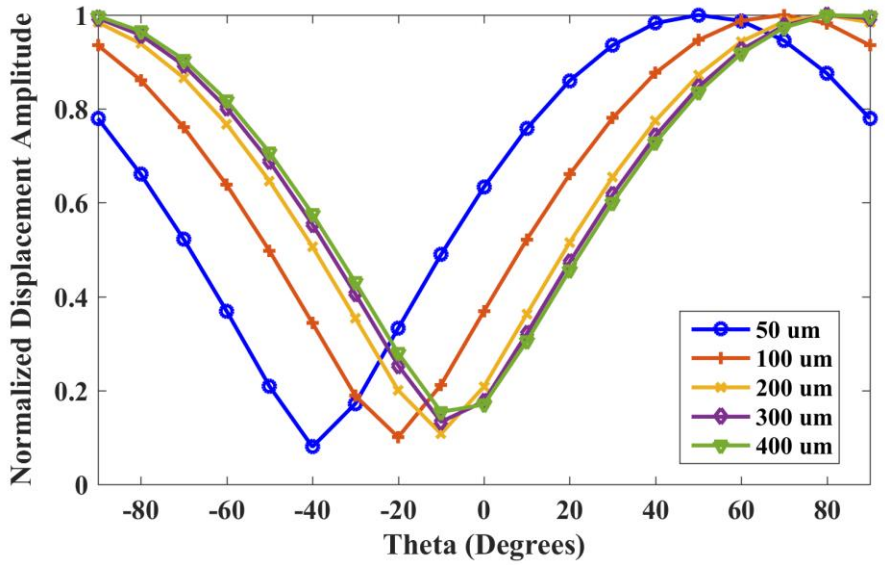

(b)

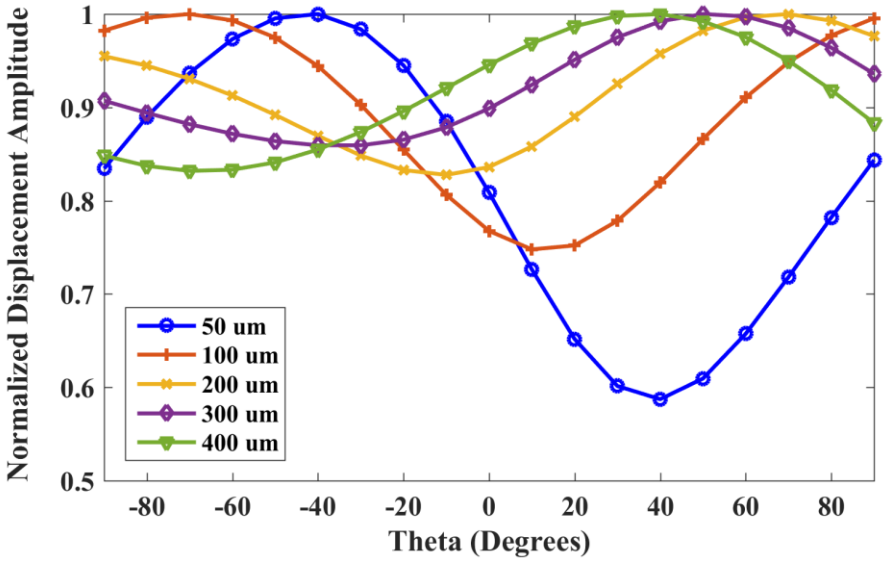

Fig. 5.5 Directivity of an asymmetric device with a 300 µm biased torsional beam, a backplate and a substrate in different thickness at (a) the 1st resonance frequency and (b) the 2nd resonance frequency

	At the 1st f_n		At the 2nd f_n	
	Symmetric	Asymmetric	Symmetric	Asymmetric
Without backplate (i.e. open-backside substrate)	Response $\propto \sin\theta$;	Response $\propto \cos\theta$, when THS $\geq$ 50μm;	Response $\propto \cos\theta$;	Response $\propto \cos\theta$;
With backplate (i.e. closed-backside substrate)	Response $\propto \sin\theta$;	Response $\propto \sin(\theta + \delta_1) + offset$ when THA $\geq$ 300μm;	Response $\propto Constant.$ when THA $\geq$ 300μm	Response $\propto \sin(2\theta + \delta_2) + offset$ when THA $\geq$ 300μm
*THA: Thickness of the substrate THS: Thickness of the air cavity δ_1: Angular offset, depending on d_{bias} δ_2: Angular offset, depending on d_{bias} and THA.				

Table 5.1 Main factors that influences the directionality of the Ormia-inspired microphones

5.2.3 Capacitive comb fingers

Because the kinetic energy concentrates on the torsional bar, the deposited piezoelectric material on the cantilevers or the membranes of the microphone usually generates a weak response at the 1st resonance frequency. This problem can be addressed by adding comb fingers on both ends of the membranes and acquiring signals through capacitive sensing, which is introduced into the microphone presented in this chapter. Using the capacitive sensing method, the electrical readout is potentially linear to the displacement of the membrane instead of the strain variation. Moreover, the introduction of the comb fingers adds more damping into the system due to air squeezed between the fingers, which then broadens the working frequency band between the two resonance frequencies.

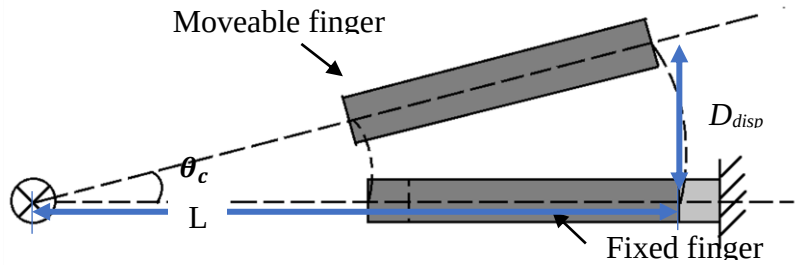

Fig. 5.6 The schematic cross section view of a comb finger unit

The total capacitance between the comb fingers is the sum of the capacitance between two neighbouring fingers and the capacitance between the tips of the comb fingers and the beam. To calculate the capacitance between the microphone's comb fingers, the COMSOL Electrostatics modules is applied. In the simulated model, the comb fingers (i.e. two fixed fingers and one moveable finger) are surrounded by a spherical air domain where the relative static permittivity is set to 1. Figure 5.6 shows the schematic of a comb finger unit when the membranes vibrate. As shown in the figure, θ_c is the angular difference between the central lines of moveable and fixed capacitive fingers, which can be expressed as

$$\theta_c = \arcsin\left(D_{disp}/L\right) \times \frac{180}{\pi}\,[\mathrm{rad}] \qquad [5.15]$$

where D_{disp} is the displacement amplitude at the end of the moveable finger relative to the central dash line, which is assumed to be in direct proportion to the displacement amplitude of the membranes. θ_c is also the angular displacement mentioned in Eq. [5.1] at the static status. Due to the extremely large computation requirements of the multi-physical study, the vibration of the membranes is replaced by the parametric sweep D_{disp}, and then the capacitance variation on the change of D_{disp} is calculated by the stationary study in the software. To get sufficient overlaps between the comb fingers and avoid touching between the fingers at high voltage, the dimensions of the fingers of the fabricated device are predicted to be $100\ \mu\mathrm{m}\,(\mathrm{length}) \times 5\ \mu\mathrm{m}(\mathrm{width}) \times 10\ \mu\mathrm{m}(\mathrm{thickness})$. The gap between the comb fixed fingers and the moveable finger is also set to $5\ \mu\mathrm{m}$. The distance between the tips of the moveable fingers and the grooves of the fixed fingers is about $10\ \mu\mathrm{m}$. Finally yet importantly, a 1 V bias voltage is applied onto the fingers. Figure 45.7 (a) demonstrates the electric field between one unit of comb fingers (two fixed comb fingers and one moveable finger) and the arrows shows the moving direction of the charges. When the numbers of the fixed comb fingers and the moveable fingers increase to the same value as the 49 that are used in the fabricated prototype, the total simulated capacitance against the diaphragm displacement is computed as in Fig. 5.7 (b). The simulated results suggest that the total capacitance of this set of comb fingers is linear over the deflection of the membranes when the initial distance between the moveable and the fixed fingers is above

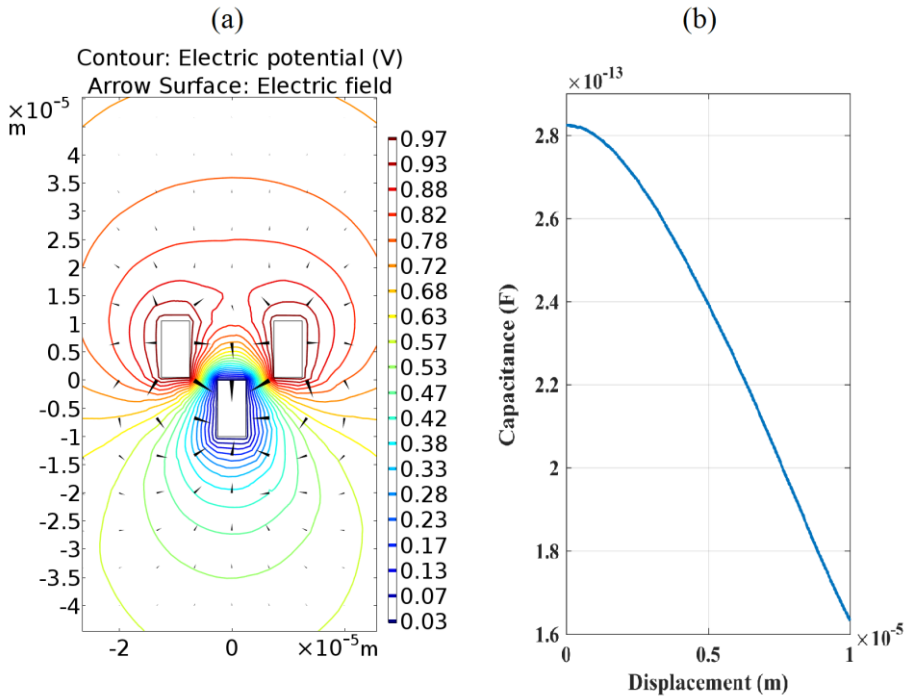

Fig. 5.7 Analysis of capacitive sensing of the device: (a) The electric field between a unit of capacitive comb fingers where the bias voltage is 1V; (b) The simulated total capacitance of a set of comb fingers.

approximately 3 μm. The capacitance at the static status is expected to be $2.83 \times 10^{-15} F$.

5.2.4 The torsional stiffness of the serpentine springs

To calculate the spring constant of the serpentine springs along the x-axis shown in Fig. 5.8, the unit-load method is applied. The unit-load method is a technique to calculate the displacement (deflection or rotation) of an equilibrium structure, which is based on the principle of virtual work. The principle of virtual work states that if a system in equilibrium under a system of forces undergoes a deformation, the work done by the external loads (EWD) equals the work done by the internal stresses (IWD) [109], which can be expressed as

$$1 \cdot \theta_x = \sum_{beams} \left(\int_0^{l_{beam}} T_V \frac{T_R}{GJ} dx + \int_0^{l_{beam}} M_V \frac{M_R}{EI} dx \right) \qquad [5.16]$$

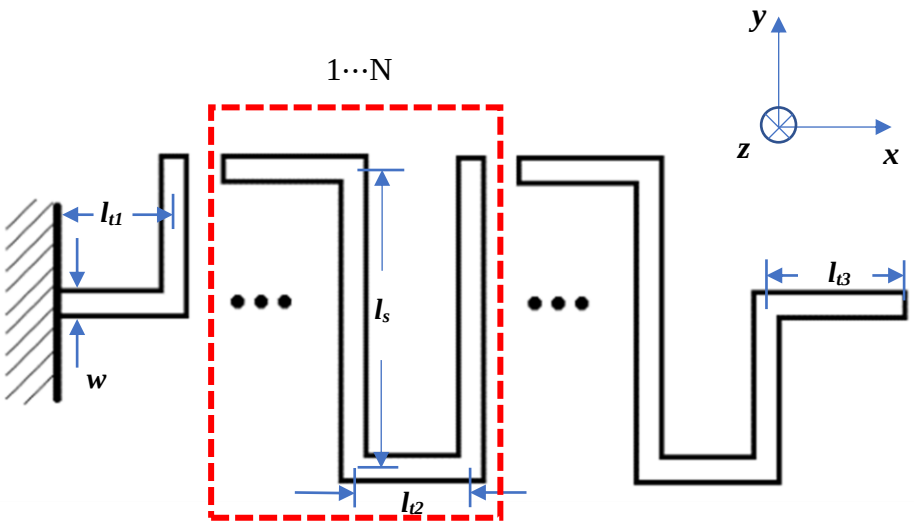

Fig. 5.8 Design variables of serpentine springs

where θ_x is the rotation angle of the spring along the x-axis. 1 represents the virtual unit load. *T* and *M*, here in this equation, are the torque and the torsion moment applied on the spring, where the subscripts *V* and *R* means the internal virtual work and the external real work, respectively. l_{beam} is the length of each beam section. The left-hand side of the Eq. [5.16] is the virtual external work while the right hand side is the internal work done. In this equation, the axis force and the shear force are neglected as it is irrelevant to calculating the torsional angle against the axis. To simplify the derivation of each beam, the reference of each beam is the end of the last beam. For the initial beam, the reference is at the fixed substrate where $x_0 = 0$. Assuming a torsion moment is applied in the z direction and substituting the internal virtual moment into Eq. [5.16], the equation of the rotation angle of a serpentine spring with N groups of folded beams can be written as follow,

$$\theta_x = \int_0^{l_{t1}} \frac{M_x}{GJ_{t1}} dx + \int_0^{\frac{l_s}{2}} \frac{M_x}{EI_s} dx + \sum_{i=1}^{N} \left(2 \times \int_0^{l_{t2}} \frac{M_x}{GJ_{t2}} dx + 2 \times \int_0^{l_s} \frac{M_x}{EI_s} dx \right) + 2 \times \int_0^{l_{t2}} \frac{M_x}{GJ_{t2}} dx + \int_0^{l_s} \frac{M_x}{EI_s} dx + \int_0^{\frac{l_s}{2}} \frac{M_x}{EI_s} dx + \int_0^{l_{t3}} \frac{M_x}{GJ_{t3}} dx \quad [5.17]$$

where J_{t1}, J_{t2}, and J_{t3} are the torsion constant of the initial beam, the middle beams along the x axis, and the final beams. I_s is the moment of inertia of the beams along the y axis distributed in the middle. For the serpentine springs used in the current application, N = 1, and the initial beam is identical to the final one. Therefore, by

rearranging Eq. [5.17)], we can get the simplified equation of the rotation angle against x-axis as

$$\theta_x = 2M_x\left(\frac{l_t}{GJ_t} + \frac{2l_{t2}}{GJ_{t2}} + \frac{2l_s}{EI_s}\right), \quad [5.18]$$

where $l_t = l_{t1} = l_{t3}$ and $J_t = J_{t1} = J_{t3}$. The moment of inertia and the torsion constant of a beam with rectangular cross section can be written as

$$I_s = \frac{wt^3}{12} \text{ (where } t < w) \quad [5.19]$$

$$J_t = wt^3\left[\frac{16}{3} - 3.36\frac{t}{w}\left(1 - \frac{t^4}{12w^4}\right)\right]. \quad [5.20]$$

Substituting Eq. [5.19] to Eq. [5.18], the derivation of the torsional stiffness of a single serpentine spring is

$$k_{\theta_x} = \frac{M_x}{\theta_x} = \left[\frac{2(l_t+2l_{t2})}{GJ_t} + \frac{48l_s}{Ewt^3}\right]^{-1}. \quad [5.21]$$

Thus, the total torsion stiffness if the structure is

$$K_t = 2k_{\theta_x} = 2\left[\frac{2(l_t+2l_{t2})}{GJ_t} + \frac{48l_s}{Ewt^3}\right]^{-1}. \quad [5.22]$$

In terms of the device presented in this chapter, the Young's modulus E of single crystal silicon equals to 169 GPa and the shear modulus G = 66 GPa. Substituting the width of the spring element $w = 30\mu m$, the thickness of the spring $t = 10\mu m$, $l_t = 25\mu m$, $l_{t2} = 40\mu m$, $l_s = 280\mu m$ and the total mass moment of inertia of the diaphragms I = 6.35×10^{-14}kg·m^2, then the analytical Eigen-frequency of the rocking mode $f_r = \frac{\omega_r}{2\pi} = 511\ Hz$. The bending stiffness K_b is obtained by a stationary study using COMSOL. Assuming different defined loads are applied on the centre of gravity of each diaphragm, then the bending stiffness could be derived from solving the equation set with known displacement value calculated via FEM. The predicted K_b equals to 4.3 N/m. Therefore, the analytical eigen-frequency of the bending mode $f_b = 2.6\ kHz$.

5.3 Fabricated device

As same as the previous designs, the device presented in this chapter is also fabricated with PiezoMUMPs. The device is constructed with two vibrational diaphragms of 10 μm thickness, which are linked to a 30μm width serpentine torsion beam by a 70 μm × 5μm central located bar and two 400 μm × 20μm beams that

(a)

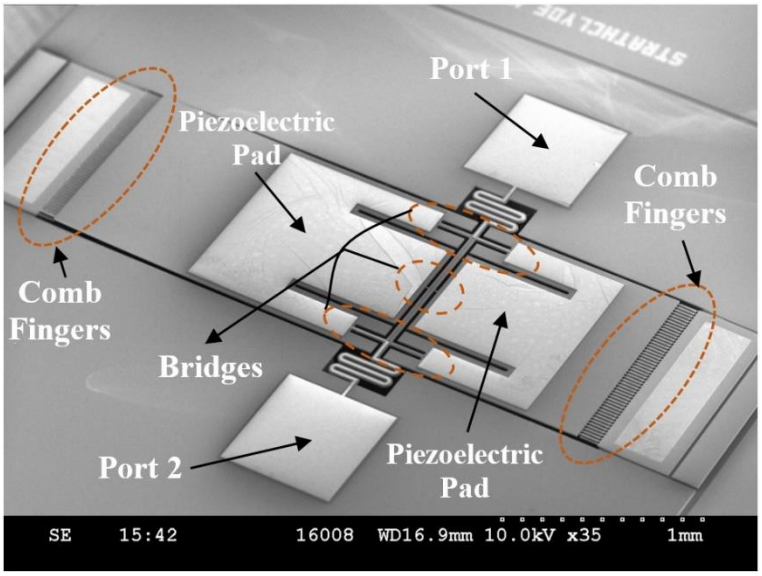

(b)

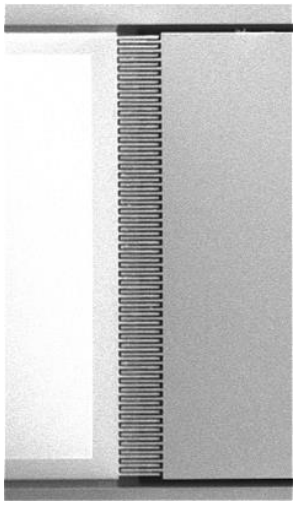

Fig. 5.9 The Scanning Electron Microscope (SEM) images of the presented asymmetric Ormia-inspired MEMS microphone. (a) The overview of the device tilted in 45 degrees. (b) The enlarged view of the comb fingers.

enhance the mechanical coupling between the two diaphragms and reduce the impact of the twisting motion on low frequency performance. The surface area of the larger diaphragm is about $1.83\,mm^2$ while the area of the smaller diaphragm is approximately $1.03\,mm^2$. The torsion beam is fixed to a 400 μm thick silicon-on-insulator (SOI) substrate with open backside. Including the comb fingers, the entire size of the activating area is $3.2\text{mm} \times 1.42\text{mm}$. A 500 nm thick Aluminum Nitride (AlN) piezoelectric layer is deposited on both the cantilevers and the region of the device that is close to the torsion beam. The voltage potential generated by the AlN layer is then transferred to the output ports via a composite metal layer attached on the piezoelectric layer and the oxide layer covering the torsion beam. In addition, the two conductors of the capacitive sensing (i.e. the fixed comb fingers and the moveable fingers) are separated by the photolithography process and deep reactive ion etching (DRIE). Figure 5.9 illustrates the SEM image of this new microphone and the enlarged view of the comb fingers on the side of the larger diaphragm.

Mainly due to the thermal stress created by the piezoelectric and SCS layers, the fabricated prototype has a 0.1 m curvature along the longitudinal axis of the device on the side of the larger diaphragm while it has a 0.14 m curvature along the axis parallel to the torsion beam (see Fig. 5.10). This brings a 15.3 μm lift-up at the end of the moveable comb fingers. If the scaling area is expanded to the comb fingers as shown in Fig. 5.11, the vertical distance between the fixed fingers and the moveable ones is even as high as 19.1 μm. Since the elevation is about 91 % higher than the thickness of the comb fingers, it does not provide sufficient overlapped area between the fingers and so causes extremely low initial capacitance. Therefore, the capacitive finger set for the larger diaphragm was not tested during experiments. On the other side, despite the close curvature in both directions, there is a just 3.6 μm elevation at the end of the smaller diaphragm due its shorter length (see Fig. 5.12). The vertical distance between the pair of fingers of the smaller diaphragm is just 4.8 μm, as shown in Fig. 5.13, thus producing enough overlapped area between the combs. Therefore, only the electrical signals from the comb fingers on the side of the smaller diaphragm are acquired during the characterization of the electrical performance of the device when using the capacitive sensing method.

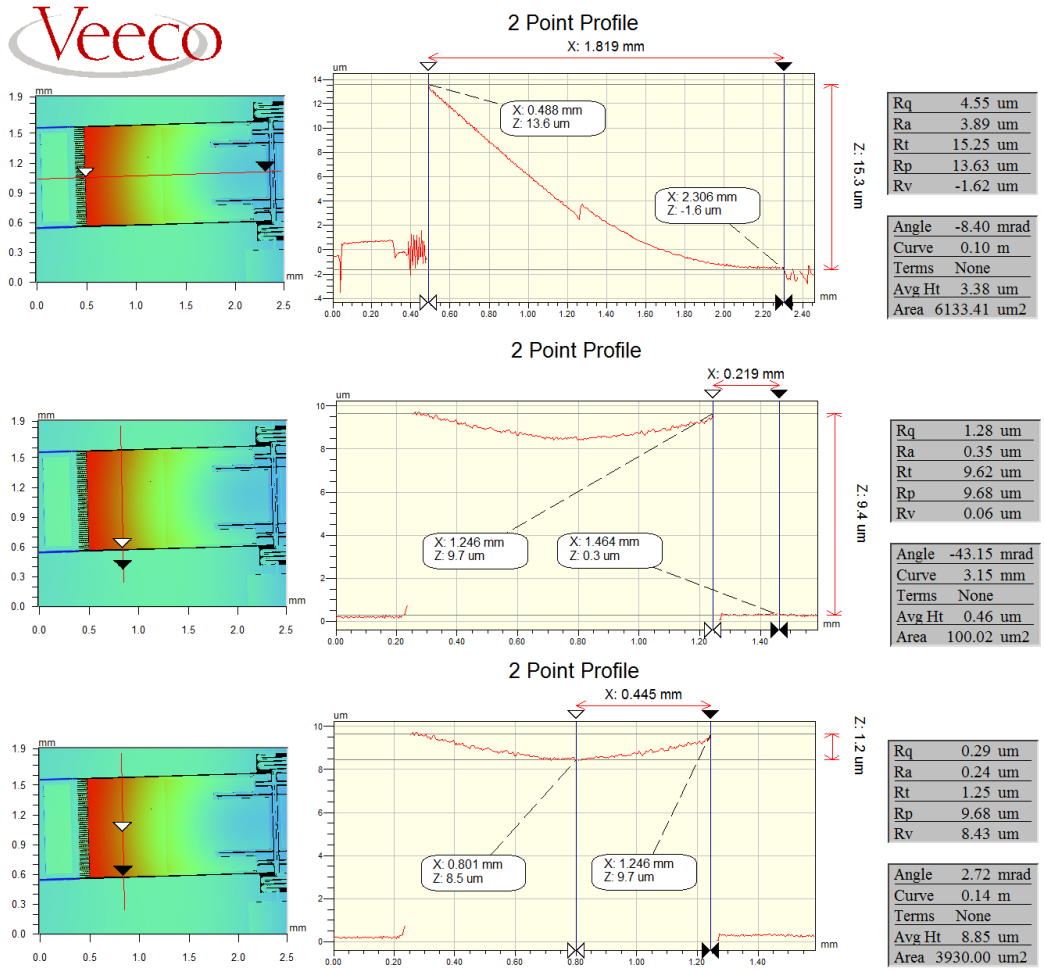

Fig. 5.10 The surface images of the larger diaphragm taken by optical profilometer and the scales of the surface curvature.

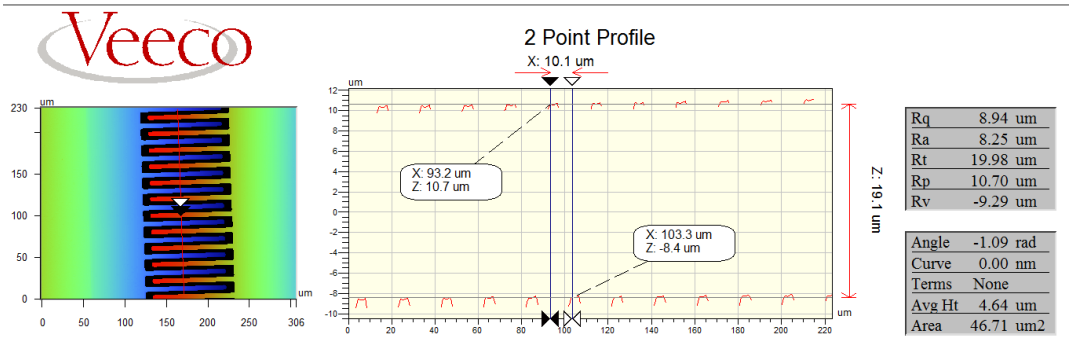

Fig. 5.11 The enlarged surface image of the comb fingers on the side of larger diaphragm, obtained using optical profilometer, and the scale of the vertical distance between the fixed and the moveable comb fingers

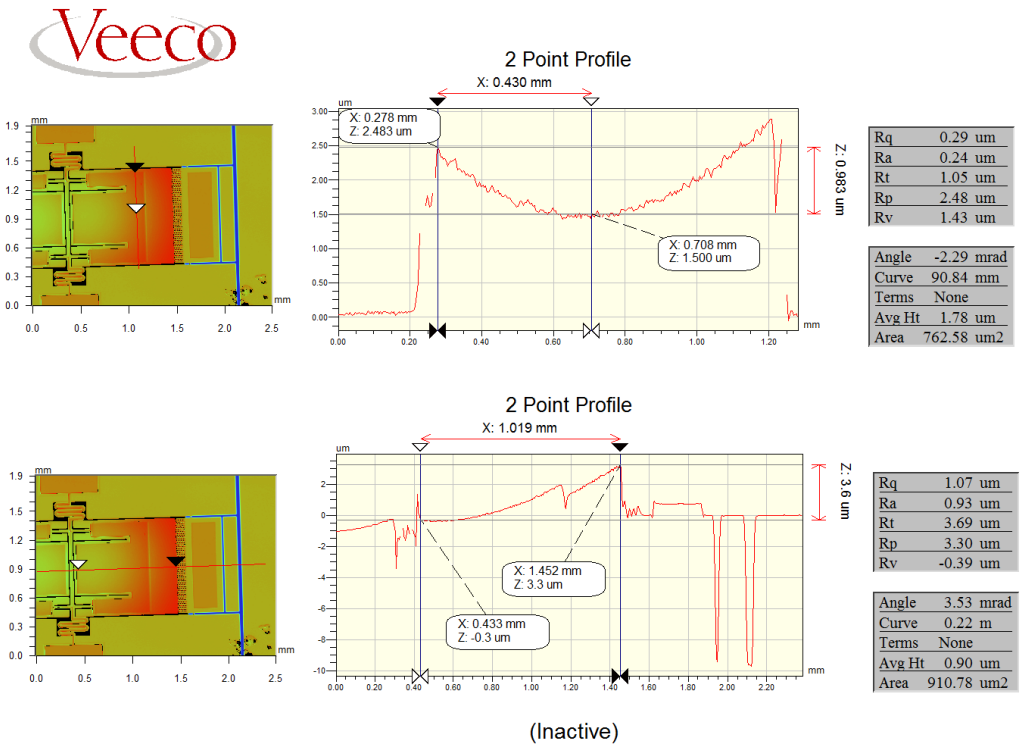

Fig. 5.12 The surface images of the smaller diaphragm taken by optical profilemeterl

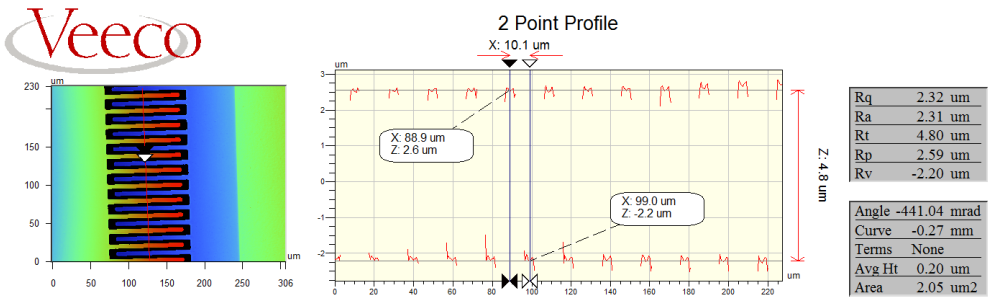

Fig. 5.13 The enlarged surface image of the comb fingers on the side of smaller diaphragm, obtained using optical profilometer, and the scale of the vertical distance between the fixed and the moveable comb fingers

5.4 Experimental setup

5.4.1 Readout circuit designed for piezoelectric sensing

Similar to the experimental setup designed for the piezoelectric sensing in earlier chapters, an instrumentation amplifier is used to amplify the small electrical signals generated by the AlN layer. Nevertheless, there is a difference from before, as the electrical outputs from the larger and the smaller diaphragms are connected to the non-inverting and inverting inputs of the amplifier, respectively. Meanwhile, the 'Ground' pad directly attached on the SCS layer is connected to the reference input of the amplifier, and further linked to the physical ground. Thus, the readout is the differential output from the two piezoelectric pads corresponding to the two diaphragms in different sizes. The schematic layout of the readout circuit for the piezoelectric sensing is shown in Fig. 5.14 (a). To minimize the parasitic capacitance and resistance in the readout circuit, both the die and amplifier are wire-bonded and

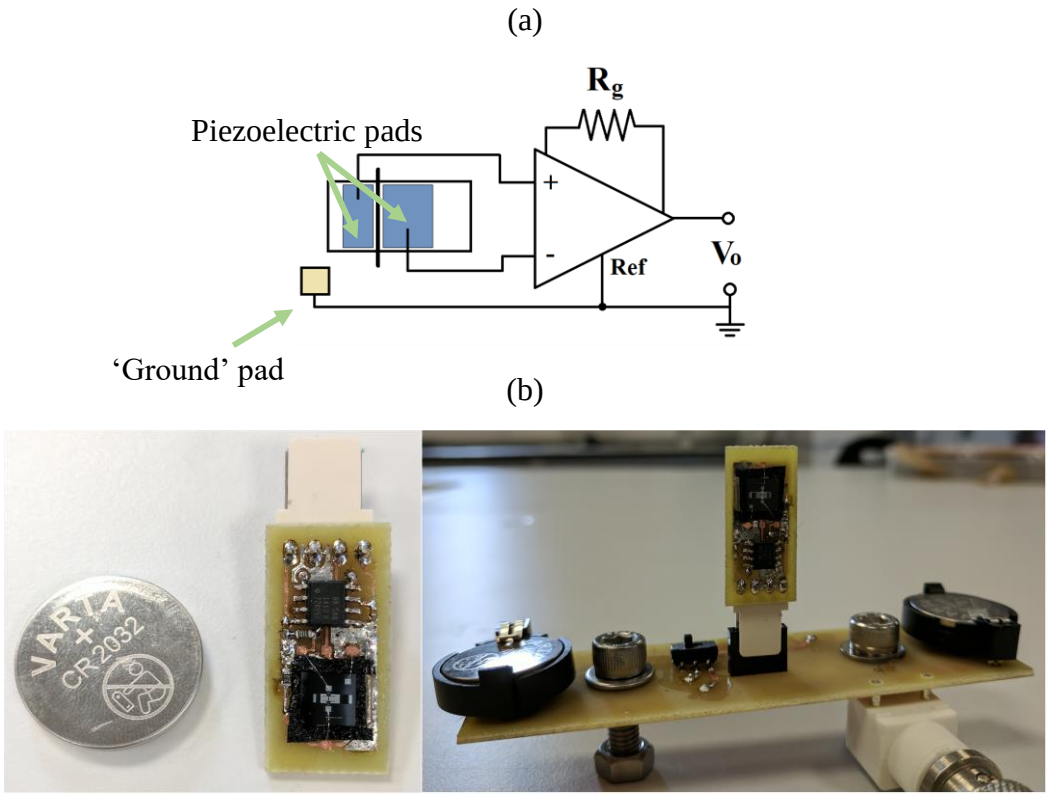

Fig. 5.14 (a) The readout circuit for piezoelectric sensing. The die is wire-bonded on frontal surface of the PCB whereas the readout circuit is soldered just beside.

soldered onto the same 1 cm × 2 cm printed circuit board that is laterally inserted onto a larger PCB built to provide mechanical support and the power supply. Furthermore, for these measurements, no filter is embedded into the circuit so that fewer operational amplifiers are included in the circuit in order to reduce the thermal noise. Then, the whole setup is mounted onto the rotary stage and followed by the lock-in amplifier and data acquisition system used previously. A commercial omni-directional MEMC microphone, InvenSense INMP411 [110], and a unidirectional MEMS microphone, Knowles TD24621 [111], are utilized as angular reference microphones for the directivity measurements using the same experimental setup. In terms of the instrumentation amplifier, to achieve a small package, fixed gained and low power amplifier the INA141 is chosen [112]. It has a very low offset voltage of about 50 µV at maximum and high common mode ratio (117 dB) and excellent noise control (~8nV/$\sqrt{Hz}$ at 1 kHz). The measured output voltage of the piezoelectric sensing is

$$V_{op}(\omega) = Gain \times \left(H_{vx1}(\omega) \times x_1(\omega) - H_{vx2}(\omega) \times x_2(\omega)\right), \qquad [5.23]$$

where H_{vx1} and H_{vx2} are the transfer functions between the open-circuit voltage at the output stage of the piezoelectric ports corresponding to the large diaphragm and the small diaphragm, respectively, and their deflection. The differential output cancels the common-mode noise from the two piezoelectric ports. The gain is set to 100.

5.4.2 Readout circuit designed for capacitive sensing

The variation of the capacitance is converted to a voltage output signal using a charge amplifier with a feedback capacitor $C_f = 1pF$ and a feedback resistor $R_f = 10M\Omega$ as shown in Fig. 5.15. The amplified signal is then filtered by a 4th order band-

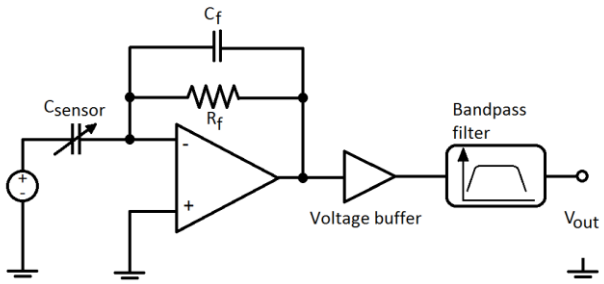

Fig. 5.15 Schematic of readout circuit for capacitive sensing

pass filter. As discussed before, only the comb fingers on the side of the smaller diaphragm are tested. The output voltage at the output stage of the charge amplifier for the capacitive sensing is

$$V_c(\omega) = \frac{V_{bias}}{C_f} \times \frac{dC_{sensor}(\omega)}{dx(\omega)}, \quad [5.24]$$

where V_{bias} is the bias voltage in the charge amplifier circuit (5V for this application, transferred from the voltage regulator) and $C_{sensor}(\omega)$ is the total capacitance of the comb fingers in the frequency domain, of which equation also refers to $x(\omega)$. Unlike the experimental setup of the piezoelectric sensing, the pre-amplifier circuit for the capacitive sensing is built on a strip PCB, as there is less impact from the parasitic capacitance of the connecting wires on the charge amplifier. Figure 4.16 shows the strip board used for measuring the electrical signals using the capacitive sensing method.

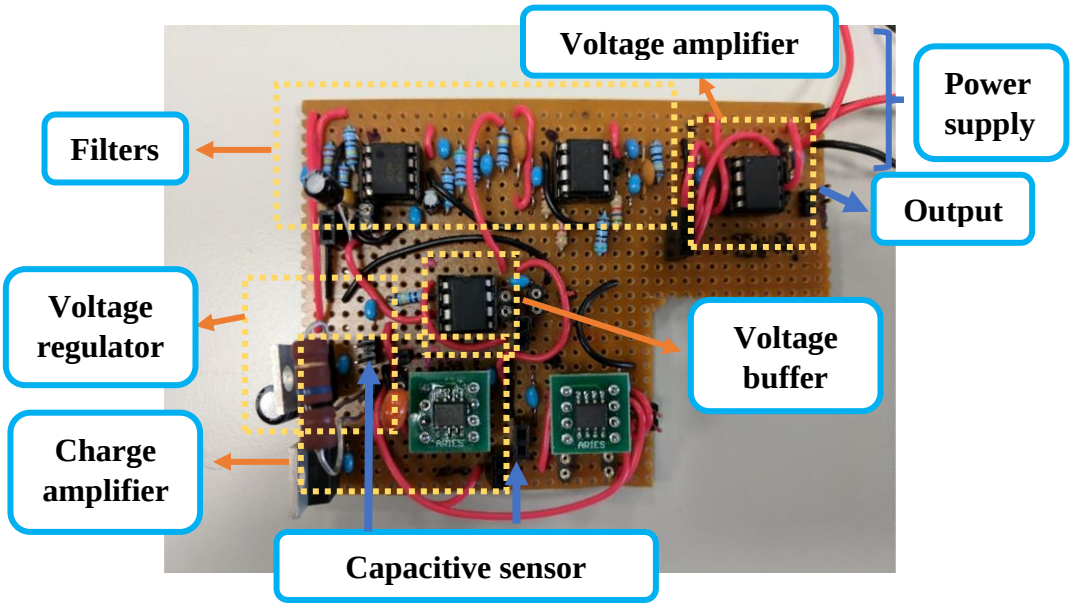

Fig. 5.16 The pre-amplifier strip broad for capacitive sensing

5.5 Experimental results

5.5.1 Mechanical response

The first two resonance frequencies measured by the LDV are about 464 Hz and 2275 Hz, which is only slightly lower than the results calculated from the lumped model and the COMSOL simulation. This is most likely due to the omission of the metal layers deposited on the piezoelectric material and the metal path on the bending

	The 1st mode (Hz)	The 2nd mode (Hz)
Analytical model	511	2600
COMSOL simulated	466	2532
LDV	464	2275

Table 5.2 Comparison between the evaluated eigenfrequenices and the values measured by LDV

(a) Rocking

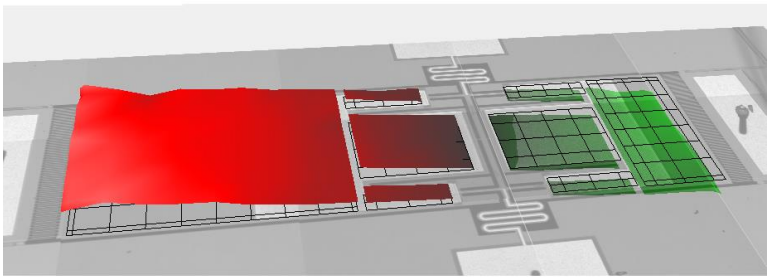

(b) Bending

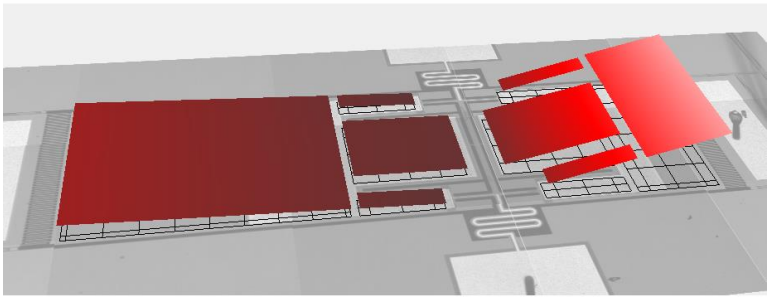

Fig. 5.17 The measured mode shapes below 3 kHz: (a) At rocking mode = 464 Hz; (b) At bending mode = 2275 Hz

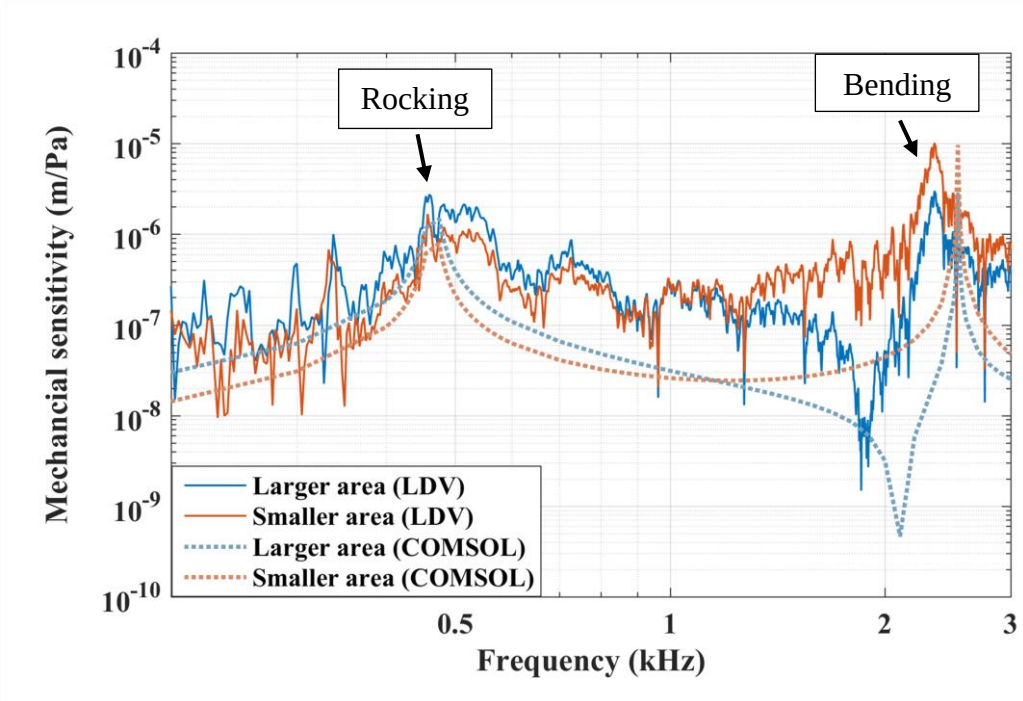

Fig. 5.18 Measured and simulated mechanical sensitivity of the prototypes below 3 kHz

bridges in the simulation. As shown in Fig. 5.17, the two diaphragms of the device vibrate out-of-plane at the 1st resonance frequency and then move in-plane at the 2nd resonance frequency, closely matching with expectations. There are two more twisting mode shapes below 15 kHz. However, due to the opposite vibration of the cantilevers, the charge generated by the piezoelectric material deposited on the cantilevers on the same side is counteracted. Table 5.2 compares the evaluated eigenfrequencies with the measured results. The maximum measured mechanical sensitivity is about 10 µm/Pa that appears on the smaller diaphragm at the 2nd resonance frequency while the mechanical sensitivity of the larger diaphragm reaches 1.9 µm/Pa at the 1st resonance frequency. Fig. 5.18 illustrates that the shape of the measured mechanical frequency response pattern matches the COMSOL simulation. Since the viscous damping due to the squeezed air in the comb fingers and the slits is neglected in the simulated model, the measured response has smaller Q factors and increases the frequency response between the two resonance frequencies. The mechanical-thermal noise is the main part of he noise occurring at the low frequencies.

5.5.2 Electrical response

Figure 5.19 gives the differential acoustic frequency spectrum of the device obtained through the piezoelectric sensors below 3 kHz. The measured open-circuit acoustic response through the piezoelectric units is about 3.6 mV/Pa at the 1st resonance frequency and then jumps to the maximum differential output response of 4.9 mV/Pa (i.e. -46 dB (V) ref. 94 dB (SPL)) when the device works at the 2nd resonance frequency. The Q factors at these two resonance frequencies are equal to 31 and 28, respectively. The experimental acoustical response measured by the piezoelectric sensing units strongly agrees with the COMSOL simulation. The noise spectral density at the input end of the preamplifier when using the piezoelectric sensing units is also measured with an Agilent 4365A spectrum analyser, which is plotted in Fig. 5.20. Due to the high input impedance of the instrumentation amplifier, two high value resistors (usually over 10 kΩ) are required to be connected between the inputs of the amplifier and ground in order to create bias current paths and prevent output saturation when measuring the differential signals, which adds a large amount of Johnson noise into the system. In addition, for a piezoelectric sensor, another

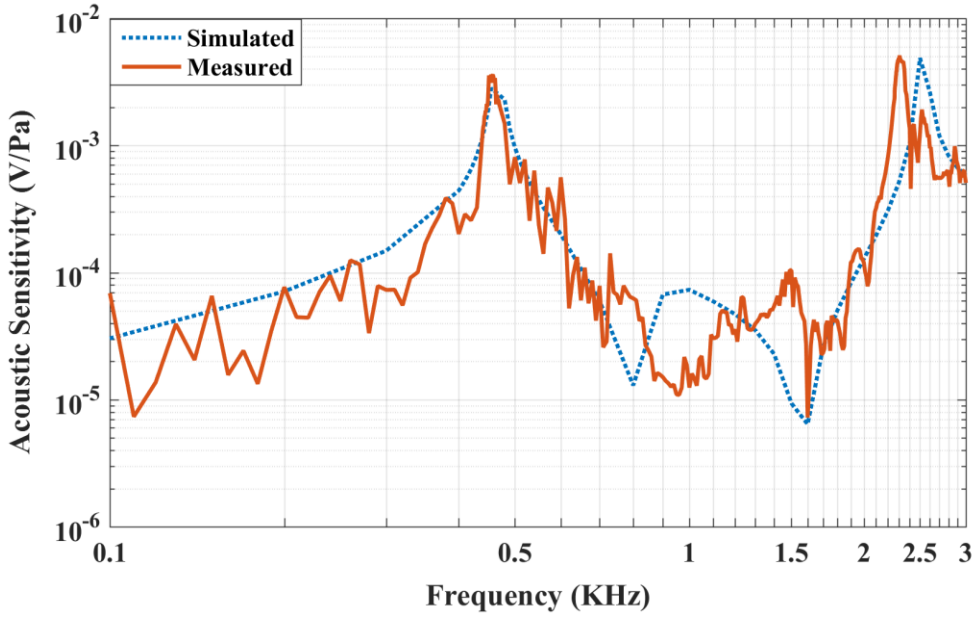

Fig. 5.19 The resonance mode shapes of the device and its differential acoustic frequency response sensed via piezoelectric material

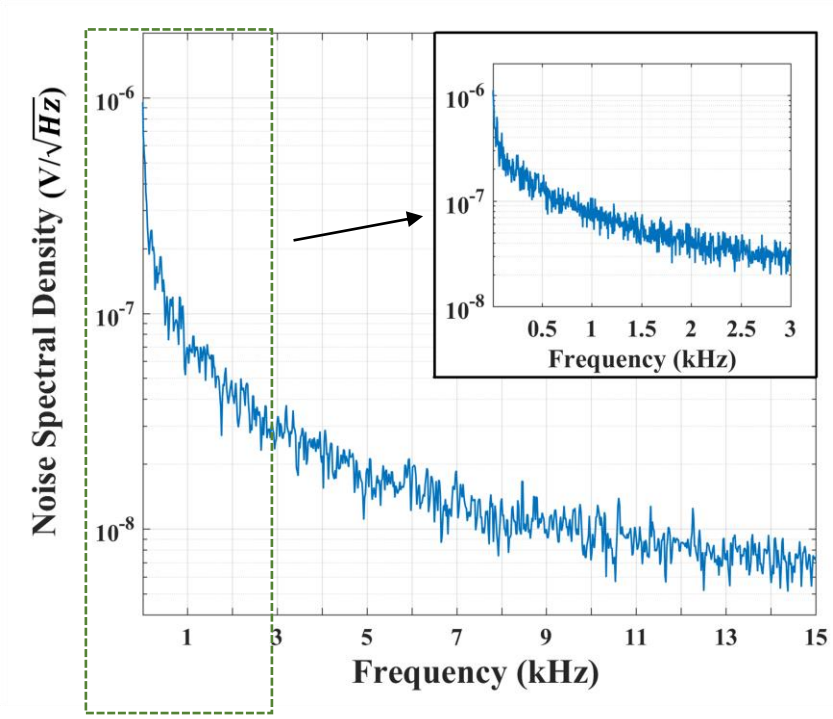

Fig. 5.20 The noise floor of the prototype when capturing signals from piezoelectric material, including the input voltage and current noise of the instrumentation preamplifier.

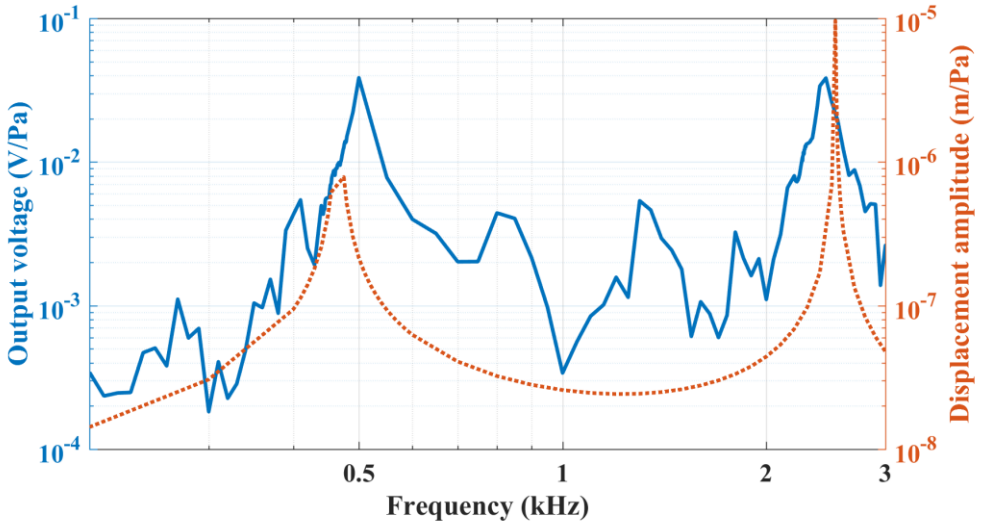

Fig. 5.21 The acoustic response measured via capacitive comb fingers, compared to the simulated mechanical response of the small diaphragm of the device

dominant noise source stems from the dielectric loss of the piezoelectric material [113], [114] which is controlled by the fabrication process. The noise around 500 Hz and 2.3 kHz is about 0.4 $\mu V/\sqrt{Hz}$ and 0.025 $\mu V/\sqrt{Hz}$, respectively, whereas the input voltage noise of the preamplifier is about 8 $nV/\sqrt{Hz}$ from 100 Hz according to the datasheet. The average noise density of the prototype below 3 kHz is about 0.087 $\mu V/\sqrt{Hz}$. Therefore, the minimum detectable sound pressure around the 1st resonance frequency is approximately 14.81 dB (SPL) and this value reduces to – 12.04 dB (SPL) around the 2nd resonance frequency. The rustle of leaves is about 15 dB (SPL).

When acquiring an electrical signal from the capacitive port sensing the deflection of the small diaphragm, an acoustic response that is similar to the acoustic response captured from the piezoelectric ports is obtained as shown in Fig. 5.21. The acoustic response at both the 1st and the 2nd resonance frequencies is approximately 38 mV/Pa (i.e. -28.4 dB (V) ref. 94 dB (SPL)). Compared to the simulated mechanical response of the diaphragm, the trend of the acoustic response spectrum is roughly matched with the simulation. As the charge amplifier has a built-in high-pass filter, this measured acoustic response takes amplification into account. The capacitive sensing is an auxiliary sensing method, and only the deformation of the small diaphragm could be detected at this stage, thus this aspect will be investigated further in the future. Despite that the results demonstrated in Fig. 5.3 do not show that the capacitive sensing unit linked to the smaller diaphragm brings a much higher response at the rocking mode than at the bending mode, it can be derived that a differential output of capacitive sensing could provide higher response at the lower resonance frequency through Eq. [5.13] and [4.14].

5.5.3 Characterization of directionality

Figure 5.22 (a) shows the directional polar patterns of this device in the plane that is normal to the diaphragms, obtained through the piezoelectric ports at the resonance frequencies and their nearby frequencies. At the resonance frequencies, the measured polar patterns are close to typical figure-8 patterns as expected from the analytical model where the diaphragm transfers the greatest portion of sound energy into mechanical deflection when sound waves are vertically incident onto its front surface. For driving frequencies off the main resonance below 3 kHz, the device gives

a slightly imbalanced response between the front and the back but still delivers directional polar patterns. Comparing the directional polar patterns of the device with the polar patterns of the omnidirectional microphone INMP411, it is clear that the device can be regarded as a bi-directional microphone at least from 400 Hz to 3000 Hz. Meanwhile, comparing the polar patterns of unidirectional microphone TD24621 with the polar patterns of the device at its resonance, the *Ormia*-inspired microphone has much clearer directional behaviour than the commercial reference in the low frequency range as shown in Figure 5.22 (b).

(a)

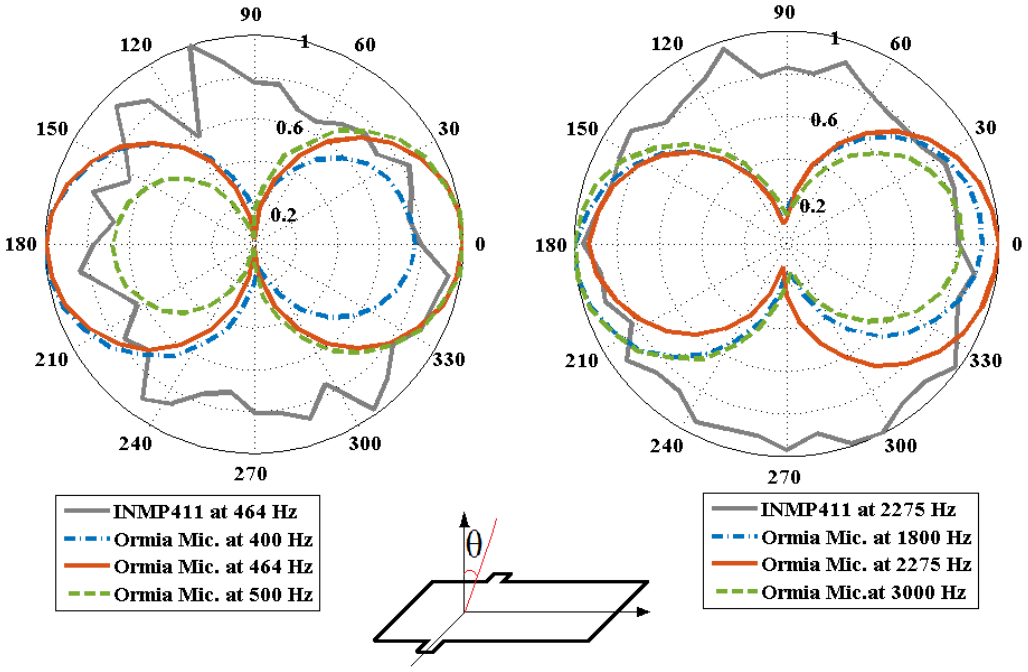

(b)

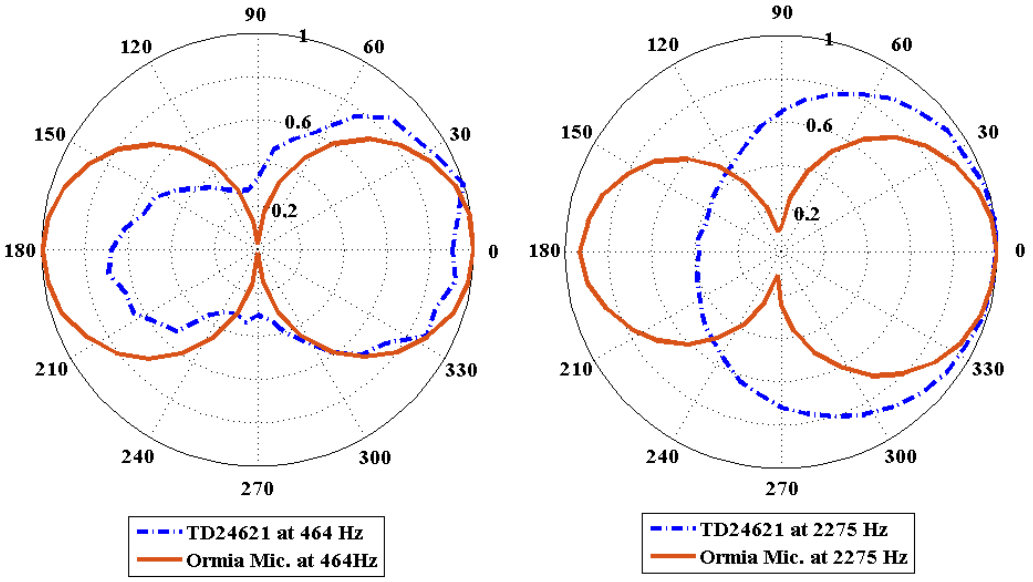

Fig. 5.22 Directional polar patterns of (a) Omni-directional MEMS microphone INMP411 and Ormia-inspired microphone at the resonance frequencies (464 Hz and 2275 Hz) and their nearby frequencies (400 Hz, 500 Hz, 1800 Hz and 3000 Hz); (b) Unidirectional MEMS microphone TD24621 and Ormia-inspired microphone at the resonance frequencies

5.6 Discussion and conclusion

For patients with low frequency impairment, most of them use hearing aids that are initially designed for high frequency hearing loss but programmed to amplify the low frequency sound by audiologists before use. However, merely amplifying the low frequencies can also increase the noise level presented. Therefore, it is worthwhile to develop a low-noise microphone that can be used particularly by people with reverse hearing loss. Previously, R. Miles et al. [115] reported a capacitive sensing *Ormia*-inspired MEMS microphone that has a 1st resonance mode at around 400 Hz. However, it has a central torsional bar to produce the low resonance frequency that has a T-shape cross-section view. Moreover, each diaphragm of the device has crossed beams underneath to increase the stiffness of the diaphragms and their mass. Such complex structural details are unlikely to be implemented in a high-yield manufacturing service. The device presented here shows an alternative solution to keep the resonance frequency at a low level, retain the directional function and reduce the complexity of the fabrication process in the meantime. Its dual-band operation below 3 kHz improves the average acoustic response in this frequency range, especially below 500 Hz where the converted electrical signals can easily be covered by 1/f noise. Combined with a carefully designed dual-band band-pass filter, the final output acoustic response could be smoothed if needed. The introduction of piezoelectric sensing also provides an advantage to applications in critical environments (e.g. high temperature, high humidity).

The device introduced in this chapter is the first fabricated design for this concept of low frequency operation, thus future work is required. The first task would be to further increase the SNR for the piezoelectric sensing, especially at the lower resonance frequency. Generally, the preamplifier dominates the noise of a piezoelectric sensor, and the fabrication process determines the self-noise of the device. If using the same fabrication process, one of the approaches to improving SNR is to add an extra bending structure covered by piezoelectric material to increase the charge created by the strain variation at the 1st resonance frequency. This kind of alternative should be taken without increasing the entire mass too much or affecting the torsional stiffness of the system. There are recent publications [116], [117] that show examples

of this solution. The modification of the structure and the distribution of piezoelectric material will also be beneficial to reduce the curvature of the larger diaphragm and so increase the initial capacitance between the comb fingers. A differential readout could then be applied to capture electric signals from both sets of capacitive sensing units to drastically increase the acoustic response around 500 Hz and reduce the common mode noise when using this sensing method. The further combination of these two sensing mechanisms should also be studied in the future, in order to expand the functionalities of the device design. For example, users may amplify signals either in low frequency range or in the middle frequency range by simply summing or subtracting the outputs from two kind of sensing ports. Last but not least, a metal-coated package could be built with well-designed interior sound path for pressure gradient and an RF shield functionality.

Chapter 6

Summary and Future Work

6.1 Summary

The design, model analysis and characterization of different types of MEMS directional microphone inspired by the parasitoid fly *Ormia ochracea* are presented in this thesis. Fortunately, the fundamental analysis of *Ormia*'s hearing mechanism and preliminary designs based on these principles have already been published thanks to the great efforts from pioneers. However, no single device strikes a balance between aspects of wide broad band response, high sensitivity at low frequency range and comparably low-cost fabrication. The research work presented is a complete process to give feasible designs to ameliorate *Ormia*-inspired MEMS microphones based on these mentioned shortcomings.

The first part of this thesis covers the design of a novel *Ormia*-inspired microphone model that has high mechanical response against sound pressure in multiple bands below 15 kHz. The novel microphone is composed of two concentric diaphragms – a circular diaphragm and a square frame (i.e. a square diaphragm but with a circular hole to leave the space for the circular diaphragm), rotating along the same beam with a rectangular cross-section, of which the ends are fixed to the substrate that is deeply etched from the back thus releasing the vibrational diaphragms. The device is built by SCS and fabricated using a multiple user foundry service supplied by a microfabrication company. This first attempt doubles the number of resonance frequencies which are all set to below the upper limit of the frequencies of interest. The increase in the number of resonance frequencies enhances the overall frequency response and adds more efficient working bands to the *Ormia*-inspired microphone. In addition, the approach establishes the process and standards of developing and characterizing this kind of microphone, including building up an analytical model for

the dual-diaphragms design, verifying its response via COMSOL simulation, and measuring both the surface properties and mechanical performance of the fabricated prototype. Despite that the new device has more resonance frequencies, it still retains mode shapes that are similar to the previous designs but with duplication, i.e. it has two rocking modes and two bending modes, showing cross distribution below 15 kHz. At the rocking modes, the device is directional with sine function, the same as the directional behavior of *Ormia*'s ears at its resonance rocking mode. But, different from the omnidirectional response shown at the resonance bending mode of *Ormia*'s ear, the new design is directional with a cosine function instead. Since the mass of the inner circular diaphragm and the outer frame are almost identical, its 2nd and the 3rd resonance frequencies are close, and their resonance response are overlapped. Therefore, the frequency response between the 2nd and the 3rd resonance frequencies is neither directional with sine nor cosine function, not meeting the basic requirement of a directional microphone. This design defect was the motivation for developing the next generation device.

The second part of this thesis includes the development of improved multiple band operational MEMS microphones. Two types of improved models are presented – a model with symmetric geometry (i.e. the torsional beam is placed in the middle of the entire structure) and a model with asymmetric geometry (i.e. the torsional beam is biased to the centre of the structure for a certain distance). The symmetric model is a shape-change design of the first-generation device, which possesses clearly separated 2nd and the 3rd resonance frequencies and higher maximum mechanical sensitivity than the first-generation model but smaller dimensions. The asymmetric model has approximative mass and values of resonance frequencies, but the directionality is the major difference between the asymmetric and the symmetric models that brings the asymmetric device closer to an ideal directional microphone having high sensitivity and uniform directionality simultaneously. Additionally, piezoelectric AlN sensing parts are embedded into the fabricated devices and turn them into truly operating sensors transferring sound energy to electric signals by a standalone matched readout circuit. The COMSOL simulation shows that the asymmetric microphone has an ideal figure-8 directional pattern at all four resonances, while the experimental results show that the manufactured device performs as a hyper-cardioid microphone at the 1st, the

2^{nd}, and the 4^{th} resonance. The error is mainly caused by the sound reflection and diffraction in the hole of the PCB that potentially reduces the sound pressure on the rear surface of the device.

All the above microphones are designed for application in hearing aids for high-frequency impaired people, but they are unsuitable for low frequency impairment people who are sensitive to the sound or totally lose hearing capability below 2 kHz. In fact, most hearing aids are designed for high frequency hearing loss, which leaves limited choices for patients having low frequency impairment. Therefore, whilst an improvement on multi-band operational devices that solves the problem from the first design, it creates a new issue that needs resolving if applying them on the hearing aids for low hearing – the asymmetric design does not have a low frequency response below 2 kHz where most vocal information locates.

Consequently, the final part of this thesis presents an *Ormia*-inspired MEMS microphone performing at the low frequency range, particularly strengthening the electric response below 2 kHz. The presented dual-sensing device is designed for this particular purpose, and two mechanisms are used to lower its resonance frequencies. First of all, the simple rectangular torsional beam is replaced by serpentine beams that reduces the torsional stiffness hence decreasing the 1^{st} resonance frequency. In addition, the introduction of two thin beams that connect the diaphragms to the torsional bar reduces the bending stiffness so that the 2^{nd} resonance frequency remains at a value in the low kHz range. Both modifications also allow the microphone to be built using a cost-effective multi-user foundry service providing high yield. Moreover, by creating a lateral shift of the position of the torsional beam in the device geometry, the presented device was predicted to retain the similar bi-directional acoustic response at the two fundamental resonance frequencies. The experimental results agree with the theoretically predicted behaviour and reveal that the presented device also achieves a bi-directional acoustic response in the frequency bands off the main resonance frequencies below 3 kHz, which improves the acoustic response especially below 500 Hz where the signal can easily be covered by $1/f$ noise. Finally, the acoustic responses measured through both the piezoelectric sensing and capacitive sensing units of the initial prototype are closely matched with the theoretical predictions.

6.2 Future Work

There is much more that can be implemented in the continuation of the project. For both the dual-plate multi-band (DPMB) operational microphone designs and the low frequency (LF) operational design, increasing the SNR for piezoelectric sensing and improving the capacitive sensing are two main tasks for the future. In terms of getting higher SNR for piezoelectric sensing, these will be achieved by adjusting the structure to increase the strain of the sensing area and modifying the distribution of the piezoelectric material on the diaphragms to reduce the total mass and increase the electrical sensitivity but not raise the resonance frequencies. The modification of piezoelectric material distribution will also be beneficial to reduce curvature of the diaphragms. Moreover, for the low frequency operational device, the elevation of larger diaphragm also adds the overlapped area between the comb fingers so that increases the initial capacitance. Since capacitive sensing may also be integrated into the future designs, not only LF operational devices but also the DPMB operational devices, the air damping between comb fingers and the any other slits is another topic of interest to be investigated for decreasing the mechanical-thermal noise. There are other possible modifications and improvements to do more than decreasing the SNR. All the resonance frequencies can be further reduced, specially the 1st resonance frequency. Further types of torsional hinge that drives the value of the 1st resonance frequency can be studied and compared. The overlapped response between the resonance could be continuously increased. One of the methods to realize this could be decreasing the stiffness of bending bridges between the diaphragms and the torsional hinge such that the resonance frequencies of the bending mode(s) are decreased.

Except for the adjusting the geometry details of the designs, a novel signal processing framework could be investigated. This includes new custom CMOS preamplifier circuits to further reduce noise for both piezoelectric and capacitive sensing units and a new DSP circuits to get the benefits from the multiple outputs and dual-sensing function, such as creating different acoustic frequency spectrum patterns for various usage purposes via simply summing or subtracting the outputs. The custom CMOS preamplifier would be individually packed with the microphone in a custom

3D printed housing which carefully considers the influence of interior sound interference and diffraction as well as RF shielding. Furthermore, any new designs and amplification-specified circuits should firstly conform to industry standards for hearing aids.

Finally, the applications of *Ormia*-inspired MEMS microphones can also be expanded beyond hearing aids. Currently, only the performance of an individual device has been investigated. In the future, an array of three or more *Ormia*-inspired MEMS microphone could also be studied for contributions to applications such as sound distance detection and spatial sound map drawing via combining with acoustic vector sensors.

References

[1] C. Shera, J. Rosowski, K. Stevens, and L. Braida, “Lecture note 1: the quantification of sound and the wave equation,” in *Acoustic of speech and hearing*, MIT Open Courseware, 2009.

[2] R. A. Rayburn and J. Eargle, *Eargle’s the microphone book,* 3rd ed. MA: Focal Press, 2012.

[3] COMSOL Multiphysics, “Acoustics module user’s guide,” CM020201, 2012.

[4] C. Shera, J. Rosowski, K. StevenS, and L. Braida, “Lecture note 3: spherical waves: near & far field, radiation impedance, and simple sources,” in *Acoustic of Speech and Hearing*, MIT Open Courseware, 2009.

[5] H. Robjohns, “A brief history of microphones,” in *Microphone Data,* C. Woolf and R. Streicher, Eds. Cambridge: Human-Computer Interface Ltd., 2001.

[6] G. M. Sessler and J. E. West, “Electroacoustic transducer,” US3118022A, 14-Jan-1964.

[7] E. C. Wente and A. L. Thuras, “Moving-coil telephone receivers and microphones,” *J. Acoust. Soc. Am.*, vol. 3, no. 1A, pp. 44–55, Jun. 1931.

[8] H. F. Olson, “Mass controlled electrodynamic microphones: the ribbon microphone,” *J. Acoust. Soc. Am.*, vol. 3, no. 1A, pp. 56–68, Jun. 1931.

[9] University of Salford, “Microphones,” 2018. [Online]. Available: http://www.acoustics.salford.ac.uk/acoustics_info/microphones/?content=index. [Accessed: 23-Aug-2018].

[10] N. Bilaniuk, “Optical microphone transduction techniques,” *Appl. Acoust.*, vol. 50, no. 1, pp. 35–63, Jan. 1997.

[11] A. Paritsky and A. Kots, “Sensor and a method for measuring distances to, and/or physical properties of, a medium,” US5771091A, 23-Jun-1998.

[12] G. W. Elko and K. P. Harney, “A history of consumer microphones: the electret condenser microphone meets Micro-Electro-Mechanical-Systems,” *Acoustics Today*, pp. 4–13, Apr-2009.

[13] H. C. Nathanson, W. E. Newell, R. A. Wickstrom, and J. R. Davis, “The resonant gate transistor,” *IEEE Trans. Electron Devices*, vol. 14, no. 3, pp. 117–133, Mar. 1967.

[14] Samaun, K. D. Wise, and J. B. Angell, “An IC piezoresistive pressure sensor for biomedical instrumentation,” *IEEE Trans. Biomed. Eng.*, vol. BME-20, no. 2, pp. 101–109, Mar. 1973.

[15] K. E. Petersen, “Silicon as a Mechanical Material,” *Proc. IEEE*, vol. 70, no. 5, pp. 420–457, 1982.

[16] M. Royer, J. O. Holmen, M. A. Wurm, O. S. Aadland, and M. Glenn, “ZnO on Si integrated acoustic sensor,” *Sensors and Actuators*, vol. 4, no. 1983, pp. 357–362, Jan. 1983.

[17] C. Liu, *Foundation of MEMS*, 2nd ed. Harlow: Pearson Education M. U. A., 2012.

[18] D. Hohm, “Subminiatur-silizium-kondensatormikrofon, fortschritte der akustik,” in *DAGA ’85*, 1985, pp. 847–850.

[19] P. V. Murphy and K. Hubschi, “Electret transducing,” US4764690A, 16-Jun-1986.

[20] J. A. Voorthuyzen, P. Bergveld, and A. J. Sprenkels, “Semiconductor-based electret sensors for sound and pressure,” *IEEE Trans. Electr. Insul.*, vol. 24, no. 2, pp. 267–276, Apr. 1989.

[21] J. Bergqvist and F. Rudolf, “A new condenser microphone in silicon,” *Sensors Actuators A Phys.*, vol. 21, no. 1–3, pp. 123–125, Feb. 1990.

[22] W. Kühnel and G. Hess, “A silicon condenser microphone with structured back plate and silicon nitride membrane,” *Sensors Actuators A Phys.*, vol. 30, no. 3, pp. 251–258, Feb. 1992.

[23] P. R. Scheeper, B. Nordstrand, J. O. Gullov, Bin Liu, T. Clausen, L. Midjord, and T. Storgaard-Larsen, “A new measurement microphone based on MEMS technology,” *J. Microelectromechanical Syst.*, vol. 12, no. 6, pp. 880–891, Dec. 2003.

[24] D. T. Martin, J. Liu, K. Kadirvel, R. M. Fox, M. Sheplak, and T. Nishida, “A Micromachined Dual-Backplate Capacitive Microphone for Aeroacoustic Measurements,” *J. Microelectromechanical Syst.*, vol. 16, no. 6, pp. 1289–1302, Dec. 2007.

[25] Eun Sok Kim and R. S. Muller, “IC-processed piezoelectric microphone,” *IEEE Electron Device Lett.*, vol. 8, no. 10, pp. 467–468, Oct. 1987.

[26] R. P. Ried, D. M. Hong, and R. S. Muller, “Piezoelectric microphone with on-chip CMOS circuits,” *J. Microelectromechanical Syst.*, vol. 2, no. 3, pp. 111–120, 1993.

[27] S. S. Lee, R. P. Ried, and R. M. White, “Piezoelectric cantilever microphone and microspeaker,” *J. Microelectromechanical Syst.*, vol. 5, no. 4, pp. 238–242, 1996.

[28] H. J. Zhao, T. L. Ren, J. S. Liu, L. T. Liu, and Z. J. Li, “A novel structure for PZT-based piezoelectric microphone,” in *2003 Nanotechnology Conference and Trade show*, 2003, pp. 356–359.

[29] M. D. Williams, B. A. Griffin, T. N. Reagan, J. R. Underbrink, and M. Sheplak, “An AlN MEMS piezoelectric microphone for aeroacoustic applications,” *J. Microelectromechanical Syst.*, vol. 21, no. 2, pp. 270–283, Jan. 2012.

[30] EE Times, “MEMS microphone market expected to hit $1B in 2017,” 2017. [Online]. Available: https://www.eetimes.com/document.asp?doc_id=1331913. [Accessed: 23-Aug-2018].

[31] HIS Markit, “Apple products are driving market growth for MEMS microphones, IHS Says,” 2016. [Online]. Available: https://news.ihsmarkit.com/press-release/apple-products-are-driving-market-growth-mems-microphones-ihs-says. [Accessed: 23-Aug-2018].

[32] S. C. Thompson, “Tutorial on microphone technologies for directional hearing aids,” *Hear. J.*, vol. 56, no. 11, pp. 14–21, Nov. 2003.

[33] L. E. Kinsler, *Fundamentals of acoustics*, 4th ed. New York: John Wiley & Sons, 2000.

[34] D. Robert, J. Amoroso, and R. R. Hoy, “The evolutionary convergence of hearing in a parasitoid fly Ormia ochracea,” *Science (80-.).*, vol. 258, no. 5085, pp. 1135–1137, Nov. 1992.

[35] S. A. Adamo, D. Robert, and R. R. Hoy, “Effects of a tachinid parasitoid, Ormia ochracea, on the behaviour and reproduction of its male and female field cricket hosts (Gryllus spp),” *J. Insect Physiol.*, vol. 41, no. 3, pp. 269–277, Mar. 1995.

[36] P. Muller and D. Robert, “A shot in the dark: the silent quest of a free-flying phonotactic fly,” *J. Exp. Biol.*, vol. 204, no. 6, pp. 1039–1052, 2001.

[37] D. Robert, R. N. Miles, and R. R. Hoy, “Directional hearing by mechanical coupling in the parasitoid fly Ormia ochracea,” *J. Comp. Physiol. A*, vol. 179, no. 1, pp. 29–44, Jul. 1996.

[38] D. Robert, R. N. Miles, and R. R. Hoy, “Tympanal mechanics in the parasitoid fly Ormia ochracea ： intertympanal coupling during mechanical vibration,” *J. Comp. Physiol. A Sensory, Neural, Behav. Physiol.*, vol. 183, no. 4, pp. 443–452, Oct. 1998.

[39] R. N. Miles, D. Robert, and R. R. Hoy, “Mechanically coupled ears for directional hearing in the parasitoid fly Ormia ochracea.,” *J. Acoust. Soc. Am.*, vol. 98, no. 6, pp. 3059–70, Dec. 1995.

[40] T. J. Walker and S. A. Wineriter, “Hosts of a Phonotactic Parasitoid and Levels of Parasitism (Diptera: Tachinidae: Ormia ochracea),” *Florida Entomol.*, vol. 74, no. 4, pp. 554–559, Dec. 1991.

[41] S. A. Adamo, D. Robert, J. Perez, and R. R. Hoy, “The response of an insect parasitoid, Ormia ochracea (Tachinidae), to the uncertainty of larval success during infestation,” *Behav. Ecol. Sociobiol.*, vol. 36, no. 2, pp. 111–118, Feb. 1995.

[42] R. S. Edgecomb, D. Robert, M. P. Read, and R. R. Hoy, “The tympanal hearing organ of a fly: phylogenetic analysis of its morphological origins,” *Cell Tissue Res.*, vol. 282, no. 2, pp. 251–268, Nov. 1995.

[43] H. J. Liu, M. Yu, L. Currano, and D. Gee, “Fly-ear inspired miniature directional microphones: modeling and experimental study,” in *ASME 2009 International Engineering Congress*, 2009, pp. 1–7.

[44] H. Liu, Z. Chen, and M. Yu, “Biology-inspired acoustic sensors for sound source localization,” in *SPIE Sensors and Smart Structures Technologies for Civil, Mechanical, and Aerospace Systems*, 2008, vol. 6932, p. 69322Y.

[45] M. Yu, “Fly Ear Inspired Miniature Acoustic Sensors for Detection and Localization,” 2011.

[46] D. Chatzopoulos, “Modeling the Performance of MEMS Based Directional Microphones,” NAVAL Postguraduate School, 2008.

[47] S. S. Rao, *Mechanical Vibrations*, 5th ed. Jurong: Pearson Education South Asia Pte Ltd., 2011.

[48] L. Tan, R. N. Miles, S. Binghamton, M. G. Weinstein, R. A. Miller, C. Stark, Q. Su, and W. Cui, “Response of a biologically inspired MEMS differential microphone diaphragm,” in *SPIE AeroSense*, 2002, pp. 1–8.

[49] R. N. Miles, S. Sundermurthy, C. Gibbons, R. Hoy, and D. Robert, “Differential microphone,” US6788796B1, 07-Sep-2004.

[50] R. N. Miles and R. R. Hoy, “The development of a biologically-inspired directional microphone for hearing aids,” *Audiol. Neurotol.*, vol. 11, no. 2, pp. 86–94, 2006.

[51] W. Cui, “Analysis, design and fabrication of a novel silicon microphone,” State Universtiy of New York at Binghamton, 2004.

[52] W. Cui, R. N. Miles, and Q. Su, “The design, fabrication and characterization of a novel miniature silicon microphone diaphragm,” *TechConnect Briefs*, vol. 1, pp. 432–435, May 2009.

[53] W. Cui, R. N. Miles, and Q. Su, “A Robust miniature silicon microphone diaphragm,” *Sensors Transducers J.*, vol. 7, no. Special Issue, pp. 63–77, 2009.

[54] J. I. A. Gao, “Structure analysis and characterization of a biomimetic silicon microphone,” State University of Yew York at Binghamton, 2005.

[55] J. Gao, R. N. Miles, and W. Cui, “Stress Analysis of a Novel MEMS Microphone Chip Using Finite Element Analysis,” *Electron. Photonic Packag. Electr. Syst. Des. Photonics, Nanotechnol.*, vol. 2005, pp. 259–267, 2005.

[56] R. N. Miles, C. Gibbons, J. Gao, K. Yoo, Q. Su, and W. Cui, “A silicon nitride microphone diaphragm inspired by the ears of the parasitoid fly *Ormia ochracea*,” *J. Acoust. Soc. Am.*, vol. 110, no. 5, pp. 2645–2645, Nov. 2001.

[57] C. Gibbons and R. N. Miles, “Design of a biomimetic directional microphone diaphragm,” in *International Mechanical Engineering Congress and Exposition*, 2000, pp. 1–7.

[58] Weili Cui, B. Bicen, N. Hall, S. A. Jones, F. L. Degertekin, and R. N. Miles, "Optical sensing in a directional MEMS microphone inspired by the ears of the parasitoid Fly, Ormia Ochracea," in *19th IEEE International Conference on Micro Electro Mechanical Systems*, 2006, pp. 614–617.

[59] R. N. Miles and F. L. Degertekin, "Optical sensing in a directional MEMS microphone," US7826629B2, 02-Nov-2010.

[60] R. N. Miles, Q. Su, W. Cui, M. Shetye, F. L. Degertekin, B. Bicen, C. Garcia, S. Jones, and N. Hall, "A low-noise differential microphone inspired by the ears of the parasitoid fly *Ormia ochracea*," *J. Acoust. Soc. Am.*, vol. 125, no. 4, pp. 2013–2026, 2009.

[61] B. Bicen, S. Jolly, K. Jeelani, C. T. Garcia, N. A. Hall, F. L. Degertekin, Q. Su, W. Cui, and R. N. Miles, "Integrated optical displacement detection and electrostatics actuation for directional optical microphones with micromachined biomimetic diaphragms," *IEEE Sens. J.*, vol. 9, no. 12, pp. 1933–1941, Oct. 2009.

[62] M. K. Jeelani, "Integration and charecterization of micromachined optical microphones," Georgia Insititute of Technology, 2009.

[63] D. H. Weili Cui, Ronald N. Miles, Quang Su, "A bio-inspired miniature comb sense differential microphone diaphram," in *ASME Micro and Nano Systems*, 2010, vol. 10, pp. 143–148.

[64] R. N. Miles, W. Cui, Q. T. Su, and D. Homentcovschi, "A MEMS Low-Noise Sound Pressure Gradient Microphone With Capacitive Sensing," *J. Microelectromechanical Syst.*, vol. 24, no. 1, pp. 241–248, Jun. 2014.

[65] M. L. Kuntzman, N. N. Hewa-Kasakarage, A. Rocha, D. Kim, and N. A. Hall, "Micromachined in-plane pressure-gradient piezoelectric microphones," *IEEE Sens. J.*, vol. 15, no. 3, pp. 1347–1357, 2015.

[66] M. L. Kuntzman and N. A. Hall, "Sound source localization inspired by the ears of the Ormia ochracea," *Appl. Phys. Lett.*, vol. 105, no. 3, p. 033701, 2014.

[67] M. L. Kuntzman, D. Kim, N. N. Hewa-Kasakarage, K. D. Kirk, and N. A. Hall, "Network modeling of multiple-port, multiple-vibration-mode transducers and resonators," *Sensors Actuators A Phys.*, vol. 201, pp. 93–100, Oct. 2013.

[68] D. Kim, M. L. Kuntzman, and N. A. Hall, "A transmission-line model of back-cavity dynamics for in-plane pressure-differential microphones.," *J. Acoust. Soc. Am.*, vol. 136, no. 5, pp. 2544–2553, Nov. 2014.

[69] M. L. Kuntzman, "Micromachined in-plane acoustic pressure gradient sensors," The University of Texas at Austin, 2014.

[70] M. L. Kuntzman, J. Gloria Lee, N. N. Hewa-Kasakarage, D. Kim, and N. A. Hall, "Micromachined piezoelectric microphones with in-plane directivity," *Appl. Phys. Lett.*, vol. 102, no. 5, pp. 10–14, 2013.

[71] M. L. Kuntzman, D. Kim, and N. A. Hall, “Microfabrication and experimental evaluation of a rotational capacitive micromachined ultrasonic transducer,” *J. Microelectromechanical Syst.*, vol. 24, no. 2, pp. 404–413, 2014.

[72] T. Shivok, “MEMS polymumps-based miniature microphone for directional sound sensing,” Naval Postgraduate School, 2007.

[73] MEMSCAP, “PolyMUMPs and MEMS Multi Project Wafer Service,” 2018. [Online]. Available: http://www.memscap.com/products/mumps/polymumps. [Accessed: 23-Aug-2018].

[74] D. Antonios, “Characterization of The MEMS directional sound sensor fabricated using The SOIMUMPS process,” Naval Postgraduate School, 2008.

[75] N. Muamad, “Characterization of MEMS a directional microphone with solid and perforated wings,” Naval Postgraduate School, 2009.

[76] K. Simsek, “Developing a capacitance readout circuitry for a directional MEMS sound sensor and sound source localization in a sensor network environment,” Naval Postgraduate School, 2009.

[77] S. C. W. Harrison, “Free field modeling of a MEMS-based pressure gradient microphone,” Naval Postgraduate School, 2009.

[78] P. An, W. Yuan, and S. Ren, “MEMS biomimetic acoustic pressure gradient sensitive structure for sound source localization.,” *Sensors (Basel).*, vol. 9, no. 7, pp. 5637–48, Jan. 2009.

[79] M. Touse, “Design, fabrication, and characterization of a microelectromechanical directional microphone,” Naval Postgraduate School, 2011.

[80] M. Touse, J. Sinibaldi, K. Simsek, J. Catterlin, S. Harrison, and G. Karunasiri, “Fabrication of a microelectromechanical directional sound sensor with electronic readout using comb fingers,” *Appl. Phys. Lett.*, vol. 96, no. 17, p. 173701, 2010.

[81] M. Touse, J. Sinibaldi, and G. Karunasiri, “MEMS directional sound sensor with simultaneous detection of two frequency bands,” in *2010 IEEE Sensors*, 2010, pp. 2422–2425.

[82] A. Ishfaque and B. Kim, “Design of centrally supported biomimetic MEMS microphone for acoustic source localization,” in *ASME Micro- and Nano-Systems Engineering and Packaging*, 2015, pp. 1–4.

[83] A. Ishfaque and B. Kim, “Squeeze film damping analysis of biomimetic micromachined microphone for sound source localization,” *Sensors Actuators A Phys.*, vol. 250, pp. 60–70, Oct. 2016.

[84] A. Ishfaque and B. Kim, “Analytical modeling of squeeze air film damping of biomimetic MEMS directional microphone,” *J. Sound Vib.*, vol. 375, pp. 422–435, Aug. 2016.

[85] D. Wilmott, F. Alves, and G. Karunasiri, “Bio-inspired miniature direction

finding acoustic sensor," *Sci. Rep.*, vol. 6, no. 29957, pp. 1–8, Jul. 2016.

[86] H. Liu and M. Yu, "Fly-Ear Inspired Miniature Acoustic Sensors," in *The 6th International Workshop on Advaned Smart Material and Smart Structures Technology*, 2011, pp. 1–8.

[87] H. Liu, X. Zhang, and M. Yu, "Understanding fly-ear inspired directional microphones," in *SPIE Sensors and Smart Structures Technologies for Civil, Mechanical, and Aerospace Systems*, 2009, vol. 7292, p. 72922M.

[88] M. Yu and H. Liu, "Biology-inspired miniature system and method for sensing and localizing acoustic signals," US8503693B2, 2013.

[89] D. N. Gee, H. J. Liu, L. Currano, and M. Yu, "Enhanced directional sensitivity of a biomimetic MEMS acoustic localization sensor," *Photonic Microdevices/Microstructures Sens. Ii*, vol. 7682, pp. 1–8, 2010.

[90] H. Liu, L. Currano, D. Gee, T. Helms, and M. Yu, "Understanding and mimicking the dual optimality of the fly ear," *Sci. Rep.*, vol. 3, no. 2489, pp. 1–6, 2013.

[91] A. P. Lisiewski, H. J. Liu, M. Yu, L. Currano, and D. Gee, "Fly-ear inspired micro-sensor for sound source localization in two dimensions," *J. Acoust. Soc. Am.*, vol. 129, no. 5, pp. EL166-EL171, 2011.

[92] N. Ono, A. Saito, and S. Ando, "Bio-mimicry Sound Source Localization with Gimbal Diaphragm.," *IEEJ Trans. Sensors Micromachines*, vol. 123, no. 3, pp. 92–97, 2003.

[93] N. Ono, A. Saito, and S. Ando, "Design and experiments of bio-mimicry sound source localization sensor with gimbal-supported circular diaphragm," in *TRANSDUCERS '03. 12th International Conference on Solid-State Sensors, Actuators and Microsystems.*, 2003, pp. 935–938.

[94] R. N. Miles, Y. Liu, Q. Su, and W. Cui, "A silicon directional microphone with second-order directivity," in *19th International Congress on Acoustics*, 2007, pp. 1–6.

[95] R. Miles, "High-order directional microphone diaphragm," US6963653B1, 2005.

[96] S. Albahri, "Design and development of second order MEMS sound pressure gradient sensor," State University of New York at Binghamton, 2011.

[97] X. Huo, "Design , analysis and characterization of a miniature second-order directional microphone," State University of New York at Binghamton, 2009.

[98] C.-C. Chen and Y.-T. Cheng, "Physical analysis of a biomimetic microphone with a central-supported (C-S) circular diaphragm for sound source localization," *IEEE Sens. J.*, vol. 12, no. 5, pp. 1504–1512, Oct. 2011.

[99] T. L. Wiley, R. Chappell, L. Carmichael, D. M. Nondahl, and K. J. Cruickshanks, "Changes in hearing thresholds over 10 years in older adults.," *J. Am. Acad. Audiol.*, vol. 19, no. 4, pp. 281–92, Apr. 2008.

[100] H. W. Turbull, *Theory of Equations*, 4th ed. London: Oliver and Boyd, 1947.

[101] M. A. Hopcroft, W. D. Nix, and T. W. Kenny, "What is the Young's Modulus of Silicon?," *J. Microelectromechanical Syst.*, vol. 19, no. 2, pp. 229–238, Mar. 2010.

[102] MEMSCAP, "SOIMUMPs Design Handbook a MUMPs® process," 2002.

[103] Polytec, "Laser Doppler vibrometry." [Online]. Available: https://www.polytec.com/uk/vibrometry/technology/. [Accessed: 24-Aug-2018].

[104] MEMSCAP, "PiezoMUMPs ™ Design Handbook a MUMPs® process," 2014.

[105] J. Karki, "Signal Conditioning Piezoelectric Sensors," 2000.

[106] E. B. Brixen, "Facts about speech intelligibility," *DPA Microphones*, 2016. [Online]. Available: https://www.dpamicrophones.com/mic-university/facts-about-speech-intelligibility. [Accessed: 24-Sep-2018].

[107] I. N. Bespalova, G. Van Camp, S. J. Bom, D. J. Brown, K. Cryns, A. T. DeWan, A. E. Erson, K. Flothmann, H. P. Kunst, P. Kurnool, T. A. Sivakumaran, C. W. Cremers, S. M. Leal, M. Burmeister, and M. M. Lesperance, "Mutations in the Wolfram syndrome 1 gene (WFS1) are a common cause of low frequency sensorineural hearing loss.," *Hum. Mol. Genet.*, vol. 10, no. 22, pp. 2501–2508, Oct. 2001.

[108] L. E. Jackson and H. Silverstein, "Meniere's Disease: Diagnosis, Natural History, and Current Management Lance E. Jackson Herbert Silverstein Balance/Dizziness/Vestibular Issues Medical & Surgical 1161," *Audiology online*, 2002. [Online]. Available: https://www.audiologyonline.com/articles/meniere-s-disease-diagnosis-natural-1161. [Accessed: 21-Sep-2018].

[109] G. Barillaro, A. Molfese, A. Nannini, and F. Pieri, "Analysis, simulation and relative performances of two kinds of serpentine springs," *J. Micromechanics Microengineering*, vol. 15, no. 4, pp. 736–746, 2005.

[110] InvenSense, "INMP411 Omnidirectional Microphone with Bottom Port and Analog Output GENERAL DESCRIPTION," 2014.

[111] Knowles Electronics, "Pro/ENGINEER-TD-24621-000," 2013.

[112] Burr-Brown, "INA141 Precision, Low Power, G = 10, 100 Instrumentation Amplifier," 2009.

[113] D. Homentcovschi, M. J. Aubrey, and R. N. Miles, "A two-dimensional model of a directional microphone: calculation of the normal force and moment on the diaphragm.," *J. Acoust. Soc. Am.*, vol. 119, no. 2, pp. 756–68, Feb. 2006.

[114] T. B. Gabrielson, "Mechanical-thermal noise in micromachined acoustic and vibration sensors," *IEEE Trans. Electron Devices*, vol. 40, no. 5, pp. 903–909, May 1993.

[115] R. N. Miles, W. Cui, Q. T. Su, and D. Homentcovschi, “A MEMS low-noise sound pressure gradient microphone with capacitive sensing,” *J. Microelectromechanical Syst.*, vol. 24, no. 1, pp. 241–248, 2015.

[116] R. Bauer, Y. Zhang, J. C. Jackson, W. M. Whitmer, W. O. Brimijoin, M. A. Akeroyd, D. Uttamchandani, and J. F. C. Windmill, “Influence of microphone housing on the directional response of piezoelectric MEMS microphones inspired by Ormia Ochracea,” *IEEE Sens. J.*, vol. 17, no. 17, pp. 5529–5536, Jul. 2017.

[117] Y. Zhang, R. Bauer, W. M. Whitmer, W. O. Brimijoin, D. Uttamchandani, J. F. C. Windmill, and J. C. Jackson, “Development of a biologically inspired MEMS microphone,” in *2017 IEEE SENSORS*, 2017, pp. 1–3.

Appendix A: Preamplifier (used in Chapter 3)

The details of how to calculate the values of resistors and capacitors of a high-order active filter are comprehensively introduced in the reference document (Texas Instruments Application Report SLO1049B – Active Low-Pass Filter Design). The mathematic principle of a high-order high-pass filter is similar to the ones of a high-order low pass filter. According to the reference and the design requirements, the Butterworth-type filters are chosen due to their maximally flat response in the pass-band and moderate overshoot and ringing transient response. In addition, in terms of the architecture of the filter, the Sallen-Key type is chosen since its output gain of this architecture is positive. To simplify the design process, a fourth-order active filter can be built by two cascading second-order filters. The following calculating process is based on the method described in the reference.

Fourth-order low-pass Butterworth filter – Gain =1

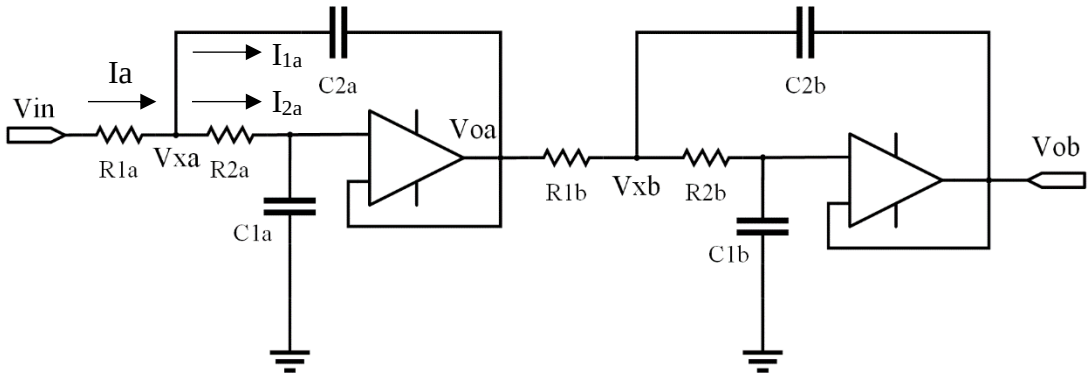

Stage a Stage b

Using Stage a (i.e. a second-order low-pass filter) as an example, the transfer function between the output stage and the input stage can be derived as follow

$$\left.\begin{aligned} &V_{x1} - V_{o1} = I_{2a}R_{2a} \\ &V_{oa} = \frac{I_{2a}}{j\omega C_{1a}} \\ &V_{in} = I_a R_{1a} + V_{xa} \\ &V_{xa} - V_{oa} = \frac{I_{1a}}{j\omega C_2} \\ &I_{1a} + I_{2a} = I_a \end{aligned}\right\} \Rightarrow \begin{aligned} I_{1a} &= -\omega^2 V_{oa} C_{1a} C_{2a} R_{2a} \\ I_{2a} &= j\omega V_{oa} C_{1a} \end{aligned}$$

$$\Rightarrow \frac{V_{oa}}{V_{in}} = \frac{1}{-\omega^2 R_{1a}R_{2a}C_{1a}C_{2a} + j\omega C_{1a}(R_{1a}+R_{2a})+1},$$

so that

$$H_a(f) = \frac{V_{oa}}{V_{in}} = \frac{1}{(j2\pi f)^2 R_{1a}R_{2a}C_{1a}C_{2a} + j2\pi f C_{1a}(R_{1a}+R_{2a})+1}. \quad [A.1]$$

As the fourth-order filter is a cascade of two second-order filters, thus the complete transfer function can be expressed as

$$\begin{aligned} H_{LP}(f) &= H_a(f) \times H_b(f) \\ &= \frac{1}{[(j2\pi f)^2 R_{1a}R_{2a}C_{1a}C_{2a} + j2\pi f C_{1a}(R_{1a}+R_{2a})+1][(j2\pi f)^2 R_{1b}R_{2b}C_{1b}C_{2b} + j2\pi f C_{1b}(R_{1b}+R_{2b})+1]}. \end{aligned} \quad [A.2]$$

Generally, a common fourth-order polynomial can be written as

$$H(f) = \frac{K}{\left[-\left(\frac{f}{fc}\right)^2 + \frac{1}{Qafc}jf + 1\right]\left[-\left(\frac{f}{fc}\right)^2 + \frac{1}{Qbfc}jf + 1\right]}, \quad [A.3]$$

Compare Eq. [A.3] with [A.2], then

$$K = 1$$

$$\sqrt{a0_1} = \sqrt{a0_2} = 1$$

$$f_c = \frac{1}{2\pi\sqrt{R_{1a}R_{2a}C_{1a}C_{2a}}} \approx \frac{1}{2\pi\sqrt{R_{1b}R_{2b}C_{1b}C_{2b}}}$$

$$Q_a = \frac{\sqrt{R_{1a}R_{2a}C_{1a}C_{2a}}}{C_{1a}(R_{1a}+R_{2a})}$$

$$Q_b = \frac{\sqrt{R_{1b}R_{2b}C_{1b}C_{2b}}}{C_{1b}(R_{1b}+R_{2b})}$$

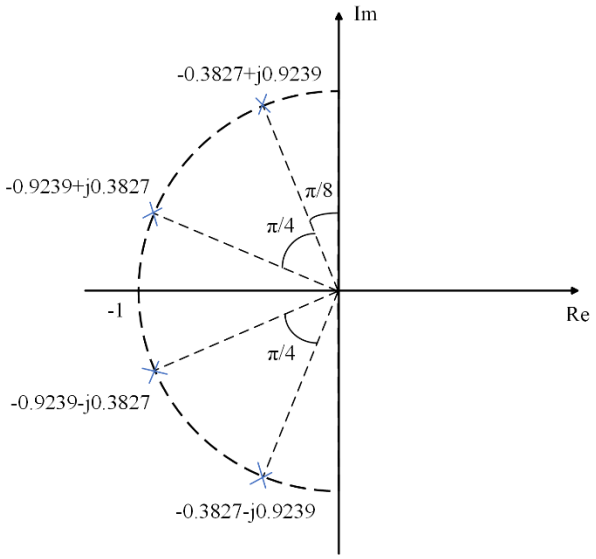

Fig. A.1: A pole-zero diaphragm of a fourth-order filter

The poles of the transfer function are figured out from the following pole-zero diaphragm as in Fig. A.1. Thus, the transfer function can also be written as

$$H(f) = \frac{K}{\left[-\left(\frac{f}{f_c}\right)^2 + 1.8478\frac{jf}{f_c} + 1\right]\left[-\left(\frac{f}{f_c}\right)^2 + 0.7654\frac{jf}{f_c} + 1\right]},$$

where

$Q_a = 0.5412, Q_a = 1.3065.$

Stage a

In terms of Stage a, if assuming that

$$R_{1a} = mR, R_{2a} = R, C_{1a} = C, C_{2a} = nC,$$

then

$$Q_a = \frac{\sqrt{mn}}{m+1} = 0.5412 \Rightarrow m = \frac{-(2Q_a^2 - n) \pm \sqrt{n^2 - 4Q_a^2 n}}{2Q_a^2} \Rightarrow n - 4Q_a^2 > 0, \quad [A.4]$$

$$f_c = \frac{1}{2\pi RC\sqrt{mn}}.$$

If $n = 2.2$,

$m = 5.323, \text{and } \sqrt{mn} = 3.322,$

When the cut-off frequency

$f_c = 20\ kHz, C_{1a} = 10\ nF$

Then,

$C_{2a} = 22\ nF$

Thus,

$R_2 \approx 232\ \Omega \rightarrow 220\Omega \text{ and } R_{1a} = 1.2\ k\Omega$

Substituting the resistor values into Eq. [A.4]

$m = 5.45 \Rightarrow Q = 0.5368 \Rightarrow f_c = 20.892\ kHz.$

Stage b

In terms of Stage b, if assuming that

$R_{1b} = mR, R_{2b} = R, C_{1b} = C, C_{2b} = nC,$

$$Q_b = \frac{\sqrt{mn}}{m+1} = 1.3065 \Rightarrow m = \frac{-(2Q_b^2 - n) \pm \sqrt{n^2 - 4Q_b^2 n}}{2Q_b^2} \Rightarrow n - 4Q_b^2 > 0 \qquad [A.5]$$

$f_c = \frac{1}{2\pi RC\sqrt{mn}}.$

If $n = 22,$

$m = 10.796, \text{and } \sqrt{mn} = 15.411$

When the cut-off frequency

$f_c = 20\ kHz, C_{1a} = 1\ nF.$

then,

$C_{2a} = 22\ nF,$

Thus,

$R_2 \approx 516\ \Omega \rightarrow 499\Omega, R_{1a} = 5.4\ k\Omega.$

Substituting the resistor values into Eq. [A.5]

$m = 10.8 \Rightarrow Q = 1.3063 \Rightarrow f_c = 20.65\ kHz$

Stage a		Stage b	
R1a	1.2 $k\Omega$	R1b	5.4 $k\Omega$
R2a	220 Ω	R2b	499 Ω
C1a	10 nF	C1b	1 nF
C2a	22 nF	C2b	22 nF

Fourth-order high-pass Butterworth filter – Gain = 1

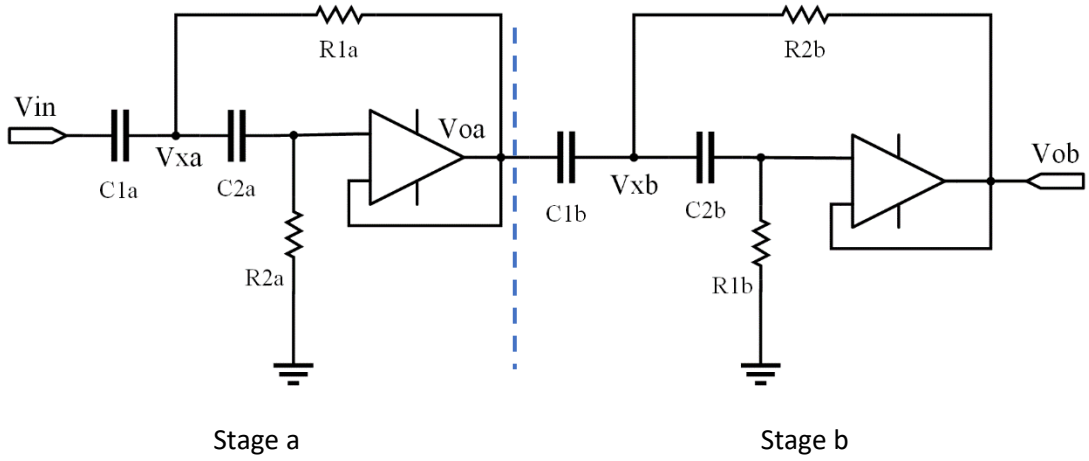

Stage a

In terms of Stage a, if assuming that

$R_{1a} = mR, R_{2a} = R, C_{1a} = C, C_{2a} = nC,$

then

$$Q_a = \frac{\sqrt{mn}}{m+1} = 0.5412 \Rightarrow m = \frac{-(2Q_a^2 - n) \pm \sqrt{n^2 - 4Q_a^2 n}}{2Q_a^2} \Rightarrow n - 4Q_a^2 > 0, \quad [A.6]$$

$f_c = \frac{1}{2\pi RC\sqrt{mn}}.$

If $n = 2.2$,

$m = 5.323$, and $\sqrt{mn} = 3.322$.

When the cut-off frequency

$f_c = 100\ Hz, C_{1a} = 100\ nF,$

then,

$C_{2a} = 220\ nF,$

Thus,

$R_2 \approx 4.65\ k\Omega \rightarrow 4.7\ \text{k}\Omega, R_{1a} = 24\ k\Omega.$

Substituting the resistor values into Eq. [A.6]

$m = 5.1063 \Rightarrow Q = 0.5488 \Rightarrow f_c = 101\ Hz$

Stage b

In terms of Stage b, if assuming that

$R_{1b} = mR, R_{2b} = R, C_{1b} = C, C_{2b} = nC,$

then

$$Q_b = \frac{\sqrt{mn}}{m+1} = 1.3065 \Rightarrow m = \frac{-(2Q_b^2-n)\pm\sqrt{n^2-4Q_b^2 n}}{2Q_b^2} \Rightarrow n - 4Q_b^2 > 0 f_c = \frac{1}{2\pi RC\sqrt{mn}}, \quad \text{[A.7]}$$

$f_c = \frac{1}{2\pi RC\sqrt{mn}}.$

If $n = 22,$

$m = 10.796,$ and $\sqrt{mn} = 15.411.$

When the cut-off frequency

$f_c = 20\ kHz, C_{1a} = 10\ nF,$

then,

$C_{2a} = 220\ nF.$

Thus,

$R_2 \approx 10.33\ \Omega \rightarrow 10\ \text{k}\Omega, R_{1a} = 107\ k\Omega.$

Substituting the resistor values into Eq. [A.7]

$m = 10.7 \Rightarrow Q = 1.3113 \Rightarrow f_c = 103\ Hz.$

Stage a		Stage b	
R1a	24 $k\Omega$	R1b	107 $k\Omega$
R2a	4.7 $k\Omega$	R2b	10 $k\Omega$
C1a	100 nF	C1b	10 nF
C2a	220 nF	C2b	220 nF

Schematic

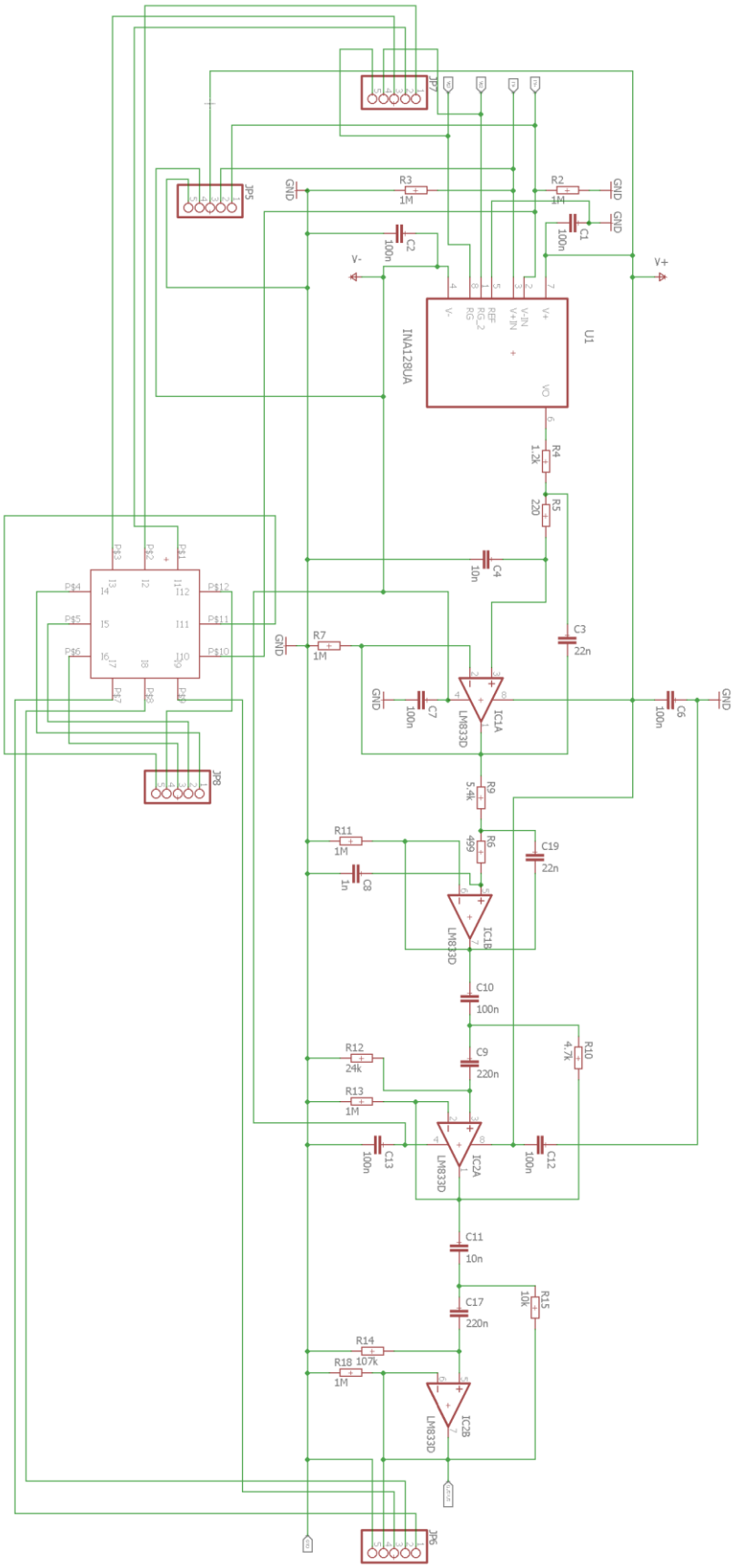
JP7
JP5
GND
R3
1M
R2
1M
C1
100n
C2
100n
V-
V+
INA128UA
U1
R4
1.2k
R5
220
C4
10n
C3
22n
R7
1M
C7
100n
IC1A
LM833D
C6
100n
R9
5.4k
R11
1M
R6
499
C19
22n
C8
1n
IC1B
C10
100n
R12
24k
C9
220n
R10
4.7k
R13
1M
C13
100n
IC2A
C12
100n
C11
10n
C17
220n
R15
10k
R14
R18 107k
1M
IC2B
JP6

Board layout

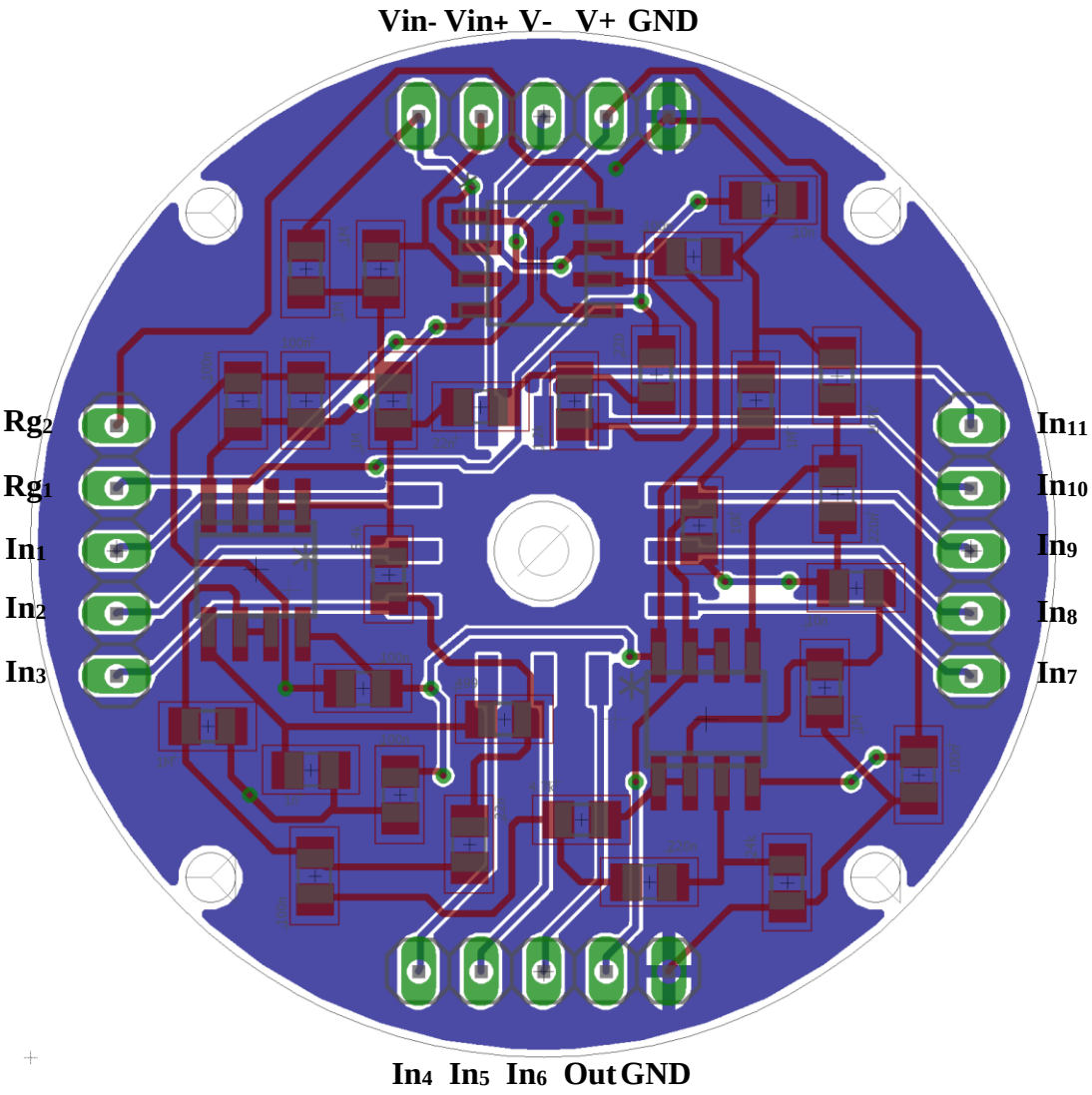

Appendix B: Preamplifier (used in Chapter 4)

Preamplifier of LF operational microphone (for Chapter 4):

Schematic

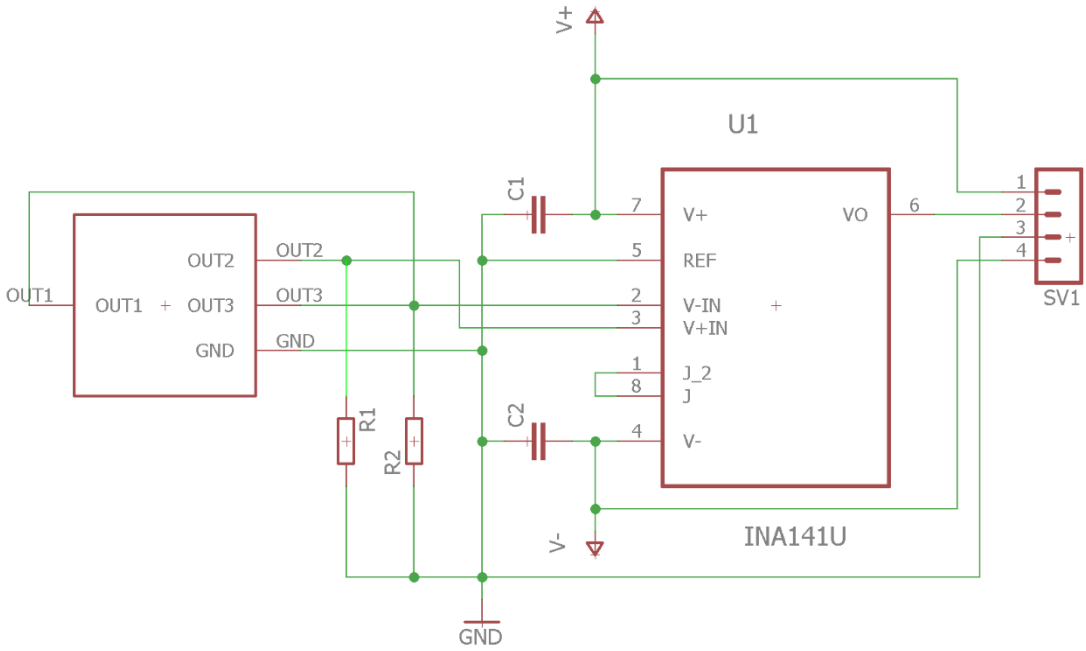

Board layout

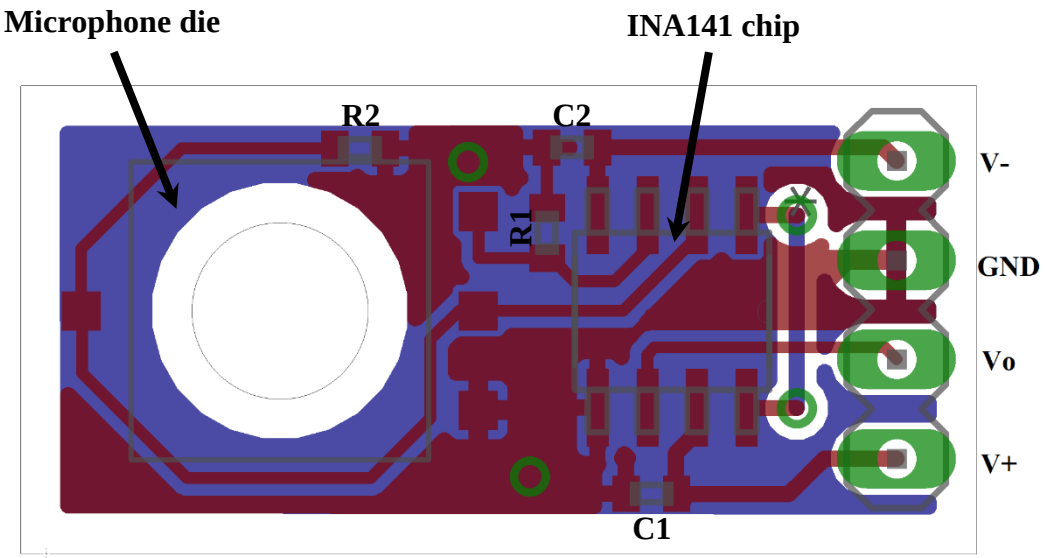

Power dock for preamplifier of LF operational microphone (for Chapter 4):

Schematic

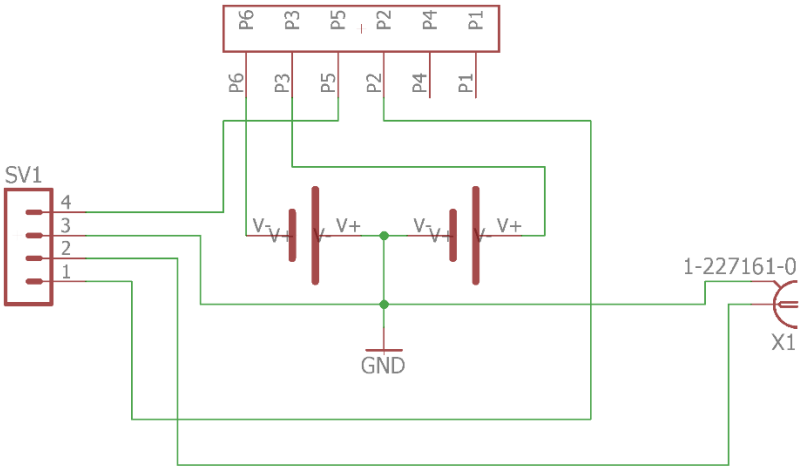

Board layout